Investigating the dynamics of Greenland's glacier-fjord systems

Benjamin Joseph Davison

A thesis submitted for the degree of PhD
at the
University of St Andrews

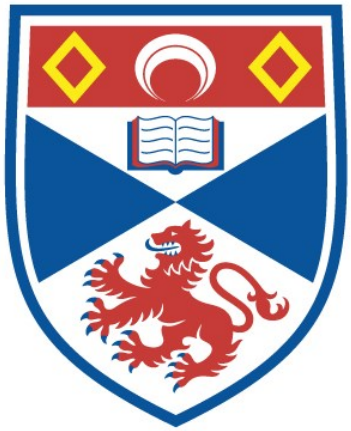

2021

Full metadata for this thesis is available in
St Andrews Research Repository
at:
https://research-repository.st-andrews.ac.uk/

Identifier to use to cite or link to this thesis:

DOI: https://doi.org/10.17630/sta/729

This item is protected by original copyright

This item is licensed under a
Creative Commons Licence

https://creativecommons.org/licenses/by-nc-nd/4.0

Declaration

Candidate's declaration

I, Benjamin Joseph Davison, do hereby certify that this thesis, submitted for the degree of PhD, which is approximately 60,000 words in length, has been written by me, and that it is the record of work carried out by me, or principally by myself in collaboration with others as acknowledged, and that it has not been submitted in any previous application for any degree. Where work has formed part of jointly-authored publications, the contributions of the candidate and the other authors are explicitly indicated below.

Chapter 4

Citation: Davison, B, J., A. J. Sole, T. R., Cowton, J. M. Lea, D. A., Slater, D. Fahrner, and P. W. Nienow (2020). Subglacial drainage evolution modulates seasonal ice flow variability of three tidewater glaciers in southwest Greenland. *Journal of Geophysical Research: Earth Surface*, 125, e2019JF005492. doi: 10.1029/2019JF005492.

Author contributions: B.J.D. and A. J. S. designed the research. A.J.S. wrote the feature tracking code, which B.J.D. used to derive the velocity estimates. J.M.L. and D.F. provided terminus position data and D.A.S. provided the plume model. B.J.D. derived or obtained all other data and analysed the results. B.J.D. wrote the paper, with input from all other authors.

Chapter 5

Citation: Davison, B. J., T. R. Cowton, F. R. Cottier, A. J. Sole (2020). Iceberg melting substantially modifies oceanic heat flux towards a major Greenlandic tidewater glacier. *Nature Communications*, 11, 5983. doi: 10.1038/s41467-020-19805-7.

Author contributions: B.J.D. and T.R.C. designed the research. B.J.D. developed the model code with support of T.R.C. and A.J.S. B.J.D. designed and conducted the simulations and analysis. T.R.C., F.R.C. and A.J.S. supported the interpretation of the model results. B.J.D. led the write up of the manuscript, with contributions from all other authors.

I was admitted as a research student at the University of St Andrews in September 2017. I received funding from an organisation or institution and have acknowledged the funder(s) in the full text of my thesis.

Benjamin Davison
8th February 2021

Supervisor's declaration

I hereby certify that the candidate has fulfilled the conditions of the Resolution and Regulations appropriate for the degree of PhD in the University of St Andrews and that the candidate is qualified to submit this thesis in application for that degree.

Tom Cowton
8th February 2021

Permission for publication

In submitting this thesis to the University of St Andrews we understand that we are giving permission for it to be made available for use in accordance with the regulations of the University Library for the time being in force, subject to any copyright vested in the work not being affected thereby. We also understand, unless exempt by an award of an embargo as requested below, that the title and the abstract will be published, and that a copy of the work may be made and supplied to any bona fide library or research worker, that this thesis will be electronically accessible for personal or research use and that the library has the right to migrate this thesis into new electronic forms as required to ensure continued access to the thesis.

I, Benjamin Joseph Davison, confirm that my thesis does not contain any third-party material that requires copyright clearance.

The following is an agreed request by candidate and supervisor regarding the publication of this thesis:

Printed copy

No embargo on print copy.

Electronic copy

No embargo on electronic copy.

Benjamin Davison
8th February 2021

Tom Cowton
8th February 2021

Underpinning Research Data or Digital Outputs

Candidate's declaration

I, Benjamin Joseph Davison, hereby certify that no requirements to deposit original research data or digital outputs apply to this thesis and that, where appropriate, secondary data used have been referenced in the full text of my thesis.

Benjamin Davison
8th February 2021

Abstract

Over the past two decades, Greenland's tidewater glaciers have dramatically retreated, thinned and accelerated, contributing significantly to sea level rise. This change in glacier behaviour is thought to have been triggered by increasing atmospheric and ocean temperatures, and mass loss from Greenland's tidewater glaciers is predicted to continue this century. Substantial research during this period of rapid glacier change has improved our understanding of Greenland's glacier-fjord systems. However, many of the processes operating in these systems that ultimately control the response of tidewater glaciers to changing atmospheric and oceanic conditions are poorly understood. This thesis combines modelling and remote sensing to investigate two particularly poorly-understood components of glacier-fjord systems, with the ultimate aim of improving understanding of recent glacier behaviour and constraining the stability of the ice sheet in a changing climate.

The research presented in this thesis begins with an investigation into the dominant controls on the seasonal dynamics of contrasting tidewater glaciers draining the Greenland Ice Sheet. To do this, high resolution estimates of ice velocity were generated and compared with detailed observations and modelling of the principal controls on seasonal glacier flow, including terminus position, ice mélange presence or absence, ice sheet surface melting and runoff, and plume presence or absence. These data revealed characteristic seasonal and shorter-term changes in ice velocity at each of the study glaciers in more detail than was available from previous remote sensing studies. Of all the environmental controls examined, seasonal evolution of subglacial hydrology (as inferred from plume observations and modelling) was best able to explain the observed ice flow variations, despite differences in geometry and flow of the study glaciers. The inferred relationships between subglacial hydrology and ice dynamics were furthermore entirely consistent with process-understanding developed at land-terminating sectors of the ice sheet. This investigation provides a more detailed understanding of tidewater glacier subglacial hydrology and its interaction with ice dynamics than was previously available and suggests that interannual variations in meltwater supply may have limited influence on annually averaged ice velocity.

The thesis then shifts its attention from the glacier part of the system into the fjords, focusing on the interaction between icebergs, fjord circulation and fjord water properties. This focus on icebergs is motivated by recent research revealing that freshwater produced

by iceberg melting constitutes an important component of fjord freshwater budgets, yet the impact of this freshwater on fjords was unknown. To investigate this, a new model for iceberg-ocean interaction is developed and incorporated into an ocean circulation model.

This new model is first applied to Sermilik Fjord — a large fjord in east Greenland that hosts Helheim Glacier, one of the largest tidewater glaciers draining the ice sheet — to further constrain iceberg freshwater production and to quantify the influence of iceberg melting on fjord circulation and water properties. These investigations reveal that iceberg freshwater flux increases with ice sheet runoff raised to the power ~0.1 and ranges from ~500-2500 m^3 s^{-1} during summer, with ~40% of that produced below the pycnocline. It is also shown that icebergs substantially modify the temperature and velocity structure of Sermilik Fjord, causing 1-5°C cooling in the upper ~100 m and invigorating fjord circulation, which in turn causes a 10-40% increase in oceanic heat flux towards Helheim Glacier. This research highlights the important role of icebergs in Greenland's iceberg congested fjords and therefore the need to include them in future studies examining ice sheet – ocean interaction.

Having investigated the effect of icebergs on fjord circulation in a realistic setting, this thesis then characterises the effect of submarine iceberg melting on water properties near the ice sheet – ocean interface by applying the new model to a range of idealised scenarios. This near-glacier region is one which is crucial for constraining ocean-driven retreat of tidewater glaciers, but which is poorly-understood. The simulations show that icebergs are important modifiers of glacier-adjacent water properties, generally acting to reduce vertical variations in water temperature. The iceberg-induced temperature changes will generally increase submarine melt rates at mid-depth and decrease rates at the surface, with less pronounced effects at greater depth. This highlights another mechanism by which iceberg melting can affect ice sheet – ocean interaction and emphasises the need to account for iceberg-ocean interaction when simulating ocean-driven retreat of Greenland's tidewater glaciers.

In summary, this thesis has helped to provide a deeper understanding of two poorly-understood components of Greenland's tidewater glacier-fjord systems: (i) interactions between subglacial hydrology and ice velocity, and; (ii) iceberg-ocean interaction. This research has enabled more precise interpretations of past glacier behaviour and can be used to inform model development that will help constrain future ice sheet mass loss in response to a changing climate.

Acknowledgements

Firstly, I must express my gratitude to the University of St Andrews and to the Scottish Alliance for Geoscience, Environment and Society (SAGES) for funding and supporting me as a research student. The Department of Geography and Sustainable Development at the University of St Andrews has been a welcoming and accommodating host throughout my time there. Through SAGES, I have been lucky to have the opportunity to engage with researchers in a wide range of fields, which has been both interesting and enriching.

I have been fortunate enough to have enjoyed the support of a great collection of supervisors and colleagues. First and foremost amongst these is Tom Cowton, my principal supervisor, without whom this research would have been impossible. Tom took me on as his first PhD student – a baptism of fire, perhaps – yet he demonstrated supervisory wisdom that one might only expect from the most experienced. He gave me the freedom and independence to follow my curiosity, whilst teaching me to make sound scientific judgements and gently guiding me back on track when my tendency for bigger (rather than smarter) ideas got the better of me. Not least, I am grateful to Tom for accommodating my numerous excursions to Sheffield and Cornwall, which were perhaps more frequent and of longer duration than we first agreed. Andrew Sole, my supervisor in Sheffield, has been a wonderful friend and mentor over the last six years and inspired me to embark on this journey during my undergraduate years. Andrew has been unfailingly generous with his time and energy – very often going far beyond the call of duty as a supervisor - and has always endeavoured to support and create opportunities for me. Thanks also for several brilliant trips to Greenland, which will live long in the memory. My other supervisors have been instrumental in my enjoyment and success during the course of preparing and writing this thesis, and I am extremely grateful to each: Pete Nienow has provided wise council whenever it was needed, and he never failed to remind me why we do this and that good research should be balanced by numerous trips into the Scottish Highlands; Finlo Cottier, for encouraging me to be ambitious; and Doug Benn, for welcoming me into the St Andrews glaciology community. In addition to this huge supervisory support, I have also benefitted from insightful discussions, support and data provision from several colleagues around the UK and elsewhere. Amongst these, I am particularly grateful to everyone in the St Andrews Glaciology group, who made my time at St Andrews a pleasure, and to Alexis Moyer, for generously sharing her data at short notice and despite being in the middle of a house move – a heroic effort.

The entertainment and support provided by friends has been a defining feature of the last three-and-a-half years. In the day-to-day work, it is my office mates and PhD colleagues who made each day a pleasure - particular kudos to Solene, for always finding the fun, and to Sonam, for being a fantastic neighbour and supportive friend during a tough year. After each day at work, the climbing community in Dundee would never fail to make me laugh (usually by lowering the tone) and always made Scotland feel like a home, particularly Duncan, Didi, Sam and Rob. Similarly, the climbing community in Sheffield always welcomed me back with open arms on each of my many trips there, particularly Dave and Mina. On the subject of regular trips, I am forever grateful to Tash and Doug in Cornwall for tolerating my comings and goings with remarkable equanimity.

I am especially grateful to my family, particularly Mum and Dad, for their unwavering support and limitless patience with my decision making. Thank you for helping me pierce through the fog of uncertainty whenever I lost my way. And lastly, but very much not least, my thanks go to Sarah, for always being by my side even when we were apart and for providing the very best of times when we were together.

.

Table of contents

List of figures

Supplementary Figures

List of tables

Supplementary Tables

Chapter 1 - General introduction

The Arctic is one of the most dynamic and rapidly changing environments on Earth. There are numerous examples one can draw on to illustrate the intensity and extent of these changes, which are apparent across all components of the Arctic cryosphere – permafrost, snow cover, sea ice and land ice. Pan-Arctic snow cover extent in June reduced by 19.8% per decade over the period 1979-2014 (Bokhorst et al., 2016). Based on a global network of observations, permafrost, which extends over ~23 million km^2 in the northern hemisphere (Zhang et al., 2008), warmed by 0.29±0.12°C during the period 2007 to 2016, largely due to increasing air temperature in the northern hemisphere (Biskaborn et al., 2019). In the Arctic Ocean, annual average sea ice extent decreased by 2.4% per decade during the 1979-2017 period (Maksym, 2019). Widespread Arctic land ice loss has also occurred over the last three decades (Figure 1.1; Moon et al. (2018)), affecting all major Arctic regions including Alaska (loss of ~38 Gt ice per year between 2003-2009), the Canadian Arctic (~60 Gt/year), the Russian High Arctic (~11 Gt/year), Svalbard (~5 Gt/year), Iceland (~11 Gt/year), and Greenland and its surrounding ice caps and glaciers (~360 Gt/year and ~38 Gt/year, respectively).

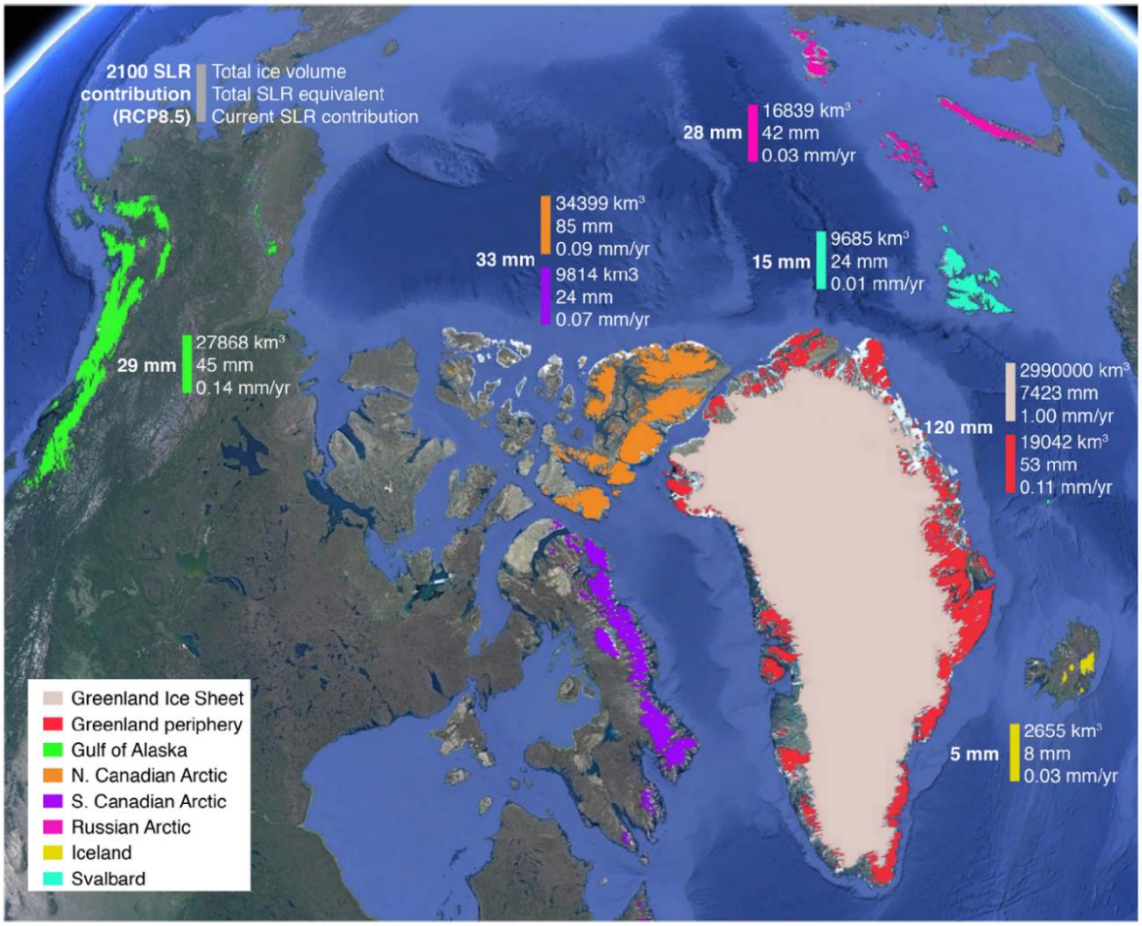

Figure 1.1. Location of Greenland and Arctic land ice. Values shown are total ice volume (km^3), equivalent sea level rise potential (mm), current (2003-2009) sea level rise contribution (mm/year) and projected contribution to sea level rise during 2006-2100 (mm) for the RCP8.5 emission scenario. Reproduced from Moon et al. (2018a).

Changes in the Arctic have global implications. Carbon pools (both carbon dioxide and methane) in permafrost regions represent a large reservoir of greenhouse gases. Thaw of permafrost exposes these reservoirs to microbial breakdown, leading to carbon release. Observed and projected emissions of carbon from thawing permafrost are comparable to, for example, land-use change (~1 Pg carbon per year), potentially creating a positive feedback between climate warming and permafrost thaw (Schuur et al., 2015). As another example, freshwater release from the Greenland Ice Sheet may slow the Atlantic Meridional Overturning Circulation by progressively reducing deep convection during winter (Böning et al., 2016), which has the potential to disrupt global ocean circulation and climate.

Perhaps the most pressing impact to society due to changes in the Arctic is sea level rise. In the Arctic, the Greenland Ice Sheet is the largest body of land ice, containing enough

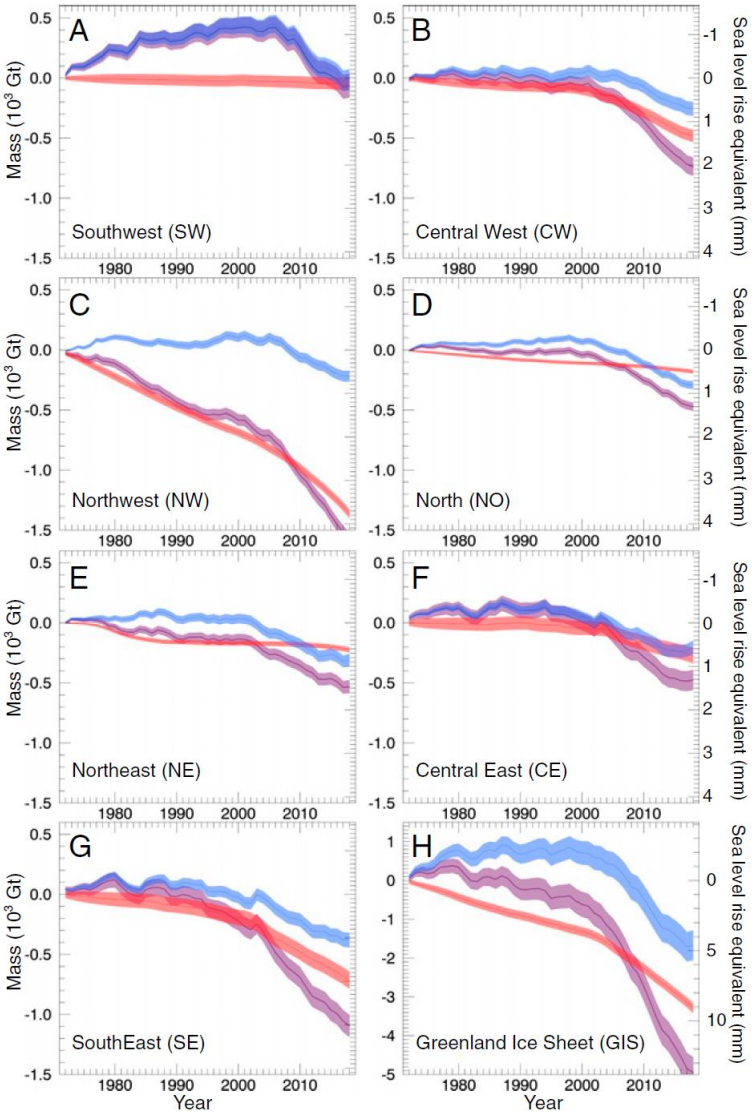

Figure 1.2. Cumulative anomalies in Greenland Ice Sheet surface mass balance (blue), discharge (red) and mass (purple). Reproduced from Mouginot et al. (2019).

freshwater to raise global sea level by around 7 m, were it to melt entirely. Complete loss of the Greenland Ice Sheet is not likely to occur within the next several thousand years (e.g. Gregory et al., 2020). However, it is already a major and growing contributor to sea level rise: from 1972-2018, the Greenland Ice Sheet caused global mean sea level to rise by 13.7±1.1 mm (Figure 1.2; Mouginot et al. (2019)). During the period 1993-2014 it was the fastest growing contributor to global mean sea level rise (Chen et al., 2017) and during 2005 to 2016 it was the largest terrestrial contributor to global sea level rise (Meredith et al., 2020). Over the 21st century, the Greenland Ice Sheet is projected to contribute 8-23 cm to global mean sea level rise under RCP4.5 (Aschwanden et al., 2019). Sea level rise of this magnitude is expected to cause (amongst other things) reductions in biodiversity

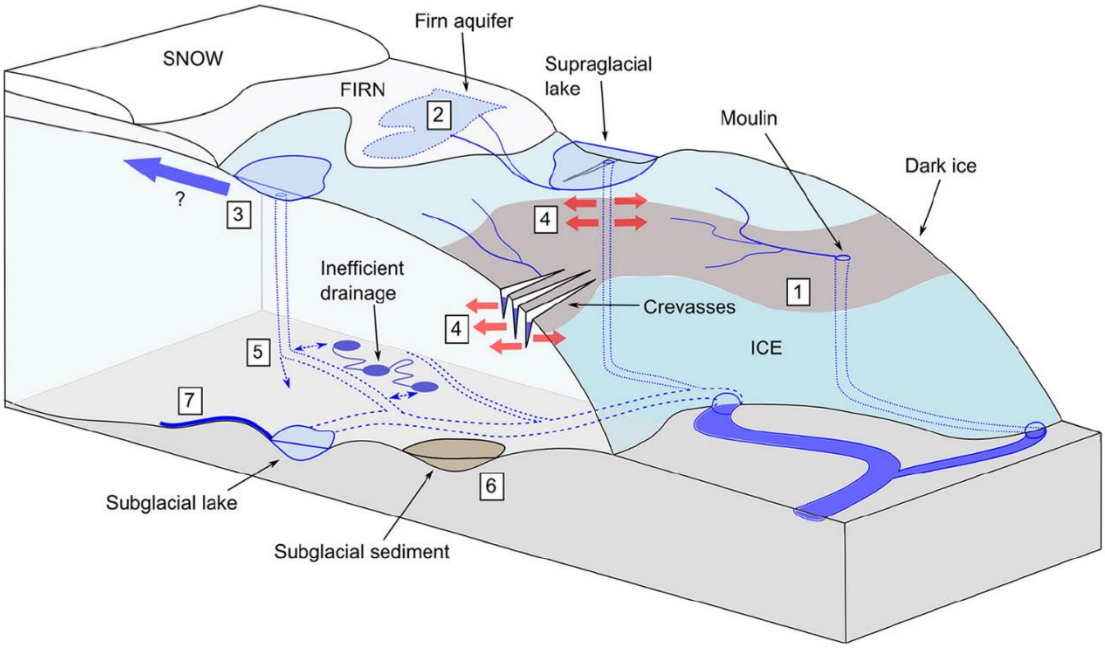

Figure 1.3. Hydrology of land-terminating sectors of the Greenland Ice Sheet.Numbers refer to different processes: (1) darkening of the ice sheet; (2) firn densification; (3) crevasse opening; (4) cryo-hydrologic warming; (5) channel growth; (6) sediment deformation, and; (7) basal melting. Reproduced from Nienow et al. (2017).

and habitat functionality, and (in the absence of effective adaptation) cause an increase in annual flood damages by 2-3 orders of magnitude (Meredith et al., 2020).

The Greenland Ice Sheet has been losing mass overall because the mass lost due to both ice sheet melting and the calving of icebergs is greater than the mass gained through snowfall. Melting occurs both at the ice sheet surface and where the ice sheet meets the ocean, with melting in the latter environment termed submarine melting. Meltwater produced at the ice sheet surface can refreeze in the surface snow pack, in which case it does not cause the ice sheet to lose mass, or it can flow off the sheet through drainage networks on, within and beneath the ice (Figure 1.3). Because the surface of glaciers and ice sheets are so crevassed, the majority of surface-derived meltwater drains to the base of the ice before being discharged into proglacial rivers or, where the ice sheet meets the ocean, into fjords (Figure 1.4). The calving of icebergs also occurs where the ice sheet meets the ocean, and so mass loss to the ocean due to both calving and submarine melting is collectively called ice discharge. During the period 1972-2018, ice discharge caused 66±8% of mass loss from the Greenland Ice Sheet (Mouginot et al., 2019).

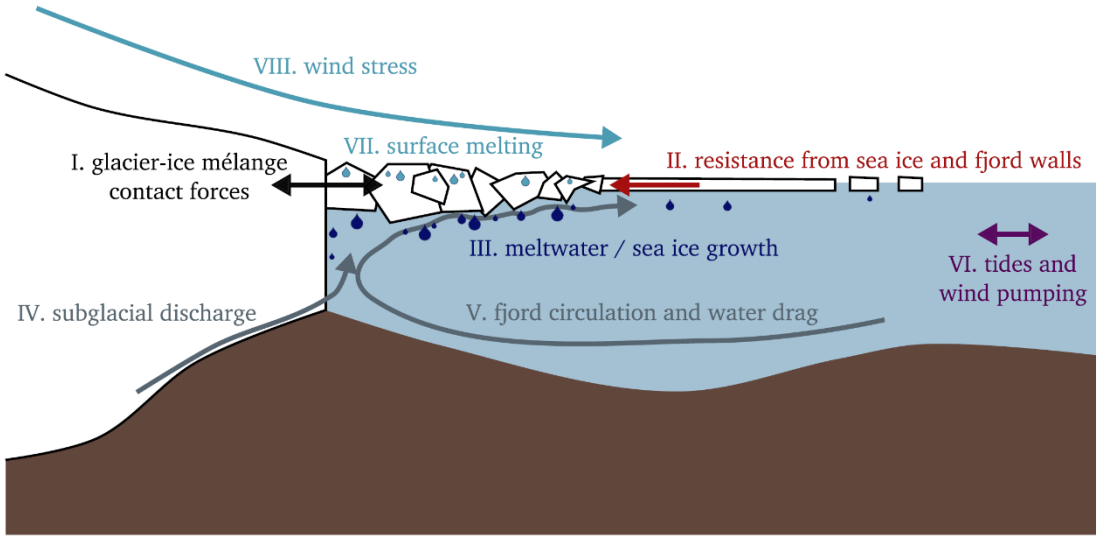

Figure 1.4. Schematic of a tidewater glacier-fjord system.Reproduced from Amundson et al. (2020).

Ice discharge from the Greenland Ice Sheet occurs through tidewater glaciers. Tidewater glaciers are fast-flowing (relative to the rest of the ice sheet), topographically-constrained rivers of ice that rapidly transport ice from the interior to the ocean, where they lose mass due to submarine melting and calving. Over 230 outlet glaciers drain the ice sheet. They typically range in width from 1 to 10 km, and depth from 200 to 1000 m. Ice velocity of tidewater glaciers can range from 1 to 50 metres per day, but all outlet glaciers measured to date are characterised by substantial variability in their flow speed over timescales of days to decades (Amundson et al., 2020; King et al., 2018).

This thesis is motivated in large part by the need to understand this variability in the ice discharge of tidewater glaciers, because of their substantial contribution to Greenland Ice Sheet mass loss and potential for rapid change (Chen et al., 2017; Mouginot et al., 2019). Over the past several decades, Greenland's tidewater glaciers have substantially retreated (Bunce et al., 2018), thinned (Krabill et al., 2004; Pritchard et al., 2009) and accelerated (King et al., 2020). These changes resulted in a 14% increase in ice discharge in 2007-2018 compared to 1985-1999 (King et al., 2020). These changes occurred at a time of atmospheric and oceanic warming, suggesting that both may have influenced tidewater glacier flow and calving.

Greenland's tidewater glaciers flow into fjords, which connect them to the open ocean. Therefore, tidewater glaciers are exposed to changes in both atmospheric and oceanic conditions, which can act independently and together to influence tidewater glacier

behaviour (Figure 1.4). Meltwater produced at the ice sheet surface can drain to and lubricate the base of tidewater glaciers, causing them to flow faster towards the ocean (Moon et al., 2014; Vijay et al., 2019), often resulting in more iceberg calving. This meltwater is eventually discharged into fjords from the base of the tidewater glaciers, often several hundred metres below sea level. This freshwater is less dense than the fjord water, and so it rises towards the fjord surface after entering the fjord, invigorating the fjord circulation (Straneo & Cenedese, 2015). In this way, surface melting caused by atmospheric processes allows changes in the open ocean to be communicated more rapidly along fjords to tidewater glaciers (Cowton et al., 2016a). Similarly, ocean warming can lead to faster submarine melting of tidewater glaciers (Sciascia et al., 2013; Xu et al., 2013), which can in turn lead to greater mass loss through calving (Cowton et al., 2019; Ma & Bassis, 2019; O'Leary & Christoffersen, 2013). If mass loss through calving and submarine melting is greater than that supplied through ice flow, the glacier will retreat, which can lead to unstable acceleration and thinning (Pfeffer, 2007). The resultant lowering of the ice surface would in turn lead to greater surface melting and can lead to further retreat and thinning, creating a positive feedback (Pfeffer, 2007; Schoof, 2007). The calving of icebergs from tidewater glaciers often chokes the fjord with icebergs, which can buttress the glacier and limit further calving (Amundson et al., 2020). These icebergs melt as they transit fjords (Enderlin et al., 2016; Moon et al., 2017; Moyer et al., 2019), affecting the properties and circulation of those fjords. In this way, investigations of tidewater glacier dynamics must acknowledge the entire glacier-fjord systems, in which interactions between the ice sheet, climate and ocean occur. This thesis focuses on these interactions and on improving our understanding of glacier-fjord systems as a whole.

1.1 Outline of thesis

This thesis aims to improve our understanding of glacier-fjord systems and their interactions with the atmosphere and ocean through investigation of tidewater glacier and fjord dynamics. It combines satellite-based remote sensing with numerical modelling to examine several poorly understood components of glacier-fjord systems – ice flow variability, subglacial hydrology, submarine melting and fjord circulation – and the interactions between those components. It considers both real and idealised environments, and a range of tidewater glacier and fjord geometries, in order to seek conclusions that can be applied to a wide range of tidewater glaciers draining the Greenland Ice Sheet. By

focusing on poorly-understood and difficult-to-observe elements of these crucial systems, this thesis provides process understanding and environmental constraints required to both understand past ice sheet change and improve projections of future ice sheet change. The work presented in this thesis is divided into two broad themes, focusing on atmosphere-ice sheet and ocean-ice sheet interactions in turn.

1. **Assessing the influence of the atmosphere on seasonal tidewater glacier dynamics**
   The primary mechanism by which changes in atmospheric conditions can affect seasonal ice dynamics is through lubrication of the glacier base. This thesis examines the nature of subglacial water flow beneath tidewater glaciers and the resulting impact of that water flow on ice dynamics. Several contrasting tidewater glaciers are considered, revealing consistent interactions between subglacial hydrology and tidewater glacier dynamics on seasonal timescales. Many other factors affecting short-term tidewater glacier dynamics are also considered, including changes in glacier terminus position and ice mélange buttressing.

2. **Quantifying the influence of icebergs on ice sheet - ocean interaction**
   This theme focuses on a little-studied aspect of ice sheet – ocean interaction: submarine iceberg melting. As icebergs melt within Greenland's fjords, they cool and freshen the surrounding water, which can in turn lead to mixing and circulation within the fjord, affecting fjord-shelf exchange and ice sheet-ocean interaction. This thesis explores how iceberg melting affects the temperature of the water column at the interface between the ice sheet and the ocean, which ultimately affects submarine melt rates of tidewater glaciers. The effect of submarine iceberg melting on fjord circulation and the implications of that for oceanic forcing of tidewater glaciers is also explored in detail.

This thesis is comprised of seven chapters. Chapter 2 follows on from this chapter and provides a more detailed description of the background and motivation for this thesis, covering the observed changes in Greenland's tidewater glacier in detail, and a summary of research on the mechanisms by which the atmosphere and the ocean can affect tidewater glacier dynamics. In Chapter 3, an overview of the methods, tools and techniques used in this thesis is provided, with more detailed descriptions provided in the subsequent chapters.

The findings of this thesis are presented in Chapters 4-6, focusing on the two themes described above. In Chapter 4, satellite-based remote sensing is combined with 1-D plume modelling to investigate the dynamics of three contrasting and neighbouring tidewater glaciers, demonstrating the consistent influence of subglacial hydrological evolution on seasonal ice dynamics. The following two chapters (Chapters 5 and 6) focus on the influence of icebergs on fjord conditions and the implications of that for ice sheet – ocean interaction. These chapters use 3-D ocean numerical modelling in real (Chapter 5) and idealised (Chapter 6) environments to quantify iceberg-induced changes at the fjord-scale and at the interface between the ice sheet and the ocean. Chapter 7 seeks to bring these findings together and expand them to the wider ice sheet. In doing so, it offers an improved understanding of glacier-fjord systems and discusses the implications of the work presented in this thesis for modelling tidewater glacier response to changes in atmospheric and oceanic conditions. Chapter 7 finally presents several concluding remarks.

1.2 Format of thesis

Chapters 4-6, which detail the principal investigations and findings of this thesis, have been written as standalone papers to facilitate dissemination of the results to the research community. Chapters 4 and 5 have already been published – the contributions of all of the authors on each of these publications are summarised at the start of each chapter. Chapter 6 is also intended for publication, though it has not yet been submitted. Supporting information for chapters 4 and 5 are included as appendices.

.

Chapter 2 - Background

The Greenland Ice Sheet switched from a small annual mass gain to a period of net annual mass loss around 1980, and has since been in a regime of net mass loss. Over this period, the rate of mass loss has increased by 80±6 Gt yr^{-1} per decade on average (Mouginot et al., 2019), reaching peak mass loss rates of 524±9 Gt yr^{-1} during June 2005 (King et al., 2018). Between 1972 and 2018, tidewater glacier dynamics contributed 66±8% of this mass loss through iceberg calving and submarine melting – the sum of which is called 'ice discharge' (Mouginot et al., 2019). This increase in dynamic mass loss from the Greenland Ice Sheet was manifested as a dramatic, quasi-synchronous period of retreat (Bunce et al., 2018; Murray et al., 2010), thinning (Krabill et al., 2004; Pritchard et al., 2009) and acceleration (Rignot & Kanagaratnam, 2006) of hundreds of tidewater glaciers, beginning during a period of atmospheric and oceanic warming between the mid-1990s and early-2000s. There is therefore substantial motivation to improve our understanding how changes in atmospheric and oceanic conditions affect tidewater glaciers and the fjords they flow in to. The societal reasons for this are numerous, but perhaps the most pressing is sea level rise – appropriate understanding of the response of glacier-fjord systems to changing environmental conditions is essential if we are to reliably predict their future contribution to sea level rise (Meredith et al., 2020). This background chapter

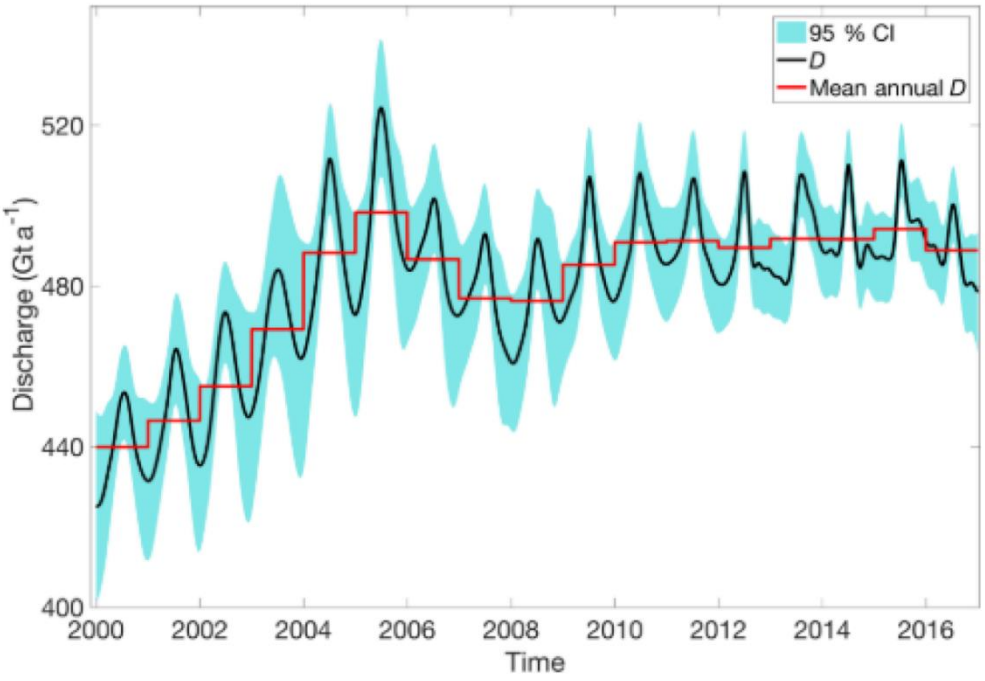

Figure 2.1. Greenland Ice Sheet discharge for the period 2000-2016. Shading represents 95% confidence interval. Reproduced from King et al. (2018).

begins by outlining tidewater glacier behaviour in recent decades, then summarises the key components of glacier-fjord systems and their interactions in the context of understanding controls on tidewater glacier mass loss, emphasising key knowledge gaps throughout.

2.1 Review of tidewater glacier dynamics

2.1.1 Regional changes during the satellite era

The large number and relatively inaccessible nature of tidewater glaciers draining from the Greenland Ice Sheet makes continuous or routine monitoring of their dynamics and mass balance impossible to conduct at scale in the field. Instead, satellite-based observations have proven invaluable for regional-scale monitoring of glacier change, with operational observations available since 1972, following the launch of the first Landsat mission. Since then, the resolution and frequency of observations has increased dramatically (Catania et al., 2020). Satellite imagery has enabled scientists to monitor (amongst other things) the changing position of glacier termini, changes in ice velocity through the tracking of surface features over time, and changes in ice surface elevation. These observations have revealed dramatic and quasi-synchronous (at the regional scale) changes in tidewater glacier dynamics in recent decades.

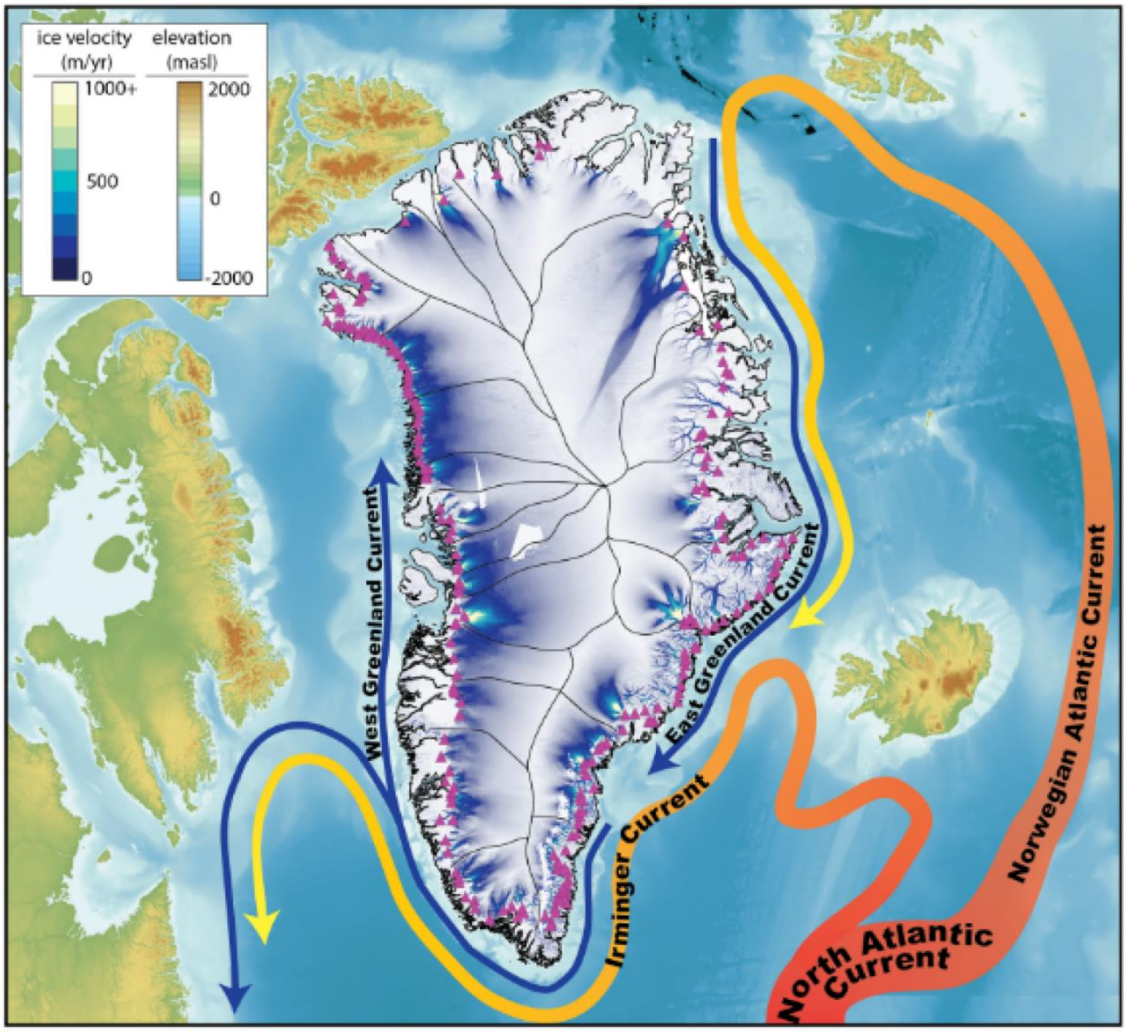

Figure 2.2. Overview of the Greenland Ice Sheet and it's oceanic setting. Surface ice flow speed (from Joughin et al., 2010) highlights fast-flowing tidewater glaciers. The outlets of all glaciers flowing over 50 m yr^{-1}, most of which are tidewater glaciers. Reproduced from Catania et al. (2020).

Records of ice sheet wide ice discharge since 2000 reveal substantial temporal variations in rates of ice discharge (Figure 2.1). Ice discharge increased substantially from 440±8 Gt yr^{-1} in 2000 to a maximum of 524±9 Gt in late June 2005 (King et al., 2018). Ice sheet wide ice discharge then decreased to a minimum in 2008 before steadily rising until 2011. Since 2011, ice discharge has remained largely stable at ~490 Gt yr^{-1} (Figure 2.1; King et al. (2018)). Of this ice discharge, the ice sheet's twenty largest glaciers accounted for over 50% of the total ice discharge, whilst the four largest glaciers together accounted for 25% of the total ice discharge and 56% of the cumulative ice sheet-wide ice discharge anomaly compared to 2000 (King et al., 2018).

Substantial inter-regional variability exists within this ice sheet wide signal, however. The southeast and northwest coasts of the Greenland Ice Sheet host the vast majority of its tidewater glaciers (Figure 2.2; Bjork et al. (2015)), and so it is dynamic changes in these locations that are primarily responsible for changes in ice sheet-wide ice discharge and which have received the most research attention (e.g. Carr et al., 2013; Cowton et al., 2018; Howat et al., 2008; Joughin et al., 2010; Moon et al., 2012, 2014, 2015; Rignot & Kanagaratnam, 2006). Other regions including the southwest, northeast and north, host fewer tidewater glaciers, but some among those are important contributors to Greenland ice sheet mass loss, and so dynamic changes in these regions will also be summarised here.

Major changes in tidewater glacier ice discharge began in the southeast in the mid-to late-1990s, with a moderate but widespread increase in flow velocity and terminus retreat (Cowton et al., 2018; Howat et al., 2008; Jiskoot et al., 2012; Joughin et al., 2010). During 2000-2005, this region underwent a pulse of very rapid retreat and acceleration (e.g. Figure 2.3), during which regional ice sheet ice discharge approximately doubled (Jiskoot et al., 2012; Murray et al., 2010). From 2005 to 2008-2009, ice discharge from this region rapidly declined, but remained elevated relative to 2000 levels (Figure 2.4). Since 2009, ice discharge from this region has largely stabilised or fallen slightly, such that ice discharge in recent years was within the region of uncertainty compared to ice discharge in 2000 (King et al., 2018). North of ~69°N, the behaviour of glaciers in east Greenland has been less dramatic, but they have nevertheless retreated proportionally to the changes in atmospheric and oceanic temperature that have occurred there (Cowton et al., 2018; Wood et al., 2021). More recently, rates of acceleration and retreat have increased again in the southeast (Bevan et al., 2019; Brough et al., 2019), though there is little evidence as yet to suggest that this behaviour is widespread.

The behaviour of glaciers in the west and northwest of Greenland was different to those in the southeast (Figures 2.3 & 2.4). At the regional scale, these glaciers have steadily accelerated and retreated since 2000. Ice discharge in this region increased approximately linearly from ~185 Gt yr^{-1} in 2000 to ~225 Gt yr^{-1} in 2016, whilst the glaciers retreated by 2.8 km on average (King et al., 2018). Tidewater glaciers in the west and northwest of the ice sheet have thus made an increasing contribution to ice sheet-wide ice discharge, particularly since 2005 when ice discharge from glaciers in the southeast began to decline.

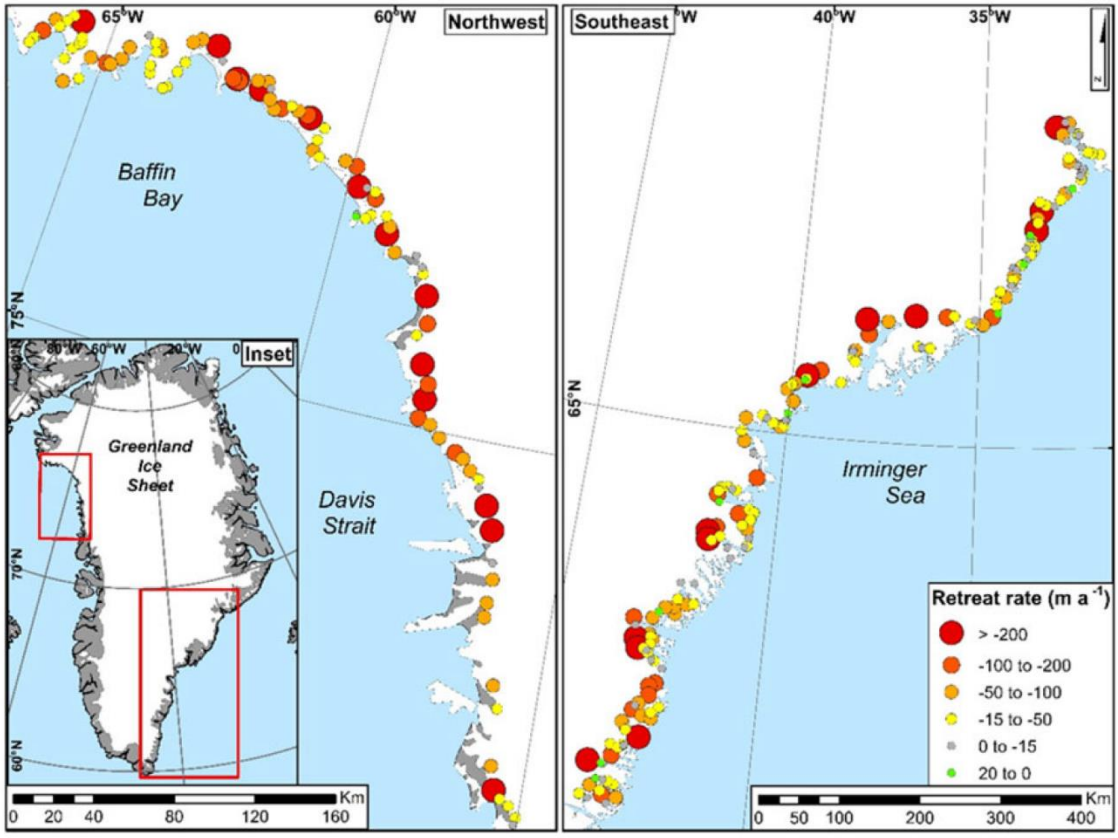

Figure 2.3. Tidewater glacier retreat rates for the period 2000-2015. Reproduced from Bunce et al. (2018).

Changes in ice discharge in the southwest, northeast and north are less dramatic, but also noteworthy (Figure 2.4). Few tidewater glaciers drain the southwest of the ice sheet, with 60% of the ice discharge from this region contributed by a single, fast-flowing glacier (Kangiata Nunaata Sermia). As a whole, ice discharge from this region has been relatively steady since 2000, with glacier dynamics dominated by seasonal, rather than interannual variability (Ahlstrøm et al., 2013; King et al., 2018; Lea et al., 2014; Motyka et al., 2017; Sole et al., 2011). Glaciers in the north and northeast of Greenland are showing some signs of change, with an overall pattern of modest (~tens of metres per year) retreat and acceleration (tens to hundreds of metres per year) beginning in the early 2000's (Hill et al., 2017). 79 North Glacier (Nioghalvferdsfjorden) and Zachariae Isstrom are the two main outlets in northeast Greenland. These two glaciers were stable for at least a quarter of a century before the floating ice tongue of Zachariae Isstrom disintegrated between 2000 and 2006 and both glaciers underwent sustained acceleration, retreat and thinning in response to sea ice clearing and an incursion of warm water (Khan et al., 2014a).

At a regional scale then, there has been widespread glacier acceleration, thinning and retreat (Figures 2.3 & 2.4). This change in behaviour began first and was most rapid in

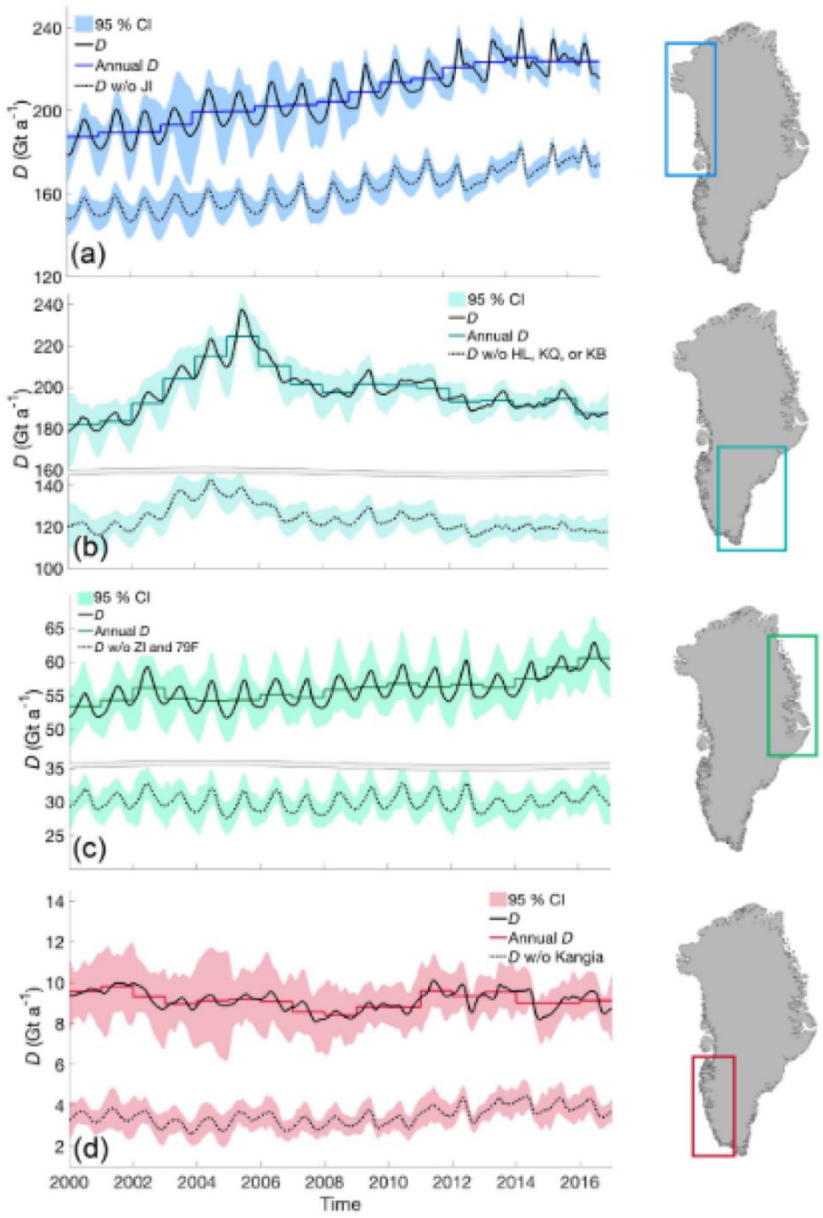

Figure 2.4. Regional ice discharge for each major ice sheet region. The dashed line for each region is the discharge excluding the dominant glaciers in each region. Shading represents the 95% confidence interval. Reproduced from King et al. (2018).

the southeast, though ice discharge from glaciers there subsequently reduced and stabilised. Meanwhile, ice discharge from glaciers in the west and northwest increased several years later than those in the southeast, but has continued relatively unabated such that ice discharge from this region is now greater than in the southeast (King et al., 2018). Elsewhere in Greenland, changes in dynamic behaviour of tidewater glaciers also occurred in the early 2000s, but more slowly than in the southeast and northwest.

2.1.2 Heterogeneity in glacier dynamics

Within these broad regional patterns, there has been substantial differences in the dynamic behaviour of neighbouring glaciers, despite being exposed to similar changes in atmospheric and oceanic conditions. Intra-regional variability in glacier behaviour is particularly important because of the disproportionate contribution to ice sheet mass loss from a small number of glaciers (King et al., 2018). There are numerous examples of this heterogeneity in glacier dynamic behaviour across the ice sheet, and the following are just a selection of the best studied ones.

The intra-regional variability in glacier dynamics is perhaps best reflected by differences in the timing, rate and pattern of glacier terminus position change (Figure 2.3). For example, a glacier in the northwest of Greenland advanced by up to 20 m yr^{-1} during 2000-2015, whilst several glaciers surrounding it retreated by 15 to 200 m yr^{-1} (Bunce et al., 2018). In west Greenland, many glaciers drain into a large fjord system called Uummannaq Bay. One of these glaciers, Store Glacier, has not retreated over the last century (Weidick & Bennike, 2007), though it does undergo a seasonal cycle of advance and retreat by ~400 m, as the glacier seasonally advances into deeper water (Ryan et al., 2015). In contrast, some of its neighbouring glaciers, such as Umiamako Isbrae, Ingia Isbrae and Eqip Sermia, have retreated significantly in recent years (Figure 2.5; Rignot et al. (2016)). For example, the northern sector of Eqip Sermia retreated dramatically in 2005-2011 and was followed by its southern sector in 2012-2014 (Rignot et al., 2016). Although much of this variability can be qualitatively explained by differing fjord and bed geometry, with faster retreat rates for glaciers retreating into widening and/or deepening fjords (Bunce et al., 2018; Carr et al., 2013; Porter et al., 2014), several aspects remain poorly understood as there is often no clear relationship between glacier retreat and ocean temperature or grounding line depth.

2.1.3 Longer-term changes in glacier dynamics

It is important to place the changing behaviour of tidewater glaciers over the past few decades in a longer term context. Reconstructions of glacier behaviour prior to the satellite era rely on glacial geomorphology, historical accounts, historical ground and aerial photographs and sediment cores. These reconstructions are therefore of a lower spatial and temporal resolution than is now available from satellite observation; nevertheless, they do still provide valuable insight into the longer-term dynamics of selected glaciers.

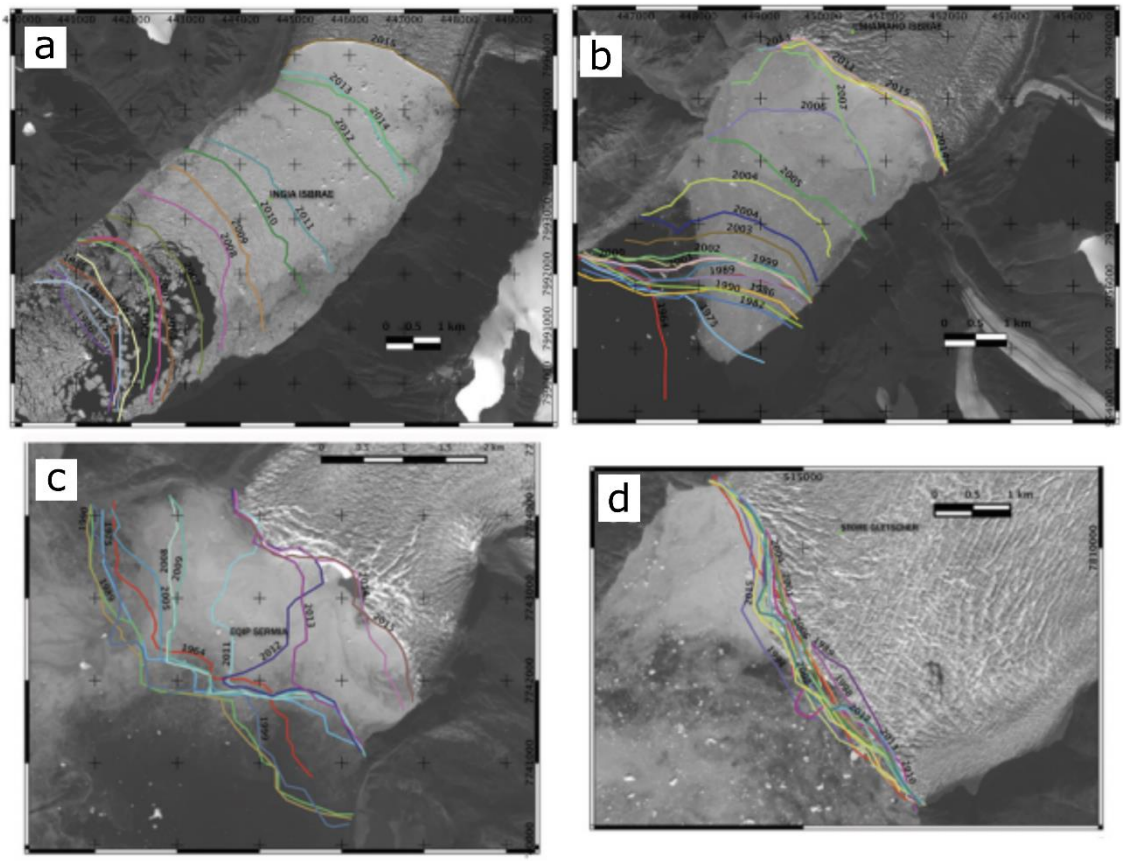

Figure 2.5. Terminus positions of Greenland glaciers from 1850, overlaid on a Landsat-8 mosaic of Greenland. (a) Ingia Isbrae. (b) Umiamako Isbrae. (c) Eqip Sermia. (d) Store Glacier. Reproduced from Rignot et al. (2016).

Many of these reconstructions have focused on the largest glaciers draining the Greenland Ice Sheet, as they have a longer and more detailed historical record. Kangerdlugssuaq Glacier in southeast Greenland is one such glacier. It likely reached its maximum recorded extent during the Little Ice Age, sometime between 1450 and 1850 (Kjeldsen et al., 2015). Several expeditions to Kangerdlugssuaq Fjord were launched during 1930-1935, reports from which note the loss of the Kangerdlugssuaq floating ice tongue sometime between 1931 and 1936 (Wager et al., 1937). An aerial photograph acquired in 1933 revealing a substantially (9 km) retreated glacier compared to 1931, and sediment cores detailing increased sedimentation, indicate that the glacier tongue rapidly collapsed between 1932 and 1933 at a time of warm sea surface temperatures (Vermassen et al., 2020). This collapse resulted in the large retreat of the glacier and substantial thinning (Khan et al., 2014b, 2020).

Further south along the east coast, Helheim Glacier also seems to have undergone a period of rapid calving activity in the 1930s. Analysis of sedimentary deposits, in which the

annual deposition of sand grains is used as a proxy for iceberg production, reveals calving rates in the 1930 and 40s that were similar to present-day rates (Andresen et al., 2012). This record also reveals large fluctuations in calving rates over periods of 1-3 years, perhaps indicating the rapid response of Helheim glacier to changes in atmospheric and oceanic forcing (Andresen et al., 2012). Following this spike in calving activity in the 1930s and 40s, Helheim glacier re-advanced to its Little Ice Age maximum and thickened (Bjørk et al., 2012; Khan et al., 2014b).

Similar changes seem to have occurred around the ice sheet. Aerial photographs and geomorphological evidence at Kangiata Nunaata Sermia, the largest tidewater glacier in southwest Greenland, indicate that the terminus retreated steadily by approximately 100 m yr^{-1} between 1921 and 1968, with a period of particularly rapid retreat in the late 1940s (Lea et al., 2014). An ice sheet wide reconstruction also suggests that annual tidewater glacier ice discharge during 1900-1983 was similar to that during 2003-2010 (Kjeldsen et al., 2015). Clearly then, the changes in tidewater glacier behaviour observed in recent decades do not seem to be unprecedented in the context of the past century. Rather than diminishing the importance of contemporary changes in glacier behaviour, these reconstructions serve to highlight that Greenland's tidewater glaciers can respond rapidly to changing environmental conditions.

2.1.4 Understanding tidewater glacier dynamics

Understanding these recent and historical changes in tidewater glacier behaviour requires understanding of the whole glacier-fjord system, including the glacier itself, the fjord and the ice-ocean interface (Figure 2.6). Numerous studies have targeted processes operating in these systems as subjects of investigation. As a result, a grainy picture is emerging of the interactions between subglacial discharge (which is ultimately produced due to atmospheric processes), plume dynamics, submarine melting, iceberg calving, mélange dynamics and fjord circulation (e.g. Amundson et al., 2020). Some of these components and phenomena are understood sufficiently well to incorporate into large-scale models (e.g. Slater et al., 2019, 2020), whilst others have only recently been recognised as important components of the system. Each of these components and their interactions are now reviewed with the aim of providing the reader with a broad overview of the key elements in glacier-fjord systems. Each of these components is a vast subject in their own right, and so a thorough synthesis of the literature relating to each would be unwieldy and beyond the scope of this chapter. Instead, this chapter will focus on the research most

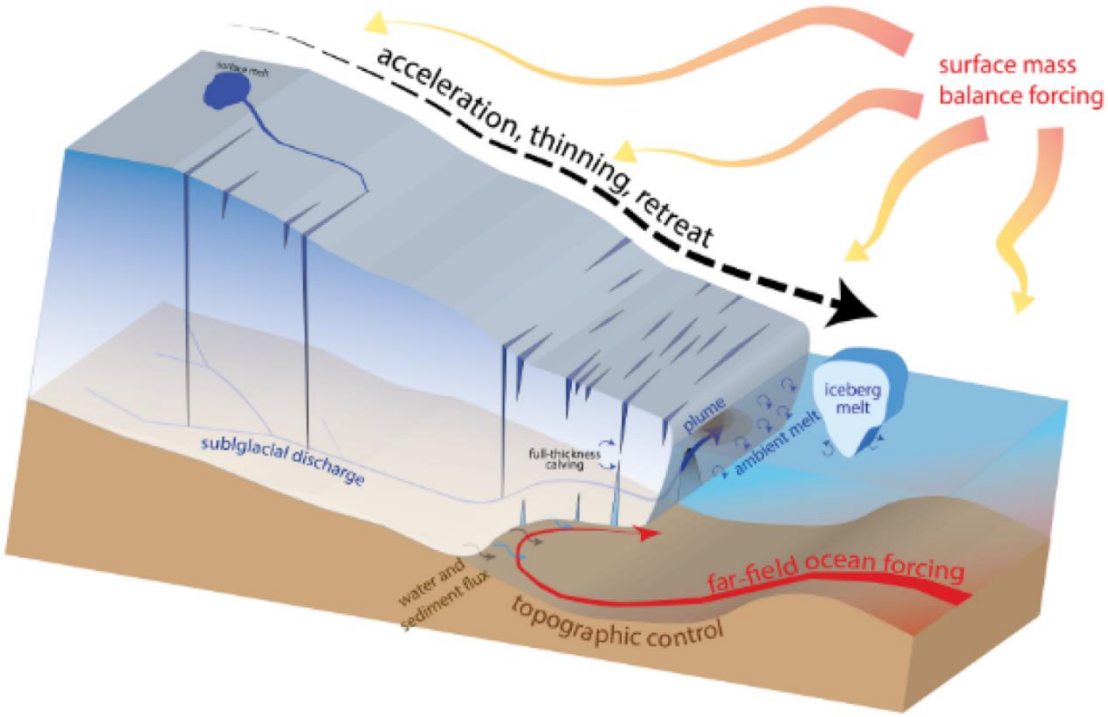

Figure 2.6. Schematic of a Greenlandic glacier-fjord system showing glacier dynamics (black dashed arrow), glacier hydrology, runoff-driven plumes, fjord circulation, iceberg melting and atmospheric forcing. Reproduced from Catania et al. (2020).

pertinent to understanding the role of each component within Greenland's glacier-fjord systems and in influencing recent glacier change. Additional context is given where appropriate and more detailed subject specific reviews will be highlighted throughout.

2.2 Tidewater glaciers and glacier hydrology

Meltwater is an important driver of tidewater glacier dynamics. Meltwater is produced at the ice sheet surface, where it can percolate into the snowpack and refreeze, or it can drain through cracks and moulins (quasi-vertical tunnels) into and beneath the ice sheet (Figure 2.6). This meltwater can then lubricate the base of the ice sheet, causing the overlying ice to flow faster. Intuitively, therefore, one might think that increased meltwater production should lead to faster ice flow. It is now clear however, that the relationship between meltwater supply and changes in ice velocity depends in large part on the efficiency of water flow beneath the ice sheet, which evolves with meltwater supply. Glacier and ice sheet hydrology, and it's interactions with ice dynamics, is a vast subject area (Davison et al., 2019; Hubbard & Nienow, 1997; Irvine-Fynn et al., 2011; Miles et al., 2020; Nienow et al., 2017). Rather than attempt to review this entire body of literature, this section focuses on how meltwater supply to tidewater glaciers has changed in recent

decades and, following a brief overview of ice sheet subglacial hydrology, the evidence for atmospheric forcing of tidewater glacier dynamics over the same time period.

2.2.1 Temporal variability in atmospheric forcing

Air temperature over the Greenland Ice Sheet has warmed since the early 1990s (Figure 2.7; Hanna et al. (2008); Box et al. (2009)). For example, summer air temperature records at seven automatic weather stations in the ablation zone of the ice sheet indicate a 1.7°C warming during 1991-2006. This warming followed a period of modest (0.5°C) cooling during 1961-1990, though this cooling is not statistically significant (Hanna et al., 2008). Air temperature at Swiss Camp, at higher elevations on the ice sheet, warmed by 2.2°C during 1991-2005 (Hanna et al., 2008). Interannual variability is superimposed on this warming trend, resulting in some relatively cool years (e.g. 2008) and some anomalously warm years, such as 2012 (Hanna et al., 2014; Van De Wal et al., 2012). In 2012, summer air temperatures over the ice sheet were three standard deviations above the 1979-2011 mean (Tedesco et al., 2013). The warming over recent decades is not unprecedented – a similar magnitude of warming (2.4°C) occurred around the 1920s and 1930s (Box et al., 2009; Chylek et al., 2006), at a similar time to the retreat of tidewater glaciers described above.

This warming has affected rates of surface ice melt and ice sheet runoff (where meltwater is discharged from the ice sheet at the margin). For example, a 65 year discharge record of the Watson River, which drains a large ice sheet catchment in west Greenland, shows that, since 2003, ice sheet runoff has increased by 46% relative to the 1949-2002 average (Van As et al., 2014). Over the ice sheet as a whole, surface mass balance has decreased largely due to increased surface melting. For example, between 2007 and 2012, increased surface melting caused 193±37 Gt yr^{-1} mass loss, compared with 22±20 Gt yr^{-1} during 1992-2006 (Shepherd et al., 2020). As well as increased air temperature, this increase in melting and runoff is due to (amongst other things) an increased frequency of slower moving or stationary summer air masses, particularly over southwest Greenland (Ahlstrøm et al., 2017), expansion of the ablation zone, particularly in northern Greenland (Noël et al., 2019) and loss of firn pore space, thereby reducing refreezing of meltwater (Machguth et al., 2016).

2.2.2 Meltwater-induced changes in basal water pressure and sliding

The subglacial environment is almost impossible observe directly. Therefore, our understanding of these drainage systems is largely based on observations of ice motion,

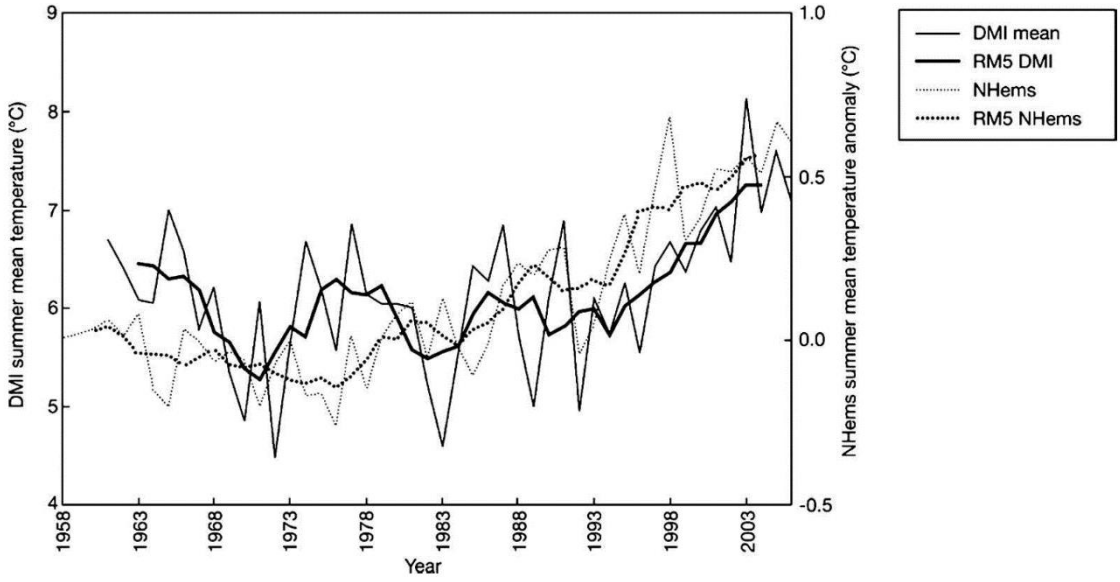

Figure 2.7. Greenland air temperature averaged over June, July and August from the mean of 7 Danish Meteorological Institute weather stations on the Greenland Ice Sheet for 1958-2006, compared with Northern Hemisphere summer mean temperature. 5 year running means (RM5) of each series are also shown. Reproduced from Hanna et al. (2008).

surface melt and proglacial river discharge, combined with theoretical relationships between water supply and ice motion developed at mountain glaciers (e.g. Hubbard & Nienow, 1997; Harper et al., 2005; Rada & Schoof, 2018). In general, it is thought that high or increasing subglacial water pressure leads to faster or increasing ice velocity (Kamb, 1987; Harper et al., 2007; Cowton et al., 2016b). At the base of glaciers and ice sheets, meltwater can drain towards the ice margin in an 'efficient' or an 'inefficient' drainage system. In this context, an efficient drainage system is one in which (in steady state) basal water pressure (and therefore ice velocity) drops as meltwater supply increases, whereas basal water pressure increases with meltwater supply in an inefficient drainage system (Schoof, 2010). These two types of drainage system can take many forms, but the quintessential efficient drainage form is a Rothlisberger channel, or R-channel (Röthlisberger, 1972), whilst inefficient systems are thought to be comprised primarily of linked-cavities where bedrock underlies the ice sheet, and porous sediment in sediment rich subglacial environments (Harper et al., 2017; Kamb, 1987).

The type of subglacial drainage system, and therefore the relationship between meltwater supply and ice velocity, can change through a melt season. Continual injection of water into the subglacial environment causes an inefficient system to transition into an efficient system (Chandler et al., 2013; Nienow et al., 1998; Sundal et al., 2011), as flowing

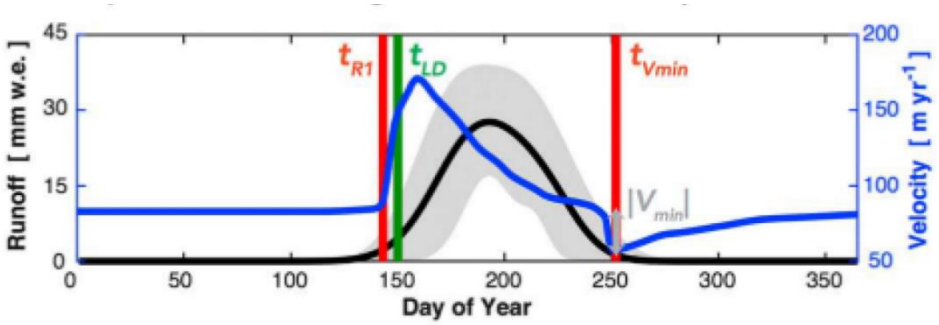

Figure 2.8. Conceptual seasonal velocity (blue) and runoff (black) for the ablation zone of land-terminating sectors of the Greenland Ice Sheet, based on data from west Greenland. Reproduced from Stevens et al. (2016).

meltwater melts the overlying ice faster than it can close, thereby creating a larger drainage pathway. Similarly, a prolonged decline in meltwater supply leads to closure of subglacial channels and the re-establishment of an inefficient drainage system (Sole et al., 2013; Stevens et al., 2016). Over a year then, it is thought that an efficient drainage will develop sometime following melt onset, and persist throughout the melt season until meltwater supply drops low or ceases entirely, such that an inefficient drainage system re-establishes until the following melt season. There is now compelling evidence to suggest that spatial transitions between these drainage systems is also possible, with efficient channels forming corridors through an otherwise inefficient subglacial environment (Lewington et al., 2020), leading to water exchange between the two during fluctuations in water supply (Hoffman et al., 2016; Hubbard et al., 1995; Nanni et al., 2020; Rada & Schoof, 2018; Tedstone et al., 2014). These drainage system transitions combine to create characteristic seasonal variations in ice velocity, with an early melt season spike in velocity following melt onset, followed by declining velocity until the end of the melt season (Figure 2.8).

Beneath vast swathes of land-terminating sectors of the Greenland Ice Sheet, field-based investigations have shown that interactions between subglacial hydrology and ice dynamics are rather similar to those at alpine glaciers and as outlined in the previous paragraph, but with some modifications due to the larger range of ice thickness and water volume transiting through the ice sheet system (Davison et al., 2019). Our understanding of tidewater glacier subglacial hydrology is, however, rather more limited because runoff from tidewater glacier grounding lines (subglacial discharge) is currently impossible to measure directly, and their crevassed surface and fast flow severely limits the deployment of most equipment on the ice surface near their termini.

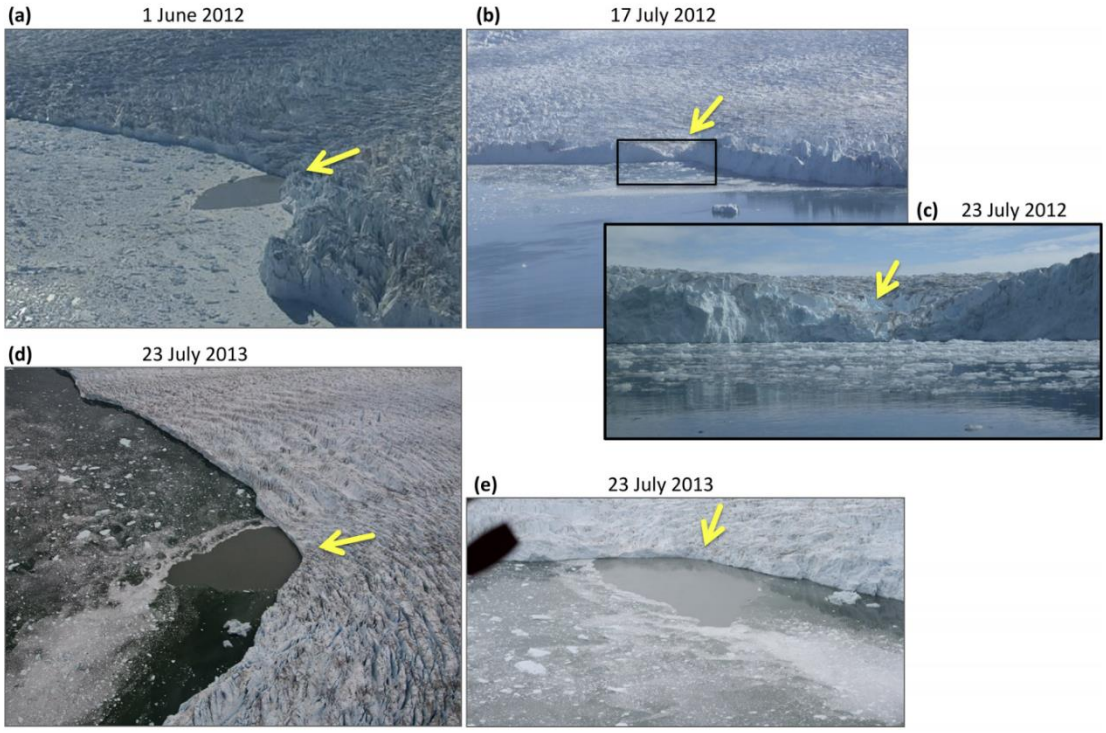

Figure 2.9. Turbid plume pools at Saqqarliup-Saqqarleq, west Greenland. Reproduced from De Andrés et al. (2020).

Theory, as well as some limited observations, do provide valuable insight into the interactions between subglacial hydrology and ice dynamics at tidewater glaciers. Theoretically, the fast-flow of tidewater glaciers should accelerate subglacial channel closure (Röthlisberger, 1972), making it less likely for them to form or persist long enough to affect tidewater glacier velocity. However, frequent observations of turbid pools or plumes at the fjord surface immediately adjacent to tidewater glacier calving fronts (Figure 2.9; e.g. Chauché et al. (2014); De Andrés et al. (2020)) - formed where sediment-laden subglacial discharge rises to the fjord surface (see Section 3.3) - indicate focused subglacial delivery of meltwater to the glacier margin, which would be consistent with a subglacial channel. Sometimes, multiple plumes or pools are visible at the fjord surface (Fried et al., 2015), indicating multiple major subglacial outlets. Using side-looking multi-beam echo sounding, it has been possible to image the shape of some tidewater glacier calving fronts. Since the shape of the front is partly influenced by the spatial pattern of meltwater efflux at the grounding line, these observations provide a snapshot-in-time fingerprint of near-terminus subglacial hydrology. These limited observations reveal a complex system, with some deep chimneys, indicative of a subglacial channel, as well as multiple smaller crenelations and varying degrees of undercutting, indicative of spatially-variable meltwater efflux (Figure 2.10; Rignot et al.

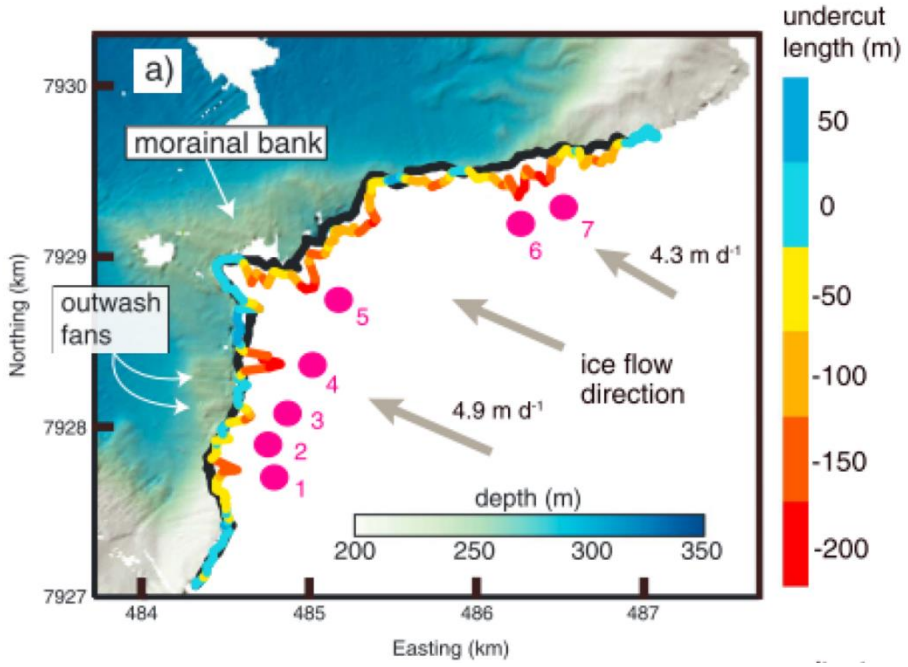

Figure 2.10. Undercutting of Greenland glacier. Map view of the near-terminus region of Kangerlussuup Sermia, west Greenland, showing the terminus (black line), subglacial discharge outlets (pink dots), and magnitude of undercutting (shaded line) from multibeam data. Reproduced from Fried et al. (2015).

(2015); Fried et al. (2015)). Overall, these observations suggest that, although there are similarities between tidewater glacier hydrology and land-terminating glacier hydrology, there are important differences in the near-terminus region that are not yet completely understood.

The relationship between meltwater supply and tidewater glacier velocity also appears to be complicated and is not fully understood. Global Navigation Satellite System observations some 35 km from the terminus of Kangiata Nunaata Sermia (Sole et al., 2011) demonstrate that seasonal ice velocity variations there are very similar to those observed over land-terminating sectors, implying that there may be a similar control. Similar observations, acquired within 20 km of the terminus, show a similar ice velocity pattern (Ahlstrøm et al., 2013). However, satellite observations, which permit lower temporal resolution estimates of ice velocity even closer (but not up to) the terminus, show variable seasonal velocity patterns of this glacier, some of which did not have the characteristic late-summer slow-down observed further up-glacier and at land-terminating sectors (Moon et al., 2014). More extensive satellite observations demonstrate that the seasonal velocity signal of around half of tidewater glaciers is

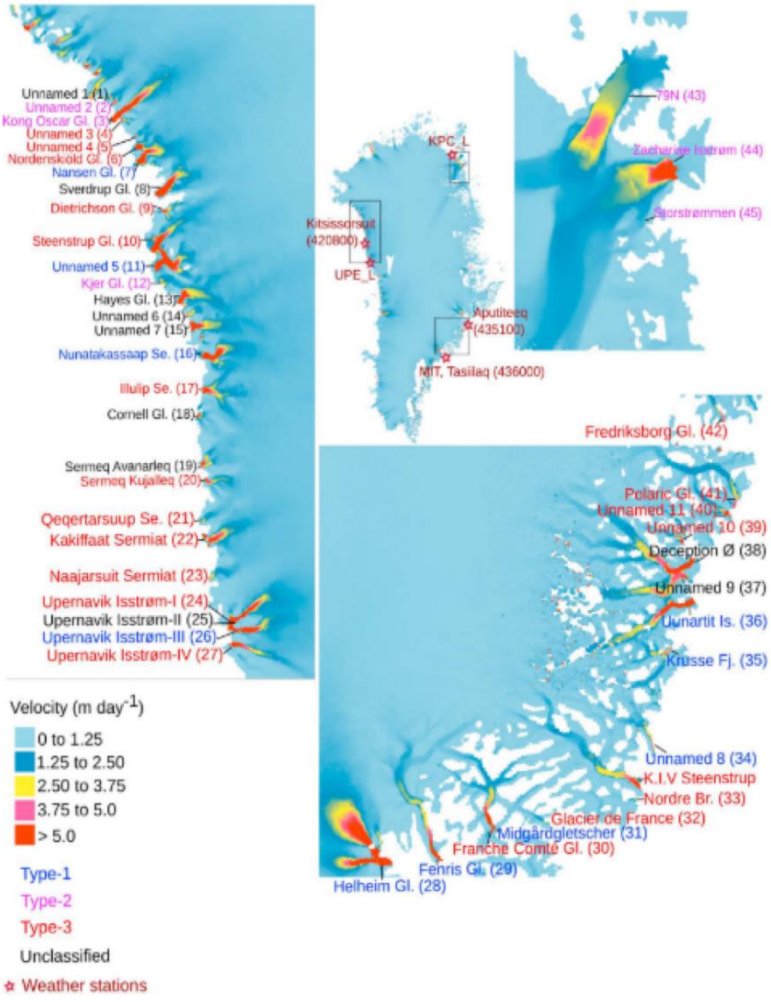

Figure 2.11. Characterising tidewater glacier seasonal velocity. Glacier types 2 and 3 are associated with melt water supply, with type 3 being most similar to the behaviour of marginal sectors of the land-terminating ice sheet (as in Figure 2.8). Type 1 glacier behaviour is typically associated with calving dominated glaciers. Reproduced from Vijay et al. (2019).

temporally associated with changes in meltwater supply, with the majority of those displaying velocity behaviour similar to that observed at land-terminating sectors (Figure 2.11; Vijay et al. (2019)). The largest tidewater glaciers typically do not show a strong meltwater-induced spike in velocity, and instead respond more sensitively to calving (Bevan et al., 2012; Kehrl et al., 2017). There is however, very little evidence directly linking seasonal changes in tidewater glacier velocity to seasonal changes in subglacial hydrology, and furthermore it is not clear whether the interannual behaviour observed at tidewater glaciers is directly related to interannual changes in meltwater supply affecting basal water pressure.

2.3 Fjords

2.3.1 Fjord overview and ocean setting

Fjords were calved by past glacier flow, indicating in places the vast size of some paleo-glaciers (e.g. Scoresby Sund, east Greenland). They can range in length from a few km to over 100 km, are typically several kilometres wide, and can reach depths of over 1000 m (Figure 2.12). They can be sinuous in plan-form and often feature one or several bathymetric troughs and sills. In many places, they form complex fjord systems, fed by numerous tributary glaciers over large stretches of the coastline (Figure 2.12). They also often connect with cross-shelf troughs which reach the continental shelf break, providing entry points for deeper coastal water masses to interact with the Greenland Ice Sheet.

Fjords act as the gateways, or connections, between the ice sheet and the ocean. They allow and, in many ways, control the exchange of heat, salt and mass between the ice sheet and the ocean (Straneo & Cenedese, 2015), and are the primary pathways for freshwater export from the ice sheet to the ocean (Mankoff et al., 2019, 2020). From an oceanography perspective then, fjord circulation and the modification of ice sheet products (i.e. solid and liquid freshwater) within the fjord are therefore important for understanding how the ice sheet influences the ocean. From a glaciology perspective, water properties and current speeds immediately adjacent to glacier calving fronts are of primary interest because these influence melt rates at glacier calving fronts. Glacier-adjacent water properties in turn depend on the properties of the source waters, fjord circulation (which affects the rate of exchange between the fjord and the shelf) and modification of water properties within the fjord. This thesis is focused primarily on the glaciology perspective, and so the emphasis in the following section is on those fjord characteristics which are most pertinent to oceanic forcing of tidewater glaciers.

The source waters feeding glacial fjords have both polar and subtropical origins (Figure 2.2). A relatively cold (generally less than 0°C), fresh water mass of polar origin (henceforth Polar Water, PW) is transported southwards along the east Greenland continental shelf break via the East Greenland Current (EGC) (Fraser et al., 2018; Inall et al., 2014; Sutherland & Pickart, 2008). This water mass generally occupies the upper 100-300 m of the water column (Bacon et al., 2002, 2014). Below the PW lies the Atlantic Water (AW), a second key water mass, which is of subtropical origin. The AW is a relatively warm (4.5-6.5°C) and salty (34.9-35.2 psu) water mass (Sutherland & Pickart, 2008), which is advected towards the east Greenland coast in the Irminger Current (IC),

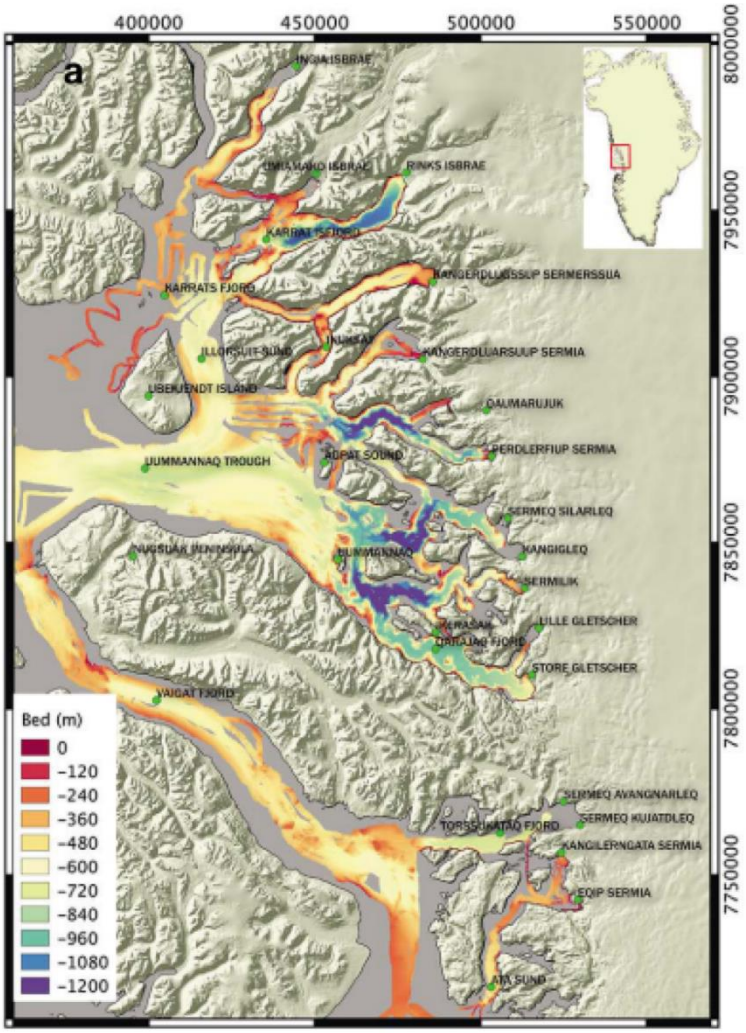

Figure 2.12. Bathymetry of Uummannaq and Vaigat Fjords, west Greenland from multibeam echo sounding data acquired in 2007-2014, illustrating the varied planform shape and bathymetry of many fjords. Reproduced from Rignot et al. (2016).

a branch of the North Atlantic Current that circulates cyclonically around the Irminger Basin (Figure 2.2). Where the IC meets the east Greenland continental shelf break, the EGC and the IC merge into a composite layered flow just south of the Denmark Strait at around 69°N. This composite flow hugs the coast of Greenland as it flows south, eventually rounding Cape Farewell and flowing either into Baffin Bay along the west coast of Greenland or towards Davis Strait and subsequently into the Subpolar Gyre (Straneo & Heimbach, 2013). Mixing between PW and AW, and between freshwater from the ice sheet and AW, tends to cool the AW during its passage round Greenland. Thus, the AW is warmest near its source in southeast Greenland and coolest towards the northwest coast of Greenland (Rignot et al., 2012; Straneo et al., 2012; Wood et al., 2021).

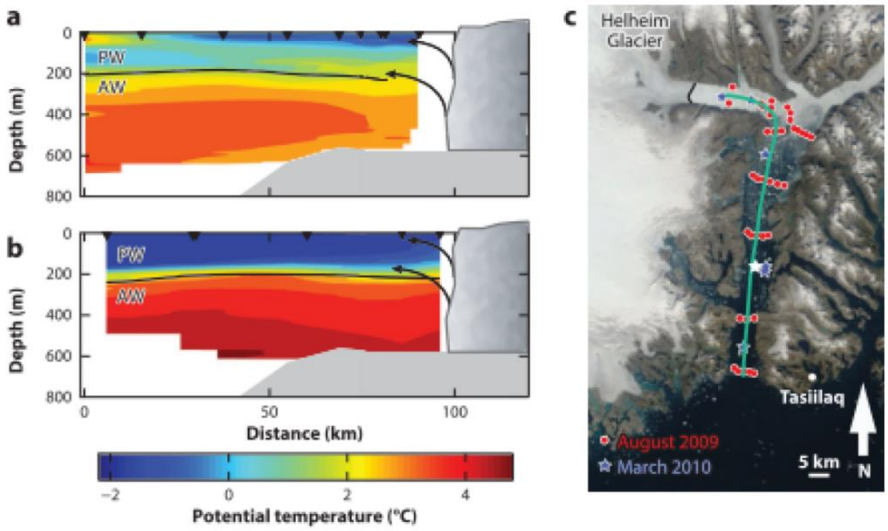

Figure 2.13. Sermilik Fjord water temperature. Panels (a) and (b) show temperature in August and March, respectively. Reproduced from Straneo and Cenedese (2015).

Where deep cross-shelf troughs extend to the continental shelf break, both PW and AW can enter Greenland's fjords. The properties of fjord waters depends in large part then on the properties of these source waters (e.g. Figure 2.13), with some modification occurring within the fjords. Modification of water properties within the fjords can be due to one or a combination of processes including ice sheet runoff, subglacial discharge, precipitation, wind-driven mixing, tidal mixing, solar radiation, glacier and iceberg melting, and sea ice melt and formation. Variable oceanic forcing of tidewater glaciers (causing a change in tidewater glacier behaviour) will therefore depend on the combined influence of changing source water properties and modification due to ice sheet and fjord processes (Straneo & Cenedese, 2015; Straneo & Heimbach, 2013).

2.3.2 Temporal variability in oceanic forcing

AW provides the greatest source of oceanic heat to the Greenland Ice Sheet. As such, most research on temporal variability in oceanic conditions has focused on changes to the temperature and depth of the AW layer and its source waters. In the mid-1990s, a warming and thickening of the AW layer was observed in west and southeast Greenland (Figure 2.14; Myers et al. (2007); Straneo and Heimbach, (2013)). For example, ocean reanalysis indicates a subsurface warming of 1.5°C from 1994 to 2005 in southeast and southwest Greenland, and warming of 2°C between 1997 and 2005 in central west and northwest Greenland (Rignot et al., 2012). In addition, a subsurface warming of 1°C was observed in Disko Bay, adjacent to Jakobshavn Isbrae in west Greenland, following the arrival of

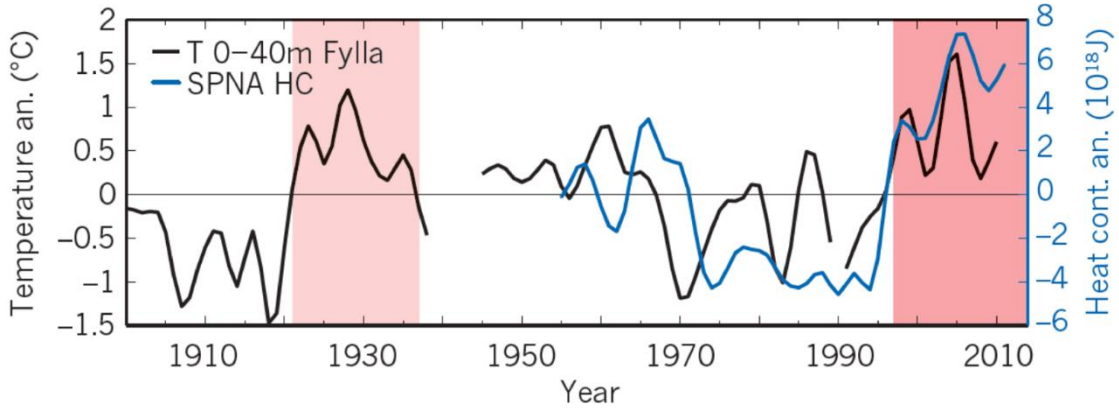

Figure 2.14. Ocean warming timeseries. Modelled subpolar North Atlantic heat content anomaly in the upper 700 m (blue) and observed near-surface (0-40 m) ocean temperature anomaly at Fylla Bank, west Greenland (black). Reproduced from Straneo and Heimbach (2013).

a warm subsurface water mass from the south (Gillard et al., 2020; Holland et al., 2008). This regional ocean warming was driven by decadal ocean warming and increased inflow of warm subtropical water to the North Atlantic, which in turn was linked to changes in the North Atlantic Oscillation and the Atlantic Multidecadal Oscillation (Hurrell, 1995; Polyakov et al., 2005), via their effect on atmospheric wind patterns.

There are few hydrographic surveys from the 1990s and 2000s, and so there is little direct evidence to demonstrate that this large scale oceanic warming did penetrate into Greenland's fjords. However, the observations that do exist demonstrate that water properties inside fjords can vary substantially from year to year. For example, hydrographic surveys of Kangerdlugssuaq Fjord in east Greenland show very warm conditions in 1991 (Andrews et al., 1994), much cooler conditions in 1993, with intermediate temperatures in 2004 (Christoffersen et al., 2011, 2012). More recent surveys and modelling indicate that rapid (days to weeks) communication between fjord and the continental shelf is common in some large fjords (e.g. Cowton et al., 2016; Gladish et al., 2015; Jackson et al., 2014), which suggests that the large scale oceanic warming observed in the mid-1990's (e.g. Figure 2.14) will likely have propagated rapidly into fjords.

2.3.3 Fjord circulation

Fjord circulation is essential for regulating fjord-shelf exchange, replenishing fjord waters, delivering oceanic heat to tidewater glacier calving fronts and for evacuating ice sheet meltwater. Several modes of fjord circulation have been identified in Greenland's

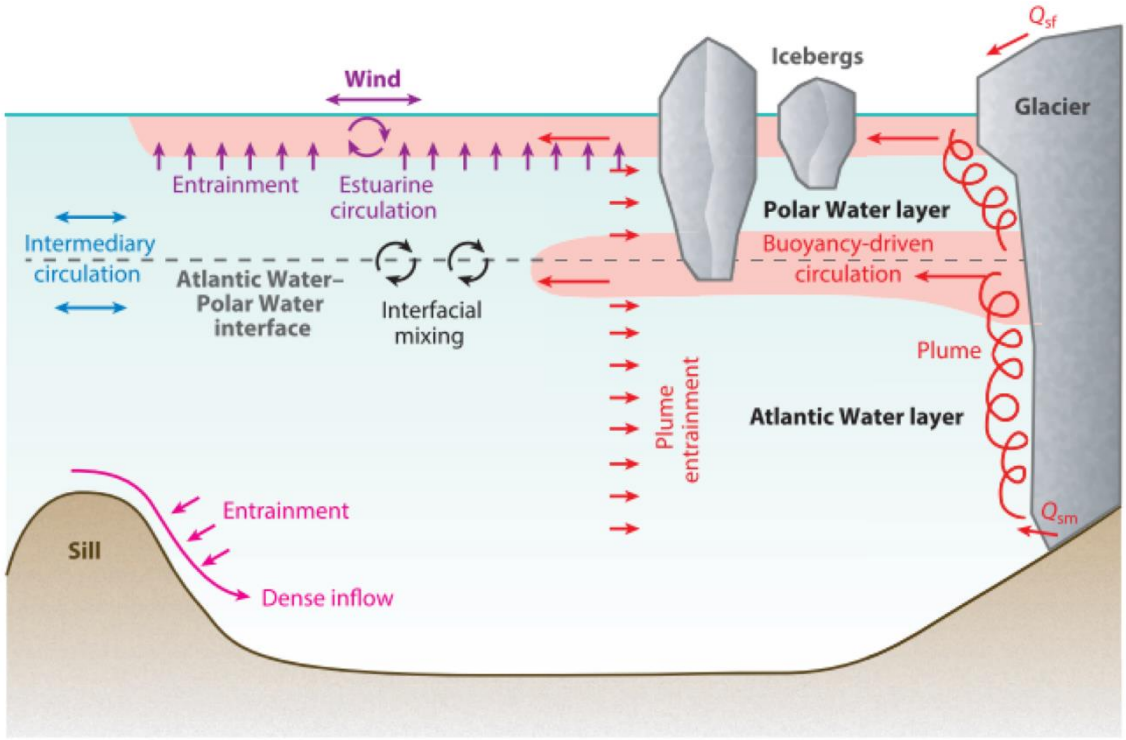

Figure 2.15. Fjord circulation schematic. This schematic shows the different key modes of circulation and processes in Greenland's glacial fjords. Red indicates the buoyancy-driven circulation resulting largely from subglacial discharge entering the fjord, but supplemented by glacier submarine melting and surface runoff. Blue represents the intermediary circulation, or one example of a shelf-forced flow. Purple represents the estuarine circulation driven only by surface runoff. Pink are currents driven by dense coastal inflows over sills. Not included is the circulation driven by submarine iceberg melting. Reproduced from Straneo and Cenedese (2015).

fjords (Figure 2.15; Straneo and Cenedese, (2015)), each of which have different implications for ice sheet-ocean interaction. Two modes have received the most research attention and are focused on here: (1) the buoyancy-driven circulation, caused by fresh water (from subglacial discharge and submarine ice melt) entering the fjord at depth, rising towards the fjord surface and driving an overturning circulation with one or more cells, and; (2) the 'intermediate circulation' or, more broadly, 'shelf-forced flows' (Jackson et al., 2018), in which density differences between the fjord and shelf drive rapid exchanges. Other modes and drivers of fjord circulation, including tidal mixing, periodic dense inflows, buoyancy supplied by iceberg melting, terrestrial runoff and along-fjord winds, may also be important but have received less research attention.

The first key mode of circulation is the buoyancy-driven circulation (Figure 2.15). This mode of circulation is a variant of the classic estuarine-type circulation driven primarily

by plumes initiated by subglacial discharge, and so is sometimes termed the 'runoff-driven circulation' in this thesis to distinguish it from circulation modes driven by other sources of buoyancy (such as iceberg melting). As subglacial discharge-driven plumes rise through the water column adjacent to glacier calving front, they entrain fjord water until they reach neutral buoyancy or the fjord surface, at which point they flow away from the glacier (Chauché et al., 2014; Motyka et al., 2013; Straneo et al., 2010). The resulting down-fjord surface or near-surface current is compensated by an up-fjord current at depth (Figure 2.15). If the down-fjord current is below the fjord surface, a second circulation cell may form above (Carroll et al., 2015, 2017; Sciascia et al., 2013; Straneo et al., 2011; Sutherland & Straneo, 2012). Detailed investigation of this circulation mode and the plumes that drive it has revealed numerous important details. Much of our understanding of this circulation mode stems from theoretical considerations of buoyant turbulent plumes (Morton et al., 1956) that have subsequently be applied to the ice-ocean interface (Jenkins, 1991, 2011). Several ocean modelling studies implementing those plume models in idealised (Cowton et al., 2015; Xu et al., 2012, 2013) and realistic (Cowton et al., 2016a) domains have demonstrated that the strength of runoff-driven plumes and the resulting buoyancy-driven circulation is sensitive to the volume of subglacial discharge entering the fjord, with more vigorous plumes and faster fjord replenishment as subglacial discharge increases (e.g. Cowton et al., 2016). For a given discharge, the strength of this circulation mode increases if runoff is divided between a larger number of smaller outlets, which increases the efficiency of plume entrainment per unit discharge (Carroll et al., 2015, 2016). Modelling studies have also demonstrated that that the down-fjord component of the plume can drive a recirculation cell that increases current velocities across the entire glacier calving front (Slater et al., 2018), with important implications for submarine melting of glacier calving fronts. Near-glacier hydrographic surveys and plume modelling have shown that, at least at one glacier, plumes are rather broad (~200 m) where they emerge at the grounding line (Jackson et al., 2017), driving upwelling and entrainment across a relatively wide swath of glacier calving fronts. Other surveys and modelling have shown that plumes can reach the fjord surface due to momentum before diving back below the fjord surface to their neutral buoyancy depth (Carroll et al., 2015; Chauché et al., 2014). In wide fjords, modelling suggests that across fjord variability may also be an important factor affecting the renewal rate of the fjord (Carroll et al., 2017). Because this mode of circulation is driven by runoff, it is thought to be most powerful during the summer months, when surface-derived meltwater is abundant, and that its

strength may have increased over the past few decades as meltwater supply has increased (Cowton et al., 2016a). During winter, surface-derived meltwater supply ceases but ice sheet basal melting will likely continue to drive weaker plumes, though these have not been observed and ice sheet basal melt rates are poorly constrained.

The second key mode of circulation is Greenland's fjords are shelf-forced flows, or fjord circulation driven by density variations on the continental shelf near fjord mouths (Figure 2.15; Sciascia et al. (2014)). Observations in Kangerdlugssuaq Fjord (Jackson & Straneo, 2016) and Sermilik Fjord (Jackson et al., 2014), both in east Greenland, revealed a variable two-layer baroclinic flow, the variability and strength of which was associated with pycnocline heaving from tens to one hundred metres in the vertical over periods of 3-10 days. This heaving was linked to density fluctuations outside the fjord, which were in turn driven by regional alongshore winds. In east Greenland, where low pressure storms are trapped against Greenland's steep topography, these winds are particularly strong (Moore & Renfrew, 2005). They can occur throughout the year, but are particularly common during winter. In general, the resulting currents appear to be much faster than those driven by runoff, but not as sustained in strength or direction, which may reduce the efficacy of this process as a means of fjord renewal (Carroll et al., 2017; Cowton et al., 2016a; Fraser & Inall, 2018; Jackson et al., 2018). The majority of studies focusing on shelf-forced flows in Greenland have focused on two fjords in east Greenland (Kangerdlugssuaq and Sermilik), where coastal winds are particularly strong, and so it is not clear how important this mode of circulation is in many other fjords in west and northwest Greenland, nor how its importance (from a glaciological perspective) may have changed over time. Other drivers of shelf variability, such as the incursion of dense water masses due to larger-scale ocean dynamics or tidal mixing might also result in fjord-shelf density contrasts and drive similar flows (Mortensen et al., 2011).

Iceberg melting has recently been identified as a substantial source of freshwater in Greenland's fjords (see Section 2.3.4.4), potentially providing a source of buoyancy that is distributed horizontally and vertically throughout the fjord. Little is known about how these freshwater fluxes can affect fjord circulation, but as they melt, these icebergs provide a mobile source of freshwater and a sink of latent heat. Numerical modelling of iceberg melting around Antarctica indicates that icebergs can cause substantial (6°C) cooling of surface waters, and both cooling and warming of deeper waters (Schloesser et al., 2019), and can lead to increased sea ice formation (Jongma et al., 2009; Stern et al.,

2016). Icebergs calved from Antarctica are very different from those of Greenlandic origin, with the former dominated by larger, less frequent, tabular icebergs which drift in relatively unconfined seas (FitzMaurice & Stern, 2018). In contrast, icebergs calved from Greenland's tidewater glaciers are rarely tabular, are calved frequently and are often confined to relatively narrow fjords (Sulak et al., 2017), so their oceanographic impact is likely to differ from the Antarctic setting. As well as likely impacting fjord circulation, icebergs are important for several other reasons in Greenland's fjords, including as direct modifiers of water properties and as sources of freshwater and nutrients. This thesis now reviews the current understanding of their distribution, thermodynamics and role in influencing tidewater glacier dynamics.

2.3.4 Icebergs and ice melange

2.3.4.1 Iceberg size and distribution

Icebergs are ubiquitous in Greenland's fjords, but until recently their importance and role in glacier-fjord systems was largely overlooked. Icebergs are calved very frequently from Greenland's tidewater glaciers. Excluding very small bergy bits, these icebergs can range in size from a few metres to several kilometres long, with smaller icebergs produced far more frequently than larger icebergs (Åström et al., 2014; Dowdeswell et al., 1992; Rezvanbehbahani et al., 2020; Sulak et al., 2017). Large icebergs also tend to breakup shortly after calving due to mechanical damage sustained during rotation and collision with other icebergs and glacier calving fronts, further increasing the prevalence of small icebergs (Sulak et al., 2017).

Until relatively recently, few observations to quantify the size-frequency distribution of Greenlandic icebergs were available. Observations of icebergs in Antarctic waters have been available for several decades, covering both the summer and winter months (e.g. Orheim, 1987; Wadhams, 1988). These observations focused initially on medium to large (i.e. greater than 100 m in length) icebergs and were obtained using radar and sextant (Romanov et al., 2017; Wadhams, 1988) or direct visual observations (Neshyba, 1980). Satellite observations have also been used to describe the dimensions of Antarctic icebergs larger than approximately 100 m (Tournadre et al., 2012, 2016). These observations indicate that Antarctic iceberg size-frequency distributions can be closely approximated with a power law of slope ~-1.5. Given the different oceanic setting and calving style of Antarctic compared to Greenland tidewater glaciers, these observations are not directly applicable to the Greenland setting.

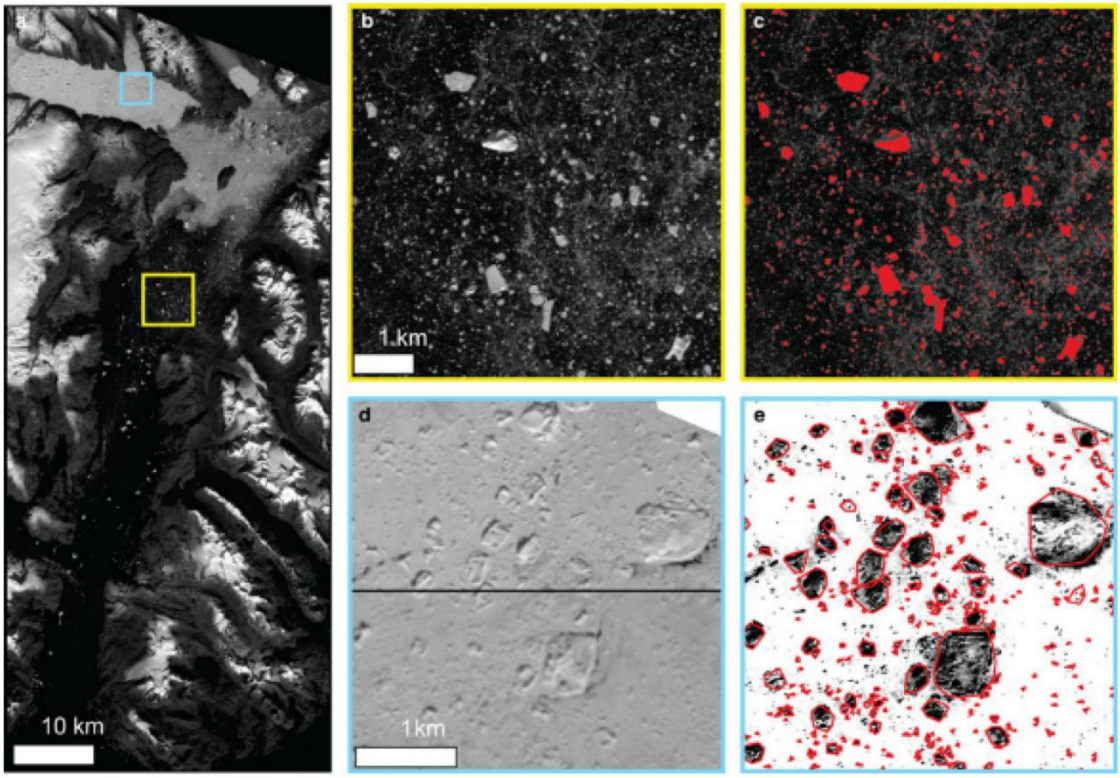

Figure 2.16. Automatic iceberg detection. Overview of the iceberg detection method used in Sulak et al. (2017). (a) A band-8 Landsat-8 image of Sermilik Fjord, east Greenland, showing the extent of panels (b) to (e). In (b) and (c) icebergs are surrounded by open water, and so are delineated (red) by a reflectance threshold. In (d), icebergs are embedded in a mélange, so the image is first smoothed using a boosted-mean filter (example in bottom half of (d), allowing iceberg delineation (e). Images show typical iceberg distribution in this fjord, with many small icebergs and fewer large ones. Reproduced from Sulak et al. (2017).

Datasets of iceberg dimensions in Greenland are relatively sparse, though are increasing in number and resolution. Until recently, most iceberg datasets were acquired from field observations, making surveys of entire fjord systems and large numbers of icebergs difficult. For example, Dowdeswell et al. (1992) used radar and sextant to survey 1900 icebergs in Scoresby Sund, east Greenland. This survey showed that iceberg concentration decreased down-fjord and that icebergs become more uniform in size with increasing distance from their source and because of the filtering effect of bathymetric highs. Similar observations elsewhere in the Arctic demonstrate some similarities in iceberg dimensions, aspect ratios and size-frequency distributions compared to icebergs in Greenland's waters (Crocker, 1993; Hotzel & Miller, 1983), likely reflecting similar calving styles and deterioration processes to the Greenland setting. More recently,

satellite observations of iceberg dimensions and distribution in Greenland's fjords have become available. These observations rely on image segmentation and edge detection to delineate icebergs largely automatically (Figure 2.16), which enables measurements of iceberg length, width and freeboard, and inferences of iceberg draught, for a large percentage of the iceberg population at the fjord scale. These observations have revealed that, at the fjord scale, summertime iceberg size-frequency distributions can be described using a power law with exponents ranging from -1.62 to -1.95 (depending on the fjord) (Sulak et al., 2017), but that the size-frequency distribution can shift towards a lognormal distribution at the fjord mouth and adjacent shelf due to uneven iceberg deterioration rates of small and large icebergs (Kirkham et al., 2017). These satellite-based observations have also shown that small icebergs (resolvable only with very high resolution satellite imagery) can significantly contribute to the freshwater budget of fjords (Rezvanbehbahani et al., 2020). As yet, observations of iceberg dimensions are limited to just a handful of fjords for a few snapshots in time, and so it is not yet clear how representative these measurements are of iceberg distributions around Greenland and at other times.

2.3.4.2 Ice mélange

Close to glacier calving fronts, iceberg concentrations are often very high, forming an 'ice mélange' – a dense, often semi-rigid, matrix of icebergs, which can be frozen together by sea ice in winter (Figure 2.17). This tends to occur adjacent to glaciers with high calving rates (Xie et al., 2019), but bathymetric obstacles and jamming of icebergs are also crucial for mélange formation (Peters et al., 2015). Some glaciers with high calving rates tend not to form an ice mélange, unless sea ice acts to contain the icebergs, because they do not have a fjord geometry or calving style conducive to iceberg jamming (e.g. Rink Glacier in northwest Greenland; Sulak et al. (2017)).

There is substantial evidence that the presence or absence of an ice mélange adjacent to tidewater glaciers can affect glacier dynamics. Based on a detailed six-year record of seasonal glacier velocity, terminus position and ice mélange condition across 16 glaciers in northwest Greenland, Moon et al. (2015) observed a strong correspondence between seasonal near-terminus mélange presence and glacier advance and between mélange absence and retreat. More detailed analysis, permitted by higher temporal resolution satellite observations covering a greater proportion of the year, demonstrated that for a sample of 13 glaciers in west Greenland, ice mélange was a relatively more important driver of seasonal terminus advance and retreat at glaciers with deep termini that typically

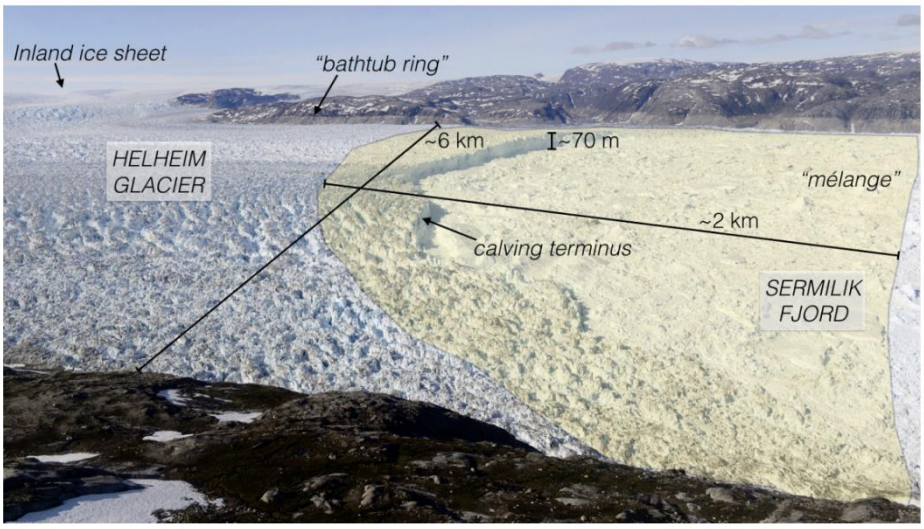

Figure 2.17. Oblique photo of ice mélange at Helheim Glacier acquired in July 2015. The yellow shaded area shows the approximate range of seasonal variability in terminus position. Reproduced from Straneo et al. (2016).

calved large icebergs through buoyant flexure, and relatively less important at shallower (<400 m) glaciers (Fried et al., 2018). Ice mélange is thought to inhibit calving at these large glaciers by providing a buttressing force against the glacier terminus (Krug et al., 2015; Robel, 2017). This effect can be important in driving seasonal, and inter-annual, changes in terminus position. For example the retreat of Kangerdlugssuaq Glacier has been linked to anomalously high calving rates during winters in which the mélange did not reach its normal rigid state (Bevan et al., 2019; Christoffersen et al., 2012). In this way, reduced seasonal ice mélange formation appears to be able to influence inter-annual glacier dynamics in some situations, a conclusion also reached through some numerical modelling approaches (Krug et al., 2015), but not others (Todd & Christoffersen, 2014).

Detailed observations of mélange and its influence on calving events are very sparse (Amundson et al., 2020; Xie et al., 2019). These reveal complexities in mélange dynamics that may be important for the buttressing force it exerts on tidewater glaciers. At Sermilik Fjord, Xie et al. (2019) showed that large (>10 m d^{-1}) variations in the flow of ice mélange occur on diurnal timescales and that the pattern and amplitude of these can vary throughout the melange. Similarly, Amundson et al. (2020) observed ice mélange formation, flow and breakup adjacent to LeConte Glacier, Alaska, noting that the mélange was highly non-uniform in terms of flow and strength, which is not easily reconciled with existing theoretical work (Amundson & Burton, 2018; Burton et al., 2018).

2.3.4.3 Iceberg drift

Once icebergs escape from the ice mélange, they drift through the fjord before either melting entirely or being discharged into the open ocean. Most observations and modelling of iceberg drift has focused on icebergs in the open ocean, with the aim of quantifying probable drift trajectories in the context of shipping and oil extraction hazards (e.g. Bigg et al., 1997). This group of studies indicate that ocean currents and wind speed are the dominant control on iceberg drift, with icebergs drifting relative to the ocean current at 2% of the wind speed (Wagner et al., 2017). However, water drag, ice drag and wave drag also influence iceberg drift, as can vertical variations in ocean current velocities if icebergs protrude through shear zones (Bigg et al., 1997). Observations within Sermilik Fjord show that icebergs there tend to drift with the vertical average of ocean currents, even when exposed to strongly sheared flows (FitzMaurice et al., 2016, 2017).

Direct observations of iceberg drift in Greenland's fjords are sparse. Using expendable Global Position System beacons, Carlson et al. (2017) tracked seven small icebergs in Godthåbsfjord, southwest Greenland, over a period of 14 to 37 days. These revealed a general down-fjord trajectory consistent with an estuarine circulation or buoyancy-driven circulation in this fjord (e.g. Mortensen et al., 2014), but with modifications due to eddies as well as abrupt wind-driven reversals over time scales of hours to days. In Sermilik Fjord, 15 larger icebergs in total were tracked over several field seasons from 2012 to 2015. Of these 15 icebergs, 12 were initially in the ice mélange 3-15 km from Helheim Glacier and took 70 days on average to exit the mélange and a similar amount of time to traverse the remaining ~60 km of the fjord to the mouth (Sulak et al., 2017). Further iceberg tracking in Sermilik Fjord found that iceberg movement within the fjord was largely affected by fjord circulation, but that the circulation was in turn controlled by winds (Jackson et al., 2014; Sutherland et al., 2014b). In addition, those iceberg trackers revealed important across-fjord velocity gradients and recirculation of fjord waters, which are often not apparent in fjord modelling studies (e.g. Cowton et al., 2016).

2.3.4.4 Iceberg melt and deterioration

Iceberg melting has recently been identified as a substantial source of freshwater in Greenland's fjords. Using repeat digital elevation models of Sermilik Fjord and Ilulissat Isfjord, Enderlin et al. (2016) demonstrated that iceberg meltwater fluxes can exceed 1000 $m^3 s^{-1}$ – similar to estimated summertime glacial runoff. Modelling of icebergs in Sermilik Fjord further showed that freshwater released by iceberg melting is a key component of

the fjords freshwater budget (Moon et al., 2017). Further observations show that iceberg freshwater flux is seasonally variable (Moyer et al., 2019) and can vary substantially between fjords and years (Enderlin et al., 2018) due to variations in iceberg draught, ocean temperature and fjord circulation. Despite this recent progress in quantifying iceberg freshwater fluxes, relatively little is known about how iceberg freshwater fluxes vary over time in response to changing environmental conditions, such as runoff supply and fjord circulation, nor how they vary between fjords or times with different iceberg concentrations and sizes.

Estimates of iceberg melt rates are sparse. The majority of iceberg melt rate estimates for Greenlandic icebergs are based on measuring the change in iceberg freeboard using digital elevation model differencing (Enderlin & Hamilton, 2014). Changes in iceberg freeboard are due to tidal height changes, elevation bias between digital elevation models, surface and submarine melting, and random error. The non-melting components must be calculated and removed in order to calculate the contribution from iceberg melting. Surface and submarine melt rates can then be disentangled somewhat using a climate model or melt model to estimate the surface melt component (Enderlin & Hamilton, 2014). Using this technique, Enderlin et al. (2018) estimated iceberg-average melt rates of 0.1 to 0.8 m d^{-1} across seven Greenlandic fjords, showing that iceberg melt rates generally increase with iceberg draught and that substantial short term variability is possible due to, for example, iceberg calving causing rapid fjord mixing (Enderlin et al., 2018).

Other estimates of iceberg melt rates and iceberg dynamics are available from modelling studies. The majority of modelling studies investigating iceberg melt rates have focused on large tabular icebergs in an Antarctic setting. Since these investigations have focused on iceberg drift around the entire continent, these models were rather simplified, often using only surface ocean conditions to calculate area-average iceberg basal melt rates (using so-called bulk melt rate parameterisations), often neglecting iceberg side melting and vertical variations in ocean conditions (e.g. Bigg et al., 1996, 1997; El-Tahan et al., 1987; Kubat et al., 2007; Martin & Adcroft, 2010; Weeks & Campbell, 1973). More recently, vertical variations in ocean properties have been implemented in Antarctic iceberg modelling (FitzMaurice & Stern, 2018; Marsh et al., 2015; Merino et al., 2016; Rackow et al., 2017; Silva et al., 2006), which generally improves modelling of iceberg trajectories (Merino et al., 2016). The model of Merino et al. (2016) has been applied to

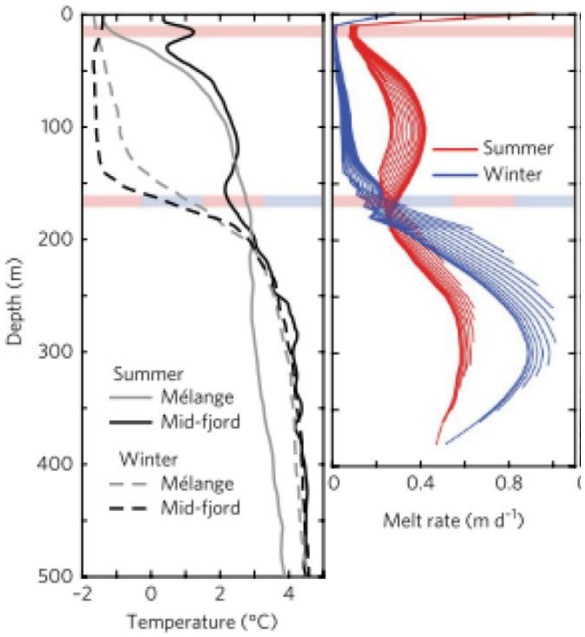

Figure 2.18. Vertical profiles of iceberg melt rates. (left) Observed temperature profiles in Sermilik Fjord. (right) Modelled submarine melt rate profiles of individual icebergs ranging in length from 50 to 1000 m. The shaded red bar indicates the summer stratification maximum at 10-20 m, and the shaded red/blue bar indicates the summer and winter stratification maximum at 160-170 m. Reproduced from Moon et al. (2017).

Greenland, showing that including vertically-averaged water properties decreased modelled iceberg lifetime by 112 days on average due to the inclusion of warm AW at depth (Marson et al., 2018), though this model did not resolve the fjords connecting the Greenland Ice Sheet and the ocean, meaning the icebergs had to be seeded in the open ocean. Modelling of iceberg melt rates within Greenland's fjords is limited to a simple iceberg melt model, which was not coupled to an ocean circulation model but was instead forced with observations acquired within Sermilik Fjord (Moon et al., 2017). This modelling effort revealed substantial vertical variation in iceberg melt rates (Figure 2.18), with melt rates generally increasing with depth where water temperatures are greatest, but with additional modification due to the strongly sheared flow in the fjord. Since this iceberg melt model was not coupled to an ocean circulation model, it is not known how this meltwater affects the circulation of Sermilik Fjord nor how iceberg melting in general can affect fjord circulation.

2.4 The ice-ocean interface

2.4.1 Submarine melting

One of the leading hypotheses seeking to explain the behaviour of tidewater glaciers in recent decades is that increased submarine melt rating of tidewater glacier calving fronts drove tidewater glacier retreat. In this context, submarine melting refers to subaqueous melting of both the quasi-vertical calving faces of tidewater glaciers and the quasi-horizontal underside of floating ice tongues and ice shelves. The former are more common in Greenland, with ice tongues and ice shelves being restricted largely to northern Greenland (Hill et al., 2017). Submarine melting of icebergs also occurs in Greenland's fjords.

Submarine melting occurs when ice is in contact with ocean waters that have a temperature greater than the *in-situ* (pressure and salinity-dependent) freezing point (Gade, 1979; Jenkins, 1999). Modelling studies indicate that submarine melt rates increase linearly with ocean temperature (Slater et al., 2016; Xu et al., 2013). Processes operating in the open ocean or fjord that affect glacier-adjacent water temperatures will therefore influence glacier submarine melt rates. Heat and freshwater exchange between the ice and the ocean is also amplified by water movement, with faster water movement associated with greater heat exchange (and therefore melting) (e.g. Holland & Jenkins, 1999). This water movement may be due to local melt-driven convection (Magorrian & Wells, 2016) or the wider circulation of fjord waters (e.g. Jenkins et al., 2010). In particular, runoff-driven plumes can rise rapidly through the water column (see Section 2.4.2), inducing powerful turbulence at the ice-ocean interface (e.g. Jenkins, 2011). When runoff is the dominant source of motion, modelling studies indicate that submarine melt rates scale sub-linearly with subglacial discharge, with submarine melting increasing with discharge raised to the power 1/3 to 3/4 depending on the plume geometry and stratification (Sciascia et al., 2013; Slater et al., 2016; Xu et al., 2012). The dominant source of water motion likely varies between locations and time periods. In Greenland, high rates of runoff during summer mean runoff-driven plumes may be the key driver of water motion across many tidewater glacier fronts during summer (Fried et al., 2015), though melt-driven convection or other drivers of circulation may be important in areas distal to glacial plumes (Cowton et al., 2015; Sutherland et al., 2019). During winter, or in low runoff environments such as Antarctica, tides and melt-driven convection are likely dominant. Because submarine melting increases with ocean temperatures and subglacial discharge, it is highly likely that submarine melt rates at Greenland's tidewater glacier

calving fronts have increased in recent decades (Wood et al., 2021). However, there are no direct observations of submarine melting available to confirm this, and the chain of events linking increased submarine melting to rapid glacier retreat is not clearly understood.

Direct observations of submarine melting are not available due to the extreme difficulty and danger in accessing submerged ice in glacial environments. In Antarctica, submarine melt rates of sea ice have been inferred through detailed measurements of oceanic heat fluxes close to the sea ice-ocean boundary (McPhee, 1992; Wettlaufer, 1991), as have melt rates of a large ice shelf through measuring ice shelf thickness changes using ice penetrating radar (Jenkins et al., 2010). Since the hydrographic environment and orientation of the ice faces are very different in Antarctica compared to those for a Greenlandic tidewater glacier, melt rates observed in these settings are not however expected to be representative of melt rates of Greenland's tidewater glaciers.

Existing observations permitting estimates of tidewater glacier submarine melt rate are either hydrographic in nature or involve imaging the shape of the submerged ice face. Submarine melt rate estimates based on the latter technique (e.g. Fried et al., 2015; Sutherland et al., 2019) require high-resolution images of the submerged calving front, in addition to synchronous estimates of ice velocity and terminus position, and the exclusion of changes to the subsurface ice geometry due to calving. Observations of this nature in Greenland reveal complex patterns of submarine melting, reaching rates of over 3.5 m d^{-1} in the proximity of runoff-driven plumes but declining to less than 1 m d^{-1} elsewhere (Fried et al., 2015). Similar, though more detailed, observations of LeConte Glacier, Alaska, reveal much higher melt rates of up to ~10 m d^{-1} due to warmer ocean waters (Sutherland et al., 2019). Since these surveys are extremely challenging, they are sparse in space and time, providing only snapshots of submarine melt rates over irregular time periods and often focusing on smaller glaciers which calve smaller icebergs, so it is not clear how representative these melt rates are of other glaciers and at other times.

Submarine melt rate estimates based on hydrographic measurements are more common than those based on calving front evolution. These hydrographic-based estimates rely on measurements of fjord temperature, salinity and velocity along a transect (or flux gate) across a fjord to calculate the heat budget of the area enclosed between the flux gate and the glacier (often called the 'control volume'; Jackson and Straneo, (2016)). The heat lost in the control volume can be used to infer the total submarine melt volume, if other heat

sinks are accounted for. If one assumes that all of this submarine melting was of the submerged calving front (and not of icebergs), a submarine melt rate can be calculated by dividing the estimated melt volume by the submerged calving front area. This method has been used extensively, providing (for example). melt rate estimates of 1.8 m d^{-1} for Helheim Glacier (Sutherland & Straneo, 2012) and 10 m d^{-1} for Kangerdlugssuaq Glacier (Inall et al., 2014). These estimates are, however, subject to considerable uncertainty. Typically, hydrographic measurements must be made many kilometres from the calving front of interest, and so will include a submarine melt signature from all icebergs within the control volume (Jackson & Straneo, 2016), which can be significant (Enderlin et al., 2016). They also usually assume that there is no re-circulation of heat within the control volume and often rely on extrapolation of measurements across the fjord (Rignot et al., 2010; Xu et al., 2013). As with monitoring calving front morphology, they also only provide snapshot-in-time measurements of submarine melting.

2.4.2 Plumes

As mentioned above, plumes form where subglacial discharge is released into fjords at depth (Figures 2.6 & 2.9). Over the past ten years, it has become clear that these plumes are a key phenomenon in glacier-fjord systems, and can strongly influence glacier submarine melt rates. Accordingly, considerable research into their dynamics has been undertaken, building on buoyant plume theory developed for non-glacial contexts (Jenkins, 2011; Morton et al., 1956). When fresh subglacial discharge enters salty, dense fjord water, it rises towards the fjord surface as a turbulent plume because it is buoyant. As the plume rises, the shear between the rapidly rising subglacial discharge and the fjord water generates turbulent mixing at the edges of the plume, causing the plume to entrain surrounding fjord water. This dilutes the subglacial discharge with fjord water, causing the properties of the plume to trend towards the ambient conditions, thus causing the buoyancy of the plume to decrease whilst its volume flux increases. The plume will continue to entrain fjord water until it either reaches the fjord surface or until it reaches a depth at which it is of equal or greater density to the overlying water and loses upward momentum (Figure 2.19). In Greenland's fjords, we have seen that the upper layer of the water column is often comprised of relatively low density PW, and so plumes often reach neutral buoyancy at the interface between the AW and PW (e.g. Carroll et al., 2015; Chauché et al., 2014; Sciascia et al., 2013). Once the plume has reached this neutral buoyancy depth it may continue to rise temporarily because of its momentum, before diving back down to the neutral buoyancy depth and subsequently flowing away from the

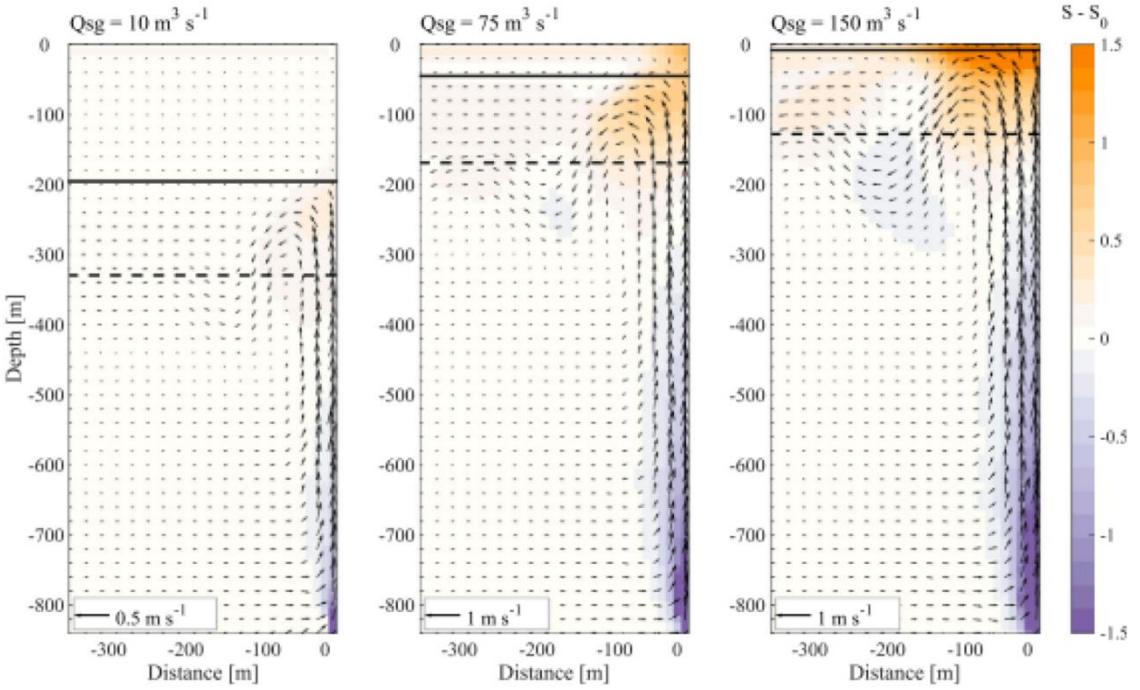

Figure 2.19. Plume dynamics. Cross-section views of runoff-driven plume velocity and the resulting near-glacier salinity anomaly for different subglacial discharge fluxes. As subglacial discharge flux increases, plumes rise higher in the water column. The dashed lines indicate the plumes neutral buoyancy depth, whilst the solid black lines indicate the plumes maximum height. For all subglacial discharge fluxes, the plumes initially overshoot their depth of neutral buoyancy, before diving back down to the neutral buoyancy depth. As subglacial discharge flux increases, the plumes rise towards the surface more rapidly and entrain more ambient water (resulting in a larger positive salinity anomaly near the plumes maximum height). Reproduced from Carroll et al. (2015).

glacier (Figure 2.19). Hydrographic observations within plumes indicate that, at the surface, plumes may be comprised of >90% entrained fjord water (Bendtsen et al., 2015; Jackson et al., 2017; Mankoff et al., 2016). Thus, plumes are highly efficient mixing engines in glacial fjords, and are responsible for drawing warm, salty water at depth towards the fjord surface (Figure 2.19) (Carroll et al., 2015, 2017; Mankoff et al., 2016; Straneo et al., 2010).

An additional aspect of plume investigations has been on the resulting impact on terminus stability. Plumes cause both vertical and lateral variations in melt rates, leading to variations in glacier terminus shape, which should in turn affect the force balance at the calving front and affect calving rates. However, there is little agreement among models regarding the effect of submarine melting on calving. On the one hand, some studies

predict that submarine melting may increase calving (Benn et al., 2017; Cowton et al., 2019; O'Leary & Christoffersen, 2013), but by two different mechanisms. Firstly, if submarine melting promotes undercutting of glacier termini, this enhances the bending stresses near the terminus and can produce calving events several times the undercut length (Benn et al., 2017; O'Leary & Christoffersen, 2013). Secondly, if plume-driven submarine melting enhances lateral variations in submarine melt rates, notches in the terminus can develop. If these notches disrupt compressive stresses near the calving front, then retreat can occur at several times the width-averaged melt rate (Cowton et al., 2019). The extent to which this occurs in reality is not yet clear: modelled submarine melt rates are generally much lower than ice velocity rates, and so sufficiently large undercuts may never develop (Benn et al., 2017). Undercut lengths of tens to hundreds of metres have been observed at some tidewater glaciers (Fried et al., 2015; Rignot et al., 2015) but these undercuts did not appear to cause instability. On the other hand, at some glaciers, particularly those that calve by buoyant flexure, submarine melt-driven undercutting appears to be a stabilizing factor (Benn et al., 2017; James et al., 2014), or has little influence on glacier stability (Cook et al., 2014; Krug et al., 2015; Todd et al., 2019; Todd & Christoffersen, 2014). The effect of submarine melting on calving therefore seems to depend on the spatial distribution of submarine melting and the calving style, and not simply the magnitude of submarine melting (Ma & Bassis, 2019). One major implication of these studies is that understanding the spatial distribution of submarine melting, and therefore near-terminus subglacial hydrology, may be important for understanding glacier behaviour.

2.5 Summary

Over the past two decades, our understanding of the drivers of tidewater glacier dynamics and of key processes in glacier-fjord systems has increased dramatically. With this improvement in understanding, our predictions of the Greenland Ice Sheets future contribution to sea level rise have improved (Goelzer et al., 2020). This chapter has shown that glacier-fjord systems are complex, with key processes operating of timescales of seconds to decades and over spatial scales ranging from sub-metre to the ocean basin scale. Many of the processes discussed in this chapter provide mechanisms by which changes in atmospheric and oceanic conditions can perturb glaciers. Once perturbed by these changes, internal glacier dynamics and glacier geometry can amplify or mute the glacier response (Felikson et al., 2017, 2020; Pfeffer, 2007), which can result in continued

glacier mass loss even if the initial perturbation is removed. This chapter has also shown that many of these processes are interconnected, and so it is difficult to address components of glacier-fjord systems in isolation. In an effort to improve our understanding of glacier-fjord systems, this thesis focuses on two particularly poorly-understood aspects of these systems. Firstly, this thesis investigates the controls on dynamic variations observed at tidewater glaciers. Secondly, the impact of icebergs on fjord systems (and the associated feedbacks on tidewater glaciers) are investigated.

Chapter 3 - Methods

This chapter provides a brief overview of the methods used in this thesis and provides some additional methodological details to those provided in the results chapters. This thesis uses two principle tools or techniques to examine glacier-fjord systems. The first uses satellite imagery to track the flow of glaciers, whilst the second uses a general circulation model to simulate the circulation in glacial fjords. The first technique is utilised in Chapter 4 to examine seasonal changes in the flow speed of contrasting tidewater glaciers. The second technique is used in chapters 5 and 6 to examine iceberg-ocean interaction in Greenland's glacial fjords, and the implications of that for ice sheet-ocean interaction. The intention of this chapter is to supplement the methodological information provided in Chapters 4 to 6, not to provide an exhaustive and detailed description of the methods used in this thesis.

3.1 Remote sensing of glacier velocity

Ice velocity is a key measure of glacier behaviour, exerting a key control on the mass balance of the glacier or ice sheet. Changes in ice velocity can occur over time-scales ranging from hours to decades, and are due to a range of processes. Some of these changes, such a rapid uplift during supraglacial lake drainage, are not resolvable using

satellite imagery. Despite this limitation, satellite-based estimates of ice velocity are still useful because many processes are resolvable using satellite imagery, and because satellite-based velocity datasets can be cheaper (for the user) and are logistically easier to obtain than *in situ* data, making this a useful tool to monitor those processes. In addition, satellite-based observations also enable tracking of ice velocity over large areas, and so are complimentary to higher temporal resolution ground-based velocity measurements. Satellite-based ice velocity estimates have been available for decades (e.g. Doake & Vaughan, 1991; Joughin et al., 1995; Lucchitta et al., 1993; Lucchitta & Ferguson, 1986; Scambos et al., 1992). Since those early estimates were made, the underlying techniques have been refined (e.g. Joughin, 2002; Luckman et al., 2015; Strozzi et al., 2002), enabling more accurate and reliable ice velocity estimates. Perhaps the greatest change, however, has been the increased availability of satellite imagery with which ice velocity estimates can be made, and the increased performance and affordability of computing and storage resources.

In this thesis, the European Space Agency's Sentinel-1 mission is the primary source of imagery used for estimating ice velocity. The Sentinel-1 mission comprises two polar-orbiting satellites – Sentinel-1a and Sentinel-1b – each equipped with a C-band (5.4 GHz) Synthetic Aperture Radar (SAR) sensor. Sentinel-1a was launched in April 2014, and its sister satellite, Sentinel-1b, in April 2016. The Sentinel-1 SAR sensor uses an active phased array antenna, which supports four different operational imaging modes that provide different resolution and coverage: Interferometric Wide swath (IW) mode, Extra Wide swath (EW) mode, Strip-Map (SM) mode, and Wave (WV) mode (Torres et al., 2012). In this thesis, I utilise images acquired in IW mode, which is the nominal mode for land areas (including ice sheets). The IW mode is operated using the Terrain Observation with Progressive Scans (TOPS) technique, which provides a large (250 km) swath width at a nominal ground resolution of 5 x 20 m (De Zan & Guarnieri, 2006).

The Sentinel-1 pair are, together, capable of providing repeat images of glacier surfaces every six days, regardless of illumination or weather conditions. The resulting increase in data availability has enabled researchers to generate continuous time-series of ice velocity over large areas and at high resolution, thereby revolutionising our ability to monitor ice velocity at large scale. In Chapter 4, Sentinel-1 imagery is used to interrogate seasonal variations in ice velocity and to determine the processes underlying those changes, providing much more detailed and spatially extensive insight into glacier dynamics than

was previously achievable. It is the generation of ice velocity estimates from Sentinel-1 imagery that this section focuses on.

The code used derive ice velocity in Chapter 4 of this thesis was developed by one of my supervisors, Dr Andrew Sole. Subsequently, I developed a system to automate this procedure and surrounding tasks. Both systems were used in this thesis and are described in turn here.

3.1.1 Offset tracking

Several techniques can be used to derive ice velocity from Sentinel-1 imagery (and indeed, from any SAR imagery). These can be classified as differential SAR interferometry (DInSAR), multi-aperture interferometry (MAI), and offset-tracking. Each method has its own strengths and weaknesses (Boncori et al., 2018). DInSAR yields measurements of displacement in the line-of-sight direction between two SAR acquisitions by exploiting the relationship between line-of-sight distance in slant range and the phase delay differences in the two co-registered images, provided that the radar returns at the times of the two acquisitions are statistically similar (coherent) (Boncori et al., 2018). The contribution of topography must be removed either using an external DEM or by using two SAR image pairs acquired with different viewing geometries. DInSAR is capable of making highly accurate (<1 cm) displacement measurements, provided that images are coherent, which is typically not the case for the fast-flowing tidewater glaciers studied here. MAI measures displacement in the azimuth (or flight) direction between two SAR acquisitions, by exploiting the relationship between image mis-registrations in the azimuth direction and phase variations (Bechor & Zebker, 2006). As with DInSAR, coherence must be maintained between images, and so this method is not optimum for measurement of fast-flowing tidewater glaciers.

In this thesis, only offset tracking is used. Offset tracking methods measure displacement in both the line-of-sight and azimuth direction by measuring the distance between corresponding patterns of surface features (such as crevasses) in sequential satellite images (image pairs). Offset tracking can be used to measure displacement in both coherent and incoherent areas of the ice sheet; however, as will be described in more detail below, the maximum achievable accuracy with offset tracking is typically an order of magnitude worse than with DInSAR.

In order to accurately track feature offset between image pairs, the respective images must be precisely aligned (or geolocated) and must be acquired with the same viewing geometry, so as not to introduce an apparent offset between features. Ensuring the latter is relatively straightforward, since Sentinel-1a and -1b follow the same orbital pathways, and so acquire so-called 'repeat imagery' (i.e. imagery acquired with the same viewing geometry and with the same ground footprint) every 6 days when both Sentinel-1a and -1b are utilised (and every 12 days when only one of the missions is used). Therefore, it is only necessary to select imagery acquired multiples of 6 days apart to achieve this. Ensuring that images are correctly geometrically aligned is more complex, and requires the use of specialised SAR software. In this thesis, the Generic Mapping Toolbox for SAR imagery (GMTSAR; Sandwell et al. (2011)) was used to align pairs of satellite imagery. In other applications using SAR image pairs, image cross-correlation itself is often used to align image pairs (Xu et al., 2017); however, this is clearly inappropriate for images acquired over regions where surface displacement is expected, like those used in Chapter 4. Instead, this software utilises orbital positioning information provided by the European Space Agency (ESA) to align image pairs. When possible, 'precise orbit ephemerides' were used, which are orbital information accurate to 5 cm (https://sentinel.esa.int/documents/247904/3455957/Sentinel-1-POD-Products-Performance.pdf). However, these are only released 3 weeks following image acquisition. Therefore, for image pairs in Chapter 4 that were processed close to the image acquisition time, 'restituted orbit files', were used, which are accurate to 10 cm. These orbital data are available from: https://qc.sentinel1.eo.esa.int/.

Following image alignment, it is advantageous to pre-process satellite imagery prior to undertaking the offset tracking itself. The principle aim of the pre-processing stage is to emphasise the visibility of those surface features that are advected with ice flow, whilst minimising that of other features. Several methods are available to do this (Boncori et al., 2018; De Lange et al., 2007). In Chapter 4, two principle pre-processing steps were used: contrast-limited adaptive histogram equalisation (CLAHE), and high-pass filtering. The purpose of CLAHE is to improve (from the point of view of identifying movable glacier-surface features) contrast in images, which ultimately enhances the definitions of edges (such as crevasse rims). High-pass filtering also improves edge detection by filtering out long-wavelength variations in backscatter that are often caused by surface topographic features (which do not move with ice flow).

The offset tracking procedure itself is described in detail in Thielicke and Stamhuis (2014). At its core, offset tracking involves breaking both images into equal chunks (often termed interrogation areas (IAs) or image chips), and cross-correlating corresponding IAs to determine the misalignment between features contained within the IAs. One can conceptualise this process by visualising the IA from the second (slave) image being iteratively moved over the corresponding IA from the first (master) image, correlating the backscatter fields each time. In this way, a 2-D field of correlation values is generated for each IA pair (Figure 3.1). In offset tracking, it is reasonably assumed that the location with the highest correlation value corresponds to location to which ice surface features have been advected between the two image acquisitions. The displacement is therefore the distance between the centre of the master IA and the centre of the cross-correlation peak. Ice velocity can then be calculated using this distance and the known time between image acquisitions. Although helpful to visualise the process in this manner, in practice the cross-correlation is undertaken in the frequency (rather than the spatial) domain using fast Fourier transform, which reduces computation time by an order of magnitude (Thielicke, 2014).

In order to obtain accurate displacement (and therefore velocity) estimates, it is essential to determine the location of the cross-correlation peak accurately at the sub-pixel level. To illustrate, mis-identifying the cross-correlation peak by 0.5 pixels over a 12-day period corresponds to a ~40 m yr^{-1} error in the range direction and ~214 m yr^{-1} in the azimuth direction (due to the different range and azimuth resolutions of Sentinel-1 imagery). For comparison, land-terminating sectors of the Greenland Ice Sheet typically flow at 200 m yr^{-1} near the margin and undergo seasonal changes in ice velocity of the order of 100%. Accurate sub-pixel displacement estimates are therefore particularly important when identifying changes in ice velocity of slower moving ice masses, but are still important for faster flowing tidewater glaciers such as those studied in Chapter 4. Several algorithms are available to make sub-pixel displacement estimates, and these can generally be grouped into two types: those that interpolate the cross-correlation matrix itself, or those that interpolate the underlying image data and perform the cross-correlation at higher resolution. In this thesis, a form of the latter technique is used (Guizar-Sicairos et al., 2008). More specifically, the chosen technique involves calculating the cross-correlation

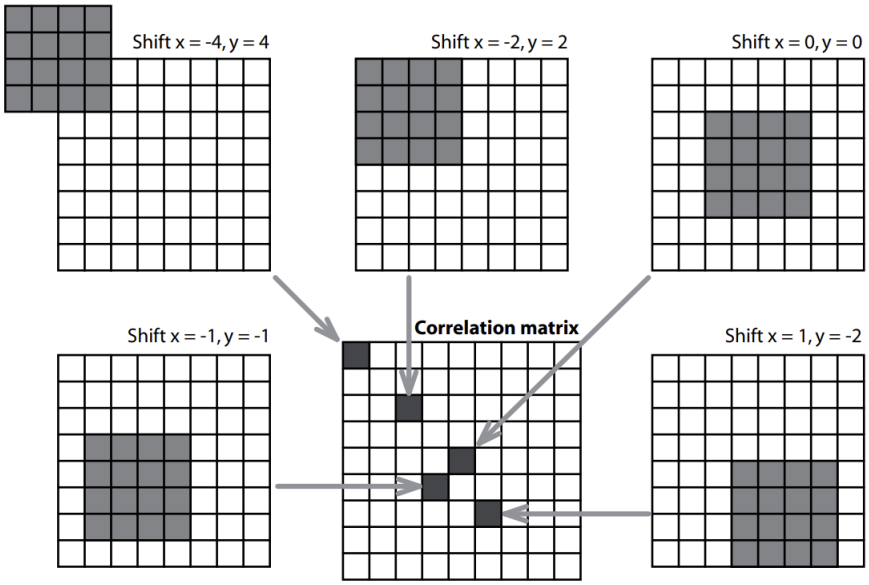

Figure 3.1. Calculation of a correlation matrix using direct cross-correlation of two unevenly sized interrogation areas. Reproduced from Thielicke (2014).

field for the IA pair in order to obtain a rough estimate of the cross-correlation peak location, up-sampling a small region around this peak by a factor of 100, then computing the cross-correlation matrix again to identify the peak location more precisely, before mapping this back to the original resolution of the IA pair.

Appropriate selection of IA size and overlap is also essential for accurate and efficient displacement estimates. This is because in the frequency domain, the IA's must be identical in size, and so any displacement leads to loss of information. Ideally, IA's must be four times larger than the maximum expected displacement, to ensure a sufficient amount of information is retained within the IA for reliable correlations to be made. However, too large IA's reduce the resolution of the resulting velocity field and increase the chance of retrieving false correlations, and therefore erroneous velocity estimates. The degree of IA overlap controls the smoothness of the resulting velocity field, and so strongly influences the fidelity of velocity estimates in areas with steep velocity gradients (such as shear margins). In general, increasing IA overlap enables sharper representation of steep velocity gradients and velocity retrieval closer to glacier termini. In Chapter 4, IA's of 400 by 180 single-look oversampled range and azimuth pixels (or approximately 1x1 km) are used, with an overlap of 300x126 pixels (approximately 800 m).

The resulting 'raw' velocity fields were post-processed to remove erroneous velocity estimates while attempting to retain accurate estimates. Many of the filters used to do this are based on known characteristics of ice flow – ice tends to vary in speed and flow direction in a relatively smooth manner, and it is unrealistic to have areas of faster flow surrounded by areas of slower flow, for example. With these characteristics in mind, several filtering methods were used in this research. Firstly, a segmentation filter (Lüttig et al., 2017) was used to remove clusters of outliers using a region growing approach (https://uk.mathworks.com/matlabcentral/fileexchange/19084-region-growing). This filter can identify and remove blocks of pixels if they are sufficiently different from surrounding pixels, even if the velocity field is smoothly varying within the pixel block. In addition, a threshold strain filter (Rosenau et al., 2015) and a kernel density filter based on the paired displacements in the range and azimuth directions for each image patch (Adrian & Westerweel, 2011) were used. Velocity fields were also filtered for unrealistic changes in flow direction (pixels deviating by more than 45 degrees from the median of the surrounding pixels were removed) and unrealistically high speeds (defined as 80% of the maximum detectable velocity based on the IA dimensions (which is over 100 m d^{-1} using the IA dimensions described above). Finally, the velocity fields were filtered using a signal-to-noise ratio filter, with a threshold of 5.8 – defined as the ratio of the cross-correlation peak to the average of the remaining cross-correlation field (De Lange et al., 2007). Finally, the filtered velocity field must be converted from radar to map coordinates, which is achieved by using a scattered interpolation and a Digital Elevation Model (DEM), and so takes into account spatial variations in ground pixel sizes that result from using a side-looking radar over uneven topography.

In Chapter 4, imagery from two optical platforms, Sentinel-2 and Landsat-8 were also used to derive velocity estimates. The offset tracking procedure is essentially the same for these images, however, there is no need to convert between radar and map coordinates and alignment of image pairs is rather more straightforward.

3.1.2 Ice velocity error sources

There are several sources of error in velocity estimates derived from offset tracking of Sentinel-1 imagery. The main sources of error are: (1) satellite positioning uncertainty due to orbital errors; (2) geolocation biases between Sentinel-1a and -1b; (3) ionospheric noise; (4) uncertainty in the elevation of the scattering surface, and; (5) cross-correlation errors. Each of these are summarised briefly in turn below. Cross-correlation errors are

largely due to identifying the location of the cross-correlation peak, which was described above, so this information is not repeated here.

Orbital errors will cause an apparent shift between the Sentinel-1 images in a pair, resulting in an image wide velocity bias. As mentioned, absolute orbital errors are approximately 5 cm for the precise orbits and 10 cm for the restituted orbits. Solgaard et al. (2021) used velocity biases over bedrock (stable) areas around Greenland to quantify orbital induced errors. They found biases of -0.5 m yr^{-1} and 0.5 m yr^{-1} in the range and azimuth direction, respectively, and no significant difference velocity estimates derived using precise and restituted orbit files. Regarding error source (2), Solgaard et al. (2021) observed a bias over bedrock areas of ~8.7 m yr^{-1} and ~29 m yr^{-1} in the range and azimuth direction, respectively, when using two 6-day Sentinel-1 pairs compared to a 12-day pair over the same period.

Ionospheric propagation errors arise due to spatial fluctuations (or scintillations) in the ionospheric total electron content with the synthetic aperture length of the SAR image (Gray et al., 2000). This fluctuations cause an azimuth variation in the raw signal phase, resulting in an azimuth shift of the focused pixel. Since these fluctuations cannot be known and corrected for in advance, the pixel shift produces an apparent motion in the velocity map. The apparent motion varies across the scene according to the ionospheric conditions along the satellite flight path, and typically appears are a series of linear streaks in the azimuth velocity map. Such errors can be large (up to 300 m yr^{-1}) and are irregularly spaced in time. At the latitude of the glaciers studied in this thesis, such ionospheric errors are rare and were not apparent in any of the velocity maps.

Uncertainty in the elevation of the scattering surface will lead to a shift in the focused pixel (i.e. the location of the intensity associated with a particular pixel will be inaccurate). In this thesis, the Greenland Ice Mapping Project (GIMP) DEM (Howat et al., 2014) was used to define the elevation of the scattering surface, in order to focus the SAR imagery. The GIMP DEM has a nominal timestamp of 2007. Since 2007, the glaciers studied in this thesis have thinned by several tens of metres, and so this DEM does not represent the scattering surface at the time of the Sentinel image acquisitions, which will lead to biases in displacement measurements over the study period. However, this source of error is expected to be constant between images and throughout the study period.

3.1.3 Automatic velocity retrieval

Generating velocity estimates using the above methods therefore requires the user to identify, download and manoeuvre satellite imagery, DEMs and orbital information. Individual Sentinel-1 images are typically 3-6 Gb each and generating the velocity time-series presented in Chapter 4 involved utilising many hundreds of these images, each with corresponding orbital information, and most of which were used twice (for sequential image pairs). In addition, at the latitudes considered in Chapter 4, multiple image footprints intersect or encompass the study area, and, over the course of the Sentinel-1 operation, image footprint locations have changed, meaning that manual selection of image pairs can become very time consuming. Clearly, when considering large areas and/or long periods of time, it is impractical to perform this processing manually. Indeed, the Centre for Polar Observation and Modelling (Lemos et al., 2018) and the Programme for Monitoring of the Greenland Ice Sheet (Colgan et al., 2019) are producing Greenland-wide estimates of ice velocity using Sentinel-1 imagery and have invested considerable effort into automating their respective processing chains.

As part of Chapter 4, and as a wider research effort, I automated the processing chain described above – including image pair identification, download, alignment and offset tracking. The user need only supply a 'configuration' file specific to their region of interest (defined using latitude and longitude coordinates), and a period of interest. This system – Sentinel-1 Cross-correlation for Accurate Determination of Ice velocity (SCADI) – is designed such that ice velocity time-series (i.e. sequential ice velocity fields, not just points) can be either generated retrospectively (for example, when examining a new region of interest) or generated operationally (for continual monitoring of an existing region of interest).

Figure 3.2 details the principle stages of this automated processing chain, which are described here. SCADI first searches the ESA API hub for metadata associated with all images on the provided dates. Using the coordinates of the images vertices (with a user specified buffer), it identifies all image pairs during the period of interest. The period of interest can, for example, be a single velocity epoch (i.e. a 6- or 12-day window would be typical for Greenland); or, it can search for an unlimited number of velocity epochs within a much larger time frame. In other words, it can identify every pair for date pairs on which there is at least one useable image pair, over any time period and for any region of the world. Metadata for all available image pairs are permanently stored for future

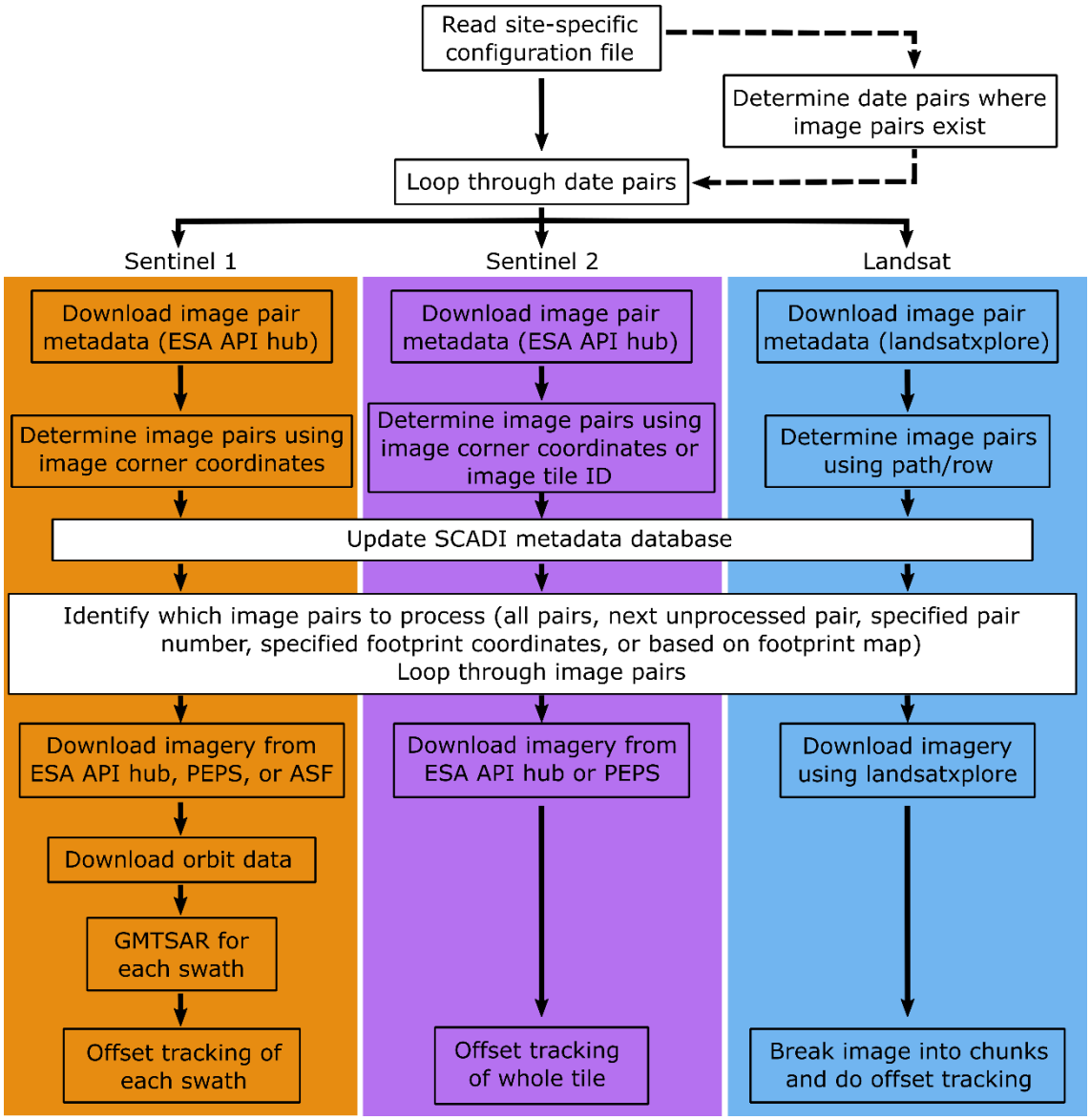

Figure 3.2. Overview of SCADI workflow. PEPS is a French mirror site operated by the Centre National D'études Spatiales (https://peps.cnes.fr/). ASF is the Alaska Satellite Facility (https://asf.alaska.edu/). Landsatxplore is a freely available python package that provides a command line interface to EarthExplorer (https://github.com/yannforget/landsatxplore).

reference. If the coordinates of the region of interest changes (e.g. if the user wishes to expand a study area), SCADI will compare future image searches to this metadata database, to identify any new image pairs and avoid reprocessing of existing image pairs.

Having identified all the available image pairs, it is necessary to choose which pairs to process. Several options are available for this. For large-scale mapping and operational purposes, it is often desirable to simply process every available image pair (or indeed, just the next pair or pairs that remain unprocessed). However, for new regions or if

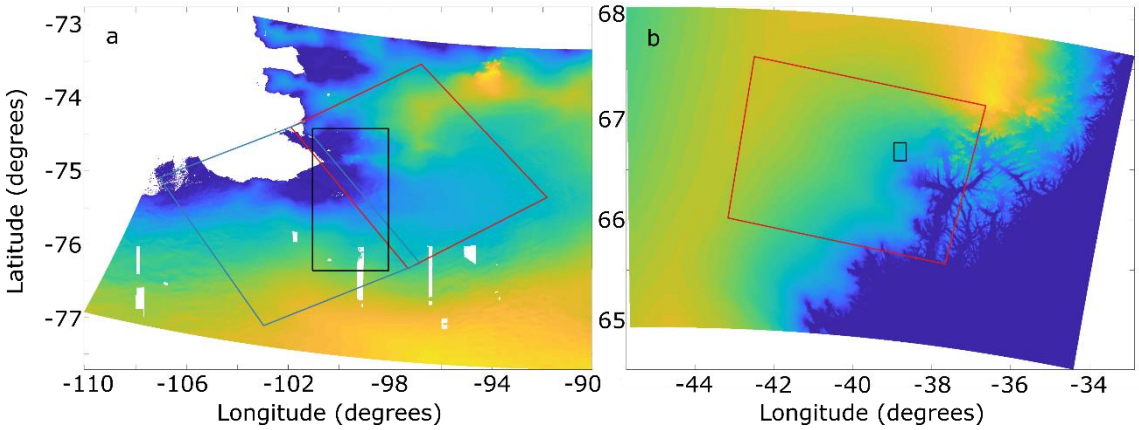

Figure 3.3. SCADI image pair footprints. Examples of image footprint selection for (a) Pine Island Glacier for date pair August 14th 2019 to August 20th 2019 and (b) Helheim Glacier for date pair October 22nd 2018 to October 28th 2018. Background colours indicate the elevation of the region (yellow is higher elevation and blue is lower elevation). The black box denotes the user defined region of interest and the coloured boxes denote image footprints identified by SCADI on these particular date pairs.

computing resources are limited, it is often desirable to only process those pairs which provide optimal coverage and which have continuous time-series. With SCADI, the user can optionally plot an image showing the location of all the available image footprints on each date pair (Figure 3.3), allowing the user to select the optimal footprint for their analysis. Lists of date pairs containing these footprints are automatically generated and saved.

Once an image pair (or pairs) has been chosen, SCADI will download the images from one of three Sentinel-1 datahubs (Figure 3.2). Multiple data hubs are used for two reasons. Firstly, when a hub is busy, download speeds can be reduced. Secondly, and more importantly, older images are archived in the ESA and PEPS hubs, and must be manually requested before they are released up to 72 hours later, and there is no possibility to set up an automatic alert once the images are released. The ASF hub has no long-term archive (all imagery in the hub are available immediately), and so this is used when older images are not available from the other hubs. However, the ASF hub is not updated as frequently as the other hubs, so those other hubs are used preferentially for newer and non-archived imagery. The downloaded images are stored in a central database within SCADI. To avoid duplications during processing, these are symbolically linked to the processing folders, thereby minimising storage requirements. Orbital data corresponding to these images are

also automatically downloaded and stored – by default, it uses the precise orbit ephemerides, but if those data are not available, it will download the restituted orbit data.

Having 'prepared' each image pair, by downloading and manoeuvring the raw data, SCADI initiates the GMTSAR processing. To optimise computing resources, SCADI processes each swath of the Sentinel-1 image separately (and individual swaths can be targeted, whilst others ignored, if desired). Processing of each swath in GMTSAR typically takes 1-3 hours. SCADI monitors each swath, and once the processing is successful, it proceeds with the offset tracking itself. Output from the offset tracking is automatically backed up, and intermediate files can be retained or removed as desired and as storage resources permit. Once a database of velocity fields has been generated, separate routines are available to extract point-location time-series and larger scale velocity maps, which can be saved as images, geotiffs, .mat files, hdf5 files, or NetCDF files, to facilitate analysis and distribution.

I have recently further developed SCADI so that it also includes Landsat (5-8) and Sentinel-2. Although this development is not utilised in this thesis, it has greatly increased the volume of satellite imagery available for automated ice velocity estimation. By combining both optical and radar imagery in this way, it will now be possible to generate continuous, dense, high-resolution velocity estimates of the Greenland Ice Sheet from the margin to the interior, with minimal user effort.

This processing system is an efficient and relatively user-friendly (MSc students with no programming background have used the system) means to generate large velocity datasets over land ice. It has been used on three high performance computing clusters, and has been used extensively by Dr. Andrew Sole (a co-supervisor of the author), by a post-doctoral researcher at the University of Sheffield, and by a handful of MSc students at the University of Sheffield, including as a bases for a published study on the effect of meltwater drainage on the velocity of Antarctic Peninsula outlet glaciers (Tuckett et al., 2019). In this thesis, SCADI was used to derive a continuous, high combined temporal and spatial resolution dataset of ice velocity for three tidewater glaciers in southwest Greenland, enabling more detailed interrogation of seasonal ice velocity patterns close to glacier termini than had previously been achieved.

3.2 Modelling Greenland's fjords

In Chapters 5 and 6 an ocean circulation model is used to examine the response of fjords to submarine iceberg melting. Prior to this work, no ocean model contained a submarine iceberg melt parameterisation suitable for simulating glacial fjords in high resolution, representing a significant gap in our ability to understand these fjords. This section provides an overview of the ocean model and the new iceberg melt package that was developed to fill this gap.

3.2.1 MITgcm

The Massachusetts Institute of Technology general circulation model (MITgcm) is a versatile tool for simulating both ocean and atmospheric dynamics. The model solves the incompressible (or Boussinesq) form of the Navier-Stokes equations using finite volume methods on an orthogonal curvilinear grid called an Arakawa-C grid, and can be used in both hydrostatic and non-hydrostatic mode (Marshall et al., 1997a, 1997b). The MITgcm has been used in a wide range of applications (http://mitgcm.org/public/r2_manual/latest/online_documents/node312.html), including investigations of large-scale ocean circulation (Stammer et al., 2003), air-sea exchange (McKinley et al., 2003) and estuarine dynamics (Stipa, 2002), to name but a few. In addition to these, MITgcm has become a popular tool for examining ice-ocean interaction in glacial settings, ranging from both large-scale horizontal ice shelves (Dansereau et al., 2013; Goldberg et al., 2019; Heimbach & Losch, 2012; Losch, 2008) to the smaller but highly turbulent environments of vertical glacier calving fronts (Carroll et al., 2017; Cowton et al., 2015, 2016a; Sciascia et al., 2013; Slater et al., 2015, 2018; Xu et al., 2013). In this thesis, MITgcm is used in Chapters 5 and 6 to examine iceberg-ocean interaction in a range of fjord environments relevant to Greenland. In both of those chapters, two key modules in MITgcm are used: the first is 'IcePlume', which simulates the dynamics of plumes generated by subglacial discharge entering the fjord as well as submarine melting of glacier calving fronts (Cowton et al., 2015), and the second is the iceberg module developed as part of this thesis. These modules are now described.

3.2.2 Parameterising subglacial discharge-driven plumes

Fresh, cold subglacial discharge enters the fjord at the grounding line of tidewater glaciers, driving vigorous turbulent plumes that rise up glacier calving fronts, entraining ambient water and increasing glacier submarine melt rates as they do so (Jenkins, 2011). Plumes continue to rise until they reach the fjord surface or until their density is greater

than the overlying water, at which point they flow down-fjord (Carroll et al., 2015; Cowton et al., 2015; Straneo et al., 2010, 2011). Plumes are therefore important drivers of glacier submarine melting (Cenedese & Gatto, 2016a, 2016b; Jenkins, 2011; Kimura et al., 2014; Slater et al., 2015) and of fjord circulation (e.g. Carroll et al., 2017; Cowton et al., 2016), and so it is important to represent them in models used to simulate Greenland's glacial fjords during summer. Numerical ocean models have been used to simulate these plumes to examine their influence on submarine melt rates and fjord circulation (e.g. Salcedo-Castro et al., 2011, 2013; Sciascia et al., 2013, 2014; Xu et al., 2012, 2013). In order to resolve the small-scale non-hydrostatic dynamics of plumes, these studies have had to employ fine grid sizes (< 10 m) and short time steps (< 1 second), which imposes a considerable computational constraint and limited those simulations to the few kilometres of the fjord closest to the glacier and to short (less than a few days) simulation times.

In order to examine the fjord-scale impact of plumes over longer timescales, an alternative approach is therefore necessary. Cowton et al. (2015) developed a module in MITgcm, 'IcePlume', which parameterises the plume rather than simulating it directly. This module captures the key effects of plumes on submarine melting and fjord dynamics, but does not necessitate the high resolution and short time steps as required by traditional approaches, enabling fjord-scale simulations of entire seasons when run in parallel. A brief description of IcePlume is provided here, but for full details the reader is referred to Cowton et al. (2015).

Within IcePlume, the glacier is 'virtual' but is backed by a closed boundary. Freshwater is injected at the base of the virtual ice wall with a constant velocity, V, of 0.1 m s^{-1}. Variations in freshwater discharge are accommodated by varying the radius of the channel through which they are injected. Channel radius, R, is calculated based on the discharge, Q, using: $R = \sqrt{2Q/(\pi V)}$. With IcePlume, the channel is not an open boundary, and so the dimensions of the channel do not directly influence the fjord; however, the channel radius (and therefore the initial plume radius) is important for determining plume dynamics. Changing the subglacial water velocity has negligible impact on plume dynamics (Cowton et al., 2015). The modelled plume itself is half-conical, and entrainment of ambient water into the plume is proportional to the plume vertical velocity (Morton et al., 1956; Straneo & Cenedese, 2015). Melting of the virtual glacier is simulated using the three-equation formulation (see Section 3.2.3.5).

3.2.3 An iceberg package for MITgcm

Our ability to model glacial fjords has improved considerably over the past decade, principally due to the development of tools to model subglacial discharge driven turbulent plumes (Cowton et al., 2015; Xu et al., 2012) and melting of submerged glacier and ice shelf faces (Losch, 2008; Xu et al., 2012), and because of new observations to constrain and force those models (e.g. Straneo et al., 2016). A significant component of fjords that was missing from these models was icebergs, which have been investigated at the ocean-scale for many years (Bigg et al., 1997), but have until recently been largely ignored in fjord-scale studies. Observations of fjord-scale iceberg melting presented in Enderlin et al. (2016) demonstrated that icebergs release huge volumes of freshwater whilst transiting glacial fjords, indicating that icebergs may be an important dynamical component of glacial fjords. Modelling of iceberg melting (Moon et al., 2017) in an iceberg-congested fjord in east Greenland indicated that iceberg freshwater fluxes are an important component of the fjord-wide freshwater budget. However, no tools were available to examine the influence of this freshwater on fjord circulation and on ice sheet-ocean interaction.

3.2.3.1 Existing iceberg models

Models of iceberg dynamics and thermodynamics have been available for decades (e.g. Bigg et al., 1997). These were developed and applied principally to examine iceberg trajectories in the open ocean, to mitigate iceberg shipping hazards. Other applications include (but are not limited to) interactions with wider ocean circulation (e.g. Starr et al., 2020) and icebergs as nutrient sources in nutrient deficient oceans (e.g. Hopwood et al., 2019). Because of the large spatial scales and long time-scales focused on in studies like these, icebergs have typically been treated as particles and were often forced (thermodynamically) with single-value hydrographic properties extracted from the model water surface, rather than at the depth at which melting occurs (Marsh et al., 2015; Martin & Adcroft, 2010; Merino et al., 2016). One major limitation of using surface conditions rather than considering conditions down the entire iceberg draught is that sheared water flow across an iceberg will not be faithfully represented, despite its influence on submarine melt rates (FitzMaurice et al., 2016; Moon et al., 2017). In addition, entire populations of icebergs were not always simulated, instead only a sample from each iceberg size class was included, to reduce computational demand (Bigg et al., 1996). A more recent study by FitzMaurice et al. (2018) used hydrographic properties from the appropriate depth to simulate iceberg melting, but the focus was on basal melting of a

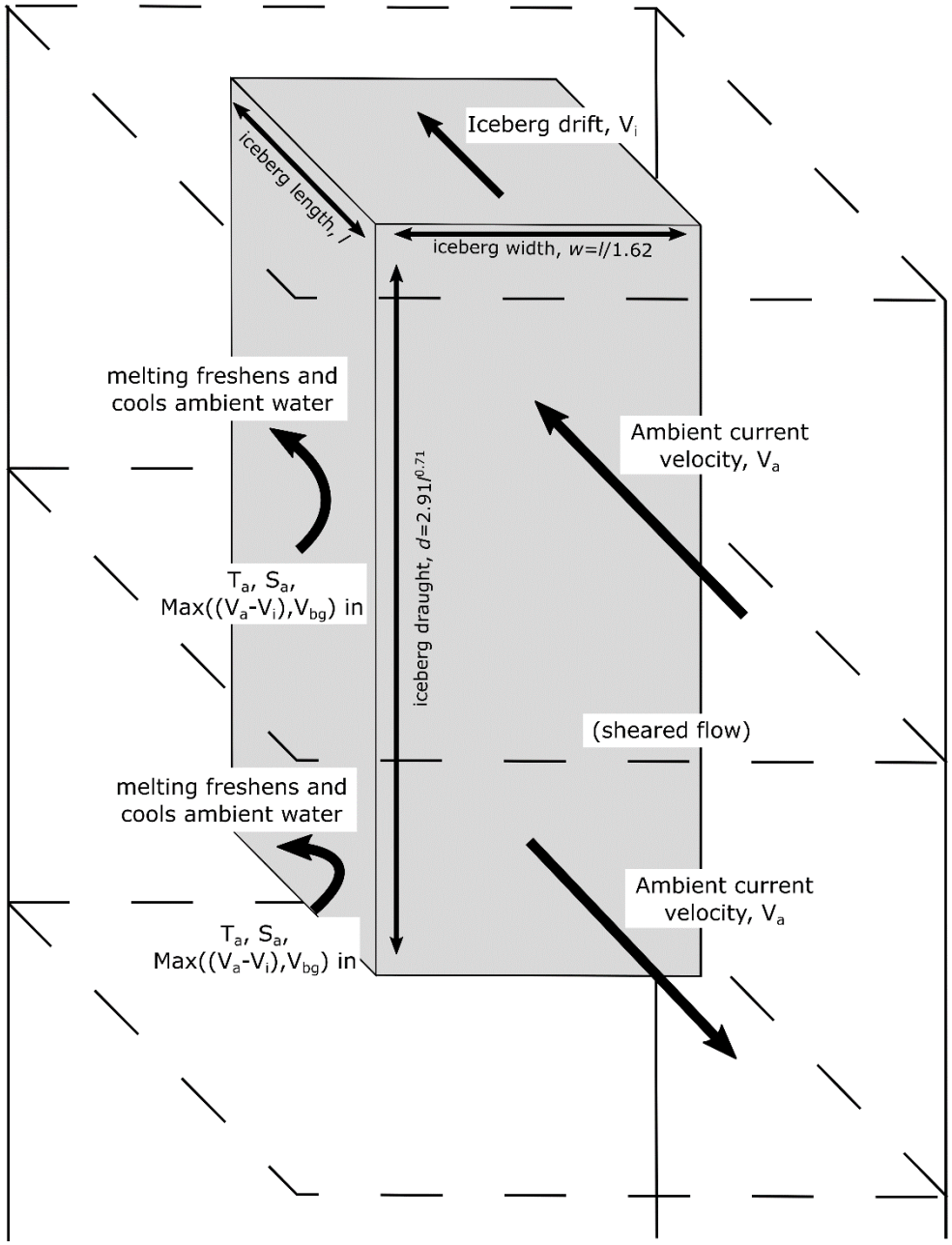

Figure 3.4. Iceberg geometry in MITgcm. T_a, S_a, V_a are the ambient temperature, salinity and velocity respectively. V_i is the iceberg drift velocity and V_{bg} is the 'minimum background velocity', which parameterises the effect of melt-driven convection. Not to scale.

single iceberg, rather like considering a small ice shelf. In this thesis, a tool capable of simulating depth-resolved submarine melting of entire populations of icebergs, with dimensions spanning multiple orders of magnitude, and distributed unevenly throughout glacial fjords, is developed. This tool therefore represents a significant improvement in our ability to model Greenland's glacial fjords.

3.2.3.2 Approach

The iceberg model developed in this thesis functions as a 'package' or 'module' integrated within MITgcm. In this package, each vertical column of cells within MITgcm may contain many icebergs, each of which can extend to any depth between the surface and the base of the water column. The dynamics and thermodynamics of each iceberg is calculated separately, and differences in the orientation of each iceberg face is also accounted for. Throughout a simulation, the icebergs are static – i.e. they do not move or change size over time. Although unrealistic, this is consistent with existing implementations of ice-ocean interaction in MITgcm and does not prevent analysis of fjord-scale response to iceberg melting as long as appropriate populations of iceberg geometry are provided as input (i.e. they should be based on fjord-wide observations and so will implicitly account for iceberg drift and mechanical deterioration).

3.2.3.3 Iceberg geometry

The modelled icebergs are rectangular in plan-view and have smooth, vertical sides and base (Figure 3.4). Iceberg horizontal length, l, is 1.62 times longer than iceberg width, W, based on sparse field observations of fairly large icebergs in Scoresby Sund (Dowdeswell et al., 1992), although very recent observations suggest than iceberg lengths and widths may in fact be similar (Schild et al., 2021). Iceberg length and iceberg keel depth, d, can be linked in several ways. In Chapters 5 and 6, the relation $d = 2.91l^{0.71}$ (Barker et al., 2004) is predominantly used. In some simulations, l and d were linked through an iceberg volume-area relationship (Sulak et al., 2017), whilst in other simulations l is simply set at double d, based on unpublished observations acquired in Sermilik Fjord (Schild et al., 2021). The results were insensitive to this choice of relationship between horizontal length and keel depth.

3.2.3.4 Iceberg size-frequency distribution

Iceberg calving events from a single glacier can vary in size by several orders of magnitude, ranging from small serac failure (with a plan-view surface area of 10s to 100s of square metres), through to full-thickness events (with a plan-view area on the order of a million square metres). Once calved, icebergs deteriorate through mechanical breakup and melting both above and below the surface. A population of icebergs within a fjord therefore spans a range of sizes that reflects (as a first order) the set of processes leading to calving, with those leading to iceberg deterioration superimposed. Since the largest calving events are rarer than small calving events, and because large icebergs tend to break up due to collision with other icebergs, small icebergs tend to greatly outnumber

large icebergs (Dowdeswell et al., 1992; Moyer et al., 2019; Rezvanbehbahani et al., 2020; Sulak et al., 2017). Observations of fjord-wide iceberg size-frequency distributions indicate that power law fits can effectively describe the majority of the iceberg population within fjords (e.g. Sulak et al., 2017). The exponent of this power law is always negative in Greenland's fjords – small icebergs always outnumber large icebergs - and a more negative exponent indicates that iceberg frequency decreases more rapidly for a given increase in iceberg size. Outside of fjords, melting and deterioration has a more dominant influence on the size-frequency distribution than calving, and so a log-normal distribution is usually more appropriate in those locations (Kirkham et al., 2017). Chapters 5 and 6 focus on fjords, and therefore use a power law to approximate the iceberg size-frequency distribution. Recent observations (Rezvanbehbahani et al., 2020) indicate that such power laws tend to underestimate the frequency of very small icebergs (those less than 1000 m^2 in plan-view), and so the number of small icebergs (and therefore the iceberg-ocean contact area in the upper 10 m) in those chapters is likely to be an underestimate.

In chapters 5 and 6, populations of icebergs are generated such that the distribution can be closely described by a power law, where the exponent of the power law varies depending on the particular setup. Whilst it is straightforward to write a power law to describe the relationship between iceberg size and frequency when there is no constraint on the total number of icebergs in the domain, it is slightly more complicated when the concentration of icebergs in the domain is an added constraint (i.e. when we must extract a sample icebergs from a continuous distribution). In other words, it is necessary to take a sample of icebergs from a continuous distribution such that (1) the sample retains the desired distribution and (2) the sampled icebergs occupy a desired fraction of the fjord surface. To achieve these aims, inverse transform sampling was used (Olver & Townsend, 2013). Inverse transform sampling is a classical approach to generating pseudo-random samples from a prescribed probability distribution in a way that preserves the prescribed distribution. In inverse transform sampling, the cumulative distribution function, F_X, of a prescribed probability distribution is inverted, F_X^{-1}. Pseudo-random samples $U_1, \ldots, U_N$ are generated from a uniform distribution U over the range [0 1] and then transformed by $F_X^{-1}(U_1), \ldots, F_X^{-1}(U_N)$. In practice, this is an iterative process, with the number of samples being adjusted on each iteration until an appropriate number of icebergs is obtained (i.e. the amount required to achieve the desired iceberg concentration). An example of the result of this process is shown in Figure 3.5.

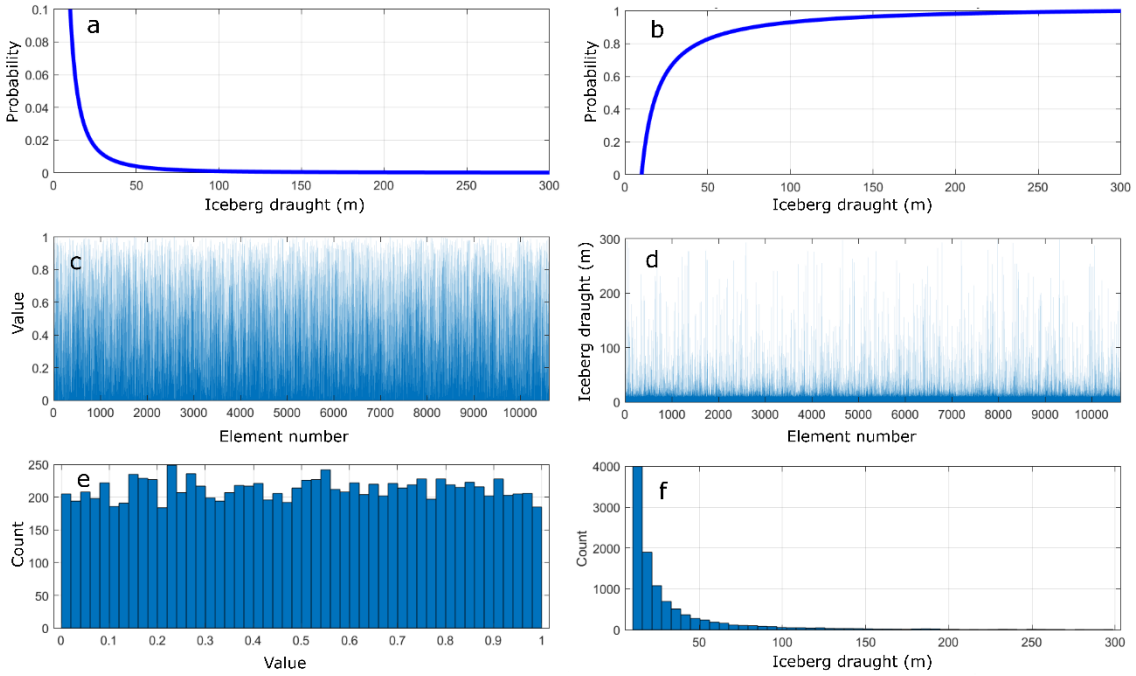

Figure 3.5. Inverse transform sampling output. (a) Inverted probability density function. (b) cumulative density function. (c) Element number of required iceberg samples. (d) Draught of iceberg samples. (e) Histogram of iceberg element numbers. (f) Histogram of iceberg draught. This distribution was generated for the Sermilik Fjord domain in Chapter 5 using a power law exponent of -2 and observed iceberg concentrations.

The resulting array of iceberg geometry provides no information about their location within the domain, and so this must be determined separately and is based on the prescribed concentration of icebergs within the fjord (i.e. the proportion of the fjord in plan-view that is occupied by icebergs). In Chapter 5, this is based on observations (Sulak et al., 2017), whereas in Chapter 6 iceberg concentration is prescribed in an idealised manner. In both chapters, the concentration of icebergs is highest in the inner part of the fjord and decreases to a minimum in the outer part of the fjord. To achieve this 2-D spatial distribution from a 1-D size-frequency distribution (such as that shown in Figure 3.5), the minimum number of icebergs required to achieve the desired iceberg concentration for each surface cell (i.e. water column) are extracted from the 1-D distribution in turn. Since the highest iceberg concentrations are found in the inner fjord, and the largest, deepest icebergs fill these cells with fewer icebergs, these larger icebergs tend to be placed in the inner fjord and the smaller icebergs in the outer part of the fjord – a pattern which is observed in Greenland's fjord (Enderlin et al., 2016) and which is expected based on iceberg production and deterioration mechanisms.

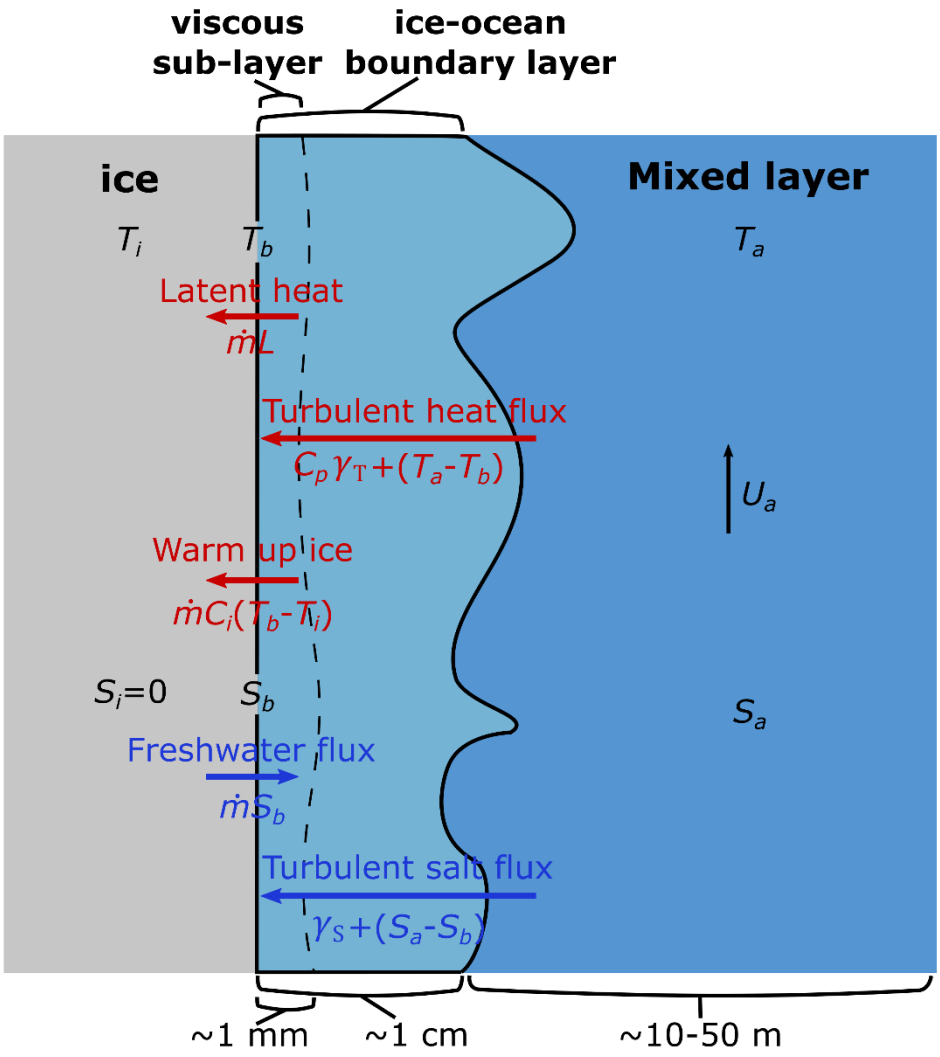

Figure 3.6. Schematic of thermodynamic equilibrium at the ice-ocean boundary. Adapted from Slater (2017).

3.2.3.5 Melt rate parameterisation

The submarine melt rate at the sides and base of each of these icebergs is calculated using the so-called 'three-equation parameterisation', which calculates the balance of heat and salt at the ice-ocean interface. This parameterisation describes an ice-ocean boundary system with three or four distinct layers (Figure 3.6). In this system, the ice and the 'mixed layer', which in this thesis is the water circulating in the model cells adjacent to the ice, are linked by the ice-ocean boundary layer. The ice-ocean boundary layer contains a sub-layer in which water flow is laminar (the possible fourth layer). In the ice-ocean boundary layer, the temperature at the outer edge is inherited from the mixed layer whilst the temperature at the ice-ocean interface is assumed to be at the *in situ* freezing point. The *in situ* freezing point, T_b, is given by

$$T_b = \lambda_1 S_b + \lambda_2 + \lambda_3 z \quad \text{Eq. 1}$$

Where $\lambda_{1\text{-}3}$ are constants, representing the freezing point slope, offset and depth, respectively (see Table 3.1 for parameter values used in this thesis). z is depth and S_b is salinity at the ice-ocean interface. The subscript b indicates that the condition is at the ice-ocean interface (or boundary).

The resulting temperature (and salinity) gradient across the mixed layer drives heat (and salt) transfer from the ocean to the ice. Assuming thermodynamic equilibrium, the turbulent and diffusive heat flux to the ice must be balanced by the heat required to warm the ice to the *in situ* melting point and the latent heat of freezing, L. Similarly, the input of salt across the mixed layer must be balanced by a freshwater flux from the ice, so that the boundary layer salinity is maintained. This balance of heat and salt can be expressed in terms of known mixed layer and ice properties (Holland & Jenkins, 1999).

$$C_w \gamma_T + (T_a - T_b) = \dot{m} C_i (T_b - T_i) + \dot{m} L \quad \text{Eq. 2}$$

$$\gamma_S (S_a - S_b) = \dot{m} (S_b - S_i) \quad \text{Eq. 3}$$

Where $\dot{m}$ is the melt rate per unit surface area, C_w and C_i are the specific heat capacities of seawater and ice, respectively, and γ_T and γ_S represent the turbulent transfer of heat and salt from the mixed layer through the ice-ocean boundary layer. The values for these exchange velocities are given by:

$$\gamma_{T,S} = C_D^{0.5} \Gamma_{T,S} U_a, \quad \text{Eq. 4}$$

where the exchange velocities are the thermal and haline Stanton numbers ($C_D^{0.5} \Gamma_{T,S}$) multiplied by the water velocity, U_a, perpendicular to the ice-ocean interface (and so for icebergs, this is the difference between the icebergs drift velocity and the ambient velocity perpendicular to the ice-ocean interface (Figure 3.6)). The values for the Stanton numbers have been derived from laboratory studies of boundary layers on flat, smooth plates (Kader & Yaglom, 1972). Close to the ice-ocean interface, turbulence is reduced and is replaced by molecular diffusivity (Mellor et al., 1986). Since temperature diffuses more rapidly than salt, and because $\gamma_{T,S}$ must capture all processes within the boundary layer, Γ_S is lower than Γ_T.

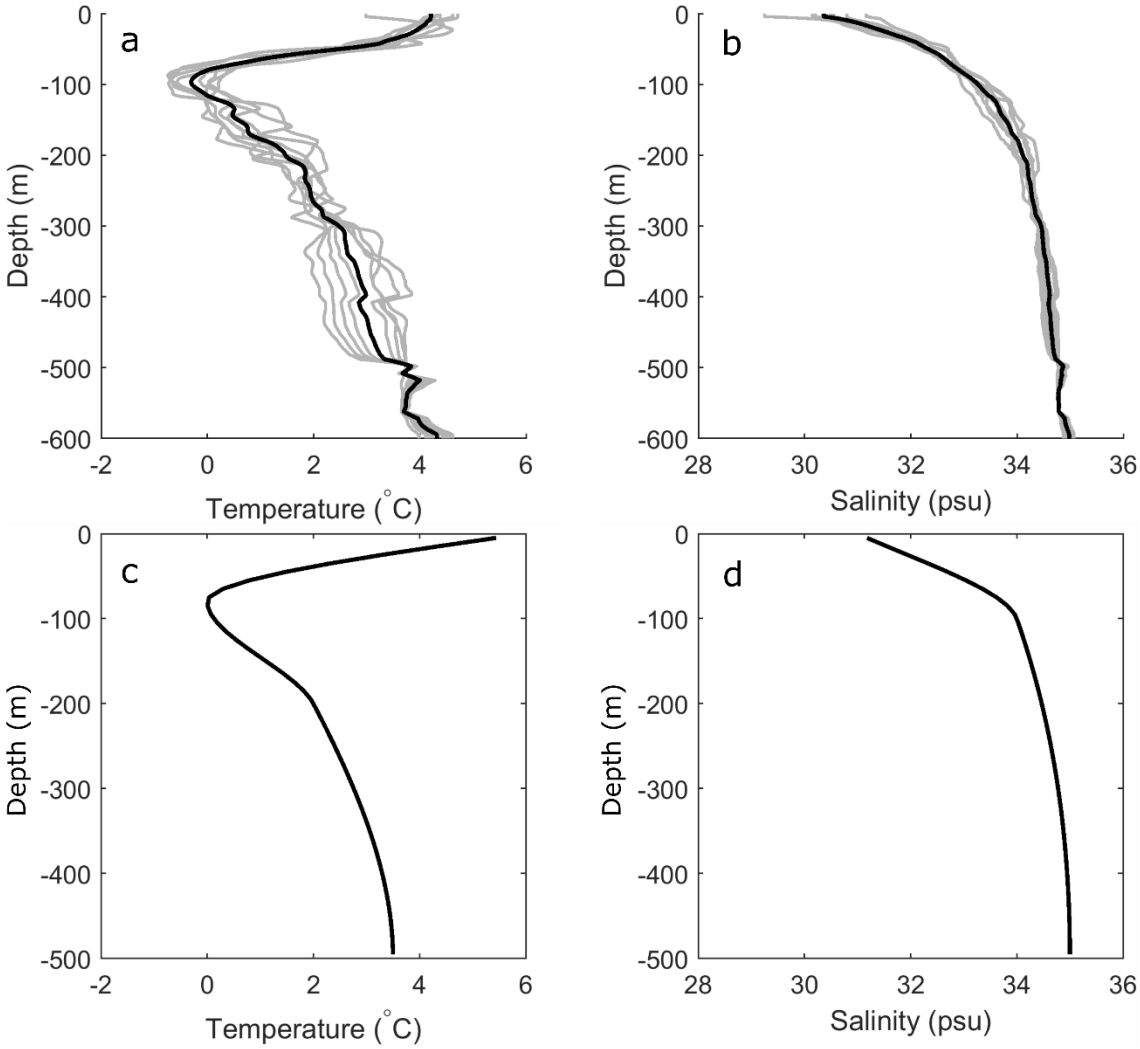

Figure 3.7. MITgcm initial conditions as used in (a) & (b) Chapter 5 and (c) & (d) Chapter 6. In (a) and (b) the thin grey lines are the profiles for the individual casts, and the thicker black line is the average of those casts.

Melt rates are extremely sensitive to the values of $\gamma_{T,S}$, and so appropriate parameter values for both C_D and $\Gamma_{T,S}$ are essential for accurate melt rate calculations. The standard values for these parameters are based on observations of submarine melting of horizontal sea ice and ice shelves (Holland & Jenkins, 1999; McPhee, 1992; McPhee et al., 1999), but comparable observations are not available for Greenlandic glaciers or icebergs, where the turbulent environment is likely to be very different. Recent hydrographic observations (Jackson et al., 2020) close to a large tidewater glacier in Alaska indicate that the standard values of these parameters greatly underestimate melting of quasi-vertical glacier ice faces. In Chapter 5, both the standard values and those based on these more recent observations are used, resulting in a very large spread of submarine iceberg melt rates.

Table 3.1. Parameter values for three-equation melt rate parameterisation.

Symbol	Description	Value *(adjusted)*	Units
C_i	Heat capacity of ice	2000	$J\,kg^{-1}\,°C^{-1}$
C_w	Heat capacity of water	3974	$J\,kg^{-1}\,°C^{-1}$
L	Latent heat of melting	3.34×10^{5}	$J\,kg^{-1}$
Γ_T	Thermal turbulent transfer coefficient	2.20×10^{-2} *(4.40×10^{-2})*	
Γ_S	Salt turbulent transfer coefficient	6.20×10^{-4} *(1.24×10^{-3})*	
C_d	Drag coefficient	0.0025 *(0.01)*	
λ_1	Freezing point slope	-5.73×10^{-2}	$°C\,psu^{-1}$
λ_2	Freezing point offset	8.32×10^{-2}	°C
λ_3	Freezing point depth	-7.61×10^{-4}	$°C\,m^{-1}$

3.2.4 Initial and open boundary conditions

Two sets of initial conditions are used in this thesis (Figure 3.7). In Chapter 5, the initial conditions are the average of several casts acquired in a single survey at the mouth of Sermilik Fjord. In Chapter 6, the initial conditions are an idealised approximation of the profiles acquired outside Sermilik Fjord, and were varied systematically between simulations. In all simulations, these initial conditions are maintained at the open boundary of the model domain, such that the fjord is initially at rest and the only forcing is generated within the fjord (from glacial runoff and/or ice melt).

In all simulations, the fjord sides are closed boundaries with a free slip condition, meaning that water cannot flow through them, but can flow alongside them with no resistance. At the open boundary, a 5 km 'sponge layer' is placed, in which temperature, salinity and velocity in the fjord are relaxed towards those at the boundary. The purpose of this sponge layer is to minimise internal reflections (Sciascia et al., 2013). In simulations in which mass is added to the fjord in the form of glacial runoff, a small outward velocity is imposed uniformly across the boundary to conserve mass.

Chapter 4 - Subglacial drainage evolution modulates seasonal ice flow variability of three tidewater glaciers in southwest Greenland

Meltwater generated at the surface of the Greenland Ice Sheet drains to the bed of tidewater glaciers and can cause seasonal changes in ice velocity (Moon et al., 2014). The magnitude, timing, and net impact on annual average ice flow of these seasonal perturbations depend on the hydraulic efficiency of the near-terminus subglacial drainage system. However, the near-terminus subglacial hydrology of tidewater glaciers and its relationship to ice velocity is poorly understood. In this first results chapter, detailed near-terminus ice velocity measurements are compared to inferred subglacial hydrology to elucidate their interactions at three contrasting tidewater glaciers. The results demonstrate that efficient subglacial channels develop and dampen the seasonal meltwater-induced speed-up at each study glacier. This suggests that increases in meltwater supply will not correspond to increased annual ice velocity via changes in basal water pressure.

Chapter 4: Tidewater glacier hydrology and dynamics

Published in **Journal of Geophysical Research: Earth Surface**, August 2020

Authors: B. J. Davison[1], A. J. Sole[2], T. R. Cowton[1], J. M. Lea[3], D. A. Slater[4], D. Fahrner[3,5], and P. W. Nienow[6].

1. Department of Geography and Sustainable Development, University of St Andrews, St Andrews, UK
2. Department of Geography, University of Sheffield, Sheffield, UK
3. Department of Geography and Planning, University of Liverpool, Liverpool, UK
4. Scripps Institution of Oceanography, San Diego, CA, USA
5. Institute for Risk and Uncertainty, University of Liverpool, Liverpool, UK
6. School of Geosciences, University of Edinburgh, Edinburgh, UK

Citation: Davison, B. J., A. J. Sole, T. R. Cowton, J. M. Lea, D. A. Slater, D. Fahrner, and P. W. Nienow. (2020). Subglacial drainage evolution modulates seasonal ice flow variability of three tidewater glaciers in southwest Greenland. *Journal of Geophysical Research: Earth Surface*, 125, e2019JF005492. doi: 10.1029/2019JF005492.

Author contributions: B.J.D. and A. J. S. designed the research. A.J.S. wrote the feature tracking code, which B.J.D. used to derive the velocity estimates. J.M.L. and D.F. provided terminus position data and D.A.S. provided the plume model. B.J.D. derived or obtained all other data and analysed the results. B.J.D. wrote the paper, with input from all other authors.

Abstract

Surface-derived meltwater can access the bed of the Greenland ice sheet, causing seasonal velocity variations. The magnitude, timing, and net impact on annual average ice flow of these seasonal perturbations depend on the hydraulic efficiency of the subglacial drainage system. We examine the relationships between drainage system efficiency and ice velocity, at three contrasting tidewater glaciers in southwest Greenland during 2014–2019, using high-resolution remotely sensed ice velocities, modelled surface melting, subglacial discharge at the terminus, and results from buoyant plume modeling. All glaciers underwent a seasonal speed-up, which usually coincided with surface melt onset, and subsequent slow-down, which usually followed inferred subglacial channelization. The amplitude and timing of these speed variations differed between glaciers, with the speed-up being larger and more prolonged at our fastest study glacier. At all glaciers, however, the seasonal variations in ice flow are consistent with inferred changes in hydraulic efficiency of the subglacial drainage system and qualitatively indicative of a flow regime in which annually averaged ice velocity is relatively insensitive to interannual variations in meltwater supply—so-called "ice flow self-regulation." These findings suggest that subglacial channel formation may exert a strong control on seasonal ice flow variations, even at fast-flowing tidewater glaciers.

4.1 Introduction

The dynamic response of Greenland's tidewater glaciers to changes in environmental conditions remains a key uncertainty in predictions of future sea level rise (Nick et al., 2013). Each summer, meltwater produced at the ice sheet surface reaches the ice sheet base, increasing basal water pressure and causing seasonal speed-ups of both land-terminating glacier margins (Davison et al., 2019) and tidewater glaciers (Moon et al., 2014; Vijay et al., 2019). At land-terminating glacier margins, continual subglacial water flow during the summer months causes the formation of hydraulically efficient subglacial channels. These enable the rapid evacuation of meltwater, decreasing basal water pressure, and ultimately cause the overlying ice to decelerate in late-summer to speeds slower than those prior to the melt season (an "extra slow-down") (e.g. Sole et al., 2013). In addition, this late-summer extra slow-down scales with meltwater supply such that annually averaged ice velocity is insensitive to interannual variations in meltwater supply—so-called "ice flow self-regulation" (Sole et al., 2013; Wal et al., 2015).

At tidewater glaciers, however, the relationship between meltwater supply and ice velocity appears to be more complicated. While the majority of tidewater glaciers undergo a seasonal meltwater-induced speed-up (an "early-summer speed-up"), only ~40% of them (Vijay et al., 2019) experience a seasonal extra slowdown, similar to that of land-terminating margins (so-called "type 3" glaciers; Moon et al. (2014)). In contrast, other tidewater glaciers do not undergo an extra slow-down and instead decelerate back to (but not below) pre-melt season speeds ("type 2"; Moon et al. (2014)). It has been widely hypothesized (e.g. Bevan et al., 2015; Kehrl et al., 2017; Moon et al., 2014; Sundal et al., 2011; Vijay et al., 2019) that the extra slow-down occurs at type 3 glaciers because they develop efficient subglacial channels during summer (as has been inferred at land-terminating margins). Due to the absence of this compensatory extra slow-down, it has been suggested that type 2 glaciers may accelerate on annual timescales as meltwater supply and the early-summer speed-up increase in a warming climate. However, the difficulty in measuring ice velocity close to tidewater glacier termini at sufficiently high temporal and spatial resolution, and in observing tidewater glacier subglacial drainage systems, has meant that these hypotheses have not been thoroughly tested, leaving a gap in our understanding of how tidewater glaciers may respond to seasonal and longer-term variations in meltwater supply.

Given the difficulty of observing the necessary components of tidewater glacier systems, much has been inferred through comparison with land-terminating sectors of the Greenland Ice Sheet (GrIS), which are more accessible. The similarity in seasonal dynamic behavior of type 3 glaciers to that of land-terminating glaciers (e.g. Bartholomew et al., 2010, 2011; Sundal et al., 2011) led Vijay et al. (2019) to suggest that the underlying processes controlling dynamics may be the same. Specifically, the development of hydraulically efficient channels during the melt season is thought to reduce water pressure across large areas of the bed (Hoffman et al., 2016; Sole et al., 2013), leading to the extra slow-down. It is not clear, however, to what extent subglacial channels can form beneath tidewater glaciers. Theoretically, fast-flowing ice and small hydraulic potential gradients expedite subglacial channel closure and promote only slow subglacial channel growth (Röthlisberger, 1972). Therefore, channel formation may be subdued at fast-flowing tidewater glaciers (Doyle et al., 2018; Kamb, 1987) especially where the bed deepens inland. Indeed, distributed near-terminus subglacial drainage systems have been inferred at fast-flowing tidewater glaciers (Bartholomaus et al., 2016; Chauché et al., 2014; Fried et al., 2015; Jackson et al., 2017; Rignot et al., 2015; Slater et

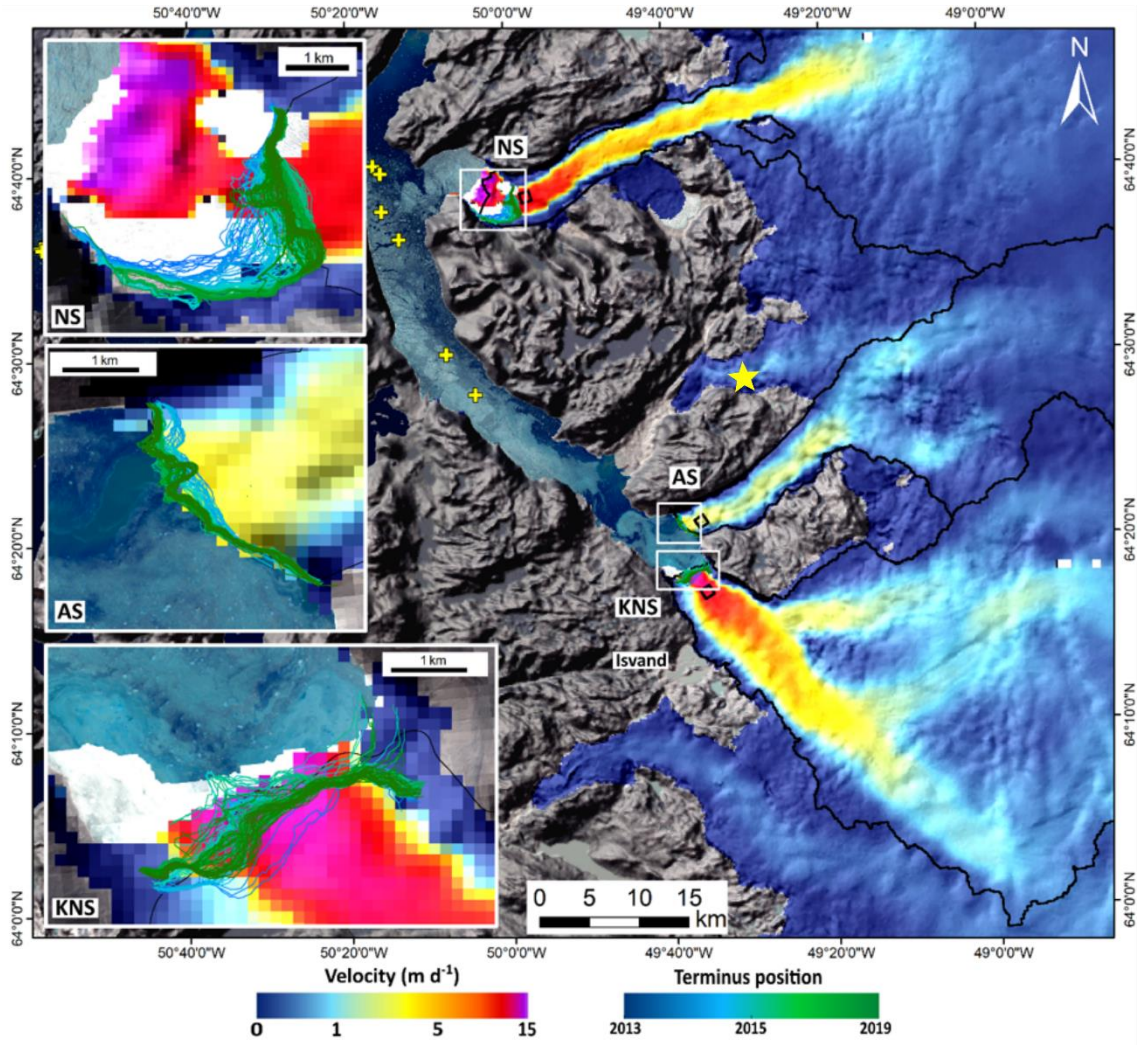

Figure 4.1. Southwest Greenland study area. Background image is a Sentinel-2 false color image (acquired on 1 August 2018) and a hillshade generated from the Greenland Ice Mapping Project (GIMP) Digital Elevation Model (Howat et al., 2014). The median ice velocity during 1 April 2016 to 31 March 2018, based on our Sentinel-1 dataset, is overlaid. The black squares indicate the regions of interest from which the median ice velocity time-series in Figures 4.2, 4.5 and 4.7 are generated. Terminus positions during 2013-2019 are shown as colored lines. The yellow crosses indicate the location of the CTD casts used in the plume modelling, and the yellow star is the location of PROMICE weather station NUK_L. The black lines indicate the derived subglacial drainage catchments of each glacier.

al., 2017). On the other hand, runoff-driven buoyant plumes are often visible adjacent to tidewater glacier termini (e.g. Bartholomaus et al., 2016; Jackson et al., 2017; Schild et al., 2016; Slater et al., 2017), indicating the efflux of large volumes of meltwater from one or more discrete sources, indicative of efficient subglacial channels. Therefore, it seems that large, efficient channels can form at times beneath some tidewater glacier

margins. However, no studies have yet linked the occurrence (or not) of these channels to seasonal changes in ice velocity, which would provide valuable insight into interactions between hydrology and ice dynamics at tidewater glaciers.

Here, we investigate the extent to which seasonal changes in ice velocity are controlled by evolution in the hydraulic efficiency of subglacial drainage at three tidewater glaciers in southwest Greenland (Figure 4.1), Kangiata Nunaata Sermia (KNS), Narsap Sermia (NS), and Akullersuup Sermia (AS), during 2014–2019. To do this, we derive high-resolution velocity estimates close to the termini of these tidewater glaciers by feature tracking of optical and radar satellite imagery. We compare these time series to observations and modelling of environmental forcings and simple inference of subglacial hydraulic efficiency. The three study glaciers, which are exposed to similar climatic variability, are representative of a spectrum of medium-sized outlet glaciers, with grounding line depths ranging from 60 m at AS to 250 m at KNS and speeds from ~2 m d^{-1} at AS to over 15 m d^{-1} at KNS. We might therefore expect a range of hydrology-dynamic responses to similar meltwater supply variability, which should be applicable to many other Greenlandic tidewater glaciers.

4.2 Methods

4.2.1 Ice velocity

4.2.1.1 Offset tracking procedure

We estimated ice velocity primarily from feature and speckle tracking of Sentinel-1a and Sentinel-1b Interferometric Wide swath mode Single-Look Complex Synthetic Aperture Radar (SAR) amplitude images, acquired using Terrain Observation with Progressive Scans (TOPS). We utilized over 350 Sentinel-1a/b repeat-pass image pairs between January 2015 and June 2019. The majority of pairs acquired since the launch of Sentinel-1b in April 2016 had a 6-day separation period (baseline), while older pairs had a 12-day baseline. In the following, the first and second images acquired in a given pair are referred to as the "master" and "slave" images, respectively. These data were supplemented, and the time series extended back to January 2014 by our own feature tracking of Landsat-8 imagery and the GoLive data set (Fahnestock et al., 2015). Below, we describe the Sentinel-1 and Landsat-8 processing chains.

Prior to tracking, Sentinel image pairs were focused and co-located to within 0.1 pixels in the Generic Mapping Toolbox for SAR imagery (GMTSAR; Sandwell et al. (2011)).

Traditional SAR image alignment using image cross-correlation or enhanced spectral diversity fails with TOPS-mode data and is not appropriate over fast-flowing ice, due to coherence loss between images (Nagler et al., 2015; Xu et al., 2017). Image co-location instead utilized precise orbit ephemerides (3–5 cm accuracy) prior to August 2018 and restituted orbit data (10 cm accuracy) afterwards (Fernández et al., 2015) (https://qc.sentinel1. eo.esa.int/) and the Greenland Ice Mapping Project (GIMP) Digital Elevation Model (DEM) (Howat et al., 2014), to interpolate the slave image to the grid of the master image.

For both Landsat and Sentinel image pairs, each image was split into overlapping image patches. Cross-correlation of corresponding image patches in co-located master and slave images was used to determine ice displacement during the baseline. Due to the different nominal range and azimuth resolution of the Sentinel imagery (~2.3 and ~14.1 m, respectively), the Sentinel images were oversampled in the azimuth direction by a factor of two prior to cross-correlation (Khvorostovsky et al., 2018). To minimize information loss over image patch edges, image patches should be approximately four times larger than the maximum expected displacement (Thielicke & Stamhuis, 2014). Therefore, Sentinel-1 image patches were approximately 1x1 km (400x180 Single-Look oversampled range and azimuth pixels), with approximately 800-m overlap in both directions (300x126 pixels). The smaller computational demands imposed by the 15-m Landsat imagery allowed us to perform multiple cross-correlation passes on each image pair, resizing and deforming image patches according the previous pass (Adrian & Westerweel, 2011; Thielicke & Stamhuis, 2014). Image patch size and spacing therefore varied from 480–1,920 and 180–960 m, respectively, equal in both directions. This enabled us to track features close to the terminus without sacrificing either resolution or accuracy further up-glacier, where flow speeds are lower. To improve feature identification, we pre-processed images using contrast-limited adaptive histogram equalization and a Butterworth high-pass spatial frequency filter. The latter removed image brightness variations with a wavelength greater than approximately 1 km (De Lange et al., 2007), ensuring that only smaller, moveable surface features were tracked.

Tracking of the co-located and filtered images was undertaken in MATLAB, within a version of PIVsuite (Thielicke & Stamhuis, 2014) (https://uk.mathworks.com/matlabcentral/fileexchange/45028-pivsuite) adapted for ice flow. Computationally efficient subpixel displacement estimates for each image patch

were made by obtaining an initial estimate of the cross-correlation peak using a fast Fourier transform and then upsampling by a factor of 100 the discrete Fourier transform using matrix multiplication of a small neighborhood (1.5x1.5 pixels) around the original peak location (Guizar-Sicairos et al., 2008). The resulting velocity estimates were filtered in several stages (Figure S1.1). Correlations with a signal-to-noise ratio (defined as the ratio of the primary cross-correlation peak to the average of the remaining cross-correlation field) less than 5.8 were removed (De Lange et al., 2007). Remaining spurious estimates were removed primarily using an image segmentation filter (Lüttig et al., 2017), a threshold strain filter (Rosenau et al., 2015), and a kernel density filter based on the paired displacements in the range and azimuth directions for each image patch (Adrian & Westerweel, 2011). Additional filtering based on velocity magnitude and flow direction removed remaining spurious estimates. The filtered velocity fields derived from Sentinel-1 imagery were transformed from radar to map coordinates using the Greenland Ice Mapping Project DEM (Howat et al., 2014) and were posted on a 150x150 m grid.

For the analysis presented here, we averaged ice velocity within 1x1 km fixed-position regions of interest, located close to the calving front of each glacier (locations in Figure 4.1). Only dates on which more than 50% of the region of interest contained data were sampled. A median velocity error of 0.06 m d^{-1} was estimated by sampling velocity over bedrock areas.

4.2.1.2 Validation of velocity estimates

To validate our method of velocity estimation, we compared our ice velocity estimates derived from Sentinel-1 imagery to those from the Programme for Monitoring of the Greenland Ice Sheet (PROMICE) Sentinel-1 dataset (https://www.promice.dk/) over identical time periods (Figure S1.2). We find that our estimates differed from those of PROMICE by 0.25% on average, with a standard deviation of 4.4% and that this difference was independent of ice velocity. The small, non-systematic difference between our estimates and those of PROMICE arise due to (i) the different spacing at which the data are binned (150 m for our data and 500 m for PROMICE); (ii) differences in the size and spacing of image patches used to estimate ice velocity, which will affect the locations over which velocity is estimated; and (iii) differences in the degree of post-processing (Boncori et al., 2018).

4.2.2 Terminus position and ice mélange

For each glacier, we digitized terminus positions from Landsat-8 and Sentinel-2 imagery during 2014–2019 using the Google Earth Engine Digitisation Tool (Lea, 2018). Terminus position change was calculated using the multi-centerline method in the Margin change Quantification Tool (Lea, 2018). Ice mélange, and (at KNS) a seasonal ice tongue (Motyka et al., 2017; Moyer et al., 2017), hindered accurate terminus identification typically during November–May each year.

The timings of ice mélange (and, at KNS, ice tongue) weakening, disintegration, and reformation were identified based on our ice velocity estimates over the mélange and using visual assessment of satellite imagery. We identified mélange weakening from crack formation, changes in color of the mélange (which we interpreted as thinning), and mobility (based on velocity estimates or loss of coherence). Mélange disintegration was defined as complete clearing of the mélange from the fjord adjacent to the calving front. These events likely bracket the period during which buttressing forces provided by ice mélange decreased each year. During times of cloud cover (when Sentinel-1 images were not available) or image sparsity, we recorded the date of the first clear image.

4.2.3 Surface melt and subglacial discharge

We extracted the time series of average RACMO2.3p2 modeled surface runoff rates (Noël et al., 2016, 2018) within the regions of interest on each of our study glaciers (black boxes in Figure 4.1). Using these, we defined the start of the melt season for each glacier as the first day of a period of at least three consecutive days when the runoff rate was greater than 1-mm water equivalent per day (i.e., following the Danish Meteorological Institute definition). To gain further insight into surface meltwater generation, we also analyzed air temperature data acquired at PROMICE weather station NUK_L (https://www.promice.dk/WeatherStations. html) and defined the onset of positive temperatures as the first day of a period of at least three consecutive days when temperatures exceeded 0°C.

We also estimated subglacial discharge at the terminus of each glacier using RACMO2.3p2 modeled surface runoff, which was spatially and temporally integrated over each glacier's subglacial catchment, delineated using hydropotential analyses (Shreve, 1972) bounded by BedMachine v3 topographic data (Morlighem et al., 2017). For simplicity, surface runoff was assumed to access the bed immediately, was routed to

the terminus at 1 m s^{-1} (Chandler et al., 2013; Cowton et al., 2013), and used to estimate mean daily subglacial discharge rates.

Our time series of subglacial discharge at the glacier terminus was derived by making several simplifying assumptions. To summarize, we assume (i) that meltwater accesses the bed immediately (no supraglacial or englacial storage), (ii) that meltwater accesses the bed where it is generated (no supraglacial routing), and (iii) a subglacial transit velocity of 1 m s^{-1}. We quantify and discuss the impact of these assumptions on our conclusions in Section S1.1.

4.2.4 Subglacial hydraulic efficiency

We used the visible presence or absence of plumes at the fjord surface adjacent to each glacier, combined with simple plume modeling, as an indicator of near-terminus subglacial hydraulic efficiency. Plumes are often, but not always, visible at the fjord surface during summer. Previous modeling work (Slater et al., 2017) demonstrates that typically, relatively little subglacial discharge (<50 m^3 s^{-1}) from a single channel is required to cause plume surfacing at these glaciers. Therefore, when modeled subglacial discharge is high, yet no plume is observed, one possible explanation is that subglacial discharge emerged from multiple points along the terminus, such that the discharge at each outlet was less than ~50 m^3 s^{-1} (Slater et al., 2017). Although this does not provide direct information about the efficiency of the near-terminus subglacial drainage system, the spatial distribution of water efflux across the grounding line is suggestive of an "inefficient" near-terminus subglacial drainage system (e.g. Slater et al., 2017).

We recorded the presence of subglacial discharge plumes at the fjord surface using all available Landsat-8, Sentinel-2, and Sentinel-1 satellite imagery during 2014–2019 (Figure S1.3). For simplicity, we adopted a binary system to classify near-terminus subglacial hydraulic efficiency. When plumes were visible at the fjord surface, we assumed that the subglacial drainage system was efficient. When plumes were not visible, we used buoyant plume theory (Jenkins, 2011; Morton et al., 1956; Slater et al., 2016) to estimate the minimum number of outlets required to prevent plume surfacing (assuming discharge was split evenly between outlets as in Slater et al. (2017)). If two or more outlets were required to prevent plume surfacing, we assumed an "inefficient" drainage system. We emphasize that we cannot provide more specific information on the likely morphology of these "inefficient" systems and that, under the terms of our classification, "inefficient" does not preclude the existence of subglacial drainage channels, so long as

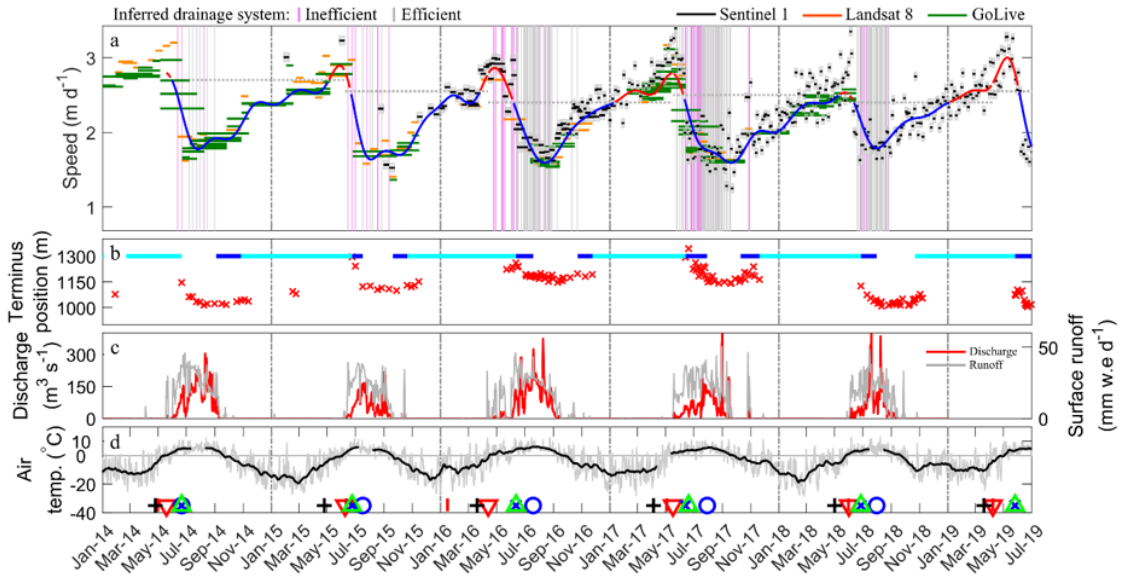

Figure 4.2. Akullersuup Sermia velocity and forcings. (a) Ice velocity estimates from Sentinel-1 (black), GoLive (green) and Landsat-8 (orange). The horizontal extent of each line indicates the image pair baseline. The dotted horizontal gray lines indicate the mean velocity during the month prior to melt onset in each year. Overlaid is a 24-day Butterworth low-pass filtered velocity timeseries, colored red (blue) when it is higher (lower) than the pre-melt season speed. The vertical violet (gray) lines indicate times of inferred inefficient (efficient) subglacial drainage. Areas with no vertical lines indicate that either no images were available or that modelled subglacial discharge was zero. The vertical dash-dot grey lines in delimit each calendar year and are for visual guidance only. (b) Width-averaged terminus position in red crosses (lower values indicate a more retreated position). The horizontal bars indicate mélange presence: cyan sections indicate a 'strong' mélange whilst blue sections indicate transition periods, when the mélange was present but appeared to be weakening or reforming. (c) Modeled subglacial discharge at the terminus (red) and modeled surface runoff (grey). (d) Air temperature from PROMICE station NUK_L and the timing of key events (black cross = acceleration; red bar = positive temperature onset; red downward pointing triangle = melt onset; green triangle = terminus retreat onset; blue cross = mélange weakening; blue circle = mélange breakup).

not more than 50% of the total discharge (and normally much less) is carried by a single channel. Very little is known about drainage system morphology near the termini of tidewater glaciers, but we speculate that this definition of inefficient could include anything from a linked cavity network or porous till through to a network of multiple transient channels.

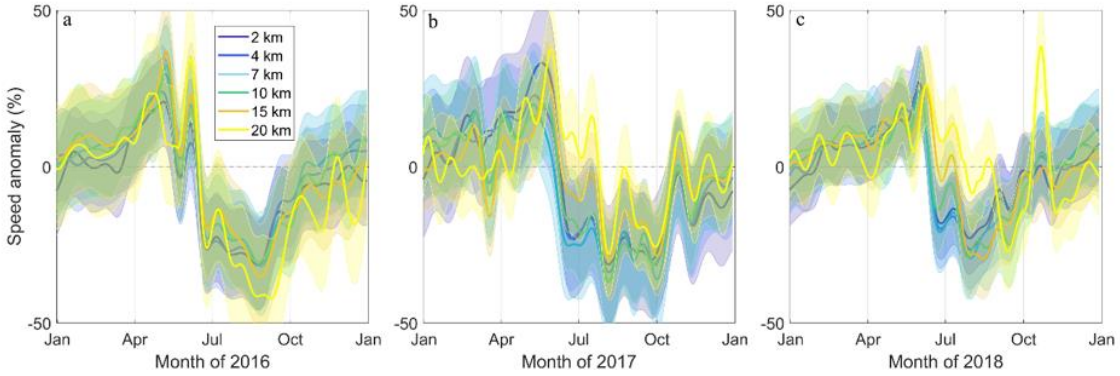

Figure 4.3. Seasonal velocity anomalies at Akullersuup Sermia during (a) 2016, (b) 2017 and (c) 2018. Anomalies were calculated relative to the average ice velocity between January 2015 and June 2019 in each region of interest. Shaded envelopes indicate the seasonal standard deviation in each year and at each region of interest.

We forced the plume model (Slater et al., 2016) with our time series of grounding line subglacial discharge, while 28 conductivity, temperature, and depth (CTD) casts, acquired 32–90 km from the KNS terminus during 2014–2016 (http://ocean.ices.dk), were used as ocean boundary conditions (Figure 4.1) (Mortensen et al., 2013, 2014, 2018). The results presented below assume a half-conical plume geometry (consistent with the geometry of plume surface expression). Changes to model boundary conditions (including subglacial discharge) and parameters, within parameter uncertainty, resulted in only minor changes to the timing of periods of inferred efficient and inefficient subglacial drainage (Section S1.1; Figures S1.4 and S1.5). On days when it was not possible to make an inference about the efficiency of the subglacial drainage system, we recorded data gaps. These gaps are due to (i) an absence of satellite images, (ii) mélange or cloud cover, or (iii) insufficient subglacial discharge for a single modeled plume to reach the fjord surface. In addition, there may be periods erroneously classified as "inefficient" during times when (i) plumes did reach the fjord surface, but were not visible in satellite imagery (e.g. due to the plumes being below the resolution of the satellite image), or (ii) there was some other reason for lack of plume surfacing, such as freshening of the fjord surface due to iceberg melt and surface runoff (De Andrés et al., 2020). We further discuss the assumptions and sensitivities of this method in Section S1.1.

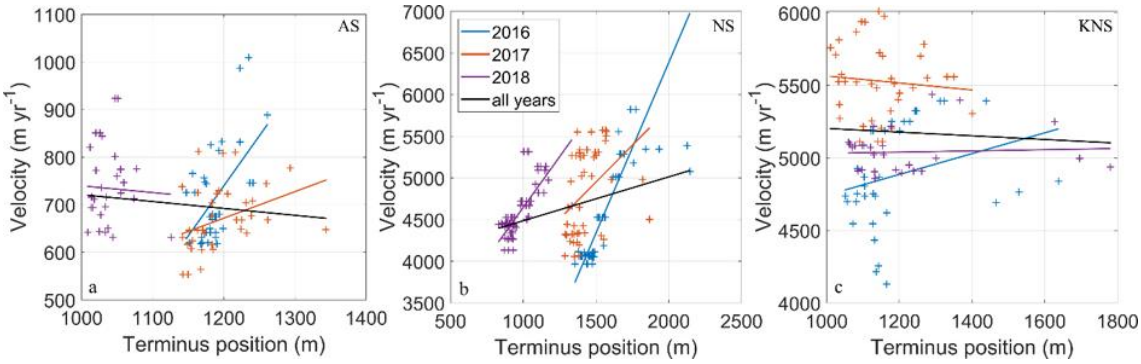

Figure 4.4. Relationship between ice velocity and terminus position at (a) Akullersuup Sermia, (b) Narsap Sermia and (c) Kangiata Nunaata Sermia. More positive x-axis values indicate a more advanced terminus. Note the different scales in each plot.

4.3 Results

We observed seasonal ice velocity variations at each glacier that were qualitatively similar to the type 2 and type 3 patterns identified by Moon et al. (2014) and Vijay et al. (2019). We compared these ice flow variations to changes in terminus position, ice mélange characteristics, runoff, and inferred subglacial hydraulic efficiency.

4.3.1 Akullersuup Sermia

AS began to accelerate between mid-March and early May each year (henceforth the "early-summer acceleration"), reaching peak speeds within about a month (Figure 4.2a). Peak speeds were on average 18% greater than those prior to the early-summer acceleration (henceforth "pre-acceleration" speeds). Ice flow then typically decelerated rapidly, falling to approximately 40% below pre-acceleration speeds by mid-summer and then remained low until early-September each year, before gradually accelerating over winter (henceforth "recovery"). This seasonal pattern was observed throughout the topographically constrained (outlet) part of the glacier (Figures 4.3 and S1.6–S1.8). Short-lived speed-ups, coincident with spikes in modeled surface melt, were superimposed on this seasonal pattern (e.g., November 2017). Average ice velocity between April and March 2016–2017 was 4.7% greater than during 2017–2018 and 0.2% lower than during 2018–2019 (Table S1.1).

The early-summer acceleration was usually difficult to distinguish from the gradual acceleration over the preceding winter, and so it was difficult to associate the onset of acceleration with a particular forcing (Figure 4.2). In most years, the early-summer

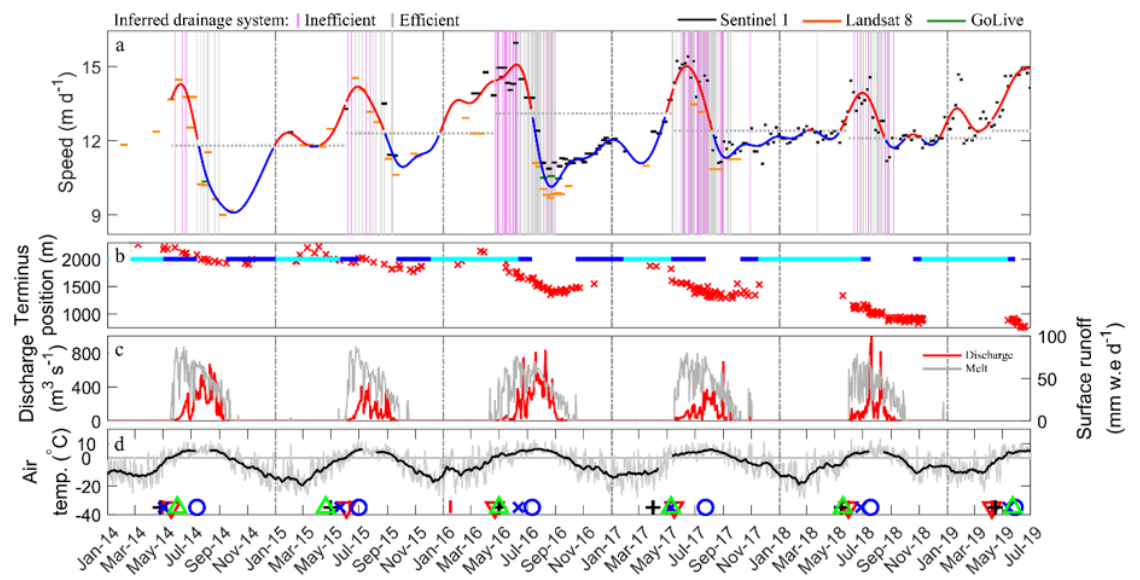

Figure 4.5. Narsap Sermia velocity and forcings timeseries. Colours are the same as for Figure 4.2. Note the different Y-axis scales in compared to Figure 4.2.

acceleration seemed to begin before any of our defined forcings; however, there were short-lived periods of above-zero air temperatures during or just prior to the onset of acceleration in every year (Figure 4.2). Peak speeds occurred within 1–2 weeks of the first observation of plume surfacing during every year except 2015, when plume surfacing occurred ~1 month later. Ice velocity subsequently decreased and usually remained low until plume surfacing ceased around September each year. The uniformity of the seasonal velocity variations across the outlet part of the glacier (Figures 4.3 and S1.6–S1.8) suggests a spatially consistent control that was not affected by proximity to the glacier terminus. We found no correlation (R^2 = 0.006, p = 0.19) between ice velocity and terminus position during our study period (Figure 4.4a).

4.3.2 Narsap Sermia

NS displayed qualitatively similar behavior to AS, but the relative magnitude and duration of the early-summer acceleration and the late-summer slow-down differed markedly (Figure 4.5a). In every year except 2017, the early-summer acceleration began around the time of both runoff onset and terminus retreat, but before visible ice mélange weakening. In 2017, the early-summer acceleration is indistinguishable from the 2016/2017 winter recovery, with ice velocity steadily increasing from around early March 2017, a time with frequent excursions to positive temperatures (Figure 4.5d). Peak speeds were up to 25% greater than pre-acceleration values, and velocity remained elevated

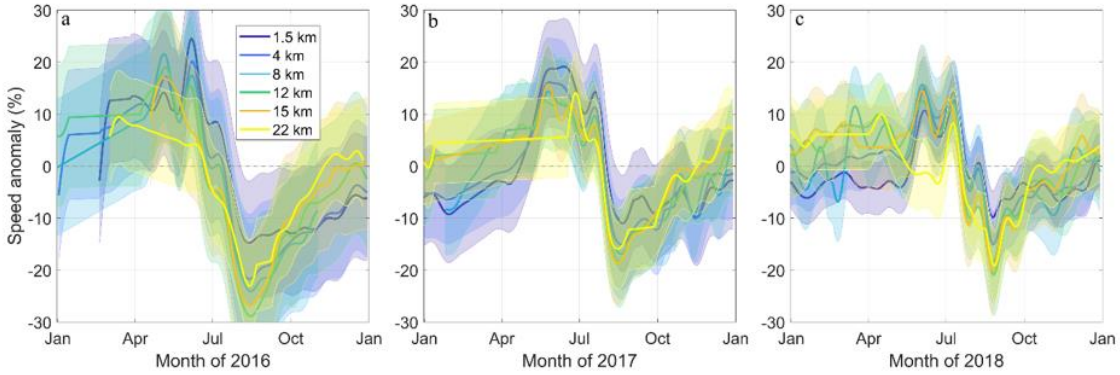

Figure 4.6. Seasonal velocity anomalies at Narsap Sermia during (a) 2016, (b) 2017 and (c) 2018. Anomalies were calculated relative to the average ice velocity between January 2015 and June 2019 in each region of interest. Shaded envelopes indicate the seasonal standard deviation in each year and at each region of interest. Note the different y-axis scales compared to Figure 4.3.

relative to pre-acceleration values for 2–3 months. Beginning in mid-summer, ice flow decelerated toward a minimum in early-September that was approximately 10% below pre-acceleration velocities. The seasonal transition from accelerating to decelerating ice flow coincided closely with a switch to inferred efficient drainage (signalled by plume surfacing) in all years except 2017. In every year, this summertime deceleration occurred despite continued terminus retreat. After reaching a velocity minimum at the end of the melt season, ice velocity gradually recovered each winter (Figure 4.5) but remained below pre-acceleration speeds for the majority of each winter. As with AS, this seasonal pattern was similar throughout the outlet part of NS (Figures 4.6 and S1.6–S1.8). An exception to this gradual winter recovery occurred during January 2019, when we observed a short-lived (1–2 weeks) and high-magnitude (~25%) speed-up throughout the outlet part of the glacier.

Annually averaged (April–March) ice velocity during 2016–2017, 2017–2018, and 2018–2019 were similar (±2.9%), despite a near doubling of annually averaged subglacial discharge during 2016 compared to other years (Table S1.1). We observe moderate positive correlations between glacier terminus position and ice velocity during individual years (R^2 = 0.13–0.68, $p < 0.007$), but a weak positive correlation when considering multiple years ($R^2 = 0.1$, $p < 0.001$) (Figure 4.4b).

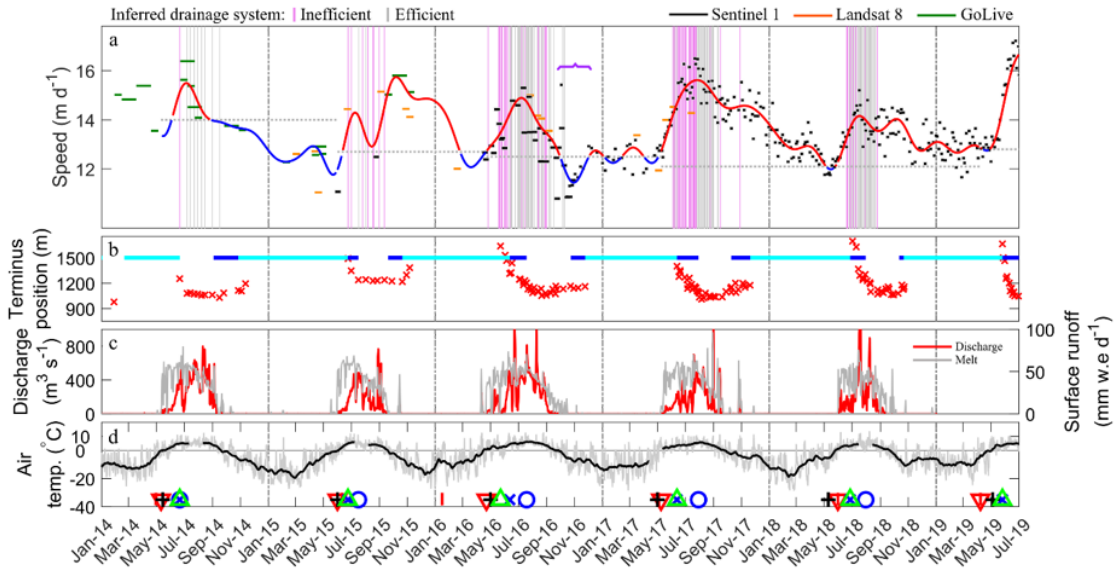

Figure 4.7. Kangiata Nunaata Sermia velocity and forcings timeseries. Colours are the same as for Figure 4.2. Note the different Y-axis scales in compared to Figure 4.2. Purple bracket in (a) indicates the approximate period of influence of the Isvand Lake drainage event.

4.3.3 Kangiata Nunaata Sermia

KNS was characterized by seasonal velocity variations that resembled the type 2 behavior described by Moon et al. (2014) and Vijay et al. (2019). The early-summer acceleration coincided closely with surface runoff and/or positive temperature onset, which was usually several weeks prior to observed terminus retreat and visible mélange weakening. The summer speed-up was both more pronounced (peaking up to 40% above pre-acceleration values) and more sustained (ice velocity remained elevated relative to pre-acceleration speeds for at least the entire melt season each year) than at either AS or NS. During 2016–2018, when our velocity and plume data are most complete, the transition from accelerating to decelerating flow occurred with, or shortly after, an increase in inferred drainage system efficiency (Figure 4.7a) and regardless of whether the terminus was still retreating. In contrast to AS and NS, there was little or no extra slow-down in any year. An exception to this occurred in October 2016, when ice velocity in the lower 6 km of KNS briefly dipped below pre-acceleration speeds (i.e. there was a minor extra slow-down) following the drainage of the large ice-dammed lake Isvand, which produced a plume adjacent to KNS (Figures 4.1, 4.7a, 4.8, and S1.9). Like AS and similar to NS, ice velocity was unrelated (R^2 = 0.002, p = 0.7) to terminus position during the study period (Figure 4.4c) and annually averaged (April–March) ice velocity was actually

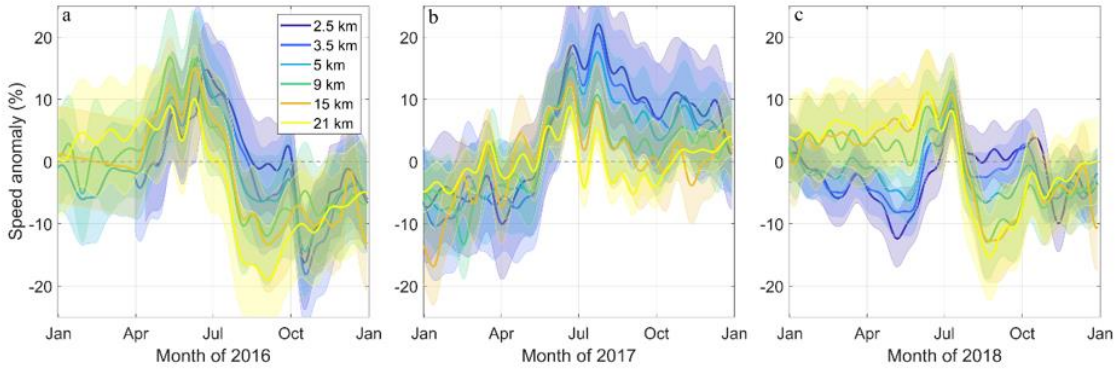

Figure 4.8. Seasonal velocity anomalies at Kangiata Nunaata Sermia during (a) 2016, (b) 2017 and (c) 2018. Anomalies were calculated relative to the average ice velocity between January 2015 and June 2019 in each region of interest. Shaded envelopes indicate the seasonal standard deviation in each year and at each region of interest. Note the different y-axis scales compared to Figures 4.3 and 4.6.

slower during a warmer year (2016–2017) than a cooler year (2017–2018), despite very similar (±50 m) terminus positions.

4.4 Discussion

We observed pronounced and differing seasonal velocity variations at three contrasting tidewater glaciers exposed to similar climatic variability. At AS and NS each year, we observed an early-summer acceleration, subsequent deceleration to below pre-acceleration speeds, and gradual acceleration over winter (Figures 4.2, 4.3, 4.5, and 4.6). Although there were differences between these glaciers (discussed below), the seasonal ice velocity pattern of both AS and NS fits the "type 3" pattern identified in Moon et al. (2014). In contrast, KNS did not usually undergo an extra slow-down and so broadly fits the type 2 classification, with perhaps some type 3 behavior (Moon et al., 2014). Our more detailed observations therefore support the classification of AS and KNS by Moon et al. (2014). At most tidewater glaciers, changes in terminus position or subglacial hydrology are thought to be the dominant drivers of seasonal dynamics (e.g. Moon et al., 2015), but disentangling these contrasting processes is difficult (e.g. Fried et al., 2018). In the discussion below, we argue that evolution in subglacial hydraulic efficiency can explain the key features of the seasonal ice flow variations at these tidewater glaciers. We therefore build on previous studies (Moon et al., 2014; Vijay et al., 2019) by providing additional evidence to support the hypothesis that subglacial drainage evolution both occurs and exerts an important control on ice dynamics at tidewater glaciers. Furthermore,

our time series enable a more detailed description of the subtle variations in these temporal velocity patterns both between glaciers and between years, allowing a more robust interpretation of their controls.

Each of the three glaciers studied underwent a temporary speed-up each year, usually commencing between mid-March and mid-May (Figures 4.2, 4.5, and 4.7). This acceleration always began before any visible mélange weakening, indicating that changes in buttressing by ice mélange do not serve as a key control on the seasonal dynamics of these glaciers. In many cases (especially at KNS but also at NS), the onset of acceleration coincided approximately (at the resolution of the data) with the onset of surface runoff and/or positive temperatures. Sometimes, this also coincided with terminus retreat, which may have contributed to the observed acceleration (Fried et al., 2018). At AS, acceleration usually occurred prior to any obvious forcing (Figure 4.2). We suggest that this is partly due to the difficulty in distinguishing the early-summer acceleration from the ice flow recovery over the preceding winter. In addition, it is possible that surface melting on the lower part of the glacier, caused by brief excursions to positive temperatures, did occur in sufficient volume to affect ice dynamics, but was not captured by RACMO2.3p2.

At all three glaciers, ice velocity was generally greatest near the beginning of the melt season, when meltwater runoff was rising rapidly. This behavior resembles that of land-terminating glaciers and occurs when the drainage system is continually challenged by rapidly increasing meltwater inputs, causing frequent spikes in water pressure (Bartholomew et al., 2012; Harper et al., 2007; Schoof, 2010), cavity expansion (Cowton et al., 2016b; Fowler, 1987; Iken, 1981; Kamb, 1987), and/or sediment deformation (Iverson et al., 1995). Our observations of seasonal meltwater-induced speed-ups were relatively small (16–40%) compared to land-terminating glaciers (180–400%) (Sole et al., 2013; van de Wal et al., 2008; Wal et al., 2015), though the maximum speed-ups we observe are likely reduced by smoothing over the 6- to 12-day image baseline. Similarly, modest seasonal meltwater-induced speed-ups (typically less than 15%) have been observed at several other Greenlandic tidewater glaciers (Ahlstrøm et al., 2013; Andersen et al., 2010; Bevan et al., 2015; Joughin et al., 2008; Kehrl et al., 2017; Moon et al., 2014; Sole et al., 2011; Sugiyama et al., 2015; Vijay et al., 2019) and may be subdued relative to land-terminating glaciers because of the already low basal resistance at tidewater glaciers (Shapero et al., 2016).

As subglacial channels become larger and more efficient, further increases in meltwater input have a more limited impact on basal water pressure, so velocity stabilizes then falls (Röthlisberger, 1972). Such behavior has been observed across land-terminating sectors of the ice sheet (Bartholomew et al., 2012; Cowton et al., 2016b). Although direct evidence of subglacial drainage evolution is even more challenging to obtain at tidewater glaciers than at their land-terminating counterparts, the velocity and plume observations and plume modeling presented here provide indirect support for a similar process at our study glaciers. At all glaciers, velocity decreased part way through the melt season, but this occurred later at the faster-flowing KNS and NS than at AS. In addition, there was in most years a seasonal progression toward more efficient drainage, as inferred from more frequent plume surfacing. In some cases (e.g., NS in 2016 and KNS in 2017), the appearance of plumes at the fjord surface coincided closely with the transition from acceleration to deceleration. This provides further support for the role of changes in subglacial hydraulic efficiency in modulating the seasonal velocity patterns at these glaciers, though this evidence is treated with caution given the approximate nature of the method used to infer hydraulic efficiency and the interannual variation in the timing of observed plume surfacing with respect to peak velocities.

After peak velocities were reached at AS and NS each year, ice velocity fell to below pre-acceleration values, despite continued surface melting, and was followed by recovery over winter. The deceleration occurred earlier and seasonal velocity minima were lower relative to pre-acceleration speeds at AS than at NS. This pattern of flow variability provides further support for the hypothesis that subglacial drainage evolution modulated the observed seasonal flow variations at these glaciers. At land-terminating margins, the extra slow-down is thought to be caused by drainage of water from weakly connected areas of the bed (Andrews et al., 2014; Hoffman et al., 2016) toward persistent and efficient subglacial channels (Sole et al., 2013). The extra slow-down is therefore more pronounced where the late-summer subglacial channels are more hydraulically efficient (Sole et al., 2013). Based on this understanding, we propose that the seasonal subglacial drainage system at AS became more efficient than at NS and KNS because the extra slow-down was most pronounced at the former. Furthermore, flow recovery at both AS and NS did not begin until the end of each melt season, presumably only after subglacial channels had closed, thereby allowing re-pressurization of the subglacial drainage system by basal melting and rain events (e.g. November 2017).

KNS displayed little or no seasonal extra slow-down near the terminus, suggesting that the subglacial drainage system was not usually efficient enough to induce a widespread reduction in basal water pressure to below pre-acceleration values. However, two sets of observations indicate that seasonal increases in subglacial hydraulic efficiency still acted to dampen the seasonal speed-up each year, thereby limiting interannual velocity. First, the transition from acceleration to deceleration each summer usually closely followed a switch to predominately channelized drainage (as inferred from the plume observations and modeling). Moreover, this transition began earlier and the subsequent deceleration was faster in 2016, when the melt season began earlier and modeled meltwater discharge was greater. Thus, although there was little seasonal meltwater-induced extra slow-down (as occurred at AS and NS), annual average ice velocity at KNS was still lower during 2016, the year with the greatest runoff (Table S1.1). Second, following the drainage of Isvand in October 2016 (Figure S1.9), we observed a plume at the fjord surface and a short-lived velocity perturbation characterized by a significant speed-up followed (crucially) by an extra slow-down and subsequent recovery (Figures 4.7 and 4.8). These observations suggest that even short-lived pulses in runoff supply can potentially form channels efficient enough to induce a compensatory slow-down. This raises the possibility that as runoff supply increases in the future, current type 2 glaciers may transition toward type 3 behavior.

There are differences in the seasonal velocity patterns of each glacier that we argue provide further insight into the evolution of the hydrological system beneath tidewater glaciers. For example, summertime peak speeds at AS were much smaller relative to pre-acceleration speeds and occurred much earlier, than at NS. Those at NS were in turn smaller and occurred earlier than those at KNS. One possible explanation for this is that subglacial channels developed earliest (and grew fastest) at AS and latest (and grew slowest) at KNS. If our assumption that plume surfacing indicates the presence of an efficient subglacial drainage system is correct, then our time series of plume surfacing supports this explanation because plumes appeared first and were most persistent at AS and appeared last at KNS. Given the difficulty of directly observing subglacial channel development at tidewater glaciers, we cannot prove that efficient subglacial channels do develop more rapidly at AS. However, it is worth briefly considering the likely theoretical conditions for channel development at each glacier (Figure 4.9). Of the three glaciers, AS is most heavily grounded close to the terminus, with a height-above-flotation of ~100 m. In contrast, the lower several km of NS is much closer to floatation, which would reduce

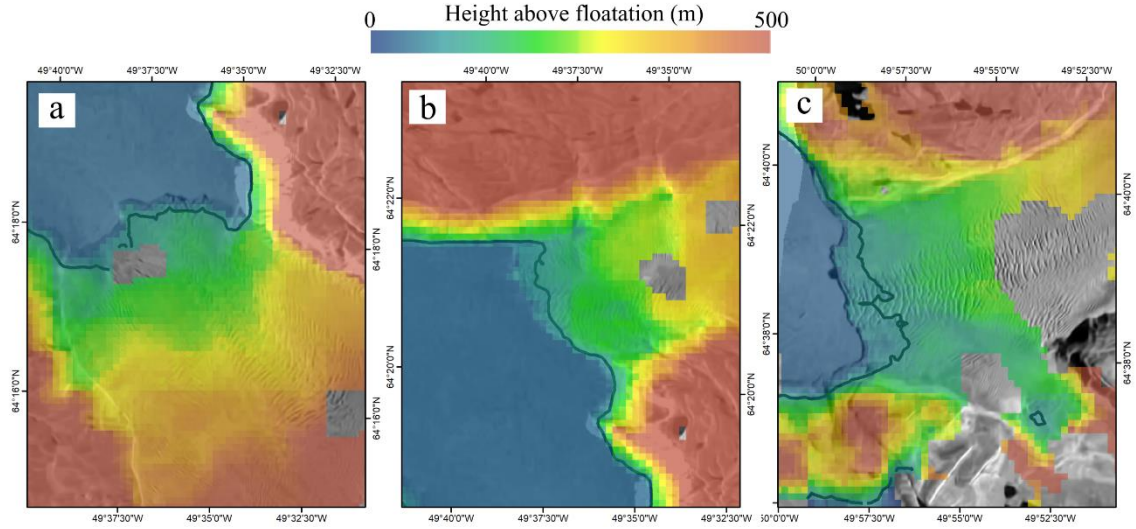

Figure 4.9. Height-above-flotation at (a) KNS, (b) AS and (c) NS. Height-above-flotation was calculated using 2 m ArcticDEM (Porter et al., 2018) strips based on WorldView imagery acquired on August 3 2015 (for panels a & b) and July 24 2017 (for panel c) and BedMachine v3 (Morlighem et al., 2017) fjord bathymetry. Background images are Sentinel 1 amplitude images acquired on August 19 2015 (panels a & b) and August 12 2017 (panel c), to indicate the glacier terminus position close to the time of DEM image acquisition.

hydraulic potential gradients and therefore reduce subglacial channel growth rates (Röthlisberger, 1972). This suggests that readily available metrics such as height-above-flotation may provide some insight into the influence of hydrology on the dynamics of other tidewater glaciers. Under this reasoning, however, it is not clear why the seasonal velocity patterns of KNS and NS differ so markedly, since their flow speed and height-above-flotation are similar.

As AS is well grounded and flows only 2–3 times faster than is typical of land-terminating sectors, it is perhaps unsurprising that seasonal velocity patterns, and inferred drainage system evolution, resemble those at land-terminating glaciers. However, it is notable that qualitatively similar seasonal velocity variations occurred at NS, which at ~12 m d^{-1} is flowing 3–4 times faster than AS and an order of magnitude faster than is typical of land-terminating glaciers. Therefore, although channel formation is theoretically hindered by fast ice flow and weak hydraulic potential gradients (Kamb, 1987), our observations suggest that efficient subglacial drainage configurations are able to form and persist long enough to modulate the relationship between meltwater runoff and ice velocity even at fast-flowing tidewater glaciers. Furthermore, our data indicate that increasing hydraulic

efficiency during the melt season can dampen or offset meltwater-induced speed-ups even at fast-flowing tidewater glaciers like NS and KNS, regardless of whether the seasonal velocity pattern is “type 2” or “type 3.”

If we accept that the dynamic behavior of these glaciers is qualitatively consistent with ice flow self-regulation, controlled by changes in subglacial hydraulic efficiency (Sole et al., 2013; Wal et al., 2015), we would expect that there would be limited sensitivity in annually averaged ice motion to interannual variations in runoff. Unfortunately, however, our time series of unbroken velocity estimates is not long enough to allow us to confirm this behavior (Table S1.1). Nevertheless, meltwater runoff is believed to be a significant influence on tidewater glaciers via other mechanisms, particularly as a driver of submarine melting at their termini (Cowton et al., 2019; Straneo et al., 2011; Xu et al., 2012). Over longer timescales, increased runoff may therefore lead to increased submarine melting, tidewater glacier retreat (Cowton et al., 2018; Slater et al., 2019), and associated acceleration and dynamic thinning (Nick et al., 2009; Pfeffer, 2007). We therefore emphasize that our findings do not preclude a potentially important role for increased meltwater runoff in the dynamic evolution of tidewater glaciers and it remains a subject requiring further investigation to determine more precisely the extent and rate of subglacial channel development, and the efficacy of ice flow self-regulation, at contrasting tidewater glaciers.

Our results contrast with studies that have identified terminus retreat and mélange disintegration as key drivers of seasonal flow variations (Howat et al., 2010; Moon et al., 2015). While we argue that the evidence presented here strongly supports the hypothesis that the seasonal velocity variations at our study glaciers are modulated by subglacial hydrology, it is possible that changes in terminus position and mélange buttressing also play a role. For example, a proportion of the early-summer acceleration at each glacier (especially KNS) occurred while the terminus was retreating each year (similar to Fried et al., 2018). However, despite the partial temporal overlap between acceleration and retreat, there are several lines of evidence indicating that variations in terminus position and mélange buttressing did not exert a dominant control on either the magnitude or timing of the velocity variations observed here: (1) the onset of acceleration always occurred several weeks prior to observed terminus retreat or visible mélange weakening; (2) peak velocity always occurred before the most retreated terminus position; (3) gradual winter acceleration began before mélange reformation and continued after mélange

reformation; and (4) over interannual timescales, we find little relationship between ice velocity and terminus position at any of our study glaciers (Figure 4.4). At NS, we observed deceleration during terminus retreat, resulting in a positive correlation between ice velocity and terminus position during individual years (Figure 4.4b)—the opposite to that expected if terminus position was driving the changes in ice velocity.

It is likely that the drivers of seasonal ice flow variations differ between glaciers, and we note that while KNS is the largest tidewater glacier in southwest Greenland, our study glaciers do not represent the full range of Greenland's tidewater glaciers. At glaciers that are faster, thicker, and more lightly grounded than KNS, basal friction may be lower (Shapero et al., 2016) and calving events tend to be larger, thereby potentially increasing the importance of terminus position changes over subglacial hydrology as a control on ice dynamics (e.g. Bevan et al., 2015; Kehrl et al., 2017). Nevertheless, an examination of a broader sample of glaciers (Vijay et al., 2019) showed that over 50% were characterized by seasonal ice flow variations similar to those observed here and which we argue are controlled primarily by subglacial hydrology. Therefore, while our study has focused in detail on a few glaciers within a single fjord system, we expect our findings concerning the role of subglacial hydrology in driving seasonal ice flow variability to be relevant to a large number of small to medium-sized tidewater glaciers around Greenland.

4.5 Conclusion

We use high-resolution ice velocity estimates, observations of terminus position and ice mélange, modeled subglacial meltwater discharge, and inferred subglacial hydraulic efficiency to investigate drivers of seasonal ice flow variability of three contrasting tidewater glaciers, with similar climatic forcing, in southwest Greenland. At all three glaciers, we find little relationship between ice velocity and variations in terminus position or ice mélange occurrence. Instead, we infer that surface-derived meltwater inputs drive pronounced seasonal changes in ice velocity characterized by early-summer flow acceleration followed by deceleration either to, or below, pre-acceleration speeds. We argue that the amplitude and longevity of the seasonal acceleration and deceleration are controlled by the development of hydraulically efficient subglacial channels. We suggest that this behavior is qualitatively consistent with ice flow self-regulation (where in warmer years, faster summer ice flow is balanced by slower winter motion, resulting in limited net annual differences in ice motion), which has been observed over extensive land-terminating sectors of the GrIS but not near the termini of tidewater glaciers.

Therefore, changes in subglacial hydraulic efficiency likely exert a strong control on the seasonal dynamics of many of Greenland's small to medium-sized tidewater glaciers. The net impact of this hydrodynamic coupling on annual and interannual timescales nevertheless remains uncertain and requires further investigation.

Chapter 5 - Iceberg melting substantially modifies oceanic heat flux towards major Greenlandic tidewater glacier

Icebergs are ubiquitous in Greenland's fjords, providing a mobile and spatially-distributed heat sink and freshwater source in Greenland's fjords. However, the impact of iceberg melting on fjord dynamics and, ultimately, ice sheet-ocean interaction is unknown. In this results chapter, an iceberg melt module is developed and coupled to an ocean circulation model to quantify iceberg-ocean interaction in Sermilik Fjord and to assess its implications for ocean forcing of Helheim Glacier. The results show that icebergs substantially modify fjord water properties and circulation, resulting in an overall increase in oceanic heat flux towards Helheim Glacier.

Chapter 5: Icebergs modify oceanic heat flux

Published in **Nature Communications**, November 2020

Authors: B. J. Davison[1], T. R. Cowton[1], F. R. Cottier[2,3], and A. J. Sole[4].

1. Department of Geography and Sustainable Development, University of St Andrews, St Andrews, UK
2. Scottish Association for Marine Science, Scottish Marine Institute, Oban, UK
3. Department of Arctic and Marine Biology, UiT The Arctic University of Norway, Tromsø, Norway
4. Department of Geography, University of Sheffield, Sheffield, UK

Citation: Davison, B. J., T. R. Cowton, F. R. Cottier, and A. J. Sole. (2020). Iceberg melting substantially modifies oceanic heat flux towards a major Greenlandic tidewater glacier. *Nature Communications,* 11, 5983. doi: 10.1038/s41467-020-19805-7.

Author contributions: B.J.D. and T.R.C. designed the research. B.J.D. developed the model code with support of T.R.C. and A.J.S. B.J.D. designed and conducted the simulations and analysis. T.R.C., F.R.C. and A.J.S. supported the interpretation of the model results. B.J.D. led the write up of the manuscript, with contributions from all other authors.

Note that this chapter was originally formatted for *Nature Communications*, with the methods provided at the end. For the purposes of this thesis, the methods have been moved to their traditional location before the results. The text is otherwise unchanged from the published version.

Abstract

Fjord dynamics influence oceanic heat flux to the Greenland ice sheet. Submarine iceberg melting releases large volumes of freshwater within Greenland's fjords, yet its impact on fjord dynamics remains unclear. We modify an ocean model to simulate submarine iceberg melting in Sermilik Fjord, east Greenland. Here we find that submarine iceberg melting cools and freshens the fjord by up to ~5°C and 0.7 psu in the upper 100-200 m. The release of freshwater from icebergs drives an overturning circulation, resulting in a ~10% increase in net up-fjord heat flux. In addition, we find that submarine iceberg melting accounts for over 95% of heat used for ice melt in Sermilik Fjord. Our results highlight the substantial impact that icebergs have on the dynamics of a major Greenlandic fjord, demonstrating the importance of including related processes in studies that seek to quantify interactions between the ice sheet and the ocean.

5.1 Introduction

The dynamics of Greenland's glacial fjords control the transport of oceanic heat to Greenland's tidewater glaciers, with potentially important implications for ice sheet stability (Nick et al., 2009) and global sea level (Shepherd & Nowicki, 2017). For example, the rapid retreat of many of Greenland's tidewater glaciers during the early 2000s has been attributed to increased oceanic forcing (Bevan et al., 2019; Cowton et al., 2018; Holland et al., 2008; Rignot et al., 2012), due to both ocean warming and invigorated fjord circulation resulting from enhanced ice sheet runoff (Cowton et al., 2016a; Straneo & Heimbach, 2013). The resultant increase in glacier submarine melt rates (Slater et al., 2016) may have led to greater undercutting of glacier calving fronts (Fried et al., 2015; Rignot et al., 2015) and an increase in glacier calving rates (Benn et al., 2017; Cowton et al., 2019; O'Leary & Christoffersen, 2013). Understanding the controls on oceanic heat flux to tidewater glacier calving fronts is therefore essential if we are to reliably predict the influence of the ocean on Greenland's tidewater glaciers in a changing climate.

Oceanic heat flux towards Greenland's tidewater glaciers depends on the rate of fjord-shelf exchange, the properties of the ocean waters entering the fjords, and how those waters are modified during fjord transit prior to interacting with tidewater glaciers (Straneo & Cenedese, 2015). Off the coast of Greenland, two water masses provide the principal oceanic input to Greenland's fjords[16]. Cooler, fresher water of Polar origin

('Polar Water') is found in the upper 100-200 m of the water column, and is typically underlain by warmer, more saline water of Atlantic origin ('Atlantic Water'). Where deep glacially-eroded troughs extend to the continental slope, they allow the passage of Atlantic Water and both water masses can access Greenland's fjords (Straneo & Heimbach, 2013). A range of processes force these water masses into the fjords, including (for example) tidal mixing (Mortensen et al., 2014), barrier winds (Fraser & Inall, 2018; Jackson et al., 2014) and buoyancy-driven circulation controlled by ice sheet runoff (Cowton et al., 2016a). Once in the fjord, the temperature-salinity structure set by these water masses is modified by a range of processes. During the spring and summer months, freshwater inputs from sea ice melt, terrestrial snow melt and precipitation cool and freshen surface and near-surface waters (Christoffersen et al., 2011). In addition, the discharge of fresh glacial runoff from tidewater glacier grounding lines (henceforth runoff) drives buoyant plumes (Chauché et al., 2014), which entrain and transport relatively warm Atlantic Water towards the glaciers and subsequently towards the fjord surface (Beaird et al., 2018; Cowton et al., 2015; Mankoff et al., 2016; Straneo & Cenedese, 2015). This drives an outflowing current of glacially-modified water in the upper layers of the fjord and a compensatory inflowing current over a broad depth range below, typically between the Atlantic Water-Polar Water interface and the sill depth (Carroll et al., 2015; Straneo et al., 2010; Sutherland & Straneo, 2012).

Icebergs are a major component of Greenland's glacial fjords. Frontal ablation (iceberg calving plus submarine melting of glacier termini) at tidewater glaciers represents ~30-50% of the freshwater export from the ice sheet into the ocean, of which calving of icebergs is the larger component (Colgan et al., 2019). Icebergs melt partially or entirely whilst transiting glacial fjords (Enderlin et al., 2016, 2018; Moyer et al., 2019), thereby providing a heat sink and freshwater source that is distributed horizontally and vertically throughout the fjord. The resultant freshwater flux comprises a key component of the freshwater budget of iceberg-congested fjords (Enderlin et al., 2016; Jackson & Straneo, 2016; Moon et al., 2017).

Despite the prevalence of icebergs in many of Greenland's fjords and the substantial release of freshwater from them, the impact of their melting on fjord water properties, fjord circulation and therefore oceanic heat flux towards tidewater glaciers remains largely unknown. This study is motivated by the hypothesis that icebergs substantially modify fjord water properties, which may in turn affect fjord circulation and the oceanic

forcing of tidewater glaciers. This is informed by summertime observations of water properties along Sermilik Fjord — one of the largest and most thoroughly surveyed fjords in east Greenland (Figure 5.1) — which show a marked up-fjord decrease in both temperature and salinity (Inall et al., 2014; Jackson & Straneo, 2016; Sutherland et al., 2014a; Sutherland & Straneo, 2012). This cooling and freshening is confined primarily to the upper few hundred metres of the water column and can be of high magnitude (~5^{o}C and 0.5 psu). The temperature-salinity signature of this along-fjord trend is consistent with ice melting in ocean water, rather than of runoff (Beaird et al., 2018; Inall et al., 2014; Jackson & Straneo, 2016). Furthermore, inferred ice melt volume within Sermilik Fjord is an order of magnitude larger than that expected from melting of glacier termini alone (Beaird et al., 2018; Jackson & Straneo, 2016), which suggests that there is a large additional input of meltwater, most likely from submarine iceberg melting. This inference is supported by a small number of hydrographic surveys conducted near icebergs, which identified areas of upwelling and cooling (Helly et al., 2011; Josberger & Neshyba, 1980; Stephenson et al., 2011). These lines of evidence suggest that submarine iceberg melting may be responsible for considerable modification of fjord water properties, which may in turn affect fjord circulation.

In this study, we quantify the impact of submarine iceberg melting on fjord circulation, fjord water properties and up-fjord oceanic heat flux during summer in Sermilik Fjord. To achieve this, we adapt a numerical ocean model to include a representation of submarine iceberg-ocean interaction, and compare model output to identical simulations without icebergs. We generate a high-fidelity model domain representative of Sermilik Fjord, with realistic bathymetry (Morlighem et al., 2017) (Figure 5.1a) and an observation-based (Sulak et al., 2017) iceberg distribution (Figure 5.1b,c; Figure S2.1). Individual cuboidal icebergs are roughly oriented with the fjord long-axis and are represented as a set of horizontal and vertical ice faces, with dimensions based on observed iceberg aspect ratios (Dowdeswell et al., 1992) and relationships between iceberg volume and submerged surface area (Barker et al., 2004; Sulak et al., 2017).

Fjords are dynamic systems, with changes in circulation, iceberg cover and hydrographic conditions occurring over timescales of days to years. It would be computationally intractable (and scientifically confusing) to simulate the full gamut of possible conditions in Sermilik Fjord. Consequently, we concentrate on the summertime regime during which most observations are acquired and when the circulation is thought to be dominated by

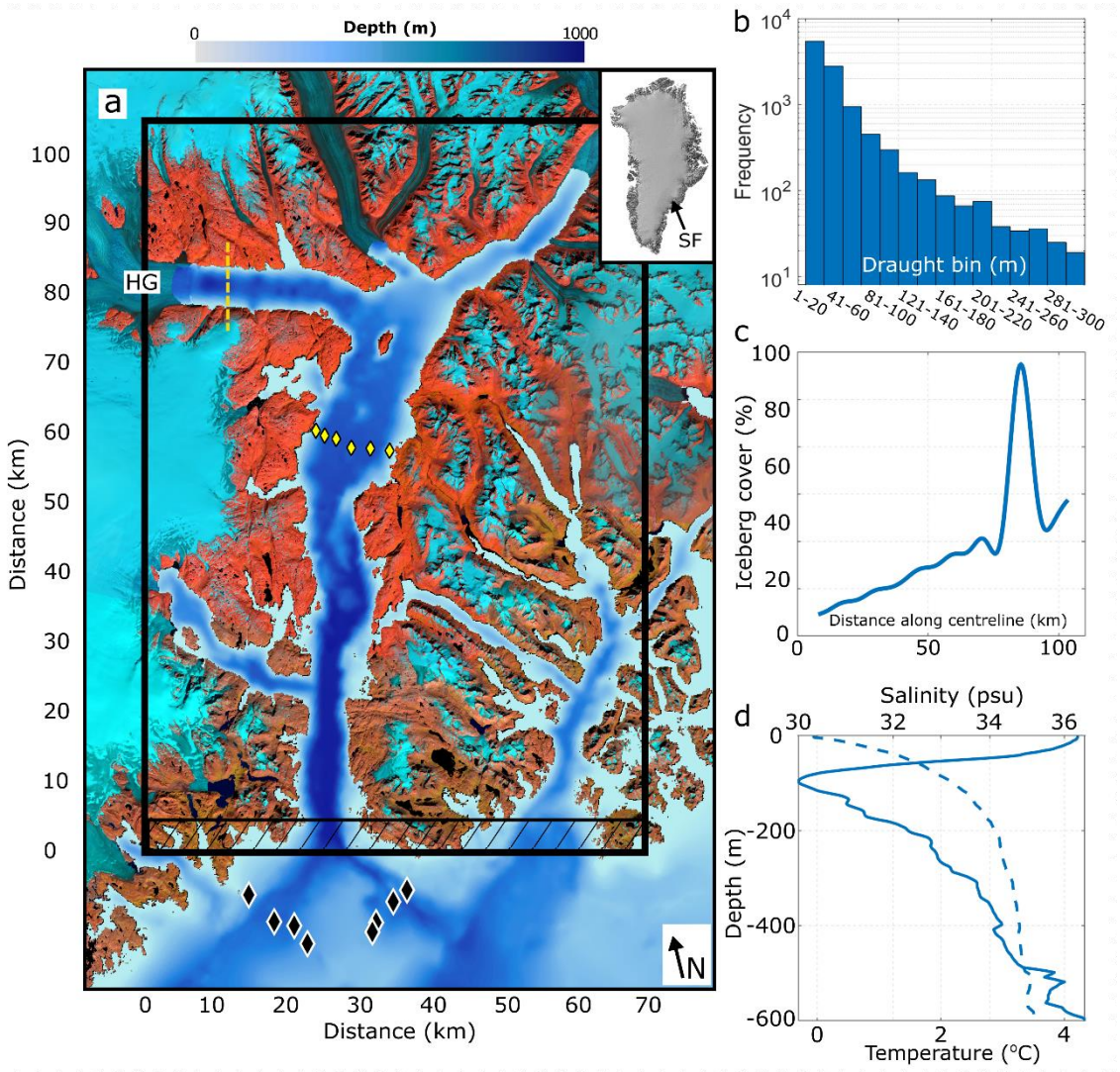

Figure 5.1. Sermilik study area and model domain. (a) BedMachine v3 (Morlighem et al., 2017) bathymetry of Sermilik Fjord, with the inset showing its location in Greenland. The inset was created using the Greenland Ice Mapping Project digital elevation model (Howat et al., 2014). The background image is a mosaic of five Landsat 8 false-colour composites (bands 6, 5 & 4) acquired on 12 July, 21, 23, 28 and 15 August 2017. HG = Helheim Glacier. (b) Iceberg draught-frequency distribution used in the primary simulations, based on observations by Sulak et al. (2017) (c) The percent of the fjord surface in plan-view covered by icebergs. (d) Temperature (solid line) and salinity (dashed line) boundary conditions. The black box in (a) denotes the limit of the model domain. The black hatching in (a) denotes the relaxation zone. The black diamonds in panel (a) indicate locations of conductivity-temperature-depth casts used for boundary conditions (panel d) and the yellow diamonds are conductivity-temperature-depth casts used in Figure 5.7. The yellow dashed line in (a) is the flux gate used in our heat flux calculations.

subglacial runoff (Cowton et al., 2016a), and use a single snapshot-in-time of iceberg cover and distribution (Sulak et al., 2017). It is therefore the interaction between

submarine iceberg melting and the circulation driven by glacial runoff that we focus on here. More specifically, we quantify the impact that submarine iceberg melting has on summertime fjord water properties, circulation and therefore oceanic heat flux towards Helheim Glacier, which is the largest glacier terminating in Sermilik Fjord (Figure 5.1a), and the second largest glacier in Greenland in terms of ice discharge (Mouginot et al., 2019). In doing so, we provide the first assessment of how submarine iceberg melting can affect oceanic heat flux towards a major Greenlandic tidewater glacier during summer.

Our simulation design is as follows (see Section 5.2 for detail). Each simulation was run for 100 days, reaching a quasi-steady-state (with domain-averaged kinetic energy changing by less than 3% over the final 10 model days; Figure S2.2). Runoff, iceberg cover (Figure 5.1b,c) and boundary conditions (Figure 5.1d) were kept constant throughout each simulation; the diagnostics presented below are averages of the final 10 model days. We used six different runoff values, ranging from 0 to 2000 m^3 s^{-1}, to represent the range of summertime runoff discharge into Sermilik Fjord (Noël et al., 2018). Simulations with these runoff values were repeated using two subglacial drainage configurations that are broadly representative of 'channelised' and 'distributed' subglacial drainage. Our primary simulations used melt rate parameter values commonly used in the literature (Cowton et al., 2016a) (Table S2.1); however, recent observations (Jackson et al., 2020; Sutherland et al., 2019) suggest that these 'standard' values may underestimate glacier melt rates. We therefore repeated each simulation using these 'adjusted' parameter values (Table S2.1) suggested by Jackson et al. (2020). For clarity, we focus primarily on two simulations using our 'channelised' runoff configuration and the standard parameter values: a 'no-runoff forcing' scenario, which allows us to quantify iceberg-fjord interaction in isolation, and a 'summer runoff forcing' scenario, in which 1200 m^3 s^{-1} runoff emerges from Helheim Glacier. All simulations are compared to identical simulations without icebergs.

5.2 Methods

5.2.1 Ocean model

We use the Massachusetts Institute of Technology General Circulation Model (MITgcm; Marshall et al. (1997a)), which solves the incompressible Navier-Stokes equations using finite volume methods on an orthogonal curvilinear grid (Adcroft et al., 1997). We take advantage of the non-hydrostatic capability of MITgcm (Marshall et al., 1997b) in order

to resolve areas of complex bathymetry. MITgcm has been used in numerous studies of ice sheet-ocean interaction in both Greenlandic (e.g. Cowton et al., 2015, 2016a) and Antarctic (Dansereau et al., 2013) settings.

5.2.2 Parameterising iceberg melting in MITgcm

Several parameterisations for bulk iceberg melting exist (Bigg et al., 1997; FitzMaurice et al., 2017; FitzMaurice & Stern, 2018), some of which have been incorporated into ocean circulation models (Marsh et al., 2015; Marson et al., 2018). These parameterisations have, for example, proven invaluable for predicting iceberg trajectories and deterioration in the open ocean (Bigg et al., 1997). To the best of our knowledge, however, these parameterisations have been designed based on iceberg-average submarine melt rates. They would not therefore be suitable tools for simulating vertical variations in iceberg melting within high-resolution domains, such as those required to simulate Greenlandic fjord circulation with high fidelity. We therefore develop a new package to simulate iceberg melting within MITgcm. This package utilises the three-equation melt formulation (Jenkins, 1991, 2011), allowing us to resolve vertical variations in iceberg melt rates, whilst faithfully representing observed iceberg size-frequency and spatial distributions (Barker et al., 2004; Dowdeswell et al., 1992; Enderlin et al., 2016; Sulak et al., 2017).

5.2.2.1 Iceberg geometry

In Greenland's glacial fjords, icebergs are produced at the fjord head through glacier calving and subsequently drift through the fjord (Sutherland et al., 2014b), eventually reaching the open ocean or melting out entirely within the fjord. The geometry of the population of icebergs within the fjord can be described in terms of: (1) their size-frequency distribution; (2) their concentration (the fraction of the fjord surface occupied by icebergs); and (3) their aspect ratio (the relationships between their length (l), width and keel depth (d)).

At a given glacier, iceberg calving events vary in size, typically with many smaller events and relatively few larger events, producing icebergs with dimensions spanning several orders of magnitude (Sulak et al., 2017). Both field-based (Dowdeswell et al., 1992) and remotely-sensed (Sulak et al., 2017) observations show that the resulting iceberg size-frequency distribution can often be approximated using a power law, with the few available observations suggesting that exponents in Greenlandic settings range from -2.1 to -1.8 (Sulak et al., 2017). In our primary simulations, we generate an array of icebergs

with a size-frequency distribution fitting a power law with an exponent of -2.0 (Sulak et al., 2017), using inverse transform sampling (Olver & Townsend, 2013) – a classical approach to generating pseudo-random samples from a prescribed probability distribution. We test the sensitivity of our results to this choice of exponent by generating alternative size-frequency distributions with slopes of -1.8 and -1.9 (Figure S2.3; Table S2.2), which encompass the range of size-frequency distributions observed in Sermilik Fjord (Moyer et al., 2019).

In our primary simulations, we based our iceberg setups on a length-draught relationship presented in Barker et al. (2004) and on remotely sensed observations of icebergs in Sermilik Fjord (Enderlin et al., 2016, 2018; Enderlin & Hamilton, 2014; Sulak et al., 2017). The icebergs are rectangular in plan-view and have vertical sides. In our primary simulations, we set the maximum iceberg draught to 300 m (Sulak et al., 2017), and iceberg keel depth was related (Barker et al., 2004) to iceberg length through $d = 2.91l^{0.71}$. The draught of the resulting icebergs and their distribution are shown in Figure 5.1b,c and Figure S2.1. We also performed secondary simulations with maximum iceberg draughts ranging from 150-400 m (Figure S2.7) and using an alternative relation (Sulak et al., 2017) between iceberg volume (V) and plan-view iceberg area (A) which states $V = 6.0A^{1.30}$ (Figures S2.3 & S2.8), and two other iceberg length to keel depth ratios of 2:1 and 1.8:1 (Table S2.2), based on unpublished observations in Sermilik Fjord (Schild et al., 2021). In all our simulations, icebergs had length-to-width ratios of 1.62:1 (Dowdeswell et al., 1992).

The proportion of the fjord surface covered by icebergs in a given area, c, generally decreases towards the fjord mouth. Remotely sensed observations (Sulak et al., 2017) show that c is high (>80%) and uniform throughout the ice mélange, then decreases towards the fjord mouth. Consistent with observations, we used a ~18 km long ice mélange. In our primary simulations, we set c to 80% in the mélange and linearly decreased it to 5% near the fjord mouth (Figure 5.1c). Slight deviations from this target cover occurred for two reasons. Firstly, icebergs are placed randomly across the width of the fjord. Secondly, these 2-D iceberg distributions must be drawn from a 1-D iceberg size-frequency distribution, resulting in small mismatches between the achieved and target spatial distribution (see Section S2.1 and Figure S2.1). Using these parameter values, our primary simulations have submerged iceberg surface areas of ~230 km^2 in the ice mélange and ~190 km^2 in the rest of the fjord. The submerged iceberg areas (Table

S2.3) fall within the range of observed values (Enderlin et al., 2016). We also tested the sensitivity of our results to wider ranges of *c* (Figure S2.6). This set of sensitivity simulations provides insight into how varying iceberg concentrations over all timescales affects the dynamics of Sermilik Fjord, and provides some indication of the role of iceberg-ocean interaction in the dynamics of other fjords with (typically) lower iceberg concentrations.

In keeping with the implementation of ice shelves (Losch, 2008) and tidewater glaciers (Xu et al., 2012) in MITgcm, and as in at least one previous representation of iceberg melting within an ocean circulation model (FitzMaurice & Stern, 2018), we represent icebergs as static entities (i.e. they do not drift or change size over time). Although in reality icebergs drift through the fjord, our representation makes the implementation significantly simpler, and is justified in that our focus is on the impact of iceberg melt on the fjord, rather than the evolution and location of individual icebergs.

5.2.2.2 Iceberg thermodynamics

Icebergs deteriorate due to several processes: melting above and below the waterline due to forced and free convection in air and water, wave erosion, and mechanical breakup (Bigg et al., 1997). In this study, we consider only submarine melting (due to both forced and free convection below the water line), which is typically the greatest contributor to iceberg freshwater fluxes because of the larger surface area over which it occurs compared to that of the other processes (Moon et al., 2017).

MITgcm includes representations of freeze-on and melting of both near-horizontal ice shelves (Dansereau et al., 2013; Losch, 2008) and vertical ice fronts (Xu et al., 2012). We adapt these representations to accommodate our iceberg geometries (i.e. thousands of relatively small vertical and horizontal ice walls scattered throughout the domain). The physics describing ice melting in ocean water remains unchanged and is not described here (see citations above for detailed descriptions of the model physics). Instead, we summarise the key characteristics of our implementation and describe in more detail the changes we have made to better represent submarine iceberg melting.

To calculate submarine iceberg melt rates, we use the velocity-dependent three-equation formulation (Dansereau et al., 2013; Jenkins, 2011; Xu et al., 2012), in which the rates of heat and salt transfer across the ice-ocean interface are related to the current velocity at the ice-ocean interface through a quadratic drag law (Dansereau et al., 2013). Recent observations (Jackson et al., 2020; Sutherland et al., 2019) adjacent to Le Conte Glacier,

Alaska, provide strong evidence that typical values used in the three-equation formulation (our 'standard' parameter set) underestimate melt rates of quasi-vertical glacier-ice faces. Based on the Le Conte Glacier observations, Jackson et al. (2020) suggested alternative values for three critical parameters in the parameterisation, which together exert a strong control on the rate of heat transfer across the ice-ocean interface. We therefore carried out an additional set of simulations using the adjusted parameter values (Table S2.1) of Jackson et al. (2020).

Melt rates derived using the velocity-dependent three-equation formulation are sensitive to the current velocity at the ice ocean interface. For icebergs, this is the difference between an iceberg's drift velocity and the ambient water velocity at any given point on the iceberg. In ice mélange — a dense matrix of icebergs and sea ice often found adjacent to large tidewater glaciers — iceberg motion is typically slow relative to the surrounding currents (Moyer et al., 2019; Sutherland et al., 2014b); therefore, in this region of our domain, we assume the icebergs are fixed in place. Elsewhere in the domain, we calculate iceberg drift velocity as the average water velocity from the fjord surface to the iceberg keel depth (FitzMaurice et al., 2016; Matsumoto, 1996) (but we do not use this to update the location of each iceberg). We acknowledge that the drift velocity of an iceberg at any time depends on the iceberg's initial drift velocity, wind and water drag, wave action and the horizontal pressure gradient force exerted by the water, due the displacement of water by the iceberg (Bigg et al., 1997). However, calculating iceberg drift in this way is computationally intensive and relies on datasets that would be impractical to obtain within MITgcm. We expect this simplification to underestimate the drift velocity (and therefore submarine melt rates) of small icebergs, whose drift is controlled predominately by surface winds (Bigg et al., 1997; Wagner et al., 2017). The current velocity past each face of a cuboidal iceberg will likely differ substantially; with the lee-side experiencing lower current velocities and the faces oriented parallel to flow experiencing the greatest relative current velocity. To represent this effect, we calculate the submarine melt rate of every face on each iceberg individually at each model vertical level using ice-parallel current speeds (relative to the calculated drift of the iceberg). We retain vertical profiles of melt rates for each iceberg, but also calculate grid cell-average rates by accounting for the iceberg surface area in each grid cell.

As well as drifting with ocean currents, icebergs also act as a barrier to water flow. We represent this effect using partial cells within MITgcm – essentially forcing a portion of

some of the cells to be 'dry'. The fraction of the cell that is dry is equivalent to the proportion of the cell volume occupied by icebergs. In this way, the blocking effect of all of the icebergs in a cell is represented using a single value, rather than representing individual icebergs as solid bodies within grid cells.

The release of meltwater during submarine iceberg melting drives weak buoyant plumes, which can in turn increase melt rates further up the ice face (Huppert & Josberger, 1980; Magorrian & Wells, 2016). Resolving such convection-driven melting requires grid cell dimensions that are computationally unfeasible at the fjord scale. Instead, we adopt the approach of Cowton et al. (2015) and impose a minimum 'background velocity' at each iceberg face. This value effectively states that there is always some movement of water along the ice face due to melt-driven convection. This approach is similar to another iceberg sidewall melt parameterisation that accounts for melt-driven plume detachment under certain flow regimes (FitzMaurice et al., 2017). In our primary simulations, we use a value of 0.06 m s^{-1}, which is based on a set of simulations utilising the line plume of Jenkins (2011) under stratification appropriate for the study fjords (Cowton et al., 2015) and on sparse field-based measurements (Josberger & Neshyba, 1980). To examine the sensitivity of our results to this choice of background velocity, we also tested values of 0.03, 0.09 and 0.12 m s^{-1} in a separate set of simulations (Figure S2.4). In addition, because the vertical velocity of these plumes theoretically varies through the water column – being greater at depth where the stratification is weaker – we also conducted sensitivity simulations using depth-varying background velocities based on two line plume simulations using the initial and the final ambient conditions in our summer runoff forcing scenario (Figure S2.5; Table S2.2).

5.2.3 Model setup

5.2.3.1 Model domains

We generated a model domain representative of Sermilik Fjord in east Greenland (Figure 5.1). We used uniform horizontal and vertical resolutions of 500 m and 10 m, respectively. The domain extends from Helheim Glacier at the head of the fjord to the area near the mouth where the fjord widens towards the open ocean, and includes all major tributary fjords and glaciers (10 in total). The bathymetry of the domain is based on BedMachine v3 (Morlighem et al., 2017). We used a 5 km relaxation zone at the seaward end of the domain, with a relaxation time that increased linearly from 200

seconds at the open boundary to 5000 seconds 5 km from the open boundary, to prevent internal reflections of currents created within the domain.

5.2.3.2 Initial and boundary conditions

We utilised conductivity-temperature-depth data (Figure 5.1d) obtained in August 2009 (Straneo et al., 2010; Sutherland et al., 2014a, 2013; Sutherland & Straneo, 2012) near the mouth of Sermilik Fjord (locations in Figure 5.1a) as the initial conditions. These data are representative of the water masses observed along the adjacent continental shelf during the summer months (Straneo et al., 2010), with warmer, saltier Atlantic Water underlying cooler, fresher Polar Water. In order for the modelled circulation to be the result of only runoff and/or subsurface iceberg melt, the initial potential temperature and salinity conditions were set as horizontally uniform and were kept constant at the boundary throughout each simulation.

5.2.3.3 Runoff-driven circulation

During summer, the primary driver of fjord circulation is usually ice sheet runoff, which generates buoyant plumes at glacier fronts. These entrain fjord waters before reaching neutral buoyancy (or the fjord surface) and flowing down-fjord (Straneo & Cenedese, 2015). In each simulation, the total runoff entering each fjord was kept constant and was split between each glacier according to the average contribution, relative to that of Helheim Glacier, of each respective glacier catchment to the fjord runoff budget during 1990-2012. Runoff from Helheim Glacier was 0-2000 $m^3\ s^{-1}$, to represent the typical summertime runoff range, based on 1 km^2 RACMO2.3 monthly-mean modelled runoff (Noël et al., 2018). Glacier catchments (Figure S2.10) were delineated using standard hydropotential analysis (Shreve, 1972) bounded by BedMachine v3 (Morlighem et al., 2017). We estimated subglacial discharge at each glacier terminus. To do this, modelled surface runoff (Noël et al., 2018) was assumed to access the bed immediately (i.e. no supraglacial storage or routing) and was routed to the terminus at 1 $m\ s^{-1}$ (Chandler et al., 2013; Cowton et al., 2013). The resulting time-series (1990-2012) of terminus subglacial discharge for each glacier (Figure S2.10) were temporally-averaged before calculating their contributions to the Sermilik Fjord runoff budget relative to that of Helheim Glacier.

The configuration of the subglacial hydrologic system at the grounding line influences the strength of glacial plumes (Slater et al., 2015). The configuration of near-terminus subglacial hydrological systems remains largely unknown, but potentially ranges from a single channel to fully distributed efflux along the grounding line. Modelling studies have

demonstrated that the resulting fjord circulation is sensitive to the strength and distribution of runoff (Carroll et al., 2015; Cowton et al., 2016a). Given this sensitivity, we ran each simulation using two drainage scenarios, using the MITgcm 'iceplume' package (Cowton et al., 2015). In the first, 'channelised', scenario, 90% of runoff at each glacier entered through a single channel (at the deepest point of the grounding line), while the remaining 10% was divided between smaller channels at 500 m intervals along the grounding line. In the second, 'distributed', scenario, runoff at each glacier was evenly distributed between channels at 500 m intervals.

5.2.4 Summary of simulation design

Our simulations (summarised in Table S2.3) are designed to enable evaluation of the impact of submarine iceberg melting on fjord circulation and water properties. As such, we ran one suite of simulations without icebergs (the 'no-iceberg' scenario') and a second suite of simulations with icebergs, which was otherwise identical to the 'no-iceberg' scenario. Within these simulation suites, we performed two sub-suites of simulations to examine the effect of contrasting subglacial hydrological structures. In addition, each of the simulations with icebergs was repeated with adjusted melt rate parameter values (Jackson et al., 2020).

For all of these suites, we ran six simulations to for 100 days with runoff from Helheim Glacier varying from 0 to 2000 $m^3 s^{-1}$ in increments of 400 $m^3 s^{-1}$. Each simulation reached a quasi-steady-state (with domain-averaged kinetic energy changing by less than 3% over the final 10 model days; Figure S2.2). This definition of steady-state is based on fjord currents; however, this does not necessarily imply steady temperature and salinity. We therefore also examined modelled time-series of density within the fjord, which show that changes in density by model day 100 were also small (Figure S2.2). Runoff and open boundary conditions were held constant throughout each simulation. In this way, runoff and submarine iceberg melting are the only forcing in our simulations. We refer to simulations without runoff as 'no-runoff forcing' simulations and note that they are not representative of winter conditions because basal frictional melting of tidewater glaciers during winter likely produces some runoff (Christoffersen et al., 2012), the conductivity-temperature-depth casts used to create the initial and boundary conditions were obtained in summer (rather than winter) and because we do not simulate the effect of barrier winds and isopycnal heaving, which are common during winter in Sermilik Fjord (Jackson et al., 2014).

5.2.5 Heat flux

From a glaciological perspective, whether and how icebergs affect the amount of oceanic heat available to melt tidewater glacier termini is of particular interest. We therefore calculated the oceanic heat transport across a flux gate placed in the ice mélange near Helheim Glacier (location in Figure 5.1a). The heat flux, H, across each gate was calculated as:

$$H = F_{\text{sea}} \rho_0 Q_{\text{gate}} (\theta_{\text{gate}} - \theta_f), \quad \text{Eq. 1}$$

where F_{sea} is the specific heat capacity of seawater (3980 J kg^{-1} K^{-1}), ρ_0 is a reference density (1027 kg m^{-3}), Q_{gate} is the volume transport across the gate in the direction of interest, θ_{gate} is the depth-averaged potential temperature across the gate (following Fofonoff and Millard (1983)) and θ_f is the freezing point, calculated as:

$$\theta_f = \lambda_1 S_0 + \lambda_2 + \lambda_3 z, \quad \text{Eq. 2}$$

where $\lambda_{1,2,3}$ are the freezing point slope (-0.0573°C psu^{-1}), offset (0.0832°C) and depth (-0.000761°C m^{-1}), respectively, and S_0 is the depth-averaged salinity. To facilitate comparison between the changes in up-fjord heat flux at different depths, and because we are primarily interested in the heat available to melt glacier termini, we use a constant, depth-averaged θ_f of -2.06°C based on the average depth of the Helheim Glacier terminus, and the initial salinity stratification (Jackson & Straneo, 2016).

5.3 Results

5.3.1 Submarine iceberg melt

Our domain-averaged submarine iceberg melt rates (using standard parameter values) are in the range ~0.09-0.20 m d^{-1} (Figure 5.2a), but grid cell-average melt rates reach 1.34 m d^{-1} in certain locations and domain-averaged melt rates with the adjusted parameters range from 0.25-0.57 m d^{-1}. Regardless of melt rate parameter values, domain-average melt rates generally increase with runoff raised to the power 0.09-0.12 (Figure 5.2a), due to the relatively fast and warm plume outflow increasing heat transfer to the icebergs (particularly those in the vicinity of glacier fronts). For a given increase in runoff, domain-averaged melt rates increase more in the 'distributed' scenario compared to the 'channelised' scenario, because the plume outflow affects a greater proportion of the fjord in the former.

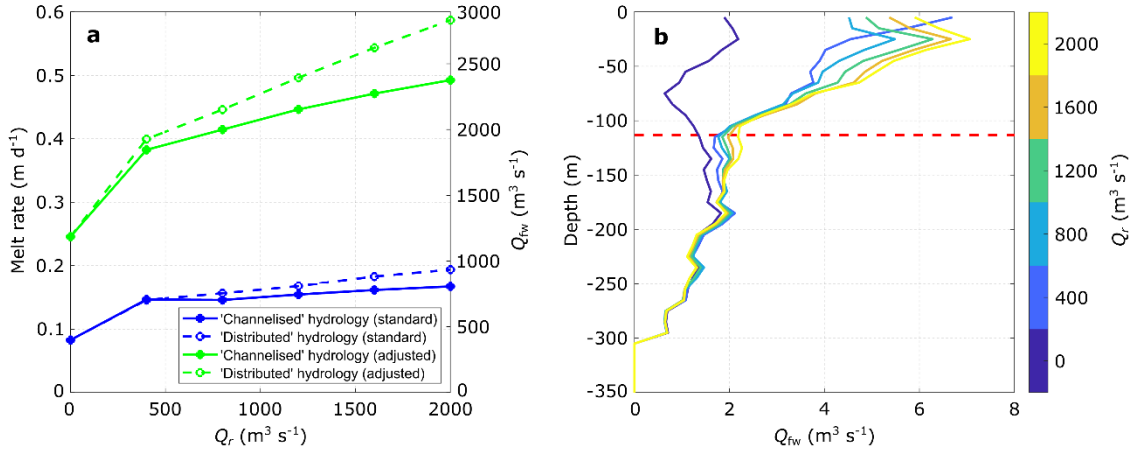

Figure 5.2. Iceberg melt rates and freshwater flux. (a) Relationship between runoff (Q_r) and domain-averaged submarine iceberg melt rate and total iceberg freshwater flux (Q_{fw}). (b) Horizontally-averaged iceberg freshwater flux profile, coloured by runoff, for the 'channelised' runoff configuration and standard melt rate parameter values. The dashed horizontal red line in (b) donates the 27.3 potential density contour, approximating the depth of the interface between Polar Water and Atlantic Water. In panel (a), the blue lines indicate simulations with standard melt rate parameter values, whilst the green lines indicate simulations with adjusted melt rate parameter values. The solid lines represent our 'channelised' drainage scenario and the dashed lines represent our 'distributed' drainage scenario.

The total freshwater flux released by submarine iceberg melting ranges from ~400 to ~2830 m^3 s^{-1}, depending on runoff, subglacial drainage system structure and melt rate parameter values (Figure 5.2a). Freshwater release of this magnitude constitutes an important component of the fjord freshwater budget. For example, in our summer runoff forcing scenario with standard parameter values, the freshwater flux from iceberg melting was 77.4% of the average runoff entering the fjord during July 1990-2012. In general, iceberg freshwater production decreased below ~100 m (Figure 5.2b). Nevertheless, iceberg melting below the Atlantic Water-Polar Water interface (defined as the 27.3 potential density isopycnal (Cowton et al., 2016a)) still contributed a substantial 39.6±11.5% to the total iceberg freshwater flux (Figure 5.2b).

Submarine iceberg melt rates are generally greatest at the head of the fjord (Figure 5.3a), where iceberg draughts are deepest (Figure S2.1). Consistent with this spatial distribution, submarine iceberg melt rates generally increase with iceberg draught (Figure 5.3b). However, the increase in melt rate with iceberg draught is not linear. There is considerable variability in the melt rates of small icebergs (those with draughts less than 140 m). Since

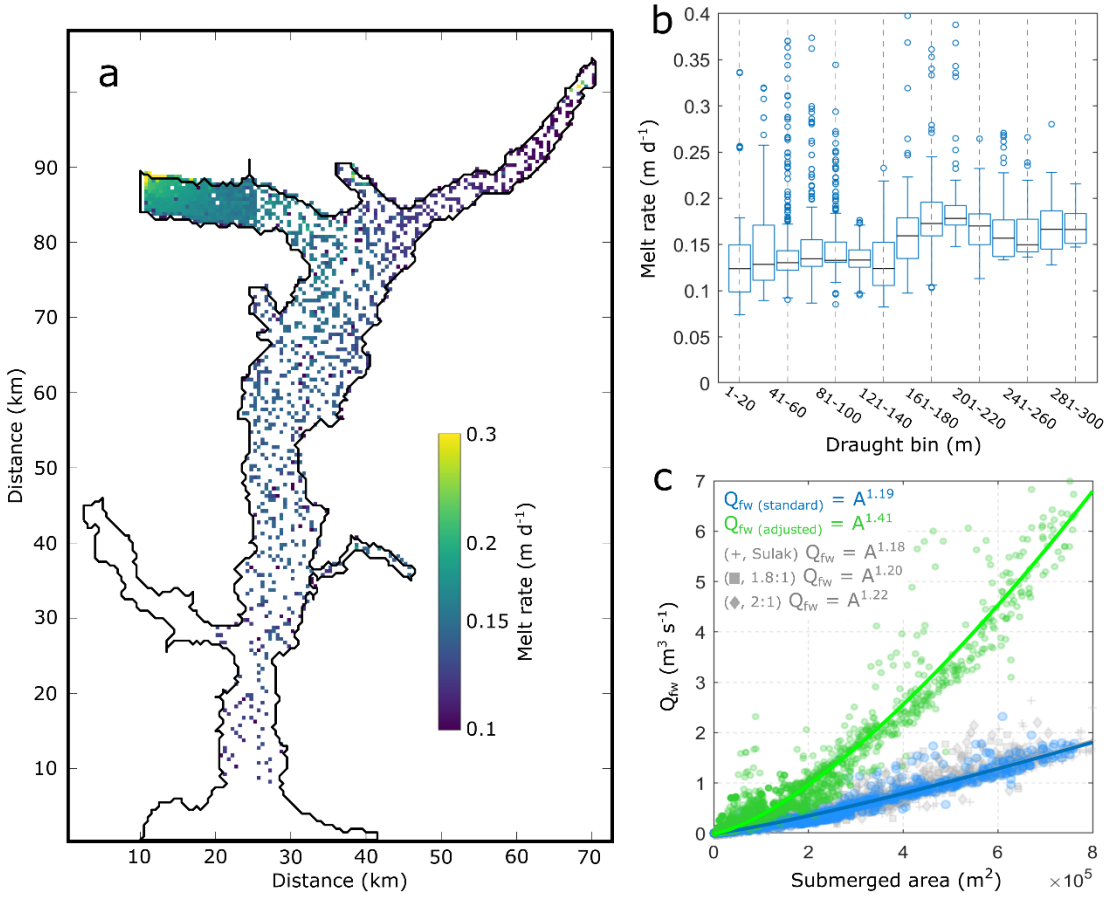

Figure 5.3. Relationship between iceberg geometry and melt rates in our summer runoff forcing scenario. (a) Vertically-averaged submarine iceberg melt rates (note log scale). (b) Box plots showing vertically-averaged submarine melt rates of individual icebergs compared to iceberg draught. Each plot shows the median value (black line), interquartile range (box) and all other data (whiskers) except outliers (circles), with outliers defined as data points more than 2.7 standard deviations from the median value. Vertical dashed grey lines in (b) are for visual aid. (c) Scatter plot of submerged iceberg area and freshwater flux (Q_{fw}) from individual icebergs, with power law fits (solid lines) and associated equations (where 'A' is the submerged iceberg surface area). The blue and green coloured circles in (c) correspond to simulations with the standard and adjusted melt rate parameter values respectively. The grey crosses, squares and diamonds in (c) correspond to simulations using the volume-area scaling of Sulak et al. (2017), and length to keel depth ratios of 1.8:1 and 2:1, respectively, all with the standard melt rate parameter values. Axis distances in (a) correspond to those in Figure 5.1a.

these comparatively small icebergs do not penetrate below the pycnocline, many of them reside in relatively cool near-surface waters and so melt more slowly. They only interact with relatively warm, fast flowing currents (and therefore melt more rapidly) where they are exposed to plume outflow in the vicinity of glacier fronts. In contrast, icebergs with

greater draughts are more consistently exposed (at least partially) to warmer waters at depth, and so generally melt faster and with less variability than small icebergs. In terms of melt rates, this results in two populations of icebergs: 'small' icebergs with generally lower, but highly spatially variable melt rates, and 'large' icebergs, with consistently higher melt rates (Figure 5.3b). The higher melt rates of deeply-draughted icebergs mean that the freshwater flux from individual icebergs increases slightly super-linearly with submerged iceberg surface area (assuming the same aspect ratio; Figure 5.3c; Figure S2.3), potentially providing a simple method to estimate iceberg freshwater flux from satellite-derived iceberg areas and volumes.

5.3.2 Impact on fjord properties and circulation

In our no-runoff forcing scenario, the freshwater flux released by submarine iceberg melting is capable of generating a weak circulation (Figure 5.4). This circulation is characterised by generally down-fjord currents between the fjord surface and ~180 m depth (0.01 m s^{-1} on average), with peak speeds of ~0.02 m s^{-1} at ~130 m, driven by the release of a freshwater flux from icebergs. This down-fjord current is underlain by a weaker (~0.006 m s^{-1}) but thicker up-fjord current, peaking at ~270 m and unidentifiable below ~500 m. This weak but broad up-fjord current compensates (in terms of volume) for the fjord water entrained in the relatively fresh and cold iceberg melt-driven outflow above (Figure 5.4c).

In the summer runoff forcing scenario, the iceberg melt-driven circulation and the runoff-driven circulation augment one another when their respective currents are aligned and compete when they are not (Figure 5.5). For example, some currents in the upper 180 m are slowed by 10-40% because icebergs act as a physical barrier to water flow and because in some places the iceberg melt-driven circulation opposes the stronger runoff-driven circulation (Figure 5.5a,b). (For example, shallow up-fjord currents, which can be formed in simulations where the plumes reach neutral buoyancy below the surface, are opposed by iceberg-melt-driven currents at the same depth). In contrast, in the mélange and near the fjord walls in the upper 180 m, the iceberg melt-driven circulation augments the runoff-driven circulation (Figure 5.5a,b). Throughout the fjord as a whole, up-fjord currents in the 190-500 m depth range are over 30% faster than the equivalent no-iceberg scenario (Figure 5.5c,d). It is worth noting that there are feedbacks here that are difficult to disentangle: the runoff-driven circulation itself increases submarine iceberg melt rates, leading to a stronger iceberg melt-driven circulation, which may in turn impede or

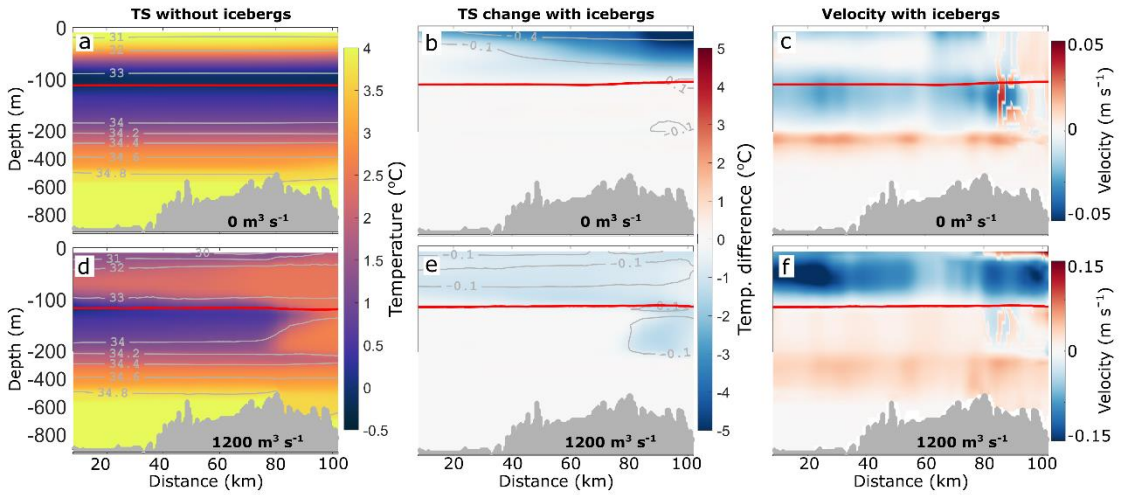

Figure 5.4. Along-fjord transects of water properties and circulation. Effect of submarine iceberg melting on fjord water properties and circulation using 'channelised' subglacial hydrology and (a-c) no runoff or (d-f) 1200 m^3 s^{-1} runoff. All panels show transects along the fjord centreline, with the ocean boundary on the left. Panels (a) and (d) show centreline temperature and salinity in the no-iceberg simulations. Panels (b) and (e) show the difference in centreline temperature and salinity in the corresponding iceberg simulations. Panels (c) and (f) show centreline current velocity in the corresponding iceberg simulations, with positive values indicating up-fjord currents. The red line in each panel denotes the 27.3 potential density contour, approximating the interface between Polar Water and Atlantic Water. Note the y-axis scale is stretched in the upper 200 m. x-axis distances correspond to those in Figure 5.1a.

augment the runoff-driven circulation depending on the respective directions of each circulatory regime. The overall effect of these modifications to the circulation is to reduce across-fjord heterogeneity in velocity and to increase fjord water export by ~10% in the summer runoff forcing scenario, compared to the equivalent no-iceberg simulation.

Submarine iceberg melting also causes marked changes in the temperature and salinity of the fjord. Without runoff, we simulate iceberg-induced cooling and freshening of up to 5°C and 0.7 psu throughout the upper ~100 m, though the changes are most pronounced near the fjord head and surface (Figure 5.4b). With the addition of runoff, the invigorated circulation results in more uniform iceberg-induced cooling of ~1°C and freshening of ~0.1 psu above the Atlantic Water-Polar Water interface (Figure 5.4e). These modifications produce along-fjord gradients in temperature and salinity in the upper ~100 m of the water column, with water properties migrating towards cooler and less saline conditions with increasing distance from the mouth, except where there is warm plume outflow (Figure 5.4). The freshening and cooling have compensating effects on the fjord

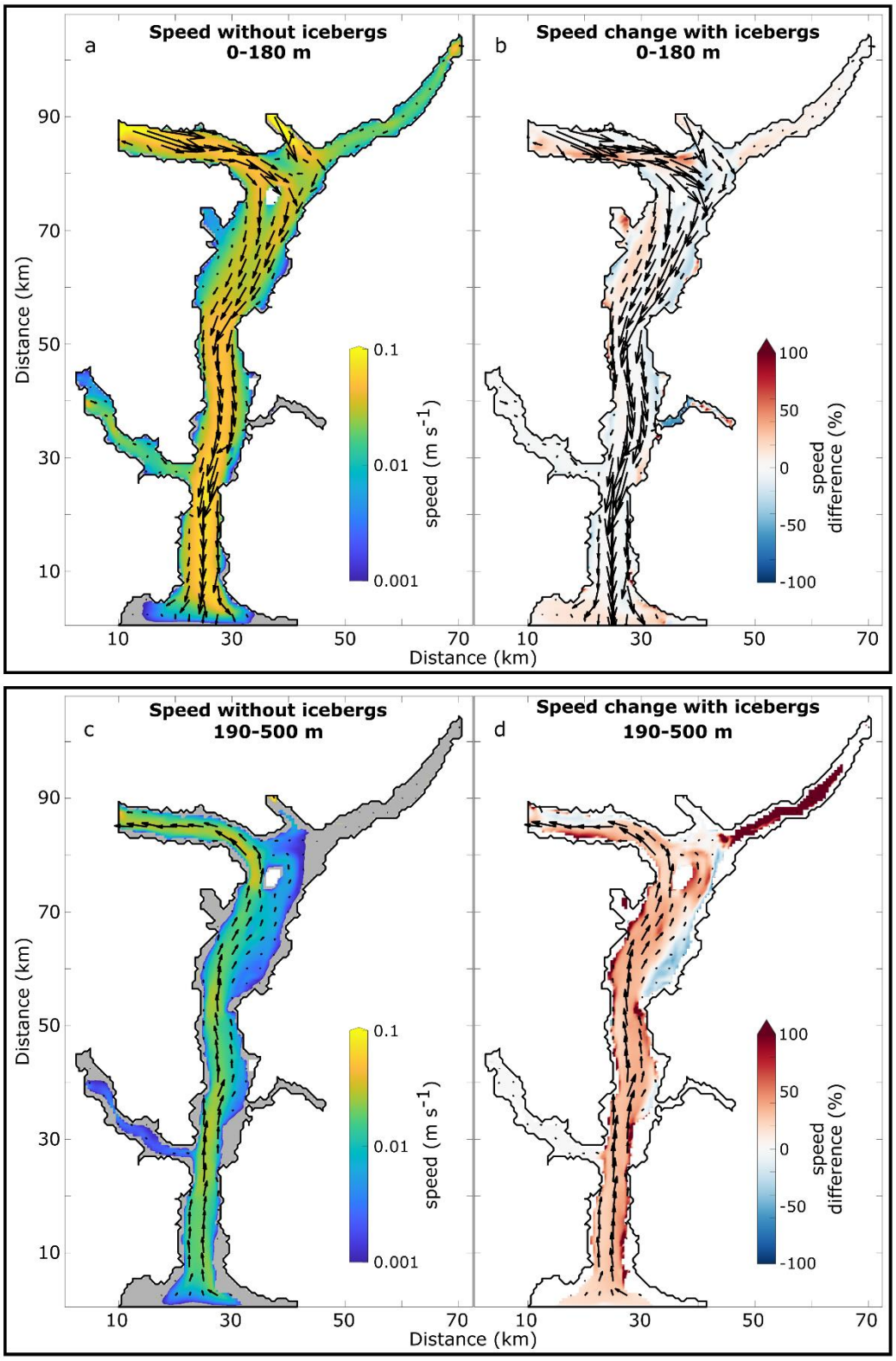

Figure 5.5. The effect of icebergs on fjord circulation in our summer runoff forcing scenario. (a) Average current speed between 0 and 180 m depth in the no-iceberg simulation. (b) Relative speed change in the summer runoff forcing scenario compared to the equivalent no-iceberg simulation between 0 and 180 m depth, with positive values indicating an increase in speed. (c and d) As for panels 'a' and 'b', but for the 190-500m depth band. The arrows indicate the current velocity in the respective simulations averaged over the indicated depths. In all plots, the ocean boundary is at the bottom. Axis distances correspond to those in Figure 5.1a.

water density. Thus, the net effect on density from iceberg melt is small (typically much less than 1% change in any location, compared to the no-iceberg scenario) and the resulting lateral density gradients within the fjord are weak.

5.3.3 Impact on oceanic heat flux

We find that the up-fjord oceanic heat flux across a flux gate placed within the ice mélange close to the fjord head increases with runoff raised to the power 0.11-0.52, with the exponent dependent on the spatial pattern of runoff efflux across each glacier's grounding line and melt rate parameter values (Figure 5.6a). The form of the relationship between runoff and up-fjord heat flux is similar in simulation suites with and without icebergs, indicating that the addition of icebergs in the model does not fundamentally modify the response of these fjords to runoff. In our 'distributed' drainage scenario, the volume transport across the flux gate increases because of more efficient entrainment of ambient waters into glacial plumes per unit volume of runoff (as in Cowton et al. (2016a)), due to the sub-linear relationship between entrainment of ambient waters into plumes and runoff (Carroll et al., 2015; Jenkins, 2011). This results in an increase in up-fjord oceanic heat flux by 45.5±23.3% compared to the 'channelised' scenario (with the precise value depending on runoff), and a larger exponent in the power law relationship between runoff and up-fjord oceanic heat flux (Figure 5.6a).

The effect of icebergs on up-fjord oceanic heat flux is complex. Excluding the no-runoff forcing scenario, the inclusion of icebergs results in an overall increase in up-fjord oceanic heat flux by 9.3±4.5% with the standard melt rate parameter values, but this increases to 38.4±10.8% with the adjusted values. This overall increase in up-fjord heat flux is most pronounced with low values of runoff and with 'channelised' hydrology (Figure 5.6a), when the iceberg melt-driven circulation is a relatively more important driver of fjord circulation. This depth-averaged effect, however, masks significant variation with depth (Figure 5.6b). We simulate a 44.9% reduction in up-fjord oceanic heat flux in the upper 20 m, but a 71.1% increase in up-fjord heat flux in the 30-500 m depth range in our summer runoff forcing scenario with the standard parameter values. This vertical pattern arises because of cooling and weakening of up-fjord surface currents found in the mélange (Figure 5.4f) and strengthening of up-fjord currents below (Figure 5.5c,d). In the no-runoff forcing simulations, the circulation is entirely driven by submarine iceberg melting, resulting in an overall >100% increase in up-fjord oceanic heat flux compared to corresponding no-iceberg simulations. We note that the magnitude

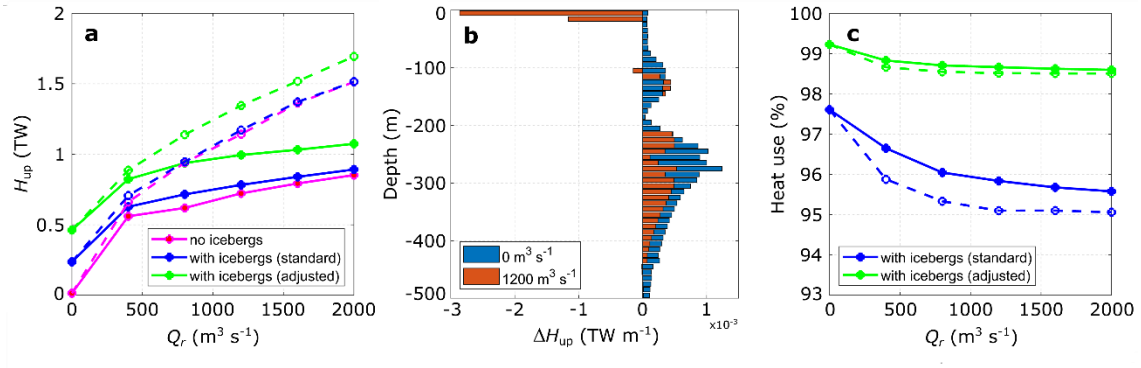

Figure 5.6. The effect of icebergs on along-fjord oceanic heat flux. (a) Relationship between runoff (Q_r) and up-fjord oceanic heat flux (H_{up}) across our flux gate (location in Figure 5.1a) in our no-iceberg scenario and in our iceberg scenarios with both the standard and adjusted melt rate parameter values. (b) Change in up-fjord heat flux (ΔH_{up}) due to icebergs (where a negative value indicates a decrease in heat flux with icebergs at that depth) for the no-runoff (blue) and summer runoff forcing (orange) scenarios. (c) The percentage of heat used for ice melt within the fjord accounted for by iceberg melting. In panels (a) and (c), the solid lines represent our 'channelised' drainage scenario and the dashed lines represent our 'distributed' drainage scenario.

of the net effect presented here will likely be sensitive to the location of our flux gate and to the boundary conditions used, and so we place more emphasis on the vertical pattern of up-fjord heat flux change.

5.4 Discussion

Domain-averaged submarine iceberg melt rates range from 0.09 to 0.57 m d^{-1} (Figure 5.2a), but melt rates in certain grid cells reach 1.34 m d^{-1}. Relatively few estimates of submarine iceberg melt rates and freshwater fluxes are available for comparison. Summertime submarine melt rate estimates for individual large icebergs in the Sermilik Fjord mélange of ~0.39±0.18 m d^{-1} and ~0.21±0.15 m d^{-1} (Enderlin et al., 2016; Enderlin & Hamilton, 2014), based on changes in iceberg freeboard, are similar to the upper-end of our estimates for deeply-draughted icebergs with the standard melt rate parameter values (Figure 5.3b). As a further point of comparison, Moon et al. (2017) found vertically-averaged melt rates of ~0.36±0.17 m d^{-1} for individual icebergs and local melt rates of up to ~1 m d^{-1}. Our modelled fjord-wide iceberg freshwater fluxes (400-930 m^3 s^{-1} or 1180-2830 m^3 s^{-1} with the adjusted parameter values) are comparable to previous estimates based on scaling up modelled (Moon et al., 2017) or inferred (Moyer et al.,

2019) melt rates for individual icebergs using observed iceberg size-frequency distributions. Therefore, although we expect our modelled melt rates to be somewhat conservative (due to excluding some melt processes), these comparisons give us confidence that our model is realistically capturing iceberg melting within the fjord. We note that modelled iceberg melt rates are sensitive to a range of uncertain or temporally variable parameter values, including currents driven by melt-driven convection (Figures S2.4 & S2.5), iceberg concentration (Figure S2.6), maximum iceberg draught (Figure S2.7) and iceberg aspect ratio (Figure S2.8), but emphasise that our simulated melt rates are in broad agreement with previous estimates, regardless of these parameter values.

We find that submarine iceberg melting causes substantial cooling and freshening of the upper 100-200 m of Sermilik Fjord (Figure 5.4b,e). The impact on water column temperature and salinity increases towards the fjord head, where iceberg concentrations are greatest, resulting in along-fjord gradients in temperature, salinity and density. A similar pattern of up-fjord cooling and freshening is also apparent in the available observations (Azetsu-Scott & Syvitski, 1999; Inall et al., 2014; Straneo et al., 2012; Sutherland et al., 2014a; Sutherland & Straneo, 2012). To facilitate comparison between our model output and these observations, we extracted temperature and salinity profiles along an across-fjord transect in the approximate position of an existing conductivity-temperature-depth transect (Straneo et al., 2010; Sutherland et al., 2014a, 2013; Sutherland & Straneo, 2012) in the middle part of the fjord (location in Figure 5.1a), which was obtained within two days of those used as boundary conditions in our simulations. Although we initiated and bounded our model with observations obtained at the fjord mouth, the inclusion of icebergs allows us to better reproduce key aspects of contemporaneous observations made over 60 km up-fjord than in simulations without icebergs (Figure 5.7). In particular, the agreement with the cooling observed in the upper ~100-200 m of the domain is greatly improved when icebergs are included, and especially when using the adjusted melt parameters (compare green and grey lines in Figure 5.7a).

Although this represents a significant improvement compared to the no-iceberg simulations, there are still differences between the observed and modelled water properties. In particular, the warm spike observed at ~180 m depth, which represents the modified Atlantic Water output (so-called ‘glacially-modified waters’) from the main plume at Helheim Glacier, occurs instead at ~100 m in the iceberg simulations and is cooler than is observed. These differences are perhaps due to the entrainment of additional

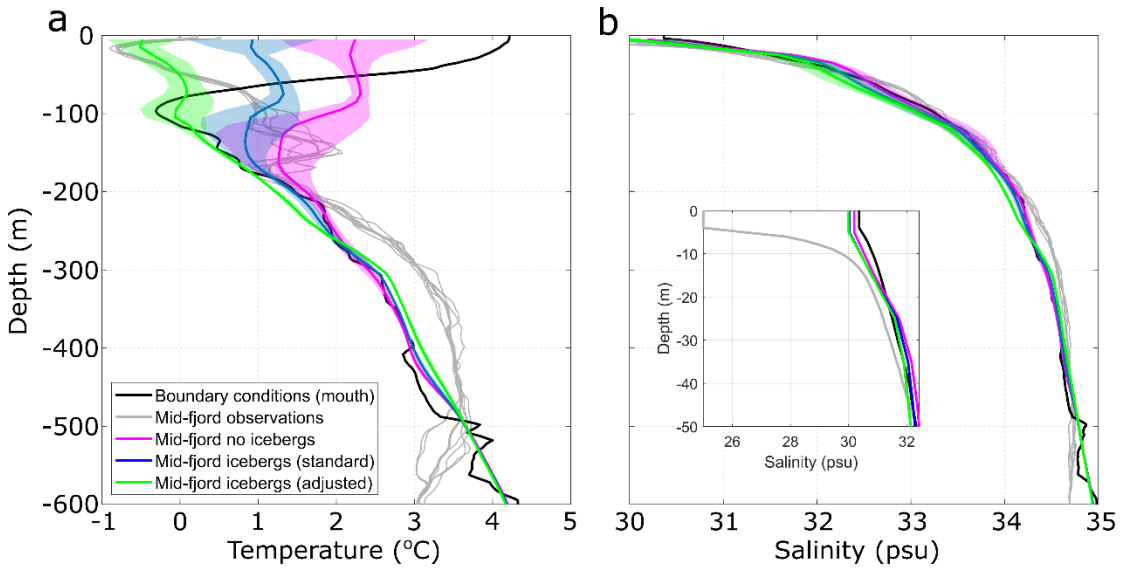

Figure 5.7. Comparison of modelled and observed water properties. The magenta lines show modelled temperature and salinity in simulations without icebergs, whilst the blue and green lines show simulations with icebergs using the standard and adjusted melt rate parameter values, respectively. The black line shows the average of conductivity-temperature-depth casts at the fjord mouth used as model boundary conditions (locations in Figure 5.1a). The grey lines are from casts obtained approximately midway along the fjord (locations in Figure 5.1a) roughly contemporaneously to those at the mouth. Modelled mid-fjord profiles were extracted in approximately the same locations as the mid-fjord casts. Blue and red shading indicates the standard deviation between simulations with both 'channelised' and 'distributed' drainage configuration scenarios and with runoff varying from 400-2000 m^3 s^{-1}, which encompasses the estimated runoff into each fjord (~1000 m^3 s^{-1}) at the time the observations were obtained, based on RACMO2.3 modelled runoff. Inset in (b) shows salinity (without shading) in the upper 50 m.

freshwater from iceberg melting or deflection of plume outflow by the icebergs. In addition, there are a number of relevant parameter values and aspects of the model setup that are poorly constrained by observations; for example, glacier grounding line depth, the rate of entrainment of ambient waters by runoff-driven plumes, the partitioning of runoff along the grounding line, the plume parameterisation used (Jackson et al., 2017) and the effect of suspended sediment on plume dynamics all affect the depth and temperature of the glacially-modified waters. Nevertheless, the addition of icebergs represents a marked increase in model realism and substantially improves our ability to model along-fjord changes in water properties compared to previous comparable studies

(Cowton et al., 2016a; Fraser & Inall, 2018) and to our no-iceberg simulations (magenta line in Figure 5.7).

The freshwater released from icebergs sets up an iceberg melt-driven circulation that is similar to the circulation driven by runoff at the head of glacial fjords. The latter — which for clarity we refer to as the 'runoff-driven circulation' rather than the commonly used 'buoyancy-driven circulation' — has received considerable attention in recent years (Cowton et al., 2015, 2016a; Inall et al., 2014; Straneo et al., 2010, 2011). The velocity structure of the iceberg melt-driven circulation simulated here is distinct from that of the runoff-driven circulation in several key aspects. Firstly, across-fjord heterogeneity in the velocity structure is diminished compared to the runoff-driven circulation (Figure 5.5). Secondly, the fastest down-fjord currents in the runoff-driven circulation are generally simulated close to the head of the fjord (i.e. near the source of buoyancy), whereas in the iceberg melt-driven circulation, the fastest down-fjord currents were generally located much further down-fjord, due to lateral constrictions focusing the flow (Figure 5.5). This pattern will, however, likely be sensitive to fjord geometry and bathymetry. Finally, the iceberg melt-driven circulation contains down-fjord currents at slightly greater depths (100-130 m) than the runoff-driven circulation due to some iceberg meltwaters reaching neutral buoyancy deeper in the water column than runoff-driven plumes. The latter pattern is also implied by inferred submarine meltwater distributions obtained from tracer studies in Sermilik Fjord (Beaird et al., 2018).

Our results suggest that iceberg melt-driven circulation is an important and overlooked driver of fjord circulation, increasing the volume of water exported from the fjord by ~10% in our summer runoff forcing scenario, and can be the dominant driver of fjord circulation when runoff is low. The relative importance of the iceberg melt-driven circulation compared to the runoff-driven circulation during summer will depend on the relative volumes of freshwater derived from icebergs and runoff. For example, in fjords with high rates of iceberg production but comparably low runoff, the iceberg melt-driven circulation may be a key driver of fjord circulation during summer. Similarly, during winter, when runoff is at a minimum, the iceberg melt-driven circulation should act to drive a weak (relative to the runoff-driven circulation) but steady circulation, which may be interrupted by stronger intermediary currents during barrier wind events (Fraser & Inall, 2018; Jackson et al., 2014). Since our modelling suggests that iceberg freshwater flux scales with submerged iceberg surface area at both the individual iceberg-scale and

the fjord-scale (Figure 5.3c; Figures S2.3 & S2.6), as well as with maximum iceberg draught and runoff (Figure 5.2b; Figure S2.7), the iceberg-driven circulation should be a relatively more important driver of fjord circulation in fjords with deeper and more extensive iceberg cover (and greater iceberg melt rates).

Furthermore, our results demonstrate that submarine iceberg melting has important implications for oceanic heat flux towards tidewater glaciers. In simulations with runoff, we simulate an overall ~10 to 40% increase in up-fjord oceanic heat flux across a flux gate located near Helheim Glacier (flux gate location in Figure 5.1a), compared to identical simulations without icebergs (Figure 5.6a). Two competing changes to the temperature and velocity structure of the fjords produced these overall changes. The up-fjord volume flux of Atlantic Water increased, thereby increasing the up-fjord heat flux over a broad depth range below ~20 m (Figure 5.6b). In contrast, cooling and weakening of up-fjord currents in the upper 20 m caused a reduction in up-fjord heat flux at these depths. The increased up-fjord heat flux below ~20 m implies greater submarine melt-driven undercutting of Helheim Glacier, which can lead to greater iceberg calving rates (Benn et al., 2017; O'Leary & Christoffersen, 2013). This result was robust to changes in iceberg size-frequency distribution (Table S2.2) and to wide ranges of iceberg cover (Figure S2.6) and maximum iceberg draught (Figure S2.7), with depth-averaged up-fjord heat flux generally increasing above the no-iceberg scenario as either iceberg cover or maximum iceberg draught increase. This suggests that these results may be applicable to many of Greenland's fjords, with the precise impact of icebergs on up-fjord heat flux varying between fjords due to variations in iceberg concentration and keel depth. In addition, these results hint at a potential positive feedback between iceberg production and up-fjord oceanic heat flux, in which greater iceberg production (and therefore freshwater flux) invigorates fjord circulation, leading to an increase in up-fjord oceanic heat flux and therefore calving.

Submarine iceberg melting potentially provides a considerable heat sink in some glacial fjords, but this is difficult to quantify with field-based observations (Inall et al., 2014; Jackson & Straneo, 2016). Our modelling suggests that submarine iceberg melting is indeed a large heat sink in Sermilik Fjord, using over 95% of the oceanic heat used for ice melt in our simulations (Figure 5.6c). Iceberg melting remained the dominant heat sink under all runoff and drainage scenarios and regardless of iceberg draught, aspect ratio or concentration (Figure S2.9). It is important to emphasise that the heat lost in our

simulations is not intended as an accurate representation of the heat budget of Sermilik Fjord because we do not include certain processes (such as atmosphere-ocean interactions, sea ice formation and refreezing, and tidal mixing) that are necessary for calculating the full fjord heat budget (Jackson & Straneo, 2016). Our modelling does, however, suggest the heat used for submarine iceberg melting is over ten times greater than that used for melting of glacier termini in iceberg-congested fjords like Sermilik Fjord. Whilst we expect that there is considerable uncertainty in this comparison due to, for example, underestimating glacier terminus melt rates in areas distal to runoff plumes (Jackson et al., 2020; Sutherland et al., 2019), these results imply that submarine iceberg melting comprises a key component of the fjord heat budget in (at least) iceberg-congested fjords.

Previous field-based investigations have found that the seasonally warm surface layer in glacial fjords has the potential to transport large quantities of oceanic heat towards tidewater glaciers, and causes the majority of the glacial ice-melt (Beaird et al., 2015; Cowton et al., 2016a; Inall et al., 2014; Jackson & Straneo, 2016). Inall et al. (2014) noted that the equivalent terminus melt rates would be unrealistically high if all the observed heat loss in Kangerdlugssuaq Fjord was used for terminus melting, leading them to suggest that much of the near-surface ocean heat was likely used to melt icebergs. This interpretation is supported by the results from our model analysis. By implication, further warming of this layer will expedite iceberg and mélange deterioration, which has in turn been associated with tidewater glacier calving and retreat (Bevan et al., 2019; Xie et al., 2019).

Several studies have linked either increases in oceanic heat availability (Holland et al., 2008; Rignot et al., 2012) or increases in up-fjord oceanic heat flux (Cowton et al., 2016a) to tidewater glacier retreat. More recently, estimates of ocean thermal forcing during the 21st century have been used to drive parameterisations of glacier retreat as part of the ISMIP6 project (Slater et al., 2019). Due to the ice-sheet wide nature and long timescale of this exercise, together with a lack of simple parameterisations for the modification of water masses during fjord transit, the ocean thermal forcing used was based on spatial averages of far-field ocean conditions (Slater et al., 2020). We show here that submarine iceberg melting can reduce ocean thermal forcing near the surface, but increase it below, resulting in substantial (~10%) changes in the depth-averaged oceanic heat flux towards tidewater glaciers, with potential implications for glacier submarine melt rates and retreat.

Furthermore, our results suggest that a uniform correction applied to ocean conditions at the mouth may not produce an appropriate representation of oceanic heat flux towards tidewater glacier termini because the effect of submarine iceberg melting on up-fjord oceanic heat flux depends on runoff (Figure 5.6), as well as on iceberg draught and concentration (Figures S2.6 & S2.7), which can vary independently from runoff. Therefore, future studies seeking to examine interactions between the Greenland Ice Sheet and the ocean, over any temporal and spatial scale, should account for iceberg-ocean interactions, particularly when estimating ocean thermal forcing of tidewater glaciers.

Chapter 6 - Characterising the effect of submarine iceberg melting on glacier-adjacent water properties

In the previous chapter, the effects of submarine iceberg melting on fjord water properties and circulation were quantified for a single, large fjord. In this chapter, the focus shifts to an idealised fjord, in order to characterise the effect of icebergs on glacier-adjacent water properties more generally. This is crucially important for two reasons. First, water properties at the ice-ocean interface will control glacier submarine melting, which is thought to be a crucial driver of glacier retreat. Secondly, iceberg dimensions and distribution vary substantially between Greenland's fjords and through time, potentially changing fjord water properties. The results in this chapter show that icebergs can cause cooling in the uppermost part of the water column and warming at mid-depth, with the degree of modification sensitive to iceberg size and distribution. These changes in glacier-adjacent water temperature can theoretically cause non-negligible (> 10%) changes in glacier submarine melt rates, which may affect calving rate and style.

Abstract

The rate of ocean-driven retreat of Greenland's tidewater glaciers remains highly uncertain in predictions of future sea level rise, in part due to poorly constrained glacier-adjacent water properties. Icebergs and their meltwater contributions are likely important modifiers of fjord water properties, yet their effect is poorly understood. Here, we use a 3-D ocean circulation model, coupled to a submarine iceberg melt module, to investigate the effect of submarine iceberg melting on glacier-adjacent water properties in a range of idealised settings. Submarine iceberg melting can modify glacier-adjacent water properties in three principle ways: (1) substantial cooling and modest freshening in the upper ~50 m of the water column; (2) warming of Polar Water at intermediate depths due to iceberg melt-induced upwelling of warm Atlantic Water, and; (3) warming of the deeper Atlantic Water layer when vertical temperature gradients through this layer are steep (due to vertical mixing of warm water at depth), but cooling of the Atlantic Water layer when vertical temperature gradients are shallow. The overall effect of iceberg melt is to make glacier-adjacent water properties more uniform with depth. When icebergs extend to, or below, the depth of a sill at the fjord mouth, they can cause cooling throughout the entire water column. All of these effects are more pronounced in fjords with higher iceberg concentrations and deeper iceberg keel depths. These iceberg melt-induced changes to glacier-adjacent water properties will reduce rates of glacier submarine melting near the surface, but increase them in the Polar Water layer, and cause typically modest impacts in the AW layer. These results characterise the important role of submarine iceberg melting icebergs in modifying ice sheet-ocean interaction, and highlight the need to improve representations of fjord processes in ice sheet-scale models.

6.1 Introduction

Predicting the rates of ocean-driven retreat of Greenland's tidewater glaciers remains one of the largest uncertainties in estimating future sea level rise (Meredith et al., 2020; Edwards et al., 2021). This uncertainty is partly due to limited constraints on the ocean-driven thermal forcing of tidewater glacier calving fronts, which reflects in part the difficulty in obtaining hydrographic observations in the proximity of tidewater glacier termini (Jackson et al., 2017, 2020; Sutherland et al., 2019). The few observations of water properties in the inner part of glacial fjords demonstrate that there are typically substantial differences between glacier-adjacent water properties and those near the fjord

mouth (e.g. Straneo et al., 2011; Inall et al., 2014; Jakobsson et al., 2020), indicating that substantial modification of water temperature and salinity can occur within glacial fjords. Due to the relatively small number of observations and insufficient model constraints on glacier-adjacent water properties, ice sheet models used to simulate glacier retreat must be forced with far-field (i.e. acquired on and beyond the continental shelf) ocean boundary conditions that do not include fjord-scale influences (e.g. Slater et al., 2019, 2020; Goelzer et al., 2020), thereby introducing uncertainty into the resulting projections of ice sheet mass loss.

Glacier-adjacent water properties can differ from those near the fjord mouth for several reasons. Meltwater runoff enters the fjord at depth where tidewater glaciers meet the ocean ('subglacial discharge'). In Greenland's fjords, warm water of Atlantic origin (Atlantic Water, AW) is generally found at depth whilst colder, fresher water of Polar origin (Polar Water, PW) is found at intermediate depths (e.g. Straneo and Heimbach, 2013; Sutherland and Pickart, 2008). The cold, fresh subglacial discharge is buoyant when it enters the fjord, so rises as a turbulent plume (Jenkins, 2011). As it rises, it entrains fjord water, which mixes with the subglacial discharge as it ascends towards the fjord surface (e.g. Beaird et al., 2018). In this way, subglacial discharge-driven plumes act as mixing engines at the head of glacial fjords. Due to the temperature stratification in Greenland's fjords, plumes at deeply-grounded glaciers (i.e. deeper than the PW-AW interface) often draw the relatively warm AW towards the fjord surface, thereby warming surface and near-surface waters (e.g. Straneo et al., 2010, 2011; Carroll et al., 2016). In contrast, plumes at shallowly-grounded glaciers can cause cooling at and near the fjord surface, as cold subglacial discharge and entrained PW is upwelled into surface layers that are seasonally warmed by solar radiation (e.g. Carroll et al., 2016). Models that include glacial plumes are able to reproduce these effects convincingly (Cowton et al., 2015; Carroll et al., 2016; Jackson et al., 2017). However, there remain substantial differences between modelled water properties and those that are observed adjacent to tidewater glaciers (e.g. Cowton et al., 2015; Frazer and Inall, 2018; Davison et al., 2020).

Several recent studies have identified icebergs as a substantial freshwater source in some of Greenland's fjords, with iceberg freshwater volumes comparable to or greater than ice sheet runoff (Jackson and Straneo, 2016; Enderlin et al., 2016, 2018; Moon et al., 2017; Moyer et al., 2019; Rezvanbebahani et al., 2020). Furthermore, modelling of one of these fjords suggests that including the heat and salt fluxes associated with submarine iceberg

melting increases greatly the model's ability to reproduce observed glacier-adjacent water properties (Davison et al., 2020). However, iceberg concentration, keel depth, and size-frequency distribution likely vary hugely between fjords as well as over time, though observations of icebergs at the fjord scale are sparse (Enderlin et al., 2016; Sulak et al., 2017; Moyer et al., 2019; Rezvanbebahani et al., 2020). As such, it is likely that the effect of icebergs on glacier-adjacent water properties will also vary both spatially (i.e. between fjords) and temporally. This variability likely results in different thermal forcing of tidewater glaciers for a given set of far-field ocean conditions. Constraining the effect of icebergs on glacier-adjacent water properties, and thus glacier submarine melt rates, is therefore a necessary step in order to improve projections of ice sheet mass loss.

Here, we use an ocean circulation model in a series of idealised fjord-scale simulations to examine how icebergs affect glacier-adjacent water properties across a range of Greenland-relevant scenarios. We first consider how iceberg concentration, keel depth and size-frequency distribution individually affect glacier-adjacent water properties. We then consider a range of representative iceberg and ocean scenarios, to examine how these parameters interact to determine water properties in the critical region adjacent to tidewater glacier termini. Greenland's fjords are complex and varied in their geometry, ranging from short, narrow inlets to those that are long and wide, each with varying sinuosity and bathymetry, and often with several tributaries and sills of varying depth along their length. It would be impractical to attempt to characterise all of these systems. Therefore, we focus here on two simple fjord geometries: one with no sills, and another with a single entrance sill of constant depth, which we expect to be of particular importance for iceberg-ocean interaction given the capacity of sills to concentrate fjord-shelf water exchange near the surface where icebergs are concentrated.

6.2 Methods

6.2.1 Model domain

We use the Massachusetts Institute of Technology general circulation model (MITgcm) in its non-hydrostatic configuration (Marshall et al., 1997a, 1997b) to model submarine ice melting and circulation in an idealised fjord 50 km in length and 5 km in width. In most simulations, the domain is uniformly 500 m deep. However, in some simulations, we include a sill which limits the overlying water depth to 100 m (uniform across the entire width of the fjord, and approximately 5 km wide in the along-fjord direction, with

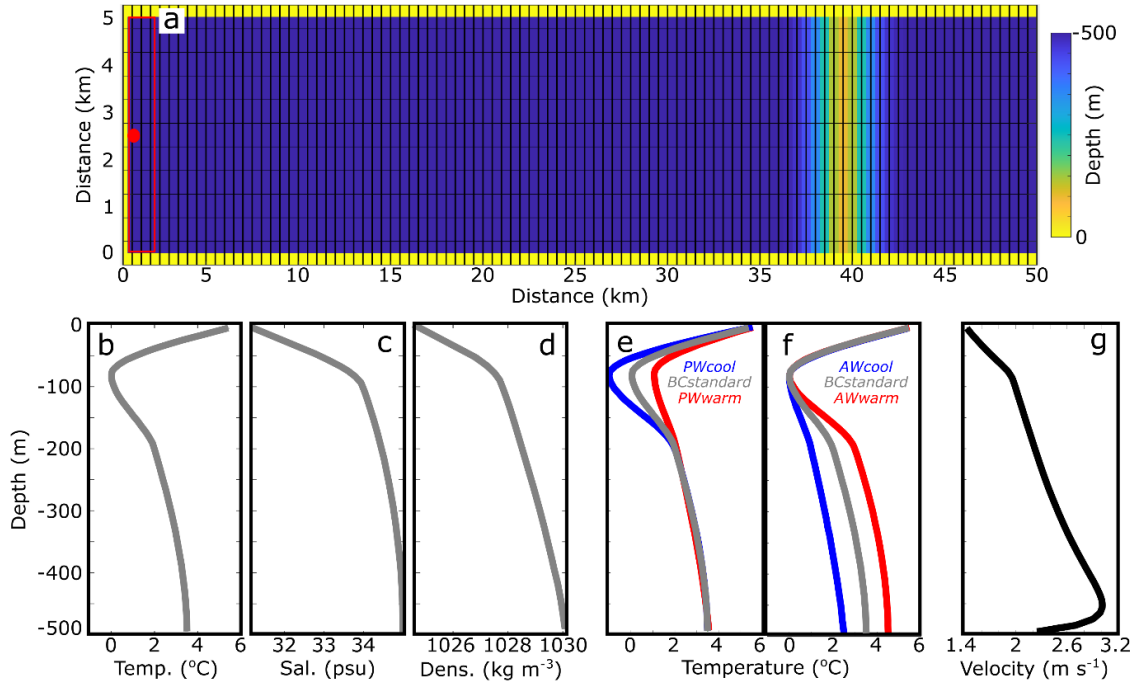

Figure 6.1. Model domain and boundary conditions.. (a) Plan-view of model bathymetry with sill, with the ice wall at the left end of the domain (0 km) and the open boundary on the right. Hatching indicates model resolution (note that grid cells are 500 m x 500 m in the horizontal). The red dot marks the location of subglacial discharge injection and the red box indicates the region from which steady-state glacier-adjacent water properties were extracted. In simulations without a sill, the domain is uniformly 500 m deep. Vertical profiles of (b) temperature, (c) salinity and (d) density with *BCstandard*. (e) Temperature profiles with varying PW temperature. (f) Temperature profiles with varying AW temperature. (g) Example plume vertical velocity from the simulation with iceberg scenario five, 500 m^3 s^{-1} runoff and *BCstandard* boundary conditions.

a Gaussian profile), centred 10 km from the open boundary (Figure 6.1a). Model resolution is uniformly 500 m horizontally and 10 m vertically. The fjord sides are closed boundaries, while at the open ocean boundary we impose a 5 km sponge layer, in which conditions are relaxed towards those imposed at the boundary (e.g. Sciascia et al., 2013; Slater et al., 2015; Cowton et al., 2016). The glacier-end of the domain is closed and consists of a virtual ice wall 5 km wide and 500 m high. In simulations incorporating runoff, this is input at a rate of 500 m^3 s^{-1}, a value typical of many of Greenland's tidewater glaciers (Mankoff et al., 2020), at the centre of the base of the ice wall (Figure 6.1a). The velocity of the runoff-driven plume (e.g. Figure 6.1g) and the melting of the ice wall were calculated using the 'IcePlume' package (Cowton et al., 2015). In common with several

previous studies (e.g. Xu et al., 2013; Kimura et al., 2014; Slater et al., 2015), we implement a free slip condition on the fjord walls and ice front.

6.2.2 Initial and open boundary conditions

We use idealised representations of temperature and salinity profiles commonly observed at the mouth of Greenland's south-eastern fjords during late-summer as initial and open boundary conditions (e.g. Sutherland et al., 2014). In our standard setup, this idealised profile is a cubic interpolation between 6°C and 31 psu at the fjord surface, 0°C and 34 psu at 100 m depth, 2°C at 200 m and 3.5°C at 500 m depth, where salinity is greatest at 35 psu (Figure 6.1b-d). In this way, the upper several tens of metres represent waters that are seasonally warmed by solar insolation, whilst the relatively cold intermediate layer, centred 100 m below the fjord surface, represents the PW layer, which is underlain by warmer, more saline water representing the AW layer. Henceforth, we refer to this set of boundary conditions as *BCstandard*. In separate simulations, we use temperature minima at 100 m of -1°C (*PWcool*) and 1°C (*PWwarm*) and temperature maxima at 500 m of 2.5°C (*AWcool*) and 4.5°C (*AWwarm*) (Figure 6.1e,f). Changing the temperature of the AW and PW layers causes corresponding changes in the vertical temperature gradient (Figure 6.1e,f), the effects of which are discussed in Section 3.2. Boundary conditions were kept constant throughout each simulation.

6.2.3 Iceberg-ocean interaction

Submarine iceberg melting is simulated using the 'IceBerg' package within MITgcm (Davison et al., 2020), with an ice temperature of -10°C (Sutherland et al., 2012; Sciascia et al., 2013; Inall et al., 2014; Luthi et al., 2017). This package uses the velocity-dependent three-equation melt rate parameterisation (Holland and Jenkins, 1999; Xu et al., 2012), with standard parameter values (e.g. Cowton et al., 2015; Jackson et al., 2020; Davison et al., 2020) for the drag coefficient (0.0025), and thermal and salt turbulent transfer coefficients (0.022 and 0.00062, respectively). The icebergs are rectangular in plan-view and have flat, vertical sides. All icebergs have length, l, to width ratios of 1.62:1 (Dowdeswell et al., 1992), and iceberg keel depth, d, is related to iceberg length through, $d=2.91l^{071}$ (Barker et al., 2004).

In Section 3.1, we consider a range of iceberg concentrations, maximum keel depths and size-frequency distributions, whilst using only the *BCstandard* boundary conditions. In all setups, iceberg concentration is uniform across the fjord and decreases linearly from a

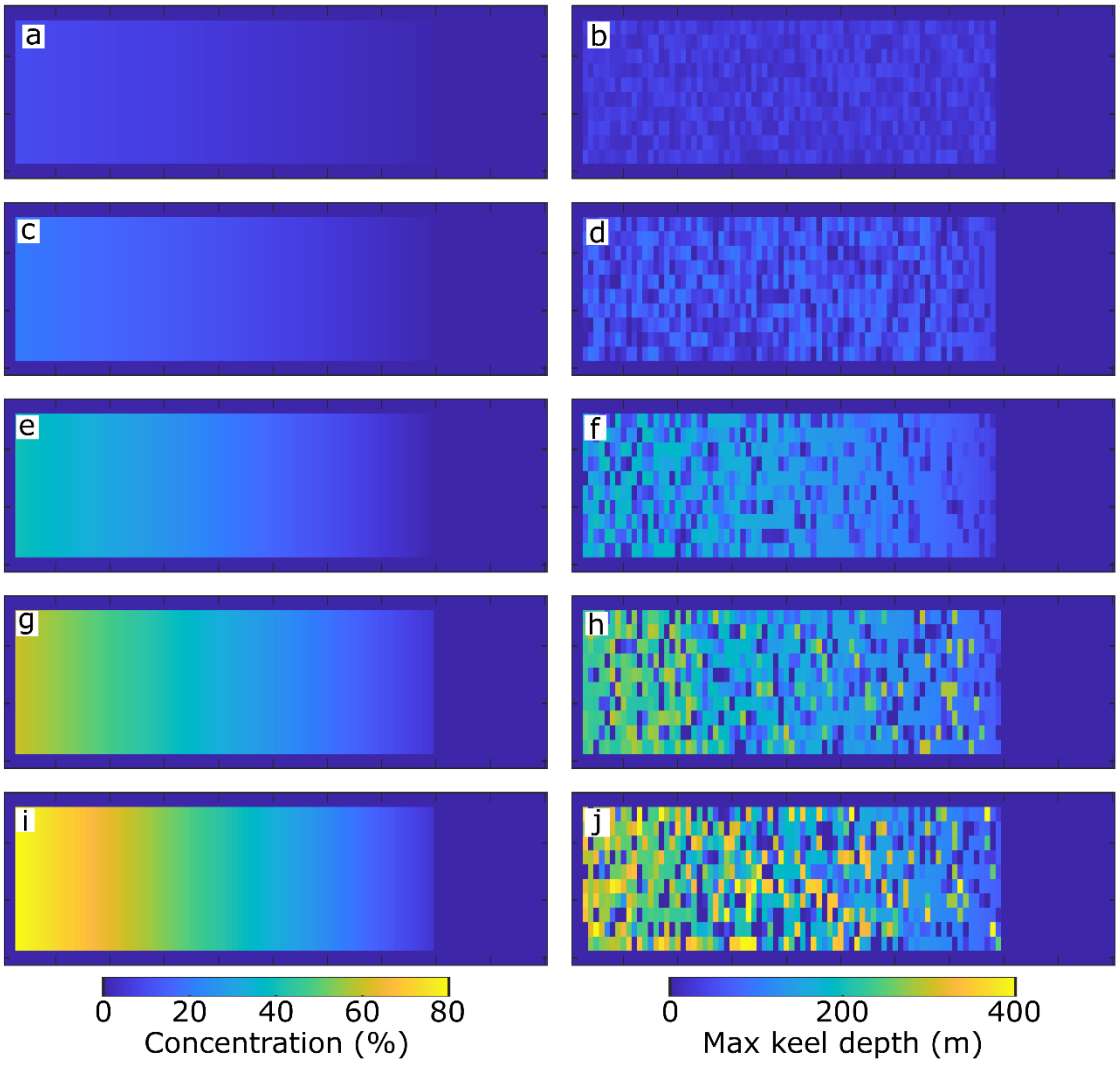

Figure 6.2. Iceberg concentration and keel depth. Iceberg concentration (left column) and maximum iceberg keel depth (right column) for iceberg scenarios one to five (top to bottom). All panels show the domain in plan-view, and are 50 km long and 5 km across.

maximum adjacent to the virtual ice wall to a minimum 10 km from the open boundary. In Section 3.1, iceberg concentration (defined as the percentage of the fjord surface in plan-view occupied by icebergs), is 80% adjacent to the ice wall and decreases to 5% in our *c1*, experiment, and is reduced to 75, 50 and 25% of these values in our *c0.75*, *c0.5*, and *c0.25* experiments, respectively. Regardless of concentration, we use a maximum iceberg keel depth of 300 m and the size-frequency distribution of the icebergs is described using a power law with an exponent of -2, which is similar to that observed in Sermilik Fjord (Sulak et al., 2017). In separate simulations, we assign maximum iceberg keel depths of 50 m, 150 m, 250 m, 350 m and 450 m, whilst maintaining the *c1*

Table 6.2. Details of each iceberg scenario.

Iceberg scenario	Max. draught (m)	Exponent	Concentration [max,min] (%)	Surface area (km²)
Scenario 1	50	1.6	[10,1]	44.5
Scenario 2	100	1.7	[20,1]	76.5
Scenario 3	200	1.8	[40,1]	141
Scenario 4	300	1.9	[60,5]	235
Scenario 5	400	2.1	[80,5]	316

concentration and the -2 power law exponent. We then vary the size-frequency distribution power law exponent from -1.6 to -2.1 in increments of 0.1 (covering the range observed to date in Greenland's fjords (Sulak et al., 2017; Rezvanbebahani et al., 2020)), whilst retaining the *c1* concentration and the 300 m maximum keel depth.

In Sections 3.2 onwards, we consider five realistic combinations of iceberg concentration, maximum iceberg keel depth and power law exponent, in order to approximate the range of iceberg geometries and distributions found in Greenland's fjords (Figure 6.2). These iceberg setups range from those representing a fjord hosting few and small icebergs, such as Kangerlussuup Sermia Fjord (Sulak et al., 2017) (scenario one), to those representing an iceberg-congested fjord, such as Sermilik Fjord (scenario five) (Figure 6.2; Table 6.1).

6.3 Results

6.3.1 The effect of iceberg concentration, keel depth and size-frequency distribution on glacier-adjacent water properties

The effect of iceberg melt on glacier-adjacent water properties depends on iceberg geometry, iceberg concentration and iceberg size-frequency distribution (Figure 6.3), as well as on the presence or absence of subglacial discharge. In the absence of subglacial discharge, icebergs modify glacier-adjacent water properties (here defined as the average properties of the water within 2 km of the ice wall; Figure 6.1a) in two main ways. Firstly, they cause substantial (6-7.5°C) cooling in the upper ~60 m of the water column, relative to the initial conditions (Figure 6.3a-c). The amount of cooling in this near-surface layer depends somewhat on iceberg concentration, with steady-state water temperature varying between ~-1.5°C and ~0°C over the range of iceberg concentrations considered, but is otherwise relatively insensitive to changing iceberg geometry and distribution (Figure 6.3a-c). Secondly, warming of up to ~1°C occurs below ~80 m because iceberg melting

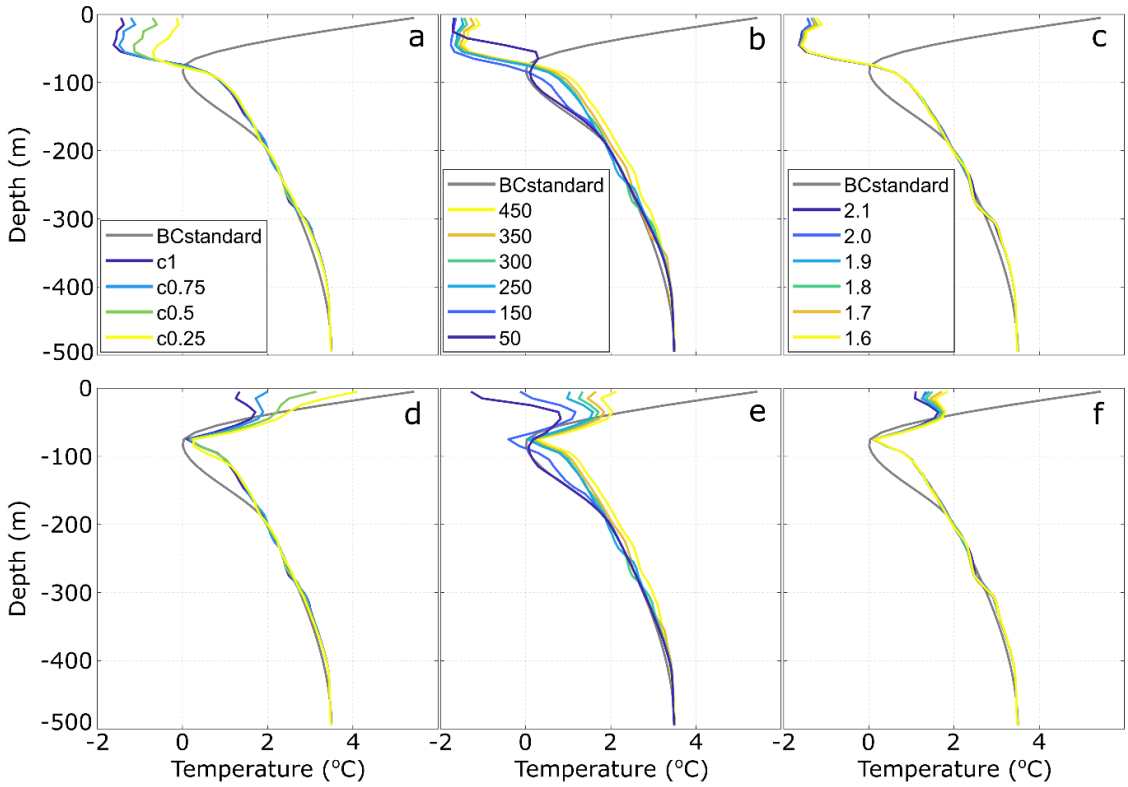

Figure 6.3. Glacier-adjacent water temperature vs iceberg geometry and distribution. Effect of iceberg concentration (a & d), maximum iceberg draught (b & e) and exponent describing the size-frequency distribution (c & f). Panels (a-c) are for simulations without runoff, whilst panels (d-f) are for simulations with 500 m^3 s^{-1} runoff.

causes localised freshening at depth. The resulting iceberg melt-modified water (i.e. the mixture of iceberg freshwater and ambient water at depth) is less dense than the surrounding water and rises buoyantly towards the fjord surface. The vertical extent and magnitude of the resulting warming generally increase with maximum iceberg keel depth (Figure 6.3b), because icebergs with deeper keels cause upwelling of deeper AW (which in this case is also warmer (Figure 6.1b)). This warming effect does not extend to the fjord surface, because the stronger stratification near the surface limits upwelling and because iceberg-ocean contact areas are much greater near the surface, so cooling due to localised iceberg melting dominates. When subglacial discharge is included, the effect of iceberg melt on glacier-adjacent water properties at depth (below 60 m) is similar to that in simulations without subglacial discharge, but glacier-adjacent water temperatures in the upper ~60 m of the water column display a greater range and the cooling of the near-surface waters is considerably reduced (Figure 6.3d-f). This is because the runoff causes

strong upwelling of AW towards the fjord surface and increases rates of fjord-shelf exchange, which counters some of the iceberg-induced cooling of near-surface waters.

6.3.2 Combining iceberg scenarios and ocean conditions

In reality, changes in iceberg concentration, keel depth and size-frequency distribution do not occur in isolation and there are characteristic relationships between those iceberg descriptors (Sulak et al., 2017). Fjords hosting large glaciers, such as Sermilik Fjord and Helheim Glacier in east Greenland, tend to contain both high iceberg concentrations and large, deeply-draughted icebergs, whilst those with lower iceberg concentrations, such as Kangerlussuup Sermia Fjord, also tend to contain smaller icebergs. To better represent the range of iceberg conditions found in Greenland's fjords, we consider five iceberg 'scenarios' (Figure 6.2; Table 6.1), ranging from a fjord with low iceberg concentration, shallow iceberg keels and fairly uniform iceberg sizes (iceberg scenario one), to a fjord with high iceberg concentration, deep iceberg keels and a large range of iceberg sizes (iceberg scenario five). For each of these scenarios, we examine steady-state glacier-adjacent water temperature for a range of ocean boundary conditions, and with and without a shallow (100 m) sill. We therefore consider three different PW and AW temperatures in turn (Figure 6.1e,f), and examine the resulting glacier-adjacent water properties for each of the five iceberg scenarios. To isolate the effect of iceberg melting from other processes, we compare each of the above simulations to identical simulations without icebergs.

6.3.2.1 Changing Polar Water temperature

Figure 6.4 shows steady-state glacier-adjacent water properties for the range of iceberg scenarios and PW temperatures considered. In all iceberg scenarios, there is substantial (~2°C or more) cooling in the upper ~60 m, with greater cooling in scenarios with higher iceberg concentrations. Other than this near-surface cooling, glacier-adjacent water properties are very similar to open ocean conditions in iceberg scenarios one and two (which have the lowest iceberg concentrations; Figure 6.2; Table 6.1). However, in

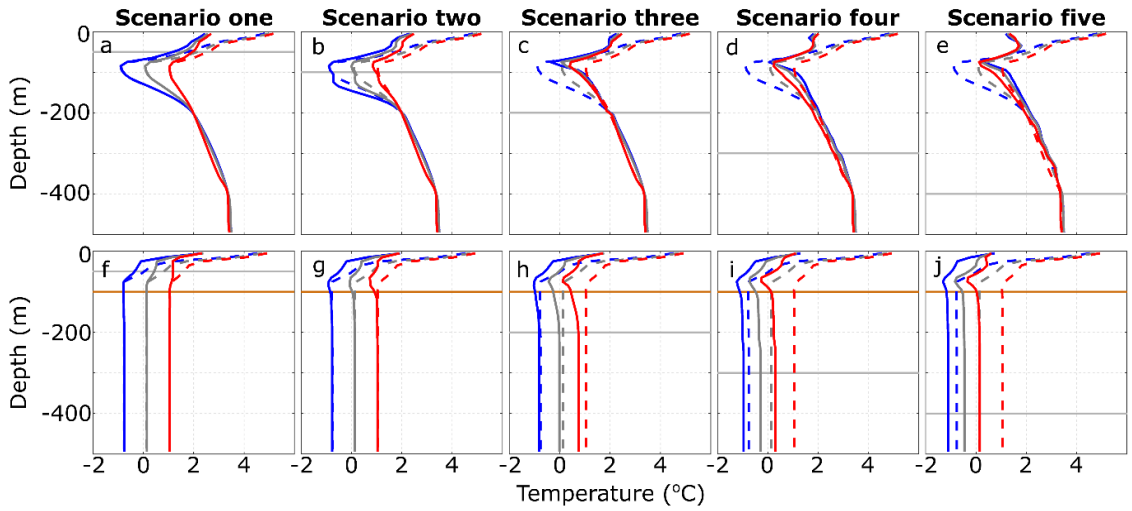

Figure 6.4. Steady-state glacier-adjacent water temperature for a range of initial Polar Water conditions. In all plots, solid and dashed lines indicate simulations with and without icebergs, respectively. Plots (a-e) show configurations with a flat-bottomed domain, whilst (f-j) show those with a 100 m deep sill. Grey, blue and red lines show scenarios using the *BCstandard*, *PWcool* and *PWwarm* boundary conditions respectively (shown in Figure 6.1e).

iceberg scenarios three to five, increasing but variable changes to the PW layer occur (Figures 6.4c-e). With *PWcool*, icebergs in these scenarios cause on average a net *warming* of 1.02°C in the 80-200 m depth range, compared to simulations without icebergs. Conversely, with *PWwarm*, the icebergs cause a net cooling of 0.30°C over the same depth range, such that the steady-state temperature profiles for both sets of initial conditions (*PWcool* and *PWwarm*) are similar. With *BCstandard*, the influence of icebergs on glacier-adjacent water properties falls between the two, with the net effect being a slight (0.43°C) warming (Figure 6.4c-e). These changes arise due to differing balances between cooling due to iceberg melting, and warming due to buoyancy-induced upwelling of relatively warm AW water. With *PWcool* there is relatively little iceberg melting in the PW layer (because the PW is close to the *in-situ* freezing point), and so warming due to upwelling of AW dominates (driven by iceberg melting at greater depth in the warmer AW layer). In contrast, with *PWwarm*, iceberg melt rates in the PW layer are comparatively high, and the temperature difference between the PW and AW layers is reduced, so localised cooling offsets warming due to turbulent upwelling. In short, under the conditions represented by these simulations, submarine iceberg melting acts to make glacier-adjacent water temperature more uniform with depth (Figure 6.4c-e).

The addition of a 100 m deep sill near the fjord mouth serves to amplify the cooling effect of icebergs (Figure 6.4f-j). Sills typically block external shelf waters below the sill depth from entering the fjord (unless external forcing causes a shallowing of isopycnals seaward of the sill), causing the fjord basin bounded by the sill to be replenished by waters sourced only from above the sill depth (e.g. Jakobsson et al., 2020). When icebergs reach down to the sill depth, all water entering the fjord may thus be subject to melt-driven cooling. The result is that icebergs cause cooling throughout the water column, even below the deepest iceberg keels and below the sill depth (Figure 6.4f-j). This cooling is increasingly pronounced as the PW temperature increases and with more concentrated and deeper icebergs (Figure 6.4f-j). For example, over the 100 to 500 m depth range with *PWcool*, icebergs cause 0.21°C cooling on average in iceberg scenarios three to five (0.06°C in scenario three and 0.35°C in scenario five); whilst with *PWwarm*, icebergs cause 0.67°C cooling on average (0.33°C in scenario three and 0.91°C in scenario five).

The varied effects of icebergs on glacier-adjacent water properties are apparent in temperature-salinity space (Figure 6.5). Initial glacier-adjacent water properties are inherited from those prescribed at the fjord mouth; however, icebergs modify fjord waters through ice melt and meltwater-driven vertical mixing. Comparing temperature-salinity profiles of simulations with and without icebergs illustrates these effects (Figure 6.5). In the upper ~60 m of all simulations with icebergs, iceberg melting causes substantial cooling and slight freshening (e.g. compare solid and open circles in Figure 6.5 – solid circles are drawn down and slightly left in temperature-salinity space). Deeper in the water column (below 100 m), the influence of iceberg melting on water properties depends on the iceberg scenario and the presence or absence of a sill. In iceberg scenario one (Figure 6.5a, b), iceberg melting causes very little modification of waters below 100 m, even in the presence of a sill (Figure 6.5b). This is because the icebergs do not extend to the sill water depth and so there is some unmodified exchange between the fjord and shelf. In iceberg scenario five, icebergs cause on average 0.19°C warming of waters below 100 m when there is no sill, and cooling of 0.61°C below 100 m when there is a sill (Figure 6.5b). This cooling below the maximum iceberg draught occurs in all iceberg scenarios in which icebergs extend to sill depth, but is most apparent in the higher iceberg concentration scenarios (e.g. Figure 6.5d). The simulated changes in water properties arise due the combined effects of local iceberg melting and fjord circulation. Submarine iceberg melting reduces the density of surrounding waters, causing upwelling until those waters equilibrate at a new neutral buoyancy depth with respect to the fjord stratification.

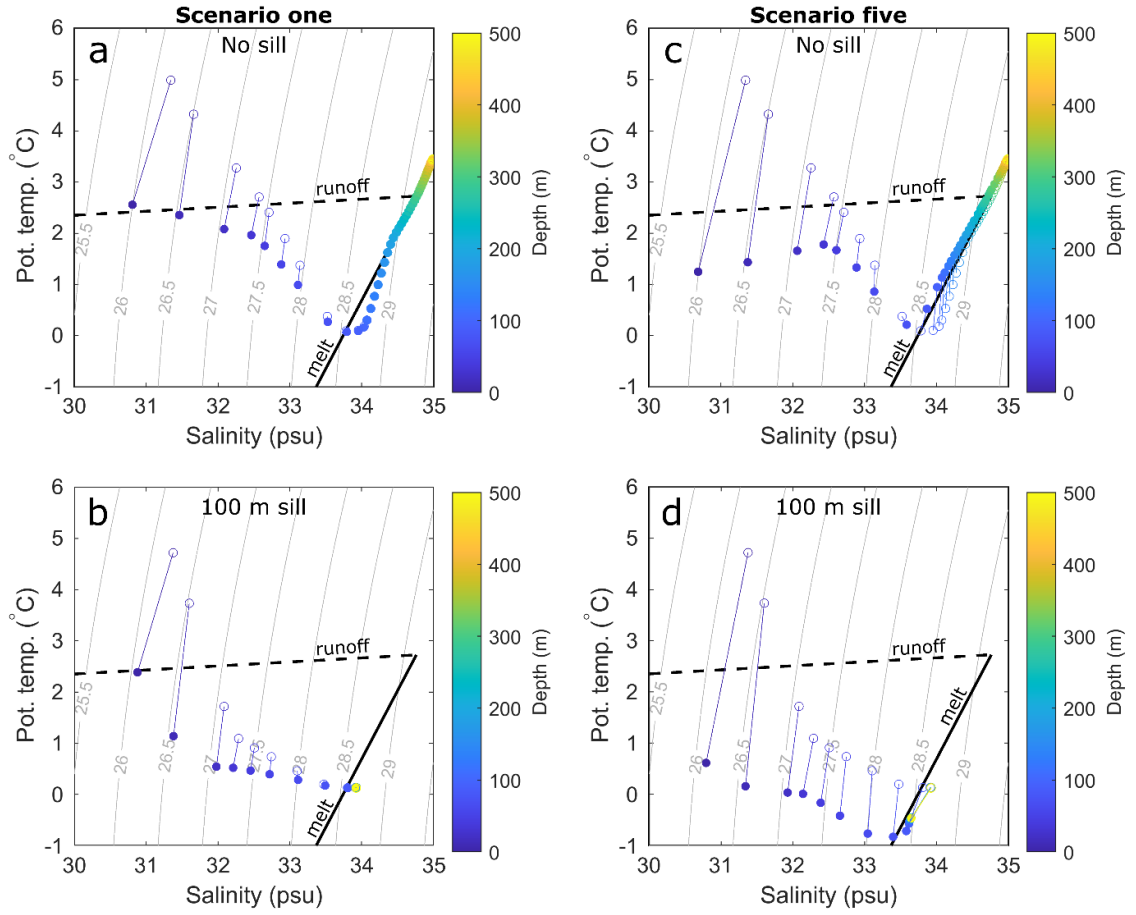

Figure 6.5. Glacier-adjacent water properties in temperature-salinity space in simulations with (solid circles) and without icebergs (open circles), for various iceberg and sill scenarios and with *BCstandard* boundary conditions. Panels (a) and (b) show iceberg scenario one without a 100 m sill (a) and with a sill (b). Panels (c) and (d) show iceberg scenario five, without a sill (c) and with a 100 m sill (d). Solid lines joining open and closed circles indicate connected data points extracted from the same model depth.

Within the temperature-salinity space of Greenland's fjords, density is predominantly salinity controlled. Therefore, the salinity stratification is little changed by iceberg melting, whilst the temperature changes are much more pronounced. This means that the iceberg melt-induced migrations through temperature-salinity space that are often steeper than predicted by the submarine melt mixing line (Gade, 1979).

6.3.2.2 Changing Atlantic Water temperature

We also examine the interactions between iceberg scenarios and changes to AW temperature (Figure 6.6). As in the PW scenarios, there is always marked cooling in the upper ~60 m of the water column and water modification below this is minimal for iceberg scenarios one and two. In iceberg scenarios three to five, icebergs penetrate to a

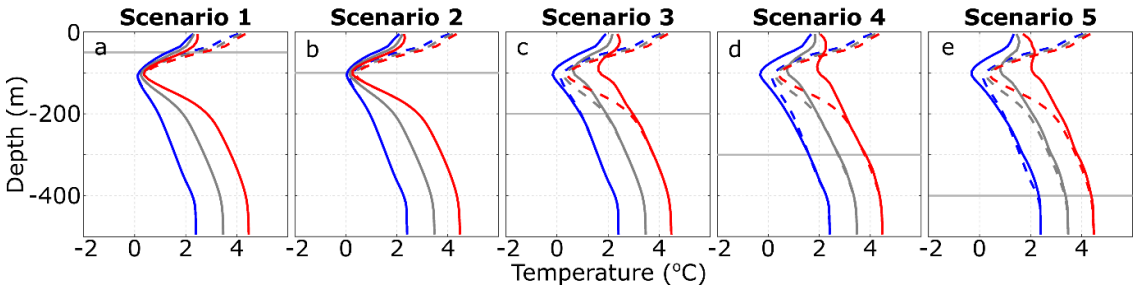

Figure 6.6. Steady-state glacier-adjacent water temperature for a range of initial Atlantic Water conditions and with a flat-bottomed domain. In all plots, solid and dashed lines indicate simulations with and without icebergs, respectively. Grey, blue and red lines show scenarios using the *BCstandard*, *AWcool* and *AWwarm* boundary conditions, respectively (shown in Figure 6.1f).

greater depth and thus into the AW layer, releasing freshwater which causes upwelling of AW. In these cases, the net effect of icebergs on water properties between ~80 m and the maximum iceberg keel depth depends on the balance between cooling due to localised iceberg melting, and warming due to upwelling of AW. With *AWwarm*, there is a steep temperature gradient between the cold PW and warmer AW layers. Consequently, upwelling of AW causes notable warming in the PW layer that offsets localised iceberg-induced cooling. In the scenarios with greater iceberg concentration (e.g. iceberg scenario five; Figure 6.6e), the icebergs penetrate deeper into the AW layer and so can induce upwelling of the deeper, warmer water, resulting in more warming and over a greater depth range than in the lower iceberg concentration scenarios. However, with *AWcool*, the vertical temperature gradient is reduced, so cooling due to localised iceberg melting dominates the signal between the maximum iceberg draught and ~80 m.

This dependence of iceberg modification of glacier-adjacent water properties on the temperature gradient through the AW layer is further illustrated by sensitivity tests in which the temperature of the AW layer was modified in two ways relative to *BCstandard*. First, to examine whether the absolute temperature of the water column affected the balance between upwelling and melting, the entire water column was uniformly warmed by 1°C. With this uniform shift in temperature, the pattern of temperature with depth is similar to that of *BCstandard* (compare dashed grey and lines in Figure 6.7b), illustrating that the additional upwelling-driven warming with *AWwarm* is due to the steeper temperature gradient between the PW and AW layers, rather than the absolute temperature of the AW. Secondly, to examine the relative importance of the absolute temperature and temperature gradient within the AW layer, the temperature gradient

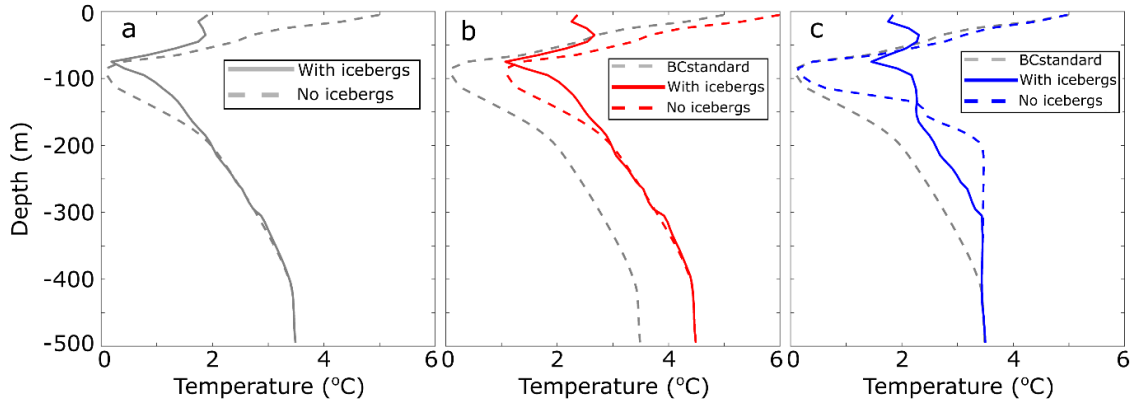

Figure 6.7. AW temperature gradient sensitivity tests. Panels show simulations using (a) *BCstandard*, (b) temperature profile shifted by 1°C throughout the water column, and (c) uniform initial AW temperature of 3.5°C. Steady-state conditions without icebergs using *BCstandard* (grey line) are also shown in (b) and (c) for reference.

between the PW and AW was steepened, such that the temperature through the AW layer was uniform. With this set of boundary conditions, upwelling-driven warming dominates in the PW layer, because of upwelling of warm AW, whilst melt-driven cooling dominates in the AW layer because upwelling-driven warming is muted (Figure 6.7c). Thus, the average warming below ~80 m that we simulate with *AWwarm* is strongly sensitive to the vertical temperature gradient, and not only the average or maximum temperature of the AW.

With the addition of a 100 m sill, AW does not propagate into the fjord under the conditions simulated here. Thus in steady-state, glacier-adjacent water properties are unaffected by AW and adopt the properties of the PW layer (modified by iceberg melting and runoff). The resulting profiles therefore resemble the dashed pale blue lines in Figure 6.4f-j and are not shown here.

6.4 Discussion

6.4.1 Comparison with observations and applicability to real fjords

Our simulations suggest that several changes to glacier-adjacent water properties can occur due to submarine iceberg melting. In almost all simulations, we simulate pronounced (>2°C) cooling in the upper several tens of metres of the water column. Deeper in the water column (between ~80 m and the maximum iceberg keel depth), both iceberg-induced cooling and warming can occur (e.g. Figures 6.4 and 6.6), depending on

the balance between cooling due local iceberg melting and warming due to melt-driven buoyancy-induced upwelling. The balance between these processes depends on the iceberg contact area at depth available for local melting (and therefore cooling) and on the temperature of the upwelling water. When vertical temperature gradients are steep (e.g. with *AWwarm*; Figure 6.6), icebergs can cause warming between their maximum keel depth and the warm surface layer. This is particularly apparent in the PW layer, where the temperature difference between an upwelled parcel of water and that at the parcel's new neutral buoyancy depth in the PW layer is greatest, and where iceberg melt rates (and therefore melt-driven cooling) are generally smaller because of the low water temperatures. In contrast, when vertical temperature gradients are shallower (e.g. with *AWcool*), cooling due to localised melting dominates (blue lines in Figure 6.7d,e and 6.7c). These effects tend to reduce vertical temperature variations of glacier-adjacent waters compared both to simulations without icebergs and compared to conditions at the fjord mouth.

Detailed near-glacier hydrographic observations against which to make comparisons are sparse, but those that do exist provide some useful insight into the applicability of our model results to Greenland's fjords. The pronounced surface and near-surface cooling (relative to conditions at the mouth) that we simulate is a common feature in Greenland's fjords. For example, a transect of conductivity, temperature, depth (CTD) casts along Sermilik Fjord revealed cooling of approximately 4°C in the upper ~50 m (Straneo et al., 2011), which was also reproduced in a detailed modelling study of Sermilik Fjord that included icebergs (Davison et al., 2020). Similar along-fjord near-surface cooling has also been observed in other iceberg-congested fjords, such as Illulissat Isfjord (Gladish et al., 2015; Beaird et al., 2017) and Upernavik Isfjord (Fenty et al., 2016), both in west Greenland. In Illulissat Isfjord, the cold surface layer usually extends along-fjord to a shallow sill at the fjord mouth, where icebergs frequently become grounded (Gladish et al., 2015).

Iceberg-induced changes to water properties below ~80 m are harder to identify in hydrographic observations, most likely because they also contain the signature of glacial-plumes resulting from subglacial discharge, or other external forcings. Our modelling suggests that, if vertical temperature gradients are shallow, then icebergs can cause cooling over large depth ranges (e.g. Figure 6.7c). As one example, hydrographic observations in Kangerdlugssuaq Fjord showed relatively uniform near-glacier

temperatures with substantial cooling in both the upper 100 m and between 300 and 400 m depth, relative to a transect acquired at the fjord mouth (Straneo et al., 2012), consistent with the modelling results presented here. Iceberg-melt-induced warming of parts of the water column is harder to identify in hydrographic observations because of the difficulty in distinguishing it from relatively warm subglacial runoff-driven plume outflow.

To further compare our modelling results to observations, we examined conductivity, temperature, depth (CTD) casts acquired as part of the Oceans Melting Greenland (OMG) project (https://omg.jpl.nasa.gov/; data available at: https://omg.jpl.nasa.gov/portal/browse/OMGEV-AXCTD/). As with the previous comparisons, and in keeping with our simulation design, we selected pairs of CTD casts acquired less than a week apart, one near or outside the fjord mouth and the other as close as possible to the tidewater glacier at the head of the fjord. These profiles (Figure 6.8) show many of the characteristics that we have simulated here. Specifically, the profiles show that near-surface water temperatures are substantially colder adjacent to tidewater glaciers compared to those observed outside each fjord, and the observed temperature differences are comparable to those simulated here. In all but two (Illulissat Isfjord and Timmiarmiut Fjord) of the surveyed fjords, the profiles also show warming at intermediate depths (~50-200 m) relative to the waters outside the fjord. These observations do not allow us to quantify the relative contributions to intermediate depth warming between plume outflow and iceberg melt-induced upwelling. However, we note that the vertical pattern and magnitudes of intermediate depth warming are similar to those simulated here. In addition, the intermediate depth warming occurs over a large depth range, which is not easily explained by plume outflow and is consistent with our simulations. Some of the profiles also show notable cooling at depth (e.g. Illulissat Isfjord), which we are only able to reproduce in simulations including a shallow sill. Our simulations may underestimate cooling at depth because power law size-frequency distributions underestimate the number of very large icebergs (Sulak et al., 2017) and because the parameter values used in our melt calculation may underestimate submarine melt rates (Jackson et al., 2020).

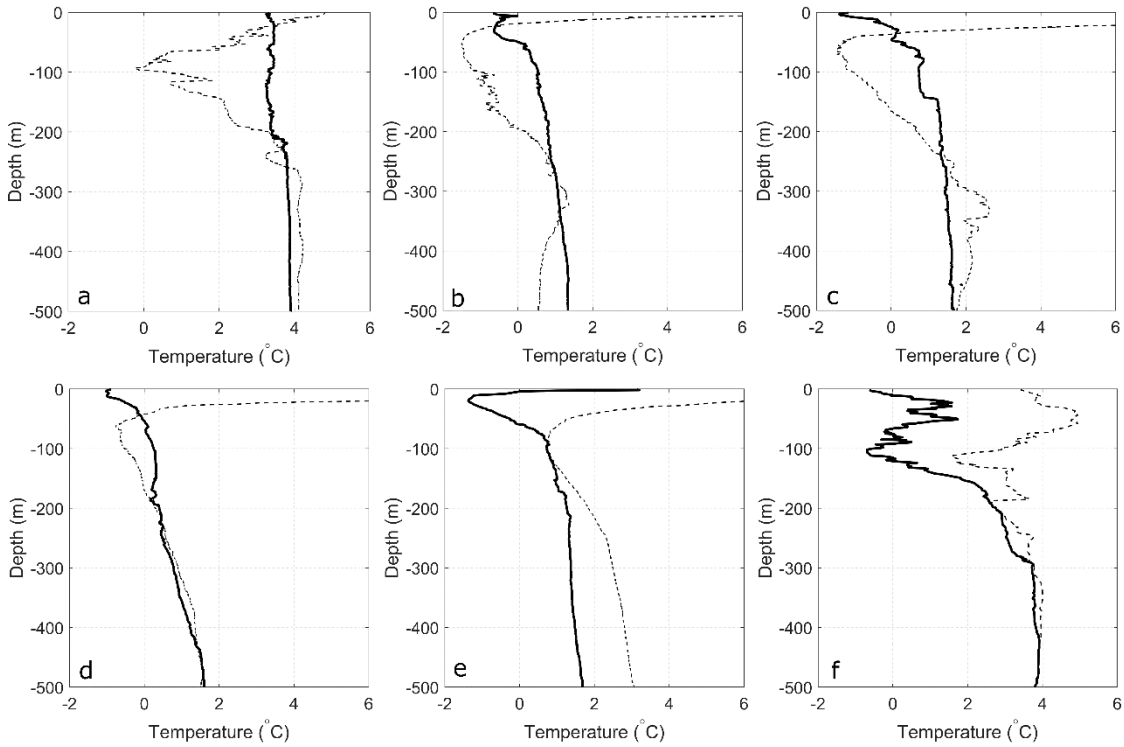

Figure 6.8. Fjord temperature profiles from the Oceans Melting Greenland project. (https://omg.jpl.nasa.gov/). In panels, solid lines are profiles acquired within the fjord, close to tidewater glacier termini, and the dashed lines are acquired at or beyond the fjord mouth. Fjords (or nearest glacier) shown are (a) Sermilik Fjord, (b) Daugaard-Jensen, (c) Upernavik Isstrom, (d) Nunatakassaap Sermia Fjord, (e) Ilulissat Isfjord, and (f) Timmiarmiut Fjord. Note, in (f), both an up- and down-cast are shown for the outer part of the fjord. Data are available from: https://omg.jpl.nasa.gov/portal/browse/OMGEV-AXCTD/

6.4.2 Implications for glacier-ocean interaction

If iceberg-induced changes to glacier-adjacent water properties significantly affect the magnitude and/or the vertical pattern of glacier submarine melting, then icebergs may play an important role in modifying glacier response to ocean forcing. To assess the effect of icebergs on glacier submarine melting, we first consider how iceberg-melt impacts subglacial runoff-driven plume dynamics and then assess how the simulated temperature changes could affect melt rates across the parts of glacier fronts that are not directly affected by runoff-driven plumes.

To examine the effect of icebergs on subglacial discharge plume-driven glacier submarine melting, we evaluate plume properties for a single set of ocean boundary conditions

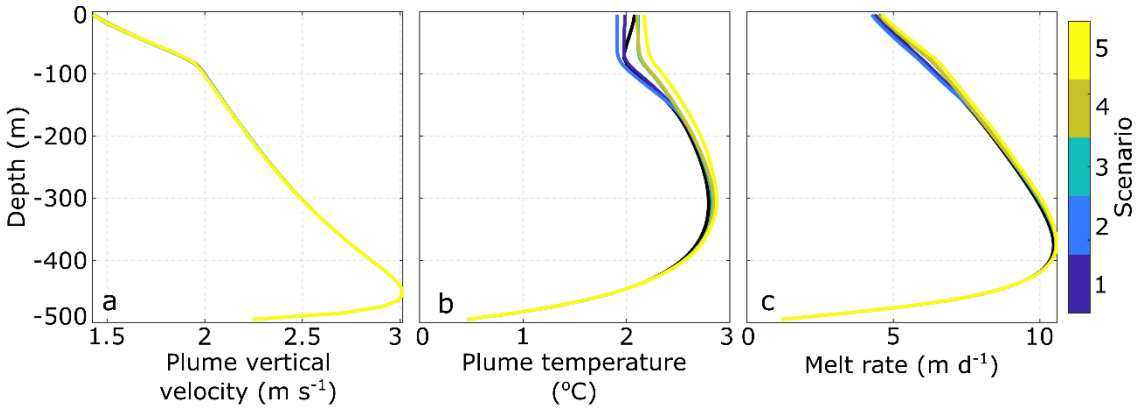

Figure 6.9. Plume dynamics and icebergs. (a) Plume vertical velocity. (b) Plume temperature. (c) Glacier submarine melt rate in the plume. All simulations are based on *BCstandard* boundary conditions and 500 m^3 s^{-1} runoff.

(*BCstandard;* Figure 6.1b-d) using each of the five iceberg scenarios. We find that submarine iceberg melting has negligible influence on plume vertical velocity and only modest influence on plume temperature, meaning plume-induced glacier submarine melt rates appear relatively insensitive to the changes in temperature and salinity induced by changes in iceberg geometry, concentration and size-frequency distribution (Figure 6.9).

Although runoff-driven plume dynamics appear to be relatively insensitive to iceberg-induced modification of glacier-adjacent water properties, submarine melting distal to glacial plumes ('background melting' (e.g. Slater et al., 2019)) may be more directly affected. Qualitatively, the iceberg-melt-induced changes to glacier-adjacent water properties presented above suggest that iceberg melt will affect background glacier melt rates in three key ways: (1) at and near the fjord surface, cooling will reduce background melt rates; (2) in the PW layer, background melting will usually increase due to upwelling of warmer AW, and; (3) in the AW layer, iceberg melt-induced changes in background melt rates are expected to be modest, with slight increases in fjords with steep vertical temperature gradients, and slight decreases in other fjords (assuming icebergs penetrate into the AW layer). These effects will be more pronounced in fjords with higher concentrations of larger (and thus deeper keeled) icebergs. In some fjords, then, where icebergs cause cooling near the surface and warming at depth, we expect icebergs will increase glacier undercutting through impacting submarine melt rates, which may in turn influence the rate and mechanism of calving (O'Leary and Christoffersen, 2013; James et al., 2014; Benn et al., 2017).

To explore these effects quantitatively, we calculate the percentage change in background melt rate of the glacier terminus due to iceberg-induced modification of glacier-adjacent water temperature (relative to simulations without icebergs). Modelling studies indicate that background melt rates scale linearly with ocean temperature (Sciascia et al., 2013; Xu et al., 2013; Slater et al., 2016); thus, changes in temperature, *T*, should cause proportional changes in background melting (Jackson et al., 2014). We choose to focus on relative changes in melt rate, rather than absolute changes (as in Jackson et al., 2014), because of poor constraints on important melt rate parameter values (Jackson et al., 2020). We calculate the relative change in submarine melt rate, *SMR*, following Jackson et al. (2014), as:

$$\Delta SMR = \frac{\left(T_{ib} - T_f\right) - \left(T_{nib} - T_f\right)}{\left(T_{nib} - T_f\right)} 100 \quad \text{Eq. 1}$$

where the subscripts *ib* and *nib* indicate simulations with 'icebergs' and 'no icebergs', respectively, and T_f is the *in-situ* freezing point, given by:

$$T_f = \lambda_1 S + \lambda_2 + \lambda_3 z, \quad \text{Eq. 2}$$

where $\lambda_{1\text{-}3}$ are constants representing the freezing point slope (-0.0573 °C psu^{-1}), offset (0.0832°C) and depth (0.000761°C m^{-1}), respectively. *S* is the local salinity (horizontally averaged within 2 km of the terminus) and *z* is depth in the water column.

Using this approach, we find that the impact on water properties resulting from iceberg melt substantially modifies background glacier submarine melt rates. Firstly, in the upper 50 m and using *BCstandard*, iceberg melt causes a 34.9% reduction in melt rate on average. Even in iceberg scenario one, iceberg melt causes a 29.5% reduction in melt rate over this depth range. Secondly, between 100 and 200 m depth, iceberg melt causes a 13.5% increase in melt rate on average when using *BCstandard*, but this increases to 59.2% when using *PWcool* (for which warming of the PW layer due to upwelling is most pronounced). Changes in iceberg melt rates in the AW layer are minimal, with the most pronounced effect being a 5.4% increase in the 200-400 m depth range using iceberg scenario five and *PWwarm*. When averaged through the entire water column, these effects largely compensate for each other, resulting in a net 3.1% decrease in melt rates with *BCstandard*. Overall therefore, this analysis suggests that iceberg melt can influence the

vertical pattern of glacier terminus background melting by decreasing melt rates at the surface and increasing them in the PW layer, with minimal changes in the AW layer.

As well as affecting glacier-adjacent water temperatures, iceberg melt likely affects submarine melt rates in other ways not examined here. For example, the cooling and freshening of the surface and near-surface layers induced by iceberg melting may prevent or hinder plume surfacing (De Andres et al., 2020), and may expedite sea ice formation after the melt season, promoting the development of an ice melange. In addition, mechanical iceberg breakup, iceberg calving and iceberg rotation can cause vigorous mixing of fjord waters which can temporarily increase glacier and iceberg submarine melt rates (Enderlin et al., 2018), and increases the iceberg-ocean contact area available for melting. Iceberg-melt-induced invigoration of fjord circulation can increase oceanic heat flux towards tidewater glaciers (Davison et al., 2020), likely resulting in faster terminus submarine melting. Icebergs likely also exert a mechanical influence on the circulation and plume dynamics at the ice-ocean interface (Amundson et al., 2020), and may prevent plume surfacing (Xie et al., 2019).

6.4.3 Implications for oceanic forcing of ice sheet-scale models

Current state-of-the-art projections of dynamic mass loss from the Greenland Ice Sheet (e.g. Goelzer et al., 2020) are forced by far-field ocean temperature profiles, provided by ocean modelling output that does not include fjord-scale processes (except for the obstruction of shelf-water intrusion by shallow sills; Slater et al., 2019, 2020). The results presented here suggest that such an approach is broadly appropriate for fjords with maximum iceberg keel depths of less than 200 m and iceberg concentrations less than ~20% on average, where iceberg modification of glacier-adjacent water properties appears to be limited other than in the upper several tens of metres (Figures 6.4 and 6.6). The majority of Greenland's fjords likely fall into this category (Sulak et al., 2017, Mankoff et al., 2019). Even in such fjords, however, this approach would not capture the surface and near-surface cooling caused by iceberg melting. In order to capture this near surface cooling, one relatively simple modification to such an approach could be to reduce surface water temperature to close to the *in-situ* melting point during winter periods, and proportionally to the iceberg surface area at the fjord surface during summer periods.

However, in fjords hosting icebergs with keel depth greater than or equal to 200 m and with average concentrations of more than ~20% (i.e. our iceberg scenario three or higher), iceberg modification of glacier-adjacent water properties becomes increasingly

important. In such fjords that also exhibit relatively shallow sills, icebergs act to cool glacier-adjacent water throughout the water column, with the amount of cooling proportional to the draught and concentration of the icebergs, as well as to the temperature of the ambient water at the fjord mouth (Figure 6.4). In such fjords that do not have shallow sills, the effect is more complicated, with both iceberg-melt-induced warming and cooling, depending on the vertical temperature gradient of the water column and iceberg concentration at depth. Overall, these changes to the water column temperature can cause non-negligible (up to several tens of percent) changes in terminus submarine melt rates across the large areas of the calving front that are not directly affected by plume-inducing subglacial discharge. The vertical pattern of changes to terminus submarine melt rates (reduced near the surface and increased at intermediate depths) induced by iceberg melting is expected to exacerbate undercutting of glacier termini, with potentially important impacts on calving rates (O'Leary and Christoffersen, 2013; Todd and Christoffersen, 2014; Benn et al., 2017; Ma and Bassis, 2019). Although fjords hosting icebergs this large and numerous are relatively few in number, it is these fjords (and the glaciers hosted by them) that contribute the most to dynamic mass loss from the Greenland Ice Sheet (Enderlin et al., 2014; Khan et al., 2020).

6.4.4 Transience vs steady-state

All of the results presented here were extracted from the final ten days of simulations that were run to a quasi-steady state (i.e. the variable of interest had stabilised). In our domains without sills, steady-state of temperature and salinity was generally reached after just ten to thirty days. However, our simulations with sills could take as many as one thousand days to reach such a steady state because fjord-shelf exchange is reduced. For an equivalent steady-state to be reached in reality, open ocean conditions, runoff and iceberg size and distribution would also have to remain quasi-stable for an equivalent time period. In reality, this is unlikely to occur (particularly in fjords with shallow sills) because runoff and coastal and open ocean conditions change on sub-seasonal to seasonal timescales (Sutherland et al., 2008, 2014; Jackson et al., 2014; Mortensen et al., 2014; Moon et al., 2018; Noël et al., 2015). In reality therefore, glacier-adjacent water properties in fjords with shallow sills are likely a complex amalgamation of temporally-evolving source waters, modified by processes operating within the fjord. In addition, some variations in coastal conditions can be transmitted towards glaciers very rapidly. During winter, strong wind events on the east coast of Greenland drive fast shelf-forced flows (or intermediary currents) in glacial fjords, delivering coastal waters to tidewater glaciers over just a period

of a few days, and potentially reducing the magnitude of iceberg-driven modification (Jackson et al., 2014, 2018). Such currents are strongest in winter, when hydrographic observations are sparse, so this remains speculative.

6.5 Conclusions

We have used a general circulation model (MITgcm) to quantify the effect of submarine iceberg melting on glacier-adjacent water properties in an idealised fjord domain. A large range of iceberg concentrations, keel depths and size-frequency distributions were examined to represent the range of iceberg conditions found in Greenland's marine terminating glacier fjords. We focused primarily on iceberg-melt-induced changes to glacier-adjacent water temperatures throughout the water column, because of their principal importance to glacier-submarine melting.

Our results suggest that icebergs can substantially modify glacier-adjacent water properties and that the precise impact depends on iceberg size and on the temperature profile and stratification of water within and beyond the fjord. In particular, we find that (1) temperature in the upper ~60 m of the water column is reduced by several degrees Celsius over a wide range of iceberg scenarios; (2) fjords with more and deeper icebergs are subject to greater iceberg-melt-induced modification, which can result in either cooling or warming at different depths depending on the balance between melt-driven cooling and upwelling-driven warming, which in turn depends on fjord temperature stratification, and; (3) when icebergs extend to or below the fjord mouth sill depth, they can cause significant cooling throughout the water column. Particularly with regard to point (2), our results highlight that oceanic forcing of large fast-flowing glaciers, which contribute the most to ice sheet dynamic mass loss, in existing projections of tidewater glacier dynamics is strongly affected by ignoring the impact of icebergs on fjord water properties. The iceberg-induced changes to the vertical temperature profile of glacier-adjacent waters identified here are likely to reduce submarine melt rates at and near the fjord surface while increasing them in the PW layer, which may influence the rate and mechanism of calving by exacerbating glacier terminus undercutting. Our results therefore identify a critical need to develop simple parameterisations of iceberg-induced modification of fjord waters, and other fjord-scale processes, to better constrain oceanic forcing of tidewater glaciers.

Chapter 7 - Synthesis

This thesis has been motivated in large part by the rapid changes that have taken place at Greenland's marine terminating outlet glaciers since the mid-1990s (e.g. Moon et al., 2020; Rignot & Kanagaratnam, 2006). This period of rapid glacier change occurred at a time of atmospheric and oceanic warming over and around the ice sheet (e.g. Hanna et al., 2008; Straneo & Heimbach, 2013), and there is a substantial body of evidence linking those changes in environmental conditions to changes in tidewater glacier behaviour. The overall aim of this thesis has been to improve understanding of the interactions between both the atmosphere and ocean with Greenland's tidewater glaciers, through a combined remote sensing and modelling approach focusing on poorly-understood elements of glacier-fjord systems.

The first section of this discussion chapter summarises the findings of the thesis. These findings are then expanded to the wider ice sheet through further analysis and discussion, and the implications of the results for modelling tidewater glacier behaviour are discussed. Finally, an outline of future directions for research and several concluding remarks are presented.

7.1 Summary of findings

In Chapter 4, the relationships between seasonal near-terminus subglacial hydrological evolution and ice velocity at three contrasting tidewater glaciers in southwest Greenland were examined. To do this, satellite images were used to derive continuous, high-resolution estimates of ice velocity near each glacier terminus during the period 2014-2019. The form of the subglacial drainage system was inferred through a combination of plume observations and plume modelling, forced by daily estimates of subglacial discharge (Noël et al., 2016, 2018) and hydrographic observations (Mortensen et al., 2011, 2013, 2014). Other variables influencing tidewater glacier behaviour, including surface melting, ice mélange condition and terminus position were also examined to help isolate the effect of seasonal subglacial hydrological evolution on ice dynamics. It was found that subglacial hydrological evolution strongly controlled the pattern and amplitude of seasonal velocity variations, despite substantial differences between glaciers. At all glaciers, the development of subglacial channels curbed an early-melt season speed-up and caused ice velocity to decline at least until the end of the melt season. At the slowest study glacier, inferred subglacial channel development occurred earliest and resulted in the most pronounced slow-down by the end of the melt season, whilst at the fastest glacier, channel development occurred latest and caused a less-pronounced slow-down. These changes in ice velocity and subglacial hydrology are qualitatively indicative of a flow regime in which annually averaged ice velocity is relatively insensitive to interannual variations in meltwater supply. These results therefore suggest that tidewater glacier retreat over the past two-decades is unlikely to have been caused by acceleration in response to increasing subglacial drainage of meltwater (though it is noted that meltwater likely plays a role in glacier dynamics through other mechanisms). Analysis of glacier surface and bed elevation further suggested that channel formation (and therefore a pronounced late summer slowdown) is more likely at slower glaciers which are heavily grounded near the terminus, potentially providing a simple means to identify glaciers whose seasonal velocity pattern is strongly influenced by subglacial hydrological evolution.

Having examined controls on tidewater glacier dynamics in Chapter 4, the research presented in Chapter 5 focused on the interaction between the icebergs discharged from tidewater glaciers and the fjords into which they drain. Previous work (Enderlin et al., 2016; Moon et al., 2017) had identified icebergs as a major source of freshwater within Sermilik Fjord, but understanding of iceberg freshwater production patterns was still

embryonic. In Chapter 5, an iceberg module was developed and added to an ocean circulation model, which was then applied to Sermilik Fjord to examine iceberg-ocean interaction in a real-world setting. The results presented in Chapter 5 revealed important new details of iceberg freshwater production, including (but not limited to): (i) that the volume of freshwater released from icebergs in Sermilik Fjord increases with subglacial discharge raised to the power 0.09 to 0.12; (ii) that iceberg melting below the AW-PW interface contributes 39.6±11.5% to total iceberg freshwater production in Sermilik Fjord, and; (iii) that freshwater flux from icebergs increases with submerged iceberg area raised to the power 1.18 to 1.22 (when standard melt rate parameter values are used).

Chapter 5 then went on to quantify the effect of this freshwater production on fjord circulation and, ultimately, oceanic heat flux towards Helheim Glacier – one of the largest glaciers draining the Greenland Ice Sheet (King et al., 2018). This analysis demonstrated that icebergs are capable of driving and invigorating fjord circulation, even in the absence of subglacial discharge, resulting in a 10% increase in fjord water export to the ocean compared to simulations in which circulation is forced by runoff alone. Iceberg melting also causes substantial cooling throughout the upper ~100 m of the fjord, but does not significantly modify the temperature of the AW layer. The combined effect of these changes to the temperature and velocity structure of the fjord is to increase oceanic heat flux towards Helheim Glacier by 9.3±4.5% to 38.4±10.8% depending on the value of the melt rate parameters used. Finally, by adding in icebergs, the model was able to much better reproduce observations acquired within the fjord compared to previous studies and simulations without icebergs. Overall, Chapter 5 shows that icebergs are an important component of glacier-fjord systems and suggests that there may be a positive feedback between iceberg production and up-fjord heat flux in some fjords.

Chapter 6 examined the effect of icebergs on water properties immediately adjacent to the ice-ocean interface – a key region for ice-ocean interaction which is particularly difficult to observe. This chapter utilised the improved ocean circulation and iceberg model presented in Chapter 5, but applied it to idealised domains rather than a particular fjord, in order to give a systematic overview of the influence of icebergs on glacier-adjacent water properties. The results presented in this chapter show that, in the parameter space represented by Greenland's glacial fjords, icebergs always cause substantial cooling in the upper few tens of metres of the water column, even in fjords with low concentrations of small icebergs. Deeper in the water column, icebergs can cause either

warming or cooling, depending on vertical temperature gradients and sills. In general, where water temperature increases rapidly with depth, the dominant effect of iceberg melting is to cause warming, due to the upwelling of deeper, warmer waters. This was particularly apparent in the PW layer when the temperature gradient between the PW and AW was steep, but also occurred when AW temperature increased rapidly with depth. When temperature gradients are less steep, however, warming due to upwelling is reduced and melt-driven cooling dominates. Notably, Chapter 6 showed that significant iceberg-induced temperature changes are likely limited to the surface layer in most fjords, but temperature changes in the PW and AW layers may be significant in fjords hosting the largest glaciers. In addition, when icebergs penetrate to-or-below the sill depth, they can cause cooling throughout the entire water column, with greater cooling in fjords hosting more and larger icebergs. Based on a simple parameterisation of glacier submarine melting, this chapter further showed that these iceberg-induced changes to glacier-adjacent water properties could cause substantial changes to rates of glacier-submarine melting distal to glacial plumes. This chapter therefore builds on Chapter 5 by demonstrating that icebergs are important modifiers of glacier-adjacent water properties with implications for the rate and vertical distribution of submarine melting, further highlighting the importance of icebergs in glacier-fjord systems.

7.2 Implications of findings at the ice sheet-scale

This thesis has looked in depth at processes at certain large glaciers in fjords, with the intention of gaining knowledge of processes that is applicable to glacier-fjord systems more generally. While the same depth of research cannot be applied to all of Greenland's glacier-fjord systems, it is useful to briefly consider more broadly the applicability of the findings presented in this thesis to the wider ice sheet. To this end, this section first examines the seasonal velocity variability of a large number of glaciers and considers the broader controls on those variations, in order to extend the results presented in Chapter 4 to the wider ice sheet. Secondly, to build on the results of Chapters 5 and 6, another large glacier-fjord system, with slightly different oceanic conditions to that of Sermilik Fjord, is examined.

7.2.1 Seasonal variations of ice velocity and subglacial hydrology

In Chapter 4, it was suggested that ice velocity and height-above-floatation were key controls on seasonal ice flow variations, via their effect on the subglacial drainage system. In order to test this hypothesis further, it is instructive to examine the seasonal ice flow

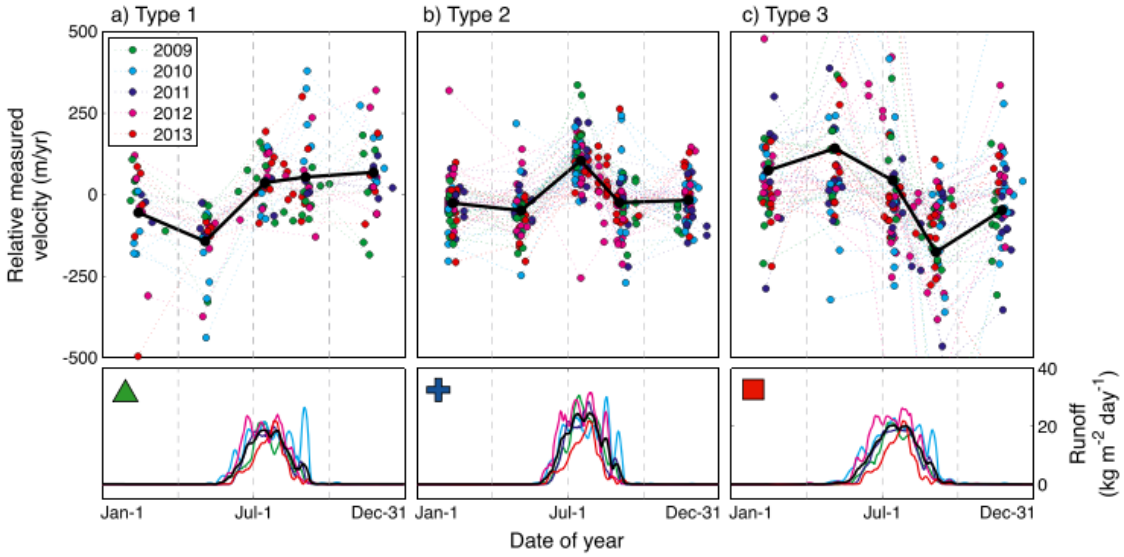

Figure 7.1. Distinct patterns of seasonal ice velocity and associated ice sheet runoff for (a) type 1, (b) type 2, and (c) type 3 tidewater glaciers (as described in text). Bottom row shows the smoothed daily runoff from RACMO2.3. Reproduced from Moon et al. (2014).

variability and height-above-floatation of a larger sample of glaciers. To do this, ice velocity data from the Programme for Monitoring of the Greenland Ice Sheet (PROMICE) was extracted close to the terminus of 75 of Greenland's tidewater glaciers during 2016 through 2019 at 24-day temporal resolution (Solgaard & Kusk, 2019). Using these timeseries, each glacier was classified based on the original classification scheme of Moon et al. (2014) and as shown in Figure 7.1. In this scheme, 'type 1' velocity behaviour is distinguished based on sustained speed-up well past the end of the melt season; 'type 2' glaciers exhibit peak seasonal speeds during mid-summer, with relatively uniform speeds over winter; and 'type 3' glaciers typically exhibit peak velocities in early summer and have a characteristic late-summer velocity minima followed by winter recovery (Figure 7.1). Using this scheme, it is expected that velocity variations of type 1 glaciers are primarily controlled by calving, whilst that of type 2 and type 3 glaciers are controlled by meltwater supply and subglacial hydrology. As was shown in Chapter 4, channels may develop at both type 2 and type 3 glaciers, but in the latter, the channels are likely able to depressurise the drainage system substantially by late-summer. For the purposes of this discussion, only ice velocity and height-above-floatation are quantified here, though it is noted that a full analysis would require consideration of subglacial discharge at the terminus and plume modelling (as in Chapter 4).

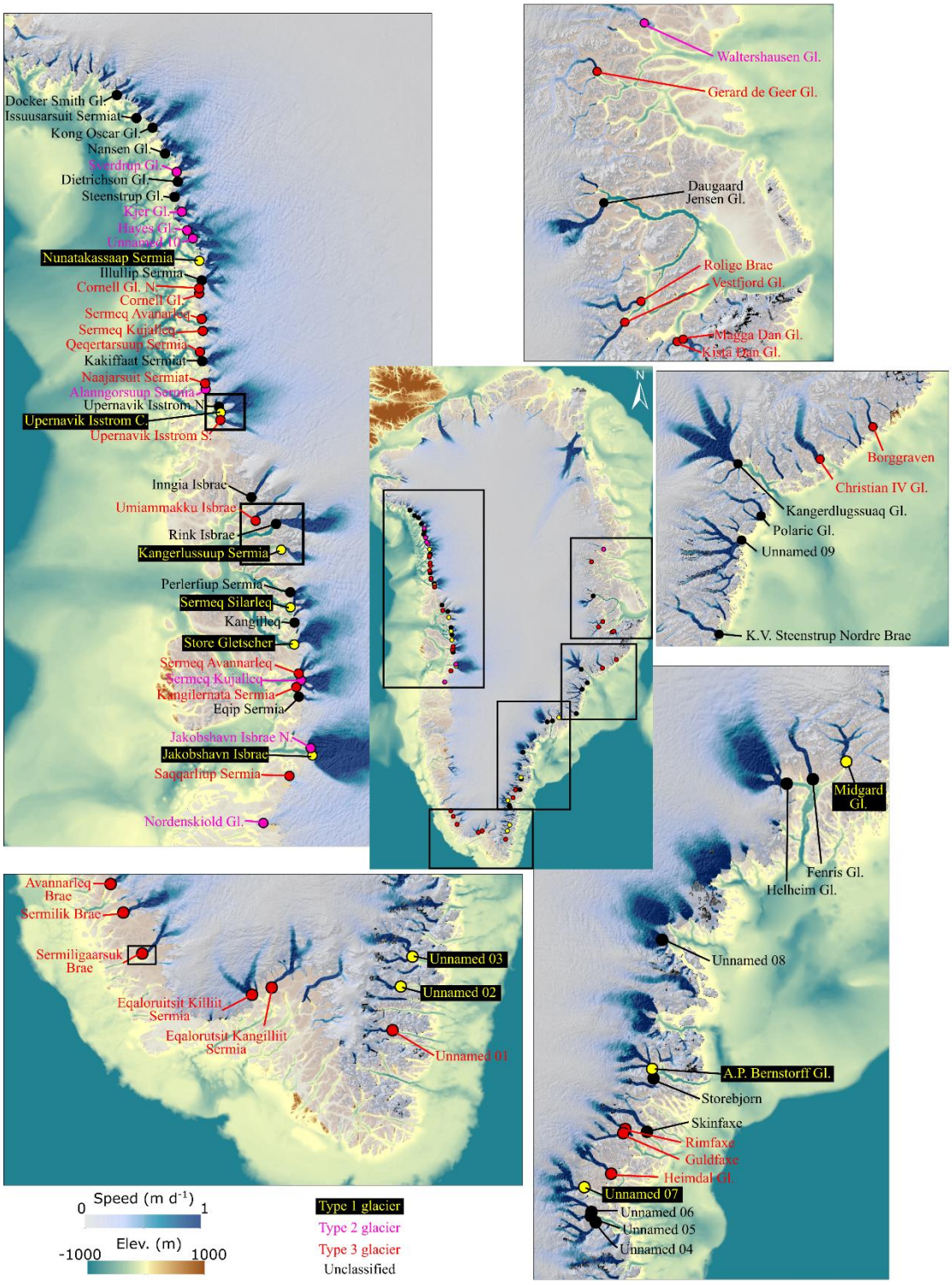

Figure 7.2. Seasonal velocity behaviour of 75 tidewater glaciers, with type 1 glaciers shown in yellow, type 2 glaciers shown in pink and type 3 glaciers shown in red. Glaciers which could not be classified are shown in black. Black box in southern zoom denotes the extent of Figure 7.3, and black boxes in the west and northwest zoon denote the extents of Figures 7.4 and 7.5.

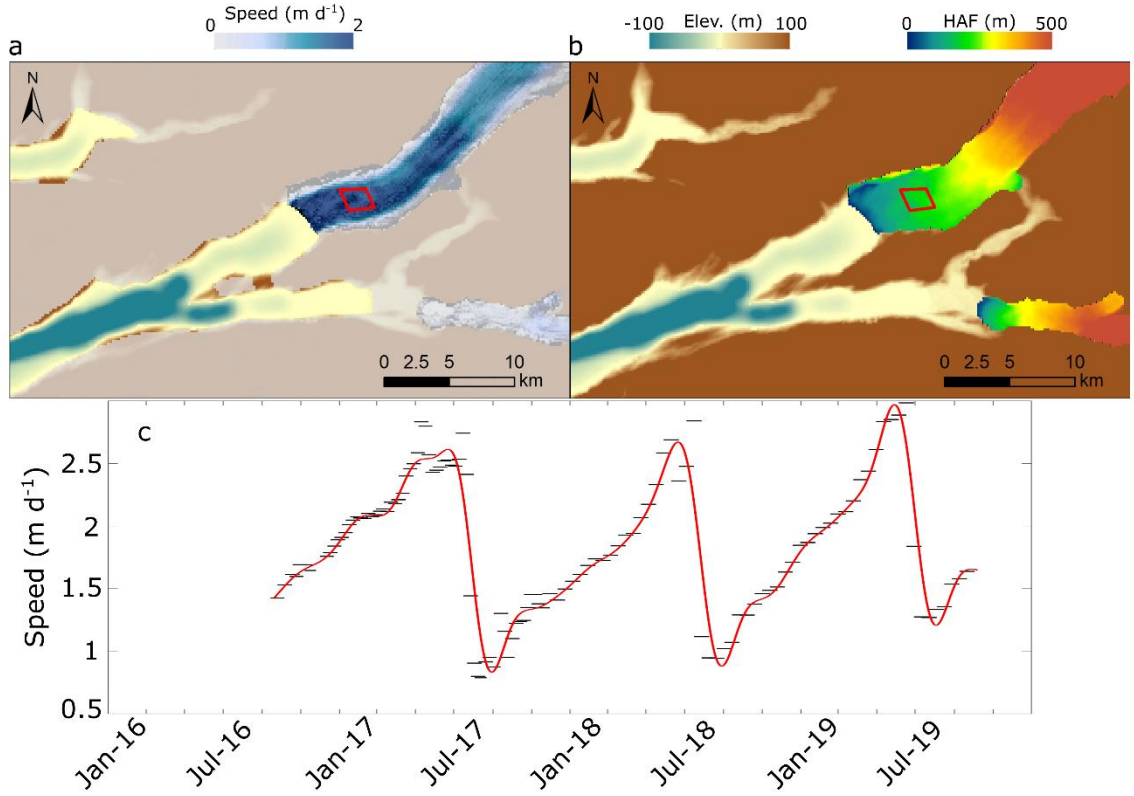

Figure 7.3. Example of type 3 glacier, Sermiligaarsuk Brae in southern Greenland (see Figure 7.2 for location). (a) Winter average ice velocity overlaid on BedMachine v3 bed elevation (Morlighem et al., 2017). (b) Height-above-floatation (HAF; clipped to glacier extent) overlaid on bed elevation. (c) Time-series of PROMICE ice velocity (see text) extracted within the red boxes shown in (a) and (b). The horizontal black lines show individual ice velocity estimates and the red curve is 24-day low-pass filtered ice velocity.

Using this approach, it was possible to classify 47 (63%) of the 75 glaciers considered. Of those 47, 11 were classified as type 1, 9 as type 2, and 27 as type 3 (Figure 7.2). Based on these classifications therefore, seasonal ice velocity at 48% of all glaciers considered (and 75% of classified glaciers) is likely affected by meltwater supply and subglacial hydrology. This is a similar proportion of glacier types as identified by Vijay et al. (2019), though it is noted that there is some overlap among glaciers sampled. Of the glaciers sampled here and in either Vijay et al. (2019) or Moon et al. (2014), there is broad agreement in the classifications given to individual glaciers. Notable differences include Rink Glacier, which here could not be classified as the seasonal signal was dwarfed by a substantial deceleration from July 2016 to March 2018, followed by irregular variations in ice velocity, but was identified as exhibiting type 1 behaviour in Moon et al. (2014).

This broad scale analysis provides some support for the hypothesis that height-above-floatation is a good indicator of glacier seasonal velocity behaviour, and is therefore a useful indicator of near-terminus subglacial channel development (or not). For example, Figure 7.3 shows a type 3 tidewater glacier, Sermiligaarsuk Brae in southern Greenland, which (like Akullersuup Sermia in Chapter 4) is well above floatation even close to the terminus. In addition, height-above-floatation decreases slowly towards the terminus.

In addition, there are instances where neighbouring glaciers exhibit different seasonal velocity signals and also differ in terms of their long-term mean speed and height-above-floatation. For example, in northwest Greenland, Rink Glacier, Umiammakku Isbrae and Kangerlussuup Sermia all drain into the same fjord system (Figure 7.4). Of these, Umiammakku Isbrae exhibits clear type 3 seasonal behaviour, flows relatively slowly on average and the most heavily grounded of the three glaciers (Figure 7.4). In contrast, Kangerlussuup Sermia exhibits type 2 velocity behaviour, has intermediate mean speeds and is less heavily grounded in its lower reaches (Figure 7.4). As mentioned above, Rink Glacier was insensitive to seasonal forcing over the time period considered here, but it exhibited type 1 behaviour during at least 2009-2013 (Moon et al., 2014) and is grounded most lightly and flows the fastest of these three glaciers (Figure 7.4). The contrasts in ice velocity and height-above-floatation of these glaciers is similar to those identified in Chapter 4, which suggests that subglacial hydrology may also be responsible for the differing seasonal velocity behaviour of these three glaciers.

Considering the sample of glaciers as a whole, however, there does not appear to be a significant difference in height-above-floatation between types of glacier (Figure 7.5). To illustrate, the median height-above floatation near the terminus for each glacier type is 240±122 m for type 1, 145±62 for type 2, and 192±141 for type 3. Accounting for uncertainty in the bed topographic data (BedMachine version 3), does not increase the explanatory power of height-above-floatation. Overall, multi-year (2016-2019 in this case) flow speed seems to be much more strongly related to glacier type, with type 1 glaciers generally flowing faster on average than type 3 glaciers, with type 2 glaciers in between (Figure 7.5). This is true when considering a small sample of neighbouring

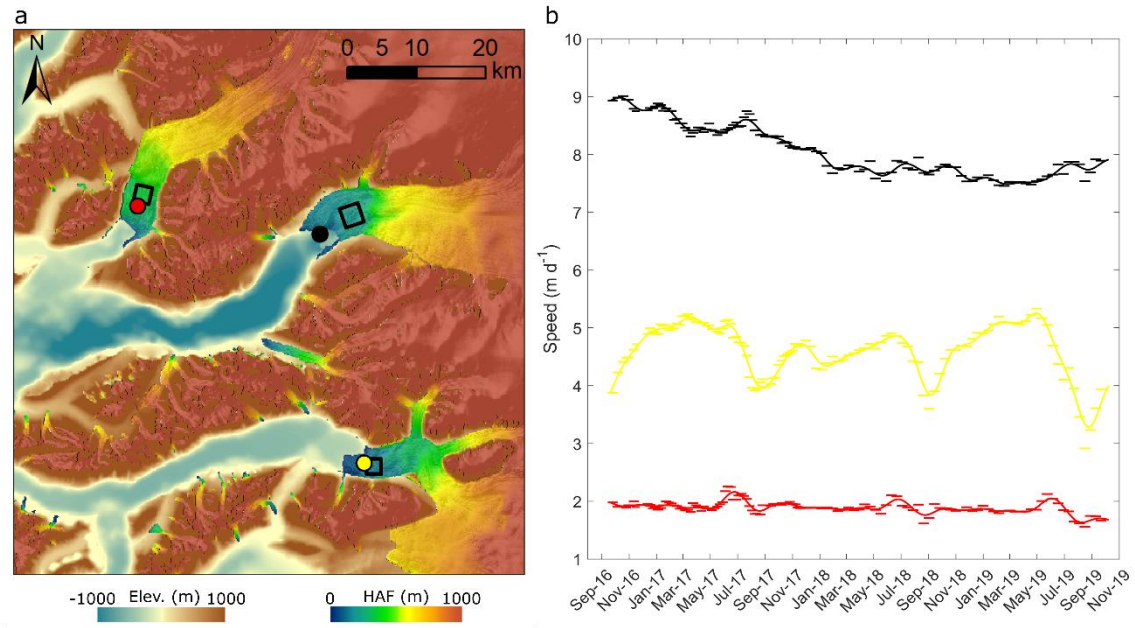

Figure 7.4. Example of glacier height-above-floatation and speed of neighbouring glaciers. (a) Height-above-floatation. (b) Speed time-series. Colours in (b) correspond to coloured dots in (a). Ice velocity time-series in (b) were extracted from black polygons in (a). Umiammakku Isbrae is the northern most glacier (red dot in panel (a)), Rink Glacier is central (black dot) and Kangerlussuup Sermia is the southern most glacier (yellow dot).

glaciers in one area (e.g. Figure 7.4) and across the ice sheet as a whole (Figure 7.5). If one assumes that the seasonal ice flow variability at these glaciers is controlled by subglacial hydrological evolution, then height-above-floatation seems to be a relatively poor indicator of seasonal subglacial hydrology-ice dynamic interactions. Instead, the differences in subglacial hydrology (and therefore seasonal ice dynamics) seem to be related to long-term average ice velocity, with limited subglacial channel formation at the faster flowing glaciers. This is consistent with the results presented in Chapter 4 and is theoretically expected because faster ice flow will expedite channel closure (Röthlisberger, 1972).

Overall, therefore, both seasonal and longer-term average ice velocity are likely useful indicators of subglacial hydrological evolution. If one assumes that all type 3 glaciers do quickly develop large subglacial channels (as in Chapter 4), this suggests that as many as ~50% of Greenland's tidewater glaciers may have efficient subglacial channels during much of the melt season, likely making them relatively insensitive to interannual changes in meltwater supply. Indeed, based on the evidence presented in Chapter 4, this discussion

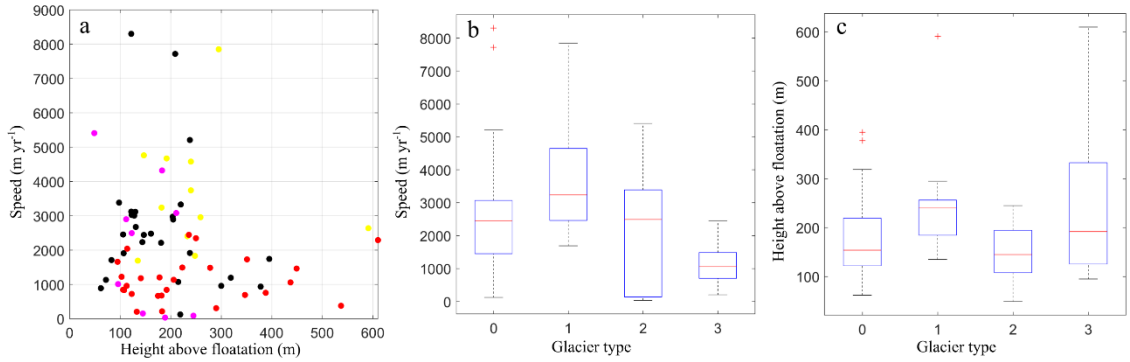

Figure 7.5. Comparison of multi-year average ice speed, height-above-floatation and glacier type. (a) Height-above-floatation and average (2016-2019) speed of each glacier type: unclassified (black), type 1 (yellow), type 2 (magenta) and type 3 (red). (b) Box plot of average speed for each glacier type. (c) Box plot of height-above-floatation for each glacier type. Height-above-floatation was extracted in the same location as ice speed (e.g. black polygons in Figures 7.3 and 7.4). Box plots show the median (red bar), the interquartile range (box), the maximum and minimum excluding outliers (whiskers) and outliners (red crosses), defined as a value more than 1.5 times the interquartile range away from the bottom or top of the box.

and existing literature (e.g. Moon et al., 2014; Vijay et al., 2019), there is convincing evidence that meltwater can affect the velocity of tidewater glaciers at seasonal timescales, but does not seem to strongly influence ice flow on annual timescales nor be capable of initiating unstable glacier retreat. The widespread development of subglacial channels at tidewater glaciers also has implications for glacier submarine melt rates by focusing melting over relatively small areas of the calving front (Cook et al., 2020; Slater et al., 2015), leading to terminus notching (Chauché et al., 2014) and reducing undercutting.

7.2.2 The impact of iceberg melting on up-fjord oceanic heat flux

In Chapter 5, it was shown that submarine iceberg melting in Sermilik Fjord increases up-fjord heat flux towards Helheim Glacier. This effect was partly dependent on the circulation and temperature stratification in the fjord – the modelled plume from Helheim Glacier terminated at the fjord surface, resulting in up-fjord currents at a depth where minimal iceberg-ocean interaction occurred and where the water was relatively warm. Submarine iceberg melting accelerated these warm up-fjord currents, resulting in a greater up-fjord heat flux. In many fjords, observations (e.g. Chauché et al., 2014; Gladish et al., 2015; Jackson et al., 2017) and modelling (Cook et al., 2020) indicate that plume

outflow at the fjord surface is not unusual, and so it is reasonable to expect that submarine iceberg melting will have a similar effect in other fjords.

However, there is also substantial evidence to suggest that plumes do not always reach the fjord surface, resulting in up-fjord currents near the fjord surface as well as at depth (e.g. De Andrés et al., 2020; Carroll et al., 2015; Chauché et al., 2014). These near-surface up-fjord currents can contribute substantially to the net up-fjord heat flux. For example, in Kangerdlugssuaq Fjord, east Greenland, Inall et al. (2014) showed that in the outer part of the fjord, this up-fjord near-surface current was responsible for approximately 20% of the up-fjord oceanic heat flux. Inall et al. (2014) also showed that the temperature of this current progressively decreased up-fjord largely due to iceberg melting within the body of the fjord, implying that icebergs reduce oceanic heat delivery to tidewater glaciers by this warm near-surface water.

To examine the influence of icebergs on up-fjord heat flux in Kangerdlugssuaq Fjord and, more generally, to characterise iceberg-ocean interaction in fjords where plumes terminate at depth, the iceberg model described in Chapters 3, 5 and 6 was applied to Kangerdlugssuaq Fjord (Figure 7.6). Due to the lack of iceberg observations in the fjord, the model was initialised using iceberg distributions guided by observations in Sermilik Fjord (described in Chapter 5), a choice that is justified based on the similarity in glaciological setting (i.e. a large iceberg-congested fjord hosting several large tidewater glaciers adjacent to which a dense ice mélange often forms). To simplify this discussion, this analysis focuses on the ‘summer runoff forcing’ and ‘no runoff’ scenarios described in Chapter 5, and only a single set of oceanic boundary conditions, iceberg size and distribution, and melt rate parameters are considered. Other than changing the ocean boundary conditions and modifying the iceberg distribution according to the geometry of Kangerdlugssuaq Fjord, the parameters and simulation details are the same as those described in Chapter 5. The resulting domain is shown in Figure 7.6.

Using the setup described above, it is clear that icebergs affect the temperature and velocity structure of Kangerdlugssuaq Fjord (Figure 7.7). As in Sermilik Fjord (Chapter

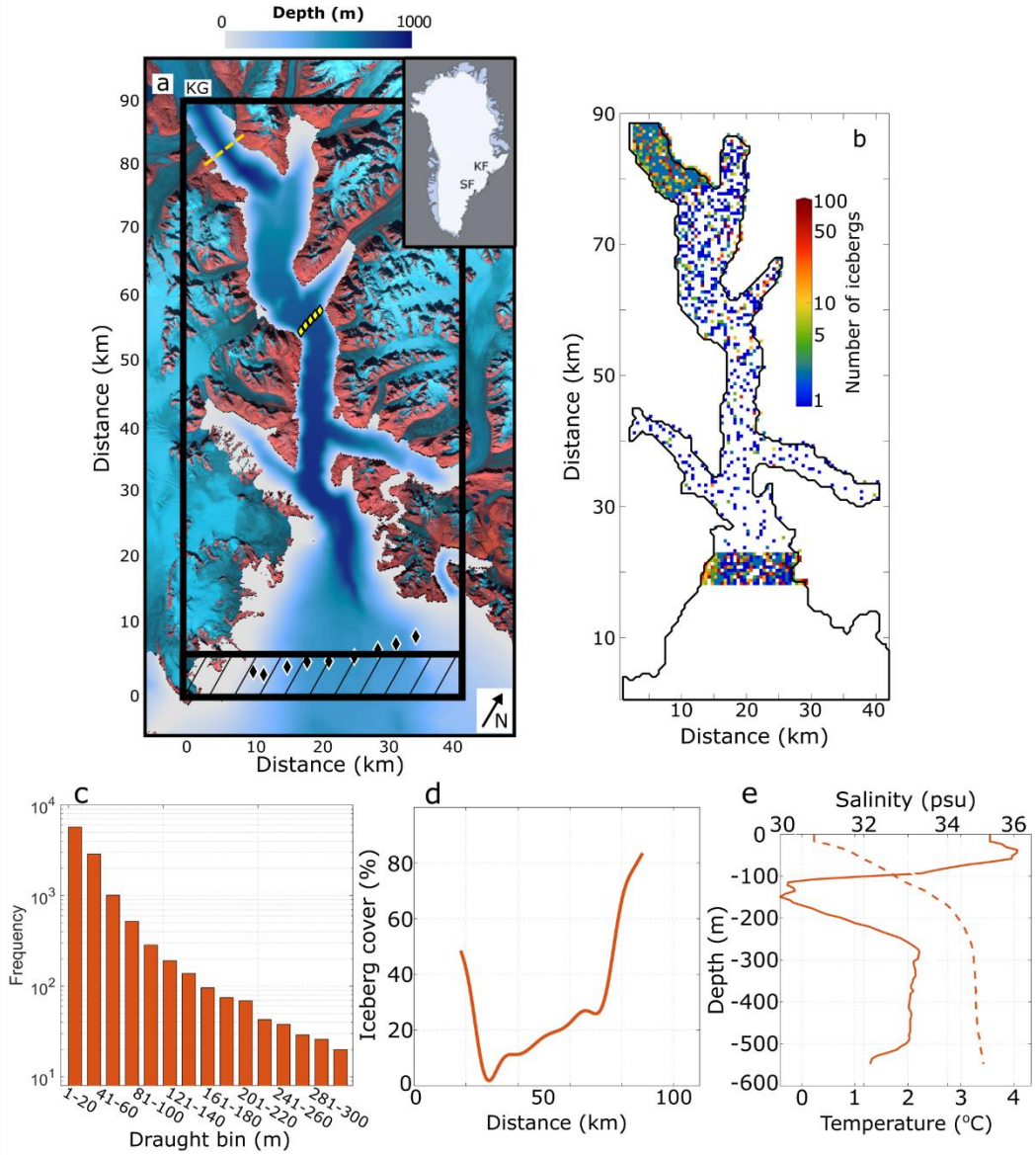

Figure 7.6. Kangerdlugssuaq Fjord model domain. (a) Model bathymetry (blue shading) from BedMachine v3 (Morlighem et al., 2017) overlaid on a false-colour (bands 4,6,7) Landsat-8 image. The black box denotes the extent of the model domain, the hashed area denotes the sponge region (Methods) and the yellow dashed line indicates the flux gate used in heat flux calculations. The black diamonds are locations of CTD casts used to create the model boundary conditions (e). Inset shows the location of Kangerdlugssuaq Fjord and also Sermilik Fjord for reference. (b) Number of icebergs in each model cell. (c) Histogram of iceberg draught. (d) Iceberg cover along fjord. (e) Initial and open boundary temperature (solid) and salinity (dashed).

5), submarine iceberg melting in Kangerdlugssuaq Fjord causes substantial cooling (up to 5°C) and some freshening (up to 0.4 psu) in the upper ~100 to 200 m of the water column. Without runoff, there is some warming (up to 0.58°C and 0.11°C on average) in the 150-250 m depth range (Figure 7.7), due to upwelling of warm AW from below

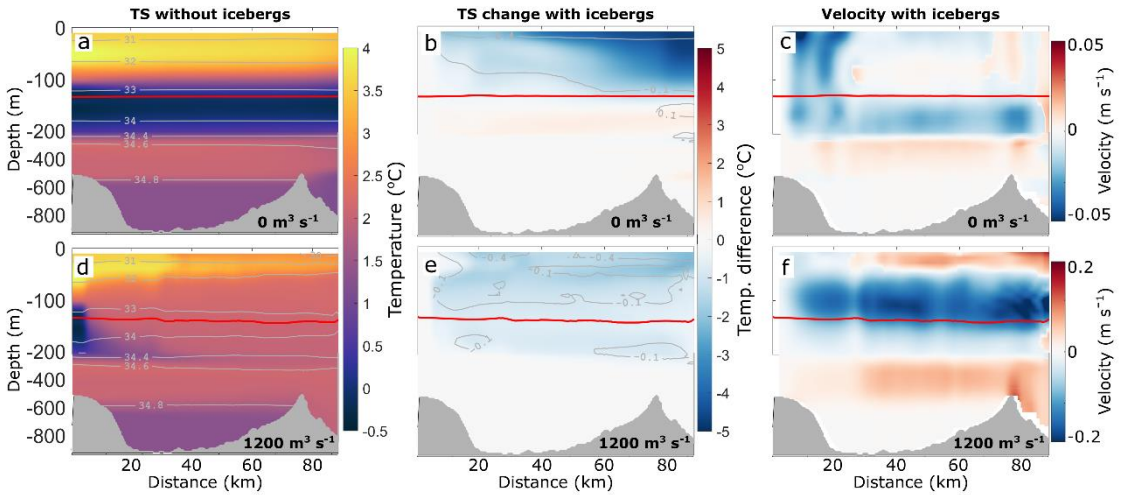

Figure 7.7. Along-fjord transects of water properties and circulation of Kangerdlugssuaq Fjord. The impact of submarine iceberg melting on fjord water properties and circulation using channelised subglacial hydrology (see Chapter 5) and (a-c) no runoff or (d-f) 1200 m^3 s^{-1} runoff. All panels show transects along the fjord centreline, with the ocean boundary on the left. (a & d): Centreline temperature and salinity (contours) in simulations without icebergs. (b & e): The difference in centreline temperature and salinity in the corresponding iceberg simulations. (c & f): Centreline current velocity in the corresponding iceberg simulations, with positive values indicating up-fjord currents. The red line in each panel denotes the 27.3 potential density contour, approximating the interface between Polar Water and Atlantic Water. Note, the y-axis scale is stretched in the upper 200 m. x-axis distances correspond to those in Figure 7.6a.

(similarly to simulations described in Chapter 6). The cooling and freshening are most pronounced in the no-runoff scenario, but are more uniform and reach greater depths in the summer runoff forcing scenario. In addition, submarine iceberg melting is capable of driving an overturning circulation in the fjord (Figure 7.7), even in the absence of subglacial discharge. As was found in Sermilik Fjord (Chapter 5), this iceberg melt-driven circulation augments the runoff-driven circulation in most places, which is particularly apparent in the AW layer (Figure 7.8). In slight contrast to Sermilik Fjord, there are extensive up-fjord currents in the upper 50 m of the Kangerdlugssuaq domain, which icebergs cool (Figure 7.7) and weaken (Figure 7.8). In many ways, therefore, the effect of submarine iceberg melting on the properties of Kangerdlugssuaq Fjord are rather similar to that of Sermilik Fjord, with the principal difference being the substantial cooling and weakening of up-fjord currents in the upper 50 m of the Kangerdlugssuaq Fjord domain. It is noted that this did occur to a degree in the Sermilik Fjord domain, but

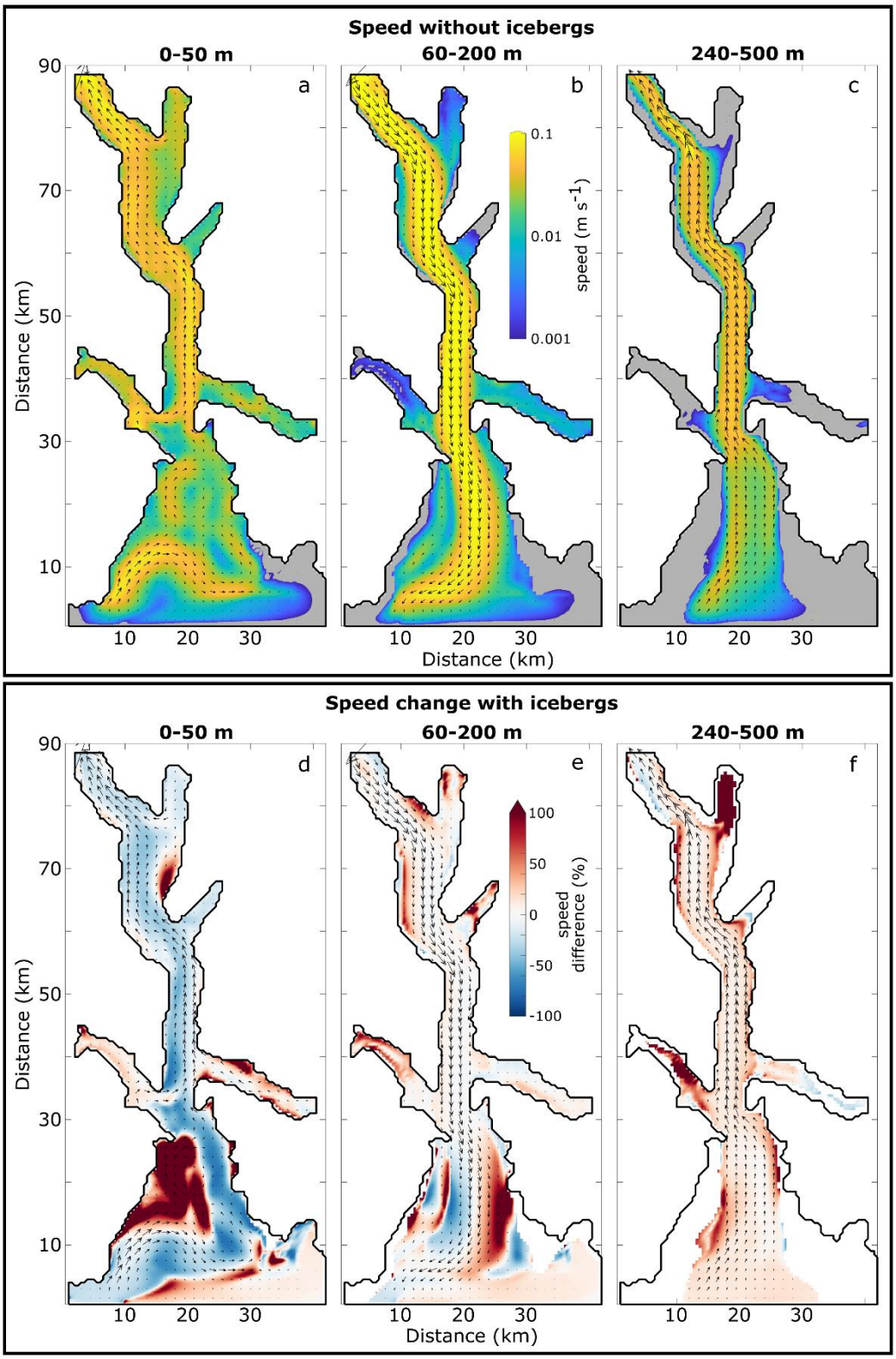

Figure 7.8. The effect of iceberg melting on the circulation of Kangerdlugssuaq Fjordin the 'summer runoff forcing' scenario. (a-c) Average current speed over the indicated depths in simulations without icebergs, with velocity vectors overlaid. (d-f) Average speed change when icebergs are included. In all panels, the ocean boundary is at the bottom. Axis distances correspond to those in Figure 7.6a.

the extent and speed of near-surface up-fjord currents in that domain were minimal even without icebergs.

The effect on up-fjord heat flux is different to that of Sermilik Fjord, largely because of the substantial cooling and weakening of near-surface up-fjord currents in the Kangerdlugssuaq domain (Figure 7.9). In the Kangerdlugssuaq domain, icebergs caused an overall 12.5% *reduction* in up-fjord heat flux across the flux gate (location in Figure 7.6). This is compared to the overall ~10-40% *increase* in up-fjord heat flux found in Sermilik Fjord in Chapter 5. Icebergs decreased net up-fjord heat flux in the Kangerdlugssuaq domain because of a 50.1% decrease in up-fjord heat flux in the upper 50 m, which offsets a 13.3% increase between 50 and 500 m in the summer runoff forcing scenario (Figure 7.9b). The vertical pattern of heat flux change due to icebergs is therefore entirely consistent with the findings presented in Chapter 5. However, the near-surface reduction in up-fjord heat flux is much more pronounced in the Kangerdlugssuaq domain because, consistent with observations (Inall et al., 2014), the near-surface up-fjord currents contribute substantially to the net up-fjord heat flux in simulations without icebergs. Since these currents are at a depth where iceberg-ocean interaction is prevalent, the icebergs have greater potential to reduce up-fjord heat flux in Kangerdlugssuaq Fjord than in Sermilik Fjord, where the primary pathway for oceanic heat delivery to Helheim Glacier is restricted to depths at which direct iceberg-ocean interaction is minimal. These two regimes, linking iceberg-ocean interaction and fjord circulation, are shown schematically in Figure 7.10 - the net effect of icebergs on up-fjord heat flux will depend on which of these regimes a fjord falls into.

Regardless of the net effect on up-fjord heat flux in either fjord, the modelling presented in this thesis suggests that submarine iceberg melting increases up-fjord heat flux in the AW layer – which is at a depth range thought to be critical to glacier stability. In the sensitivity tests presented in Chapter 5, icebergs increased up-fjord heat flux in the AW layer for almost all combinations of iceberg concentration, draught and size-frequency distribution. Although these sensitivity tests did not cover the entire parameter range relevant to Greenland's glacier-fjord system systems, nor all fjord geometries, they do nonetheless indicate that icebergs likely increase up-fjord heat flux at depth in many of Greenland's fjords, with the effect being greater in fjords with greater submerged iceberg areas. In addition, the results presented in Chapter 6 suggest that icebergs may also increase water temperature at the ice-ocean interface over certain depth ranges by

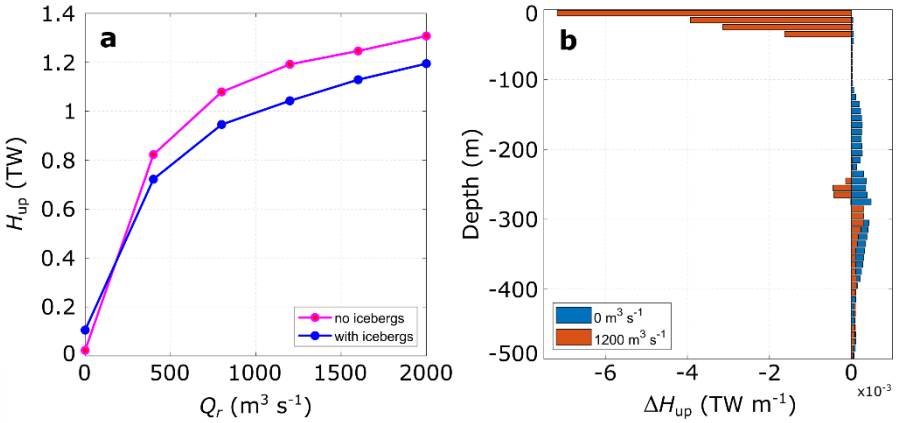

Figure 7.9. The effect of submarine iceberg melting on up-fjord oceanic heat flux in the Kangerdlugssuaq Fjord domain. (a) Relationship between runoff (Q_r) and up-fjord oceanic heat flux (H_{up}) across the flux gate shown in Figure 7.6. (b) Change in up-fjord heat flux (ΔH_{up}) due to icebergs.

upwelling warm water from below, further demonstrating the important role of icebergs in influencing ice sheet - ocean interaction. Chapter 6 also showed that even high concentrations of very deep icebergs do not cause substantial cooling in the AW layer, and so it is expected that icebergs will increase up-fjord heat flux in the AW layer in the majority of Greenland's fjords. As yet, observations of iceberg dimensions and distributions are relatively sparse (Barker et al., 2004; Dowdeswell et al., 1992; Kirkham et al., 2017; Rezvanbehbahani et al., 2020; Sulak et al., 2017), and there are even fewer observations of changing iceberg distributions through time (Moyer et al., 2019), and so it is not yet possible to quantify the impact of icebergs on ice sheet – ocean interaction in many fjords nor how this has changed over time. Generating measurements of iceberg draught, length, concentration and size-frequency distribution for entire fjords, as well as over seasonal and longer-term timescales, is therefore important if we are to better constrain the impact of icebergs on the ice sheet.

7.3 Implications for modelling tidewater glacier behaviour

The first major implication of this thesis for glacier modelling concerns the interactions between subglacial hydrology and ice velocity. At tidewater glaciers where a seasonal meltwater-induced velocity change is observed, the results presented in this thesis suggest that seasonal subglacial channel formation acts to curb the meltwater-induced speed-up, in much the same way as is observed at land-terminating sectors (e.g. Sundal et al., 2011)

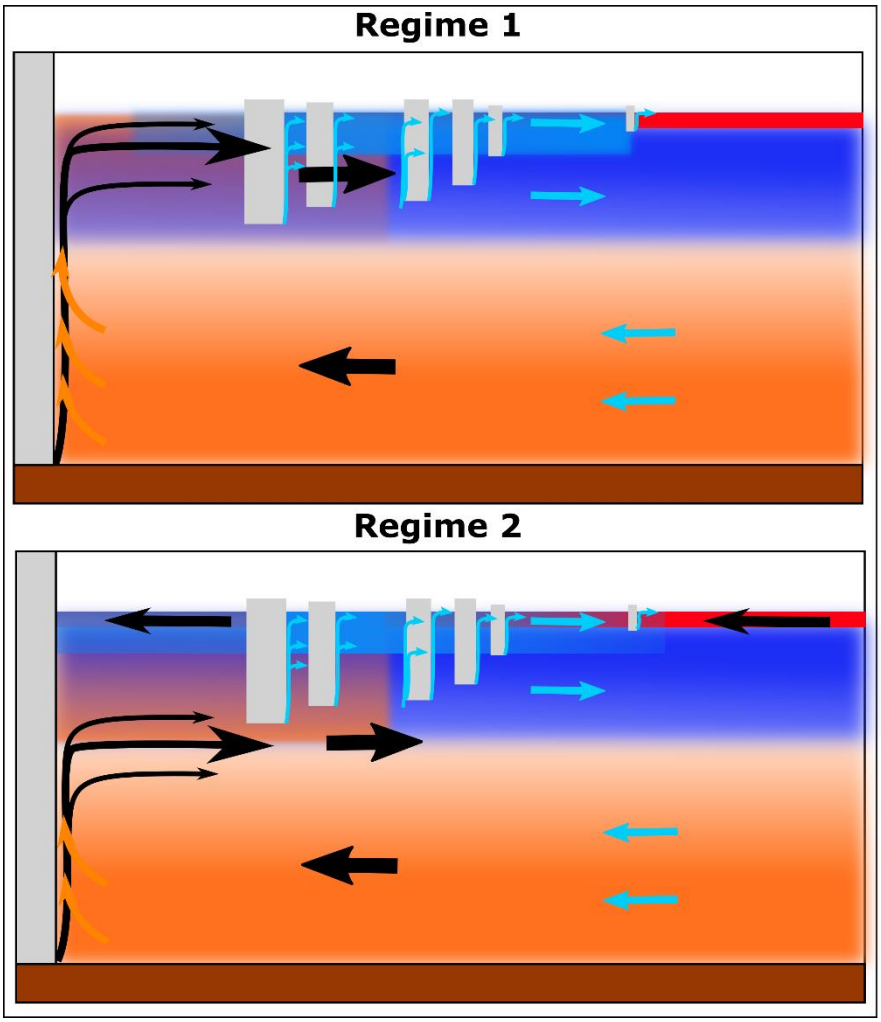

Figure 7.10. Schematic of the two modes of iceberg-ocean interaction identified in this thesis, showing the buoyancy-driven circulation (or runoff-driven circulation) with black arrows and the iceberg melt-driven circulation (cyan arrows). In 'Regime 1' the plume terminates at or very near the fjord surface, so the only compensatory current is at depth. Whereas in 'Regime 2', the plume terminates at the Polar Water-Atlantic Water interface, generating compensatory currents near the fjord surface as well as at depth. Icebergs substantially cool surface and near-surface waters, and so in Regime 2, icebergs cool the near-surface up-fjord current. In both regimes, icebergs generate down-fjord currents at and near the fjord surface and augment the up-fjord current at depth.

and at many Alpine glaciers (e.g. Hubbard & Nienow, 1997). Given the similarity in observed flow variations, which are thought to be caused by the same underlying physical processes, it is expected that this result is applicable to other tidewater and lake-terminating glaciers on Greenland outside of the ice sheet and elsewhere on Earth where sufficient volumes of meltwater are produced to cause seasonal subglacial channel growth. In addition, and as previously reported (e.g. Moon et al., 2014; Vijay et al., 2019),

this thesis found no evidence of systematic variation in glacier velocity in response to variation in meltwater supply on interannual timescales. This suggests therefore that future increases in meltwater runoff will not lead to higher basal water pressures and thus ice velocities at tidewater glaciers, when considered on interannual timescales. Including these processes in ice sheet models may not therefore be necessary in order to generate accurate estimates of glacier behaviour on annual-and-longer time scales. It should be noted, however, that seasonally evolving subglacial hydrology and changes in meltwater supply may affect tidewater glacier dynamics in other ways, such as by modifying the temporal and spatial distribution of terminus submarine melting (Cook et al., 2020; Cowton et al., 2019; Slater et al., 2015).

The second major implication of this thesis for modelling tidewater glacier dynamics relates to iceberg-induced modification of ocean forcing of Greenland's tidewater glaciers. This thesis has shown that submarine iceberg melting can (i) increase up-fjord oceanic heat flux at depth by increasing the velocity of up-fjord currents and/or by inducing upwelling of warmer water, and; (ii) reduce up-fjord heat flux near the surface due to cooling and opposing of otherwise-warm near-surface waters. In Chapter 6, it was shown that even relatively low concentrations of small icebergs can cause substantial cooling in the upper several tens of metres of the water column, potentially making iceberg-modification of near-surface waters important in many of Greenland's fjords. In addition, in fjords with high concentrations of icebergs (which is typical of those hosting large glaciers that contribute substantially to ice sheet mass loss), icebergs can substantially modify water temperature throughout large parts of the water column, particularly in the PW layer. Therefore, it will be necessary to incorporate the effect of iceberg-ocean interaction on fjord water properties into simulations of glacier behaviour, even for fjords with relatively few icebergs. At present, this is perhaps only achievable in the most sophisticated ice sheet models that are capable of representing vertical variations in terminus submarine melt rates (e.g. Goelzer et al., 2020). Arguably the simplest approach to represent the effect of icebergs would be to adjust the temperature profiles used to force the ice sheet so that they reflect the temperature modifications induced by submarine iceberg melting. This will likely require the development of ways to parameterise iceberg-ocean interaction in numerous fjords, such as by using a box model approach (e.g. Gillibrand et al., 2013).

The insights (particularly Figure 7.10) gained from the iceberg-ocean interaction research in this thesis are applicable to tidewater and lake-terminating glaciers outside of the Greenland Ice Sheet; however, the specific impact on near-glacier circulation and glacier submarine melting are, as has been demonstrated here, dependent upon the water column stratification. In settings where sub-aqueous heat delivery to calving fronts is concentrated near the water column surface, icebergs will greatly reduce the heat available for glacier submarine melting, whereas in settings where the majority of heat is delivered below the maximum iceberg keel depth, icebergs are not expected to reduce the heat available for glacier submarine melting. The effect of iceberg melting on the circulation of proglacial lakes may be further complicated by the diverging effects of temperature changes on density around 3.98°C – in freshwater lakes that are warmer than this, the addition of freshwater will increase water density and therefore promote sinking of the melt-ambient water mixture. Exploration of the effect of icebergs on lake-terminating glacier submarine melt rates should be considered a future research avenue.

7.4 Further work

The research presented in this thesis has helped to improve understanding of key processes operating in glacier-fjord systems. As should be clear from the preceding discussion, however, considerable further work is required to develop a deeper understanding of glacier-fjord systems and particularly how the processes operating in them affect the behaviour of the ice sheet.

This thesis has shown that submarine iceberg melting is capable of significantly modifying water properties within Greenland's fjords. An important next step is to incorporate this process within ice sheet scale projections of future glacier behaviour. Doing so will require progress in several areas of related research. Firstly, an appropriate parameterisation for processes operating within Greenland's fjords that modify water properties is required. Such a parameterisation may be based on relationships between subglacial discharge, water properties and various iceberg descriptors (or simply iceberg surface area) to calculate temperature and salinity change through the water column, or a box-model approach that captures the key physical processes may be more successful (e.g. Gillibrand et al., 2013). Regardless of approach, the aim of these parameterisations should be to derive realistic estimates of water column temperature and salinity at the ice sheet-ocean interface, rather than rely on unmodified measurements or reanalysis data from outside Greenland's fjords.

In order to inform the development of such a parameterisation, and to test it on fjords around Greenland, further observations of fjord water properties in a range of glacial fjords, particularly close to glacier termini are required. Project Oceans Melting Greenland (https://omg.jpl.nasa.gov/) has already contributed substantially to this effort, acquiring roughly annual measurements of water properties in many of Greenland's fjords, including close to many tidewater glaciers, since 2016 (Fenty et al., 2016). This should be supplemented by intensive and long-term surveys of fjords, such as those that have been conducted in Kangerdlugssuaq and Sermilik fjords (e.g. Straneo et al., 2016). In many ways then, this avenue of research and data collection is underway, but the research presented in this thesis adds greater impetus to this endeavour.

Many more measurements of iceberg size and distribution are also required to inform and test parameterisations of iceberg-ocean interaction. These measurements should focus on two keys spatial scales. Firstly, detailed surveys of individual icebergs, focusing on deriving iceberg aspect ratios, shape and submarine melt rates are required to refine and test models such as that presented in Chapter 5. Secondly, measurements of iceberg length, draught and size-frequency distribution are required at the fjord scale (such as those presented in Sulak et al. (2017)). Measurements in many fjords with concurrent oceanographic data, as well as time-series observations of icebergs, would be desirable.

Such data could effectively be utilised in simulations such as those presented in Chapters 5 and 6, but to build on the work presented in this thesis it will be necessary to examine a range of fjords with different characteristics (such as iceberg concentration and grounding line depth) or a single fjord over time. This approach would allow identification and better characterisation of the key mechanisms by which iceberg melting affects fjord circulation, as well as better quantification of oceanic heat flux to key glaciers during periods of rapid change (as in Cowton et al. (2016a)). A second avenue of experimental design would be to extend the research presented in Chapter 6 by examining temporal variations in oceanographic conditions, in order to, for example, quantify the extent to which iceberg melting buffers or amplifies changes in open ocean conditions over timescales ranging from a few days to a season. In this avenue of research, it would be informative to examine the propagation of tracers into the fjord in response to a Greenland-relevant range of iceberg conditions and forcing mechanisms (such as runoff and barrier wind events). This would greatly improve our understanding of the nature and

timescales of forcing that can propagate down fjords and modify glacier-adjacent water properties enough to perturb tidewater glaciers.

Although seasonal changes in subglacial hydrology and meltwater supply do not appear to lead to significant changes in annual ice velocity at tidewater glaciers, subglacial hydrology is likely to be an important control on the spatial distribution of submarine melting and should therefore be a focus of further research. From the research presented in this thesis, it is clear that subglacial channels (or at least relatively narrow drainage forms) can develop beneath fast-flowing glaciers. However, our understanding of tidewater glacier subglacial hydrology is not yet mature enough to characterise how evolving subglacial hydrology will affect the spatial and temporal distribution of meltwater efflux across glacier grounding lines; therefore, further observations are required to both improve subglacial drainage theories and to constrain the timing and extent of channelisation beneath tidewater glaciers. One approach to achieve this could be to expand the analysis presented in Chapter 4, to infer the timing of subglacial channelisation over multiple melt seasons at a large number of tidewater glaciers, and to compare the resulting dataset to models of subglacial channel evolution. Another approach would be to obtain geophysical observations, such as by using seismic arrays to observe glaciohydraulic tremor induced by subglacial water flow, from which subglacial drainage characteristics can be inferred (e.g. Bartholomaus et al., 2015; Nanni et al., 2020; Vore et al., 2019). Ideally, these geophysical observations should be obtained as close to glacier termini as possible and covering time periods with different melt characteristics.

7.5 Concluding remarks

This thesis has undertaken detailed observations and novel modelling of Greenland's glacier-fjord systems in order to improve understanding of key processes affecting the behaviour of Greenland's tidewater glaciers. It is clear from this thesis and related research that glacier-fjord systems are complex, being affected by a range of atmospheric and ocean phenomena over a large range of spatial and temporal scales. Despite considerable progress in recent decades, our incomplete understanding of glacier-fjord systems limits our ability to reliably predict the future evolution of the Greenland Ice Sheet.

This thesis has progressed our understanding of glacier-fjord systems in several ways. Firstly, this thesis has examined in detail the seasonal variations in ice velocity of

tidewater glaciers and has demonstrated that, in many cases, these variations can be explained as a consequence of evolving subglacial hydrology. More specifically, the seasonal development of efficient subglacial channels curbs seasonal meltwater-induced increases in ice velocity, even close to the terminus of very fast-flowing tidewater glaciers. There was little evidence to suggest that seasonal meltwater-induced velocity variations are capable of driving interannual changes in glacier behaviour. Therefore, it is not expected that further investigation of interactions between subglacial hydrology, meltwater supply and tidewater glacier dynamics is likely to lead to substantially improved understanding or predictions of tidewater glacier behaviour on annual-and-longer timescales. Further observations would help to test whether this conclusion applies at the ice sheet scale and would help to constrain the key controls on subglacial channel formation at tidewater glaciers. Evolving subglacial hydrology on seasonal timescales may however be an important control on terminus submarine melting and fjord circulation, and so improved understanding of tidewater glacier subglacial hydrology should still be sought.

Secondly, the effect of icebergs on fjord circulation and fjord water properties has been investigated in detail. A new model for submarine iceberg melting was developed and applied to two major fjords in east Greenland and to several idealised domains. This research demonstrated that iceberg melting can increase oceanic heat flux to tidewater glacier grounding lines and that icebergs can modify glacier-adjacent water properties in a variety of ways and non-uniformly through the water column. In this way, icebergs will likely have affected oceanic forcing of the Greenland Ice Sheet in recent decades. Therefore, icebergs should be included in estimates of ocean forcing of the Greenland Ice Sheet, but further work is required to quantify their role in affecting temporal variations in oceanic forcing of tidewater glaciers, which will allow more reliable predictions of future tidewater glacier behaviour.

Chapter S1: Supporting information for 'Subglacial drainage evolution modulates seasonal ice flow variability of three tidewater glaciers in southwest Greenland'

This supporting information contains additional analysis details and figures, which support the conclusions and discussion presented in the main text. Figures are numbered in the order they are mentioned in the main text. This supporting information examines the sensitivity of our plume modelling to boundary conditions and key model parameters and is supported by Figures S1.4 and S1.5. Other supporting figures are not discussed here but provide details not available in the main text.

S1.1. Plume modelling sensitivity analysis

Subglacial discharge and sediment concentration, fjord water temperature and salinity, grounding line depth and the rate at which plumes entrain ambient fjord water can all affect whether modelled plumes reach the fjord surface. The effect of variations in subglacial discharge sediment load are discussed by Slater et al. (2017), who show that plumes still readily reached the fjord surface, even with high sediment load (as represented by a high initial salinity). Slater et al. (2017) also considered the effect of

bathymetric uncertainty in their modelling and found that it did not alter their conclusions. Since then, bathymetric surveys and expendable CTD casts deployed adjacent to the glacier calving fronts studied here (Motyka et al., 2017) have increased our confidence in the glacier grounding line depths used here (250 m for Kangiata Nunaata Sermia (KNS), 175 m for Narsap Sermia (NS) and 140 m for Akullersuup Sermia (AS)).

First, we consider catchment runoff. RACMO2.3p2 is a leading regional climate model for simulating surfacing melting of the Greenland Ice Sheet (Noël et al., 2016) and its high spatial resolution makes it particularly suitable for estimating surface melting of narrow tidewater outlet glaciers, such as those studied here. The area over which surface melting was integrated was determined by hydropotential analyses. These assumed that basal water pressure was equal to ice overburden pressure and were sensitive to uncertainties in the ice surface and bed topography dataset (Morlighem et al., 2017). Carroll et al. (2016) assessed the effect of bed topographic uncertainties using a Monte Carlo-based approach and showed that, although the size of KNS catchment varied, most of the variation was at high elevations, where little surface melting occurs. Subglacial water transport velocities, and neglecting supraglacial routing and storage, affect the temporal integration of discharge at the terminus from each glacier. We used end-member estimates of subglacial water transport velocities (0.05 and 1 m s-1 for distributed and channelised drainage configurations, respectively (Cowton et al., 2013)) to assess the effect of these assumptions. Even with very slow transport velocities, and therefore subdued subglacial discharge, modelled discharge was usually much greater than the critical discharge required for a plume to reach the fjord surface and, therefore, resulted in just a 2.8% reduction in the number of occurrences of inferred inefficient drainage (Figure S1.4). The sudden release of meltwater from supraglacial stores (i.e. rapid supraglacial lake drainage) would cause spikes in discharge that are not captured by our method. This could be a possible explanation for instances of plume surfacing at times of relatively low subglacial discharge in the latter half of each melt season. Finally, RACMO2.3p2 may underestimate non-radiative energy fluxes, resulting in an underestimation of runoff. Van As et al. (2018) estimated this to be ~20% for the Watson River catchment, west Greenland. We therefore performed experiments with runoff increased by 20%. At KNS, this resulted in only 2 additional occasions of inferred inefficient drainage during the study period, but increased the number of outlets required to prevent plume surfacing by approximately 3, on average. The overall effect – little

change in the temporal pattern of inferred drainage state, but with more outlets required to prevent plume surfacing - was similar at AS and NS.

We also consider the effect of variations in the rate of modelled plume entrainment on our conclusions. In buoyant plume theory, the rate at which the plume entrains fjord water is proportional to the vertical velocity of the plume. In the main text, the constant of proportionality, α, was set to 0.1. We assess the sensitivity of our results to this choice by considering low (α=0.05) and high (α=0.15) values, which are lower and upper bounds on the range of values used in the literature. As in Slater et al. (2017), the value of α did not strongly affect the height reached by the plume or greatly reduce the number of outlets required to prevent modelled plume surfacing (Figure S1.4). For example, increasing the entrainment coefficient in the plume model by 50% reduced the total number of occurrences of predicted inefficient drainage by 13.1%, but did not alter the seasonal pattern.

In the main text, we defined periods of inefficient drainage as occasions where the number of modelled outlets required to prevent plume surfacing was greater than or equal to two. We examined the sensitivity of our results to this choice by using thresholds of 3-5 (an example for KNS is shown in Figure S1.5). For all threshold values, the seasonal pattern of inferred changes in subglacial hydraulic efficiency is similar, with frequent occurrences of inefficient drainage in the first half of the melt season, and more occurrences of efficient drainage afterwards. The number of occurrences of inefficient drainage decreases as we increase the threshold value, and with threshold of five there are far fewer occurrences of inefficient subglacial drainage. However, given the narrow width of the glaciers considered here, we think it unlikely that these glaciers host four efficient subglacial channels. Instead, it seems probable that one of the smaller thresholds provides a suitable indication of the times in which the drainage system is likely to be overwhelmed by the supply of meltwater, and therefore operate at high pressure.

We finally discuss the effect of the fjord water temperature and salinity profiles used here. In the main text, we used CTD data acquired over 30 km from the glacier during 2014-2016. Unfortunately, there were no data available closer to the glacier throughout the study period or in the inner fjord during 2017-2019. Ice melting near tidewater glacier termini and ice sheet runoff strengthens fjord stratification, hindering plume surfacing (De Andrés et al., 2020). Using relatively far-field CTD data may therefore have biased our results towards indicating an inefficient drainage system. However, bounding our

plume model with a single CTD cast, acquired ~70 km from KNS in August 2016 (when fjord stratification was strongest), reduced the occurrence of inferred inefficient drainage by just 4.6%. We attempted to fill the 2017-2019 data gap using monthly CTD casts acquired at the fjord mouth by the Greenland Ecosystem Monitoring service (not shown; data available at www.g-e-m.dk). However, there was often very little water stratification at the mouth, which meant that extremely low discharges (less than 1e-6 m3 s-1) could still generate modelled plumes that reached the fjord surface (i.e. even when meltwater discharge was split between thousands of outlets, plumes still reached the fjord surface). We therefore chose not to use these data for our analysis.

In reality, freshwater is likely discharged heterogeneously across the grounding line of individual tidewater glaciers (e.g. Chauché et al., 2014; Fried et al., 2015; Jackson et al., 2017; Rignot et al., 2015) and it is plausible that freshwater may be discharged efficiently from more than one outlet (Bartholomaus et al., 2016; Slater et al., 2018). While our choice to assume an even division of discharge between outlets is likely a simplification, our approach is a practical means to gain an indication of when the drainage system was relatively efficient and inefficient (Slater et al., 2017).

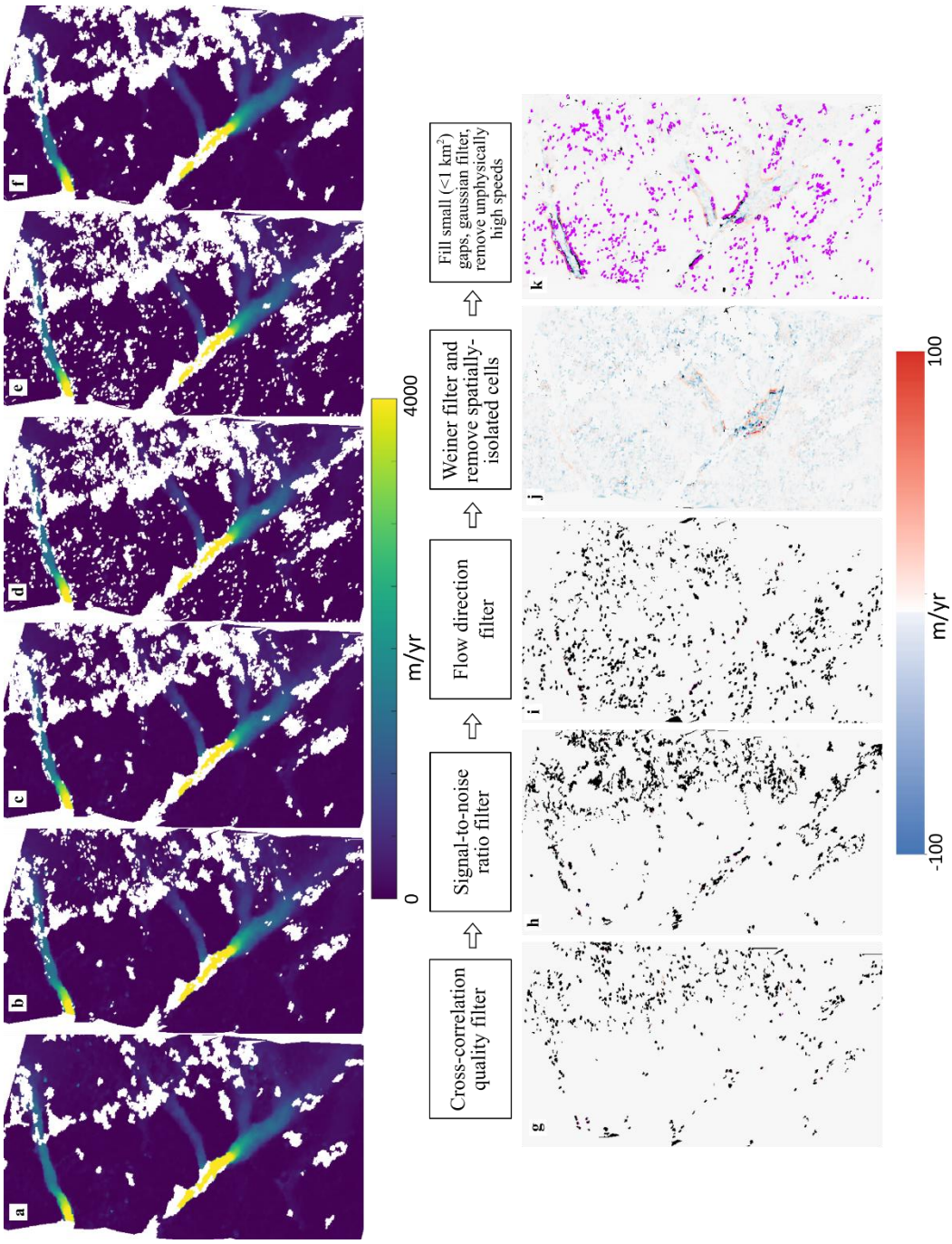

Figure S1.1. Velocity filtering stages. (a-f) Velocity estimates during 28 April 2019 to 4 May 2019 at each of the filtering stages. (g-k) change in velocity between the above filtering stages. The black areas indicate complete removal of velocity estimates whilst the purple areas indicate empty areas that have been filled during the filtering.

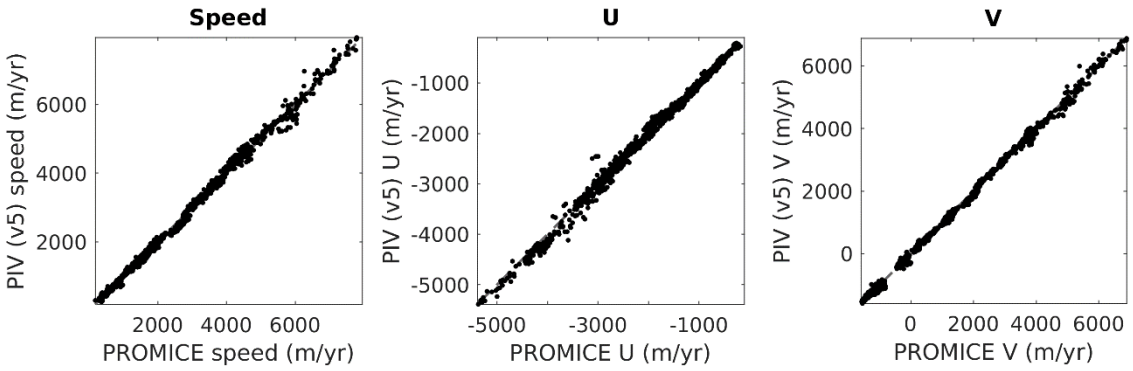

Figure S1.2. SCADI vs PROMICE velocity estimate. Comparison of our Sentinel 1 velocity estimates with those from PROMICE (https://www.promice.dk/).

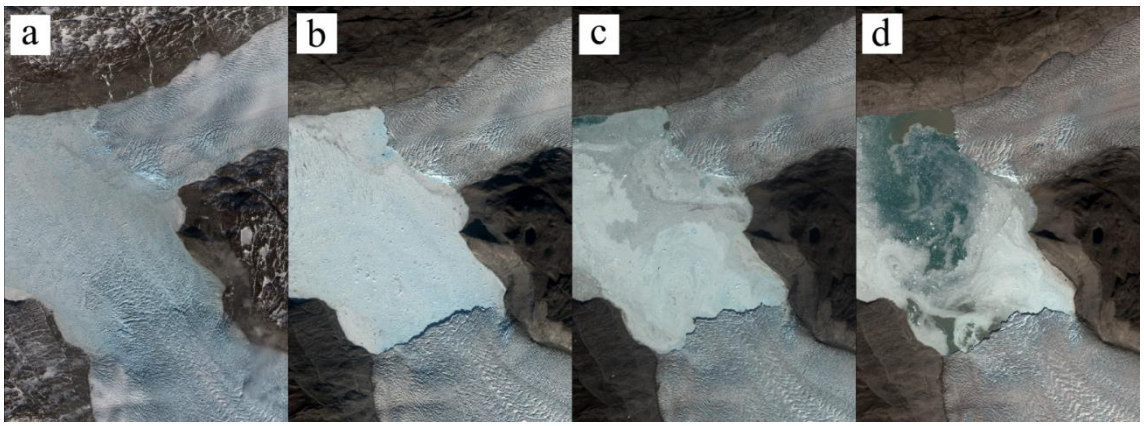

Figure S1.3. Observed plume surfacing states. (a) Ice tongue, or plume state -1. (b) No ice tongue and no plume surfacing, or plume state 0. (c) No ice tongue and plume surfacing adjacent to each glacier terminus, or plume state 1. (d) No ice tongue and plumes remain at the fjord surface, or plume state 2. When plume state was -1 or 0, we use modelled discharge to determine whether the lack of plume surfacing is due to distributed subglacial drainage.

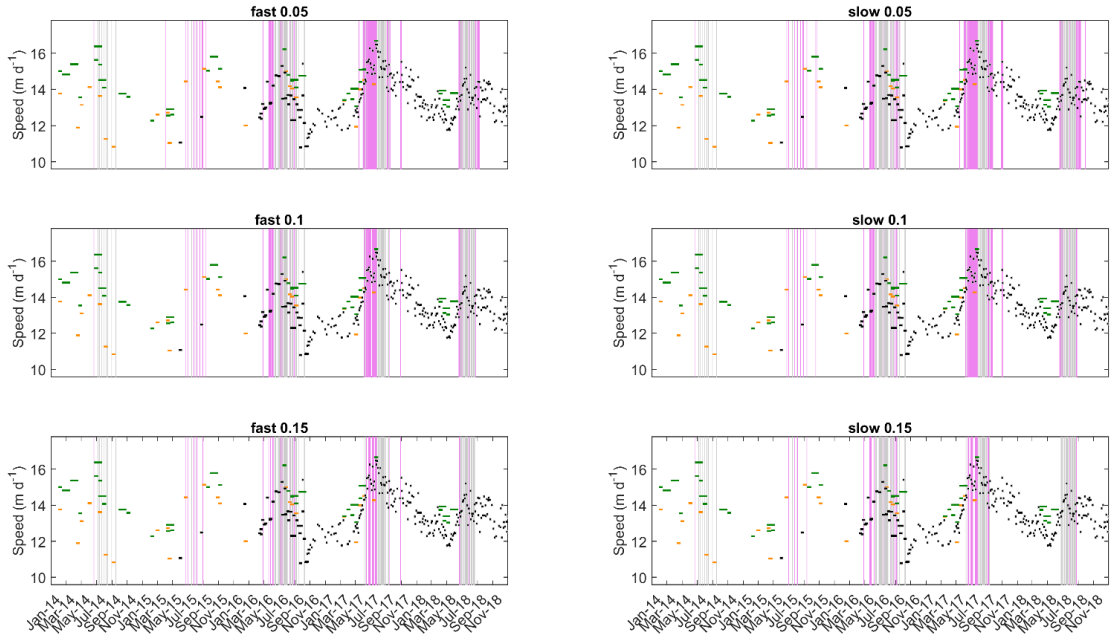

Figure S1.4. Plume sensitivity to subglacial water routing speed and entrainment coefficient at KNS. Colours are the same as in Chapter 4.

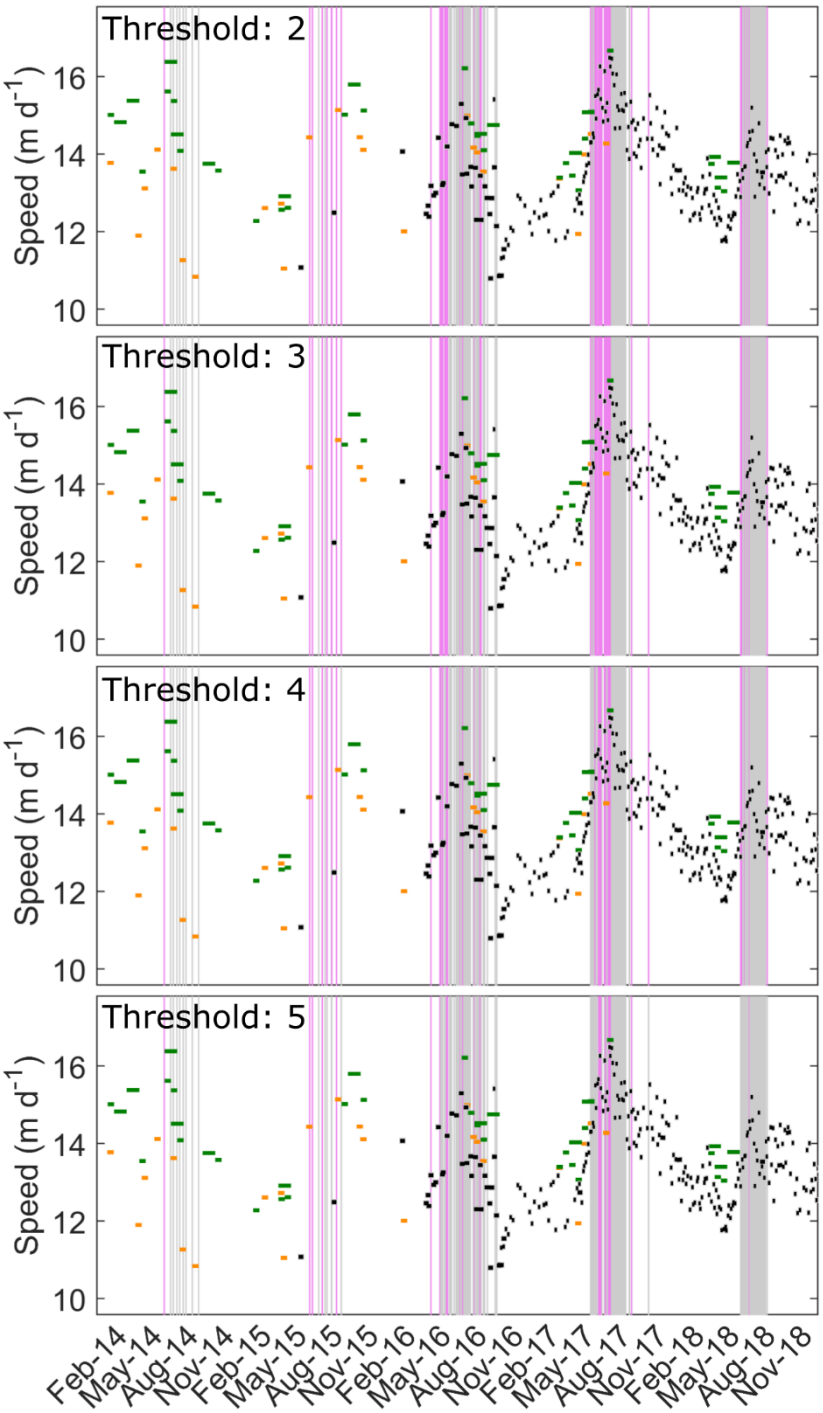

Figure S1.5. Sensitivity of drainage system classification to threshold number of outlets, where occurrences of inefficient subglacial drainage are defined as times where the number of modelled outlets is equal to or greater than the threshold number of outlets.

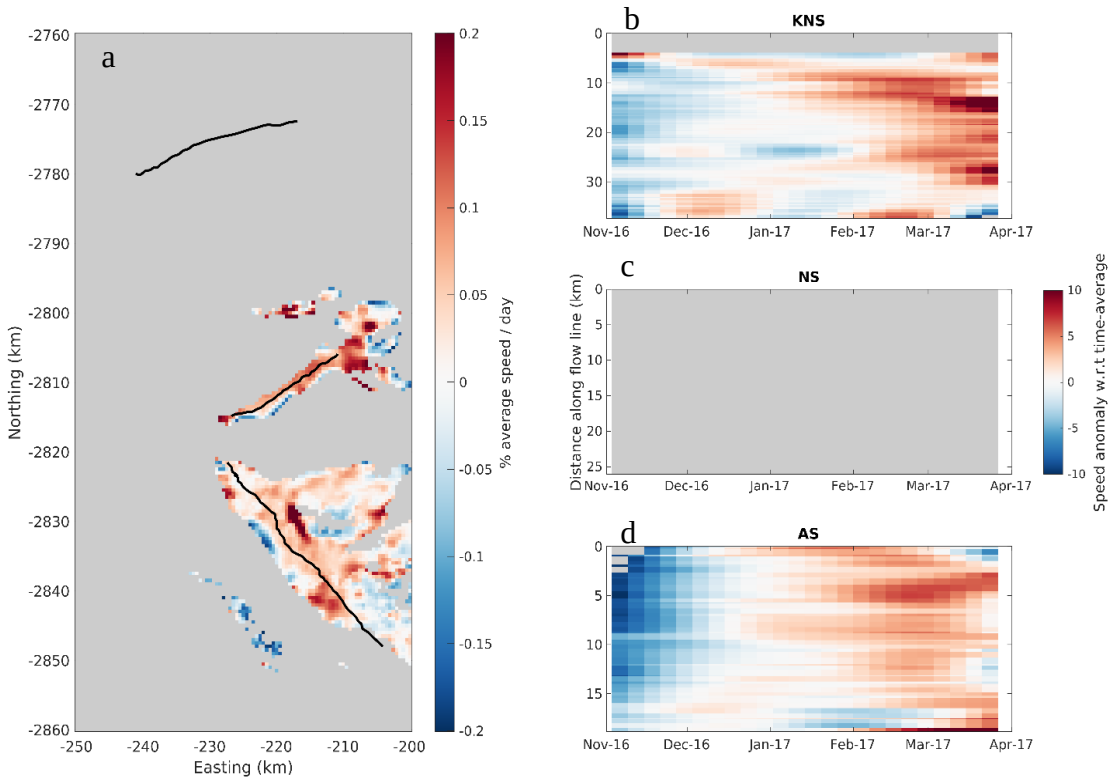

Figure S1.7. Winter recovery gradients 2016/2017. (a) average rate of speed change during November-April 2016/2017. (b-d) Time-series of speed, relative to the time-average, along the black flowlines plotted in (a). Flowlines start (0 km) near the terminus of each glacier. Data were extracted within a 1x1 km region around each flowline point.

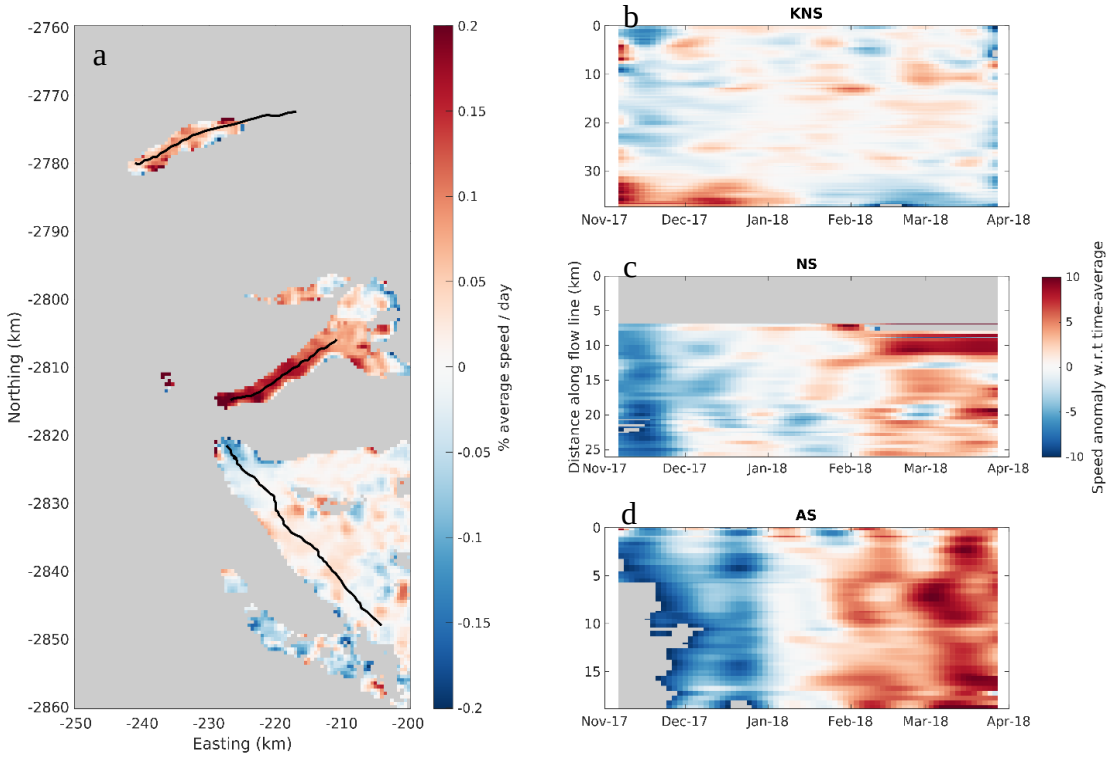

Figure S1.9. Winter recovery gradients 2017/2018. (a) average rate of speed change during November-April 2017/2018. (b-d) Time-series of speed, relative to the time-average, along the black flowlines plotted in (a). Flowlines start (0 km) near the terminus of each glacier. Data were extracted within a 1x1 km region around each flowline point.

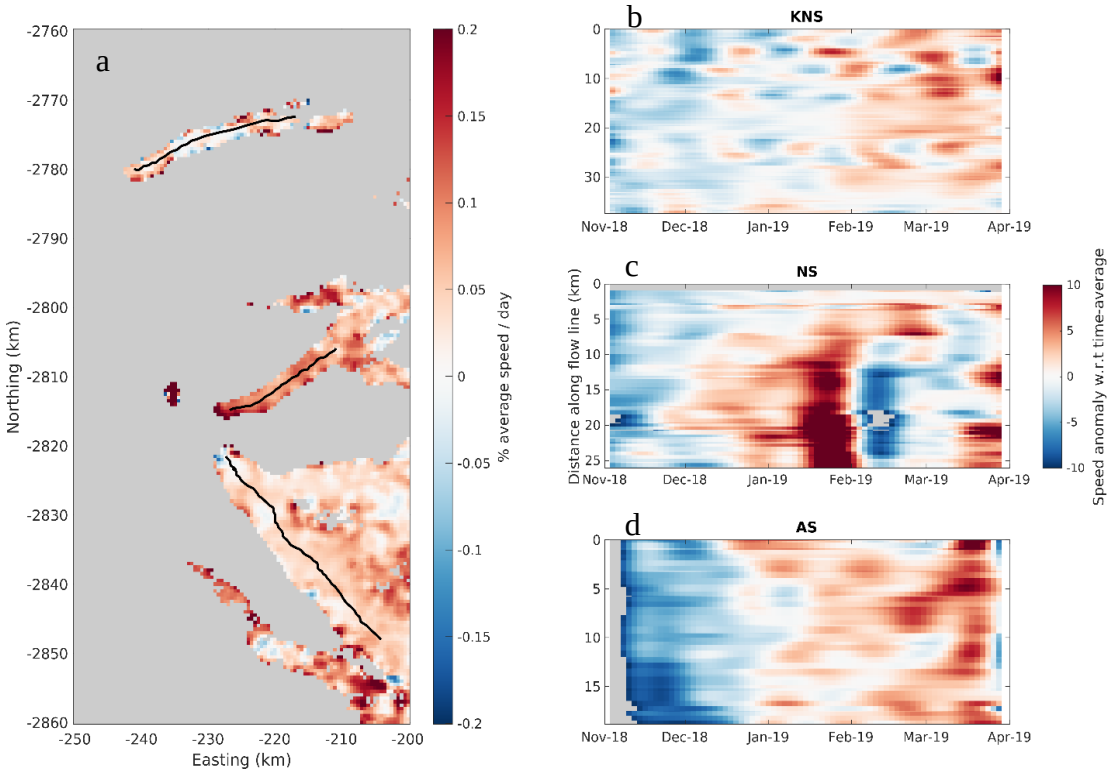

Figure S1.11. Winter recovery gradients 2018/2019. (a) average rate of speed change during November-April 2018/2019. (b-d) Time-series of speed, relative to the time-average, along the black flowlines plotted in (a). Flowlines start (0 km) near the terminus of each glacier. Data were extracted within a 1x1 km region around each flowline point.

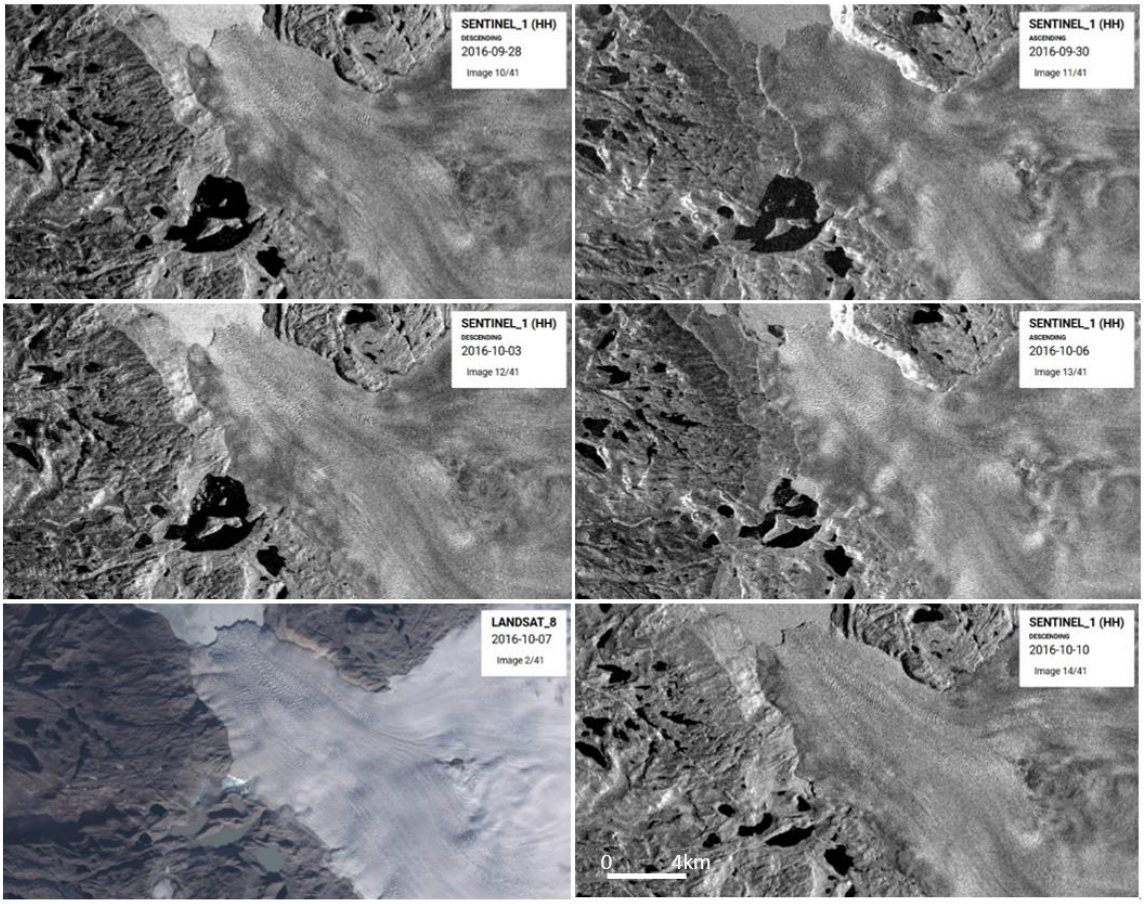

Figure S1.12. Isvand lake drainage. Note the plume on 06/10/2016 (second row and right column). Images are screenshots from GEEDiT (Lea, 2018).

Table S1.1. Annually averaged ice velocity and modelled subglacial discharge.

Velocity (m yr^{-1}; April 1st – March 31st)			
	2016/2017	**2017/2018**	**2018/2019**
KNS	4641	5177	4804
NS	4493	4627	4600
AS	837	800	839

Subglacial discharge (m^3 s^{-1}; January 1st – December 31st)			
	2016	**2017**	**2018**
KNS	105.8	70.2	59.6
NS	84.1	42.4	42.7
AS	33.8	22.0	19.8

Chapter S2: Supporting information for 'Iceberg melting substantially modifies oceanic heat flux towards a major Greenlandic tidewater glacier'

This auxiliary material supports the results, discussion and conclusions presented in the main text. More specifically, it provides further detail on the methodology and reasoning underlying the generation of icebergs in our model, and is supported by Figure S2.1. Figures S2.2-10 and Tables S2.1-3 are not discussed here but support the arguments in the main text. Figures are included in the order they are mentioned in the main text.

S2.1. Iceberg distributions

For our model, it is necessary to prescribe both the location of icebergs within the model domain, and their dimensions. To achieve this, the user provides the exponent of the power law describing the size-frequency distribution of icebergs throughout the fjord as whole, the maximum draught (or length) of the icebergs to be generated (i.e. the upper limit in the size-frequency distribution), and a 2-D array of desired iceberg cover (at the fjord surface) in plan-view — that is, the proportion of each cell in plan-view that is to be taken up by icebergs. This array is used to calculate the total area of the fjord surface that should be taken up by icebergs (henceforth the fjord-wide target area). Each of these

inputs are available in the form of existing observations (Sulak et al., 2017) or can be idealised. We then generate the fjord-wide size-frequency distribution such that the total surface area of the generated icebergs in plan-view is within 1% of the fjord-wide target area. Individual icebergs from this distribution are allocated to cells throughout the fjord, in such a way as to minimise the difference with the desired iceberg cover (Figure S2.1). Throughout this process, we account for the bathymetry of the fjord (i.e. icebergs cannot extend below the seafloor), which (in the setup used here) generally resulted in the deeper icebergs being placed close to the head of the fjord (Figure S2.1).

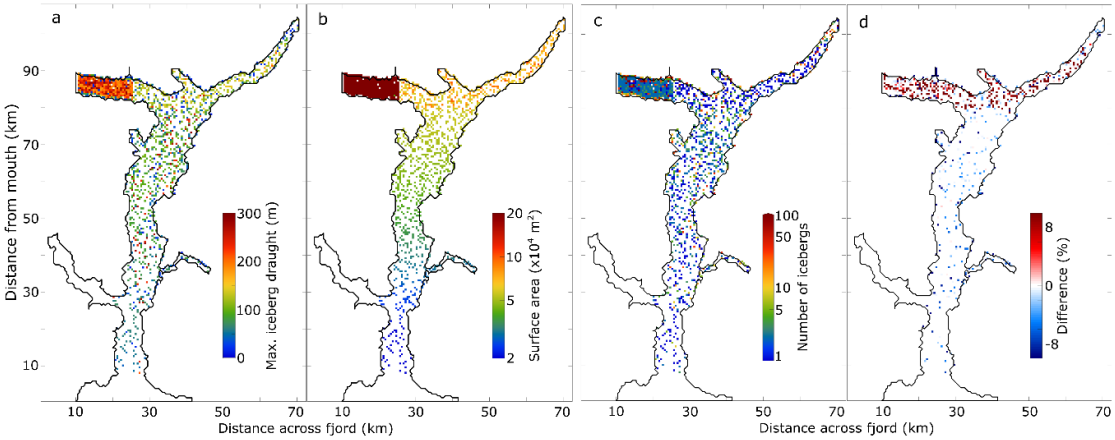

Figure S2.1. Iceberg distributions in Sermilik Fjord. (a) Maximum iceberg draught in each cell. (b) Derived iceberg surface area at the fjord surface in plan-view. (c) Number of icebergs per cell. (d) Difference between derived and target iceberg surface area, as a percentage of the target surface area, with positive values indicating that the derived surface area was greater than the target.

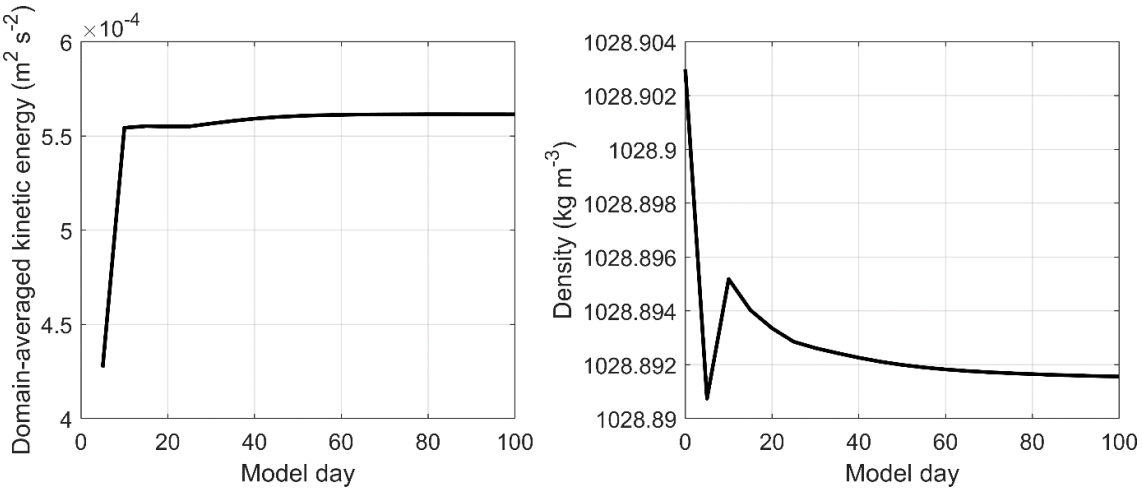

Figure S2.2. Example assessment of simulation steady-state conditions from the summer runoff forcing scenario. (a) Domain-averaged kinetic energy. (b) Depth-averaged modelled density through a water column in the middle of the fjord.

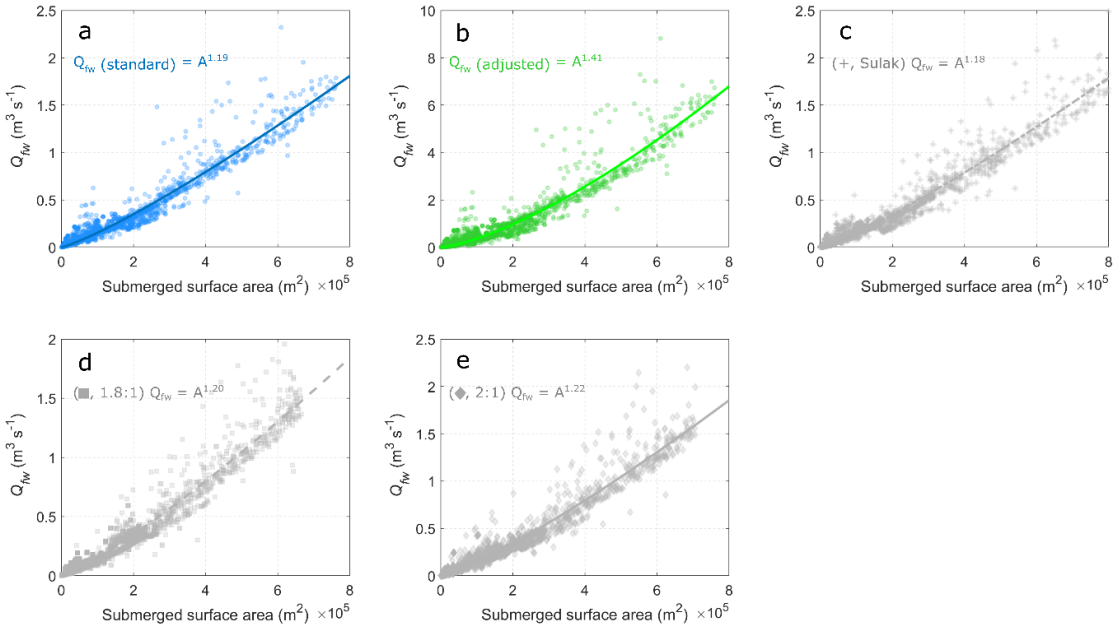

Figure S2.3. Relationship between submerged iceberg surface area and freshwater flux for individual icebergs. All plots show simulations with 'channelised' subglacial hydrology and 1200 m^3 s^{-1} runoff with: (a) standard melt rate parameter values (i.e. the summer runoff forcing scenario), (b) adjusted melt rate parameter values (Jackson et al., 2020), (c) volume-area relationship of Sulak et al. (2017), (d) length to keel depth ratio of 1.8:1 and, (e) length to keel depth ratio of 2:1. Note the differing y-axis scales between plots.

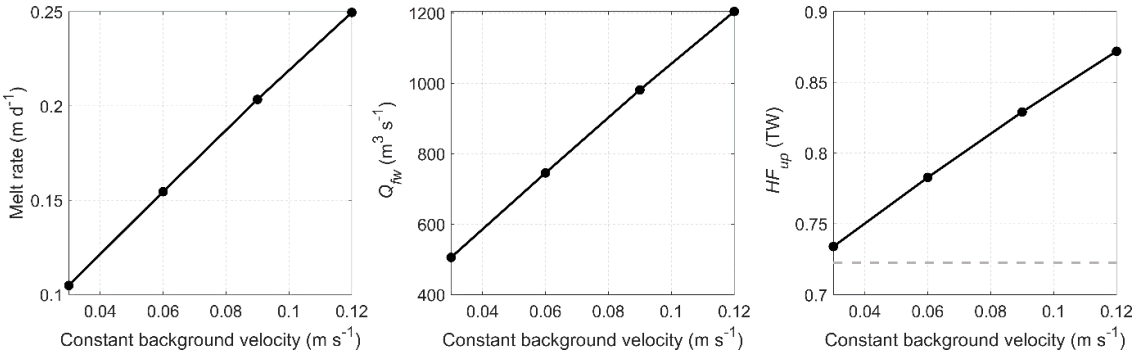

Figure S2.4. Sensitivity of key results to constant background velocity at iceberg-ocean interface. The dashed grey line in the right panel is the up-fjord heat flux across the mélange flux gate in the no-iceberg scenario (location in Figure 5.1a).

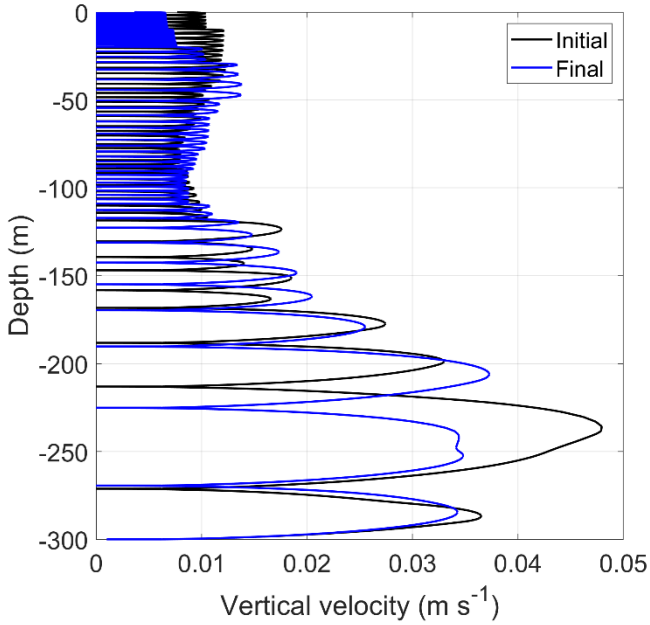

Figure S2.5. Depth-varying background velocity used to bound sensitivity simulations. Background velocities were estimated using the line plume model of Jenkins (2011), which was bounded by the initial conditions (black line) and domain-averaged final conditions (blue line) of the summer runoff forcing scenario.

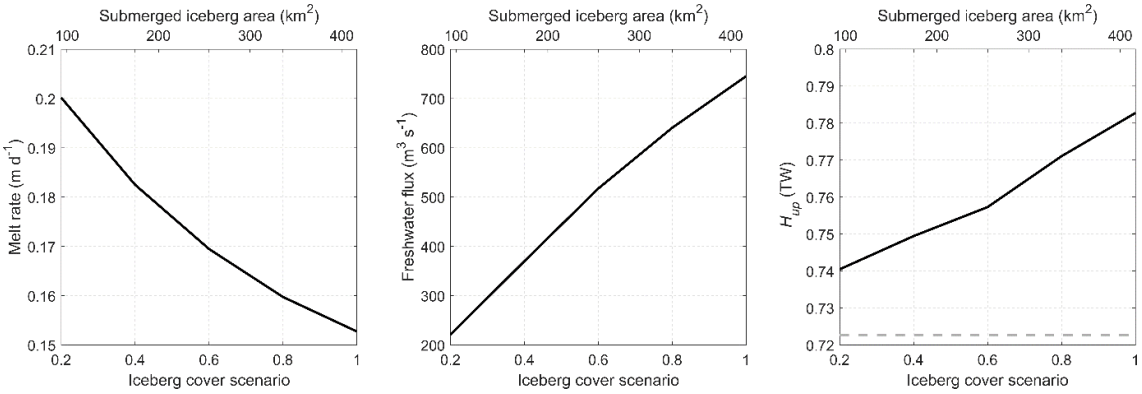

Figure S2.6. Sensitivity of key results to maximum iceberg cover and submerged surface area. Iceberg cover scenarios 0.2-0.8 have approximately 20-80% of the plan-view iceberg surface area as the primary simulations discussed in them main text (cover scenario 1 here). The dashed grey line in the right panel is the up-fjord heat flux across the mélange flux gate in the no-iceberg scenario (location in Figure 5.1a).

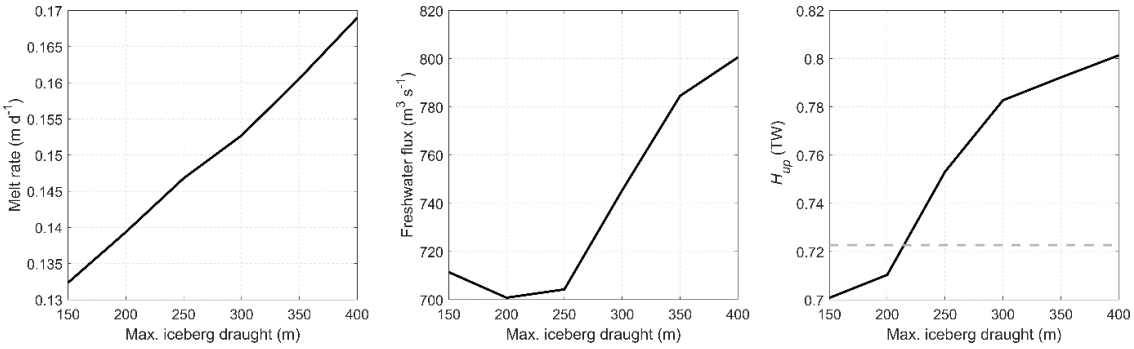

Figure S2.7. Sensitivity of key results to maximum iceberg draught. The dashed grey line in the right panel is the up-fjord heat flux across the mélange flux gate in the no-iceberg scenario (location in Figure 5.1a).

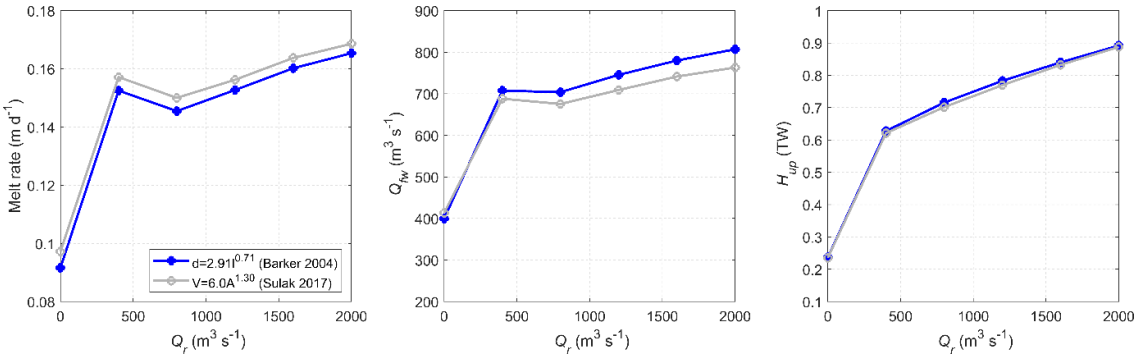

Figure S2.8. Sensitivity to iceberg aspect ratio used. The aspect ratio of Barker (2004) was used in the primary simulations discussed in the main text.

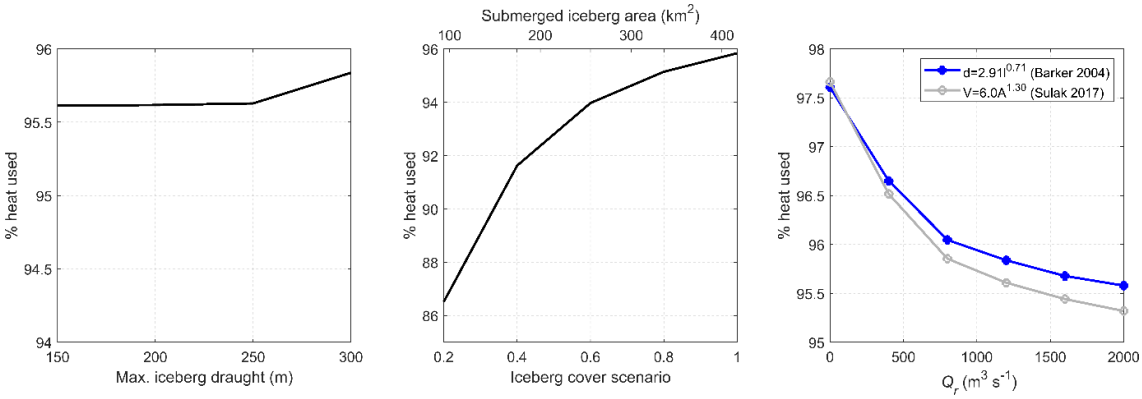

Figure S2.9. Sensitivity of heat used by icebergs to iceberg geometry. As in Figure 5.6, the y-axis values are the proportion of the heat used for ice melt that is used by icebergs. Iceberg cover scenarios 0.2-0.8 have approximately 20-80% of the plan-view iceberg surface area as the primary simulations discussed in them main text (cover scenario 1 here). Note the different y-axis scales on each of the panels.

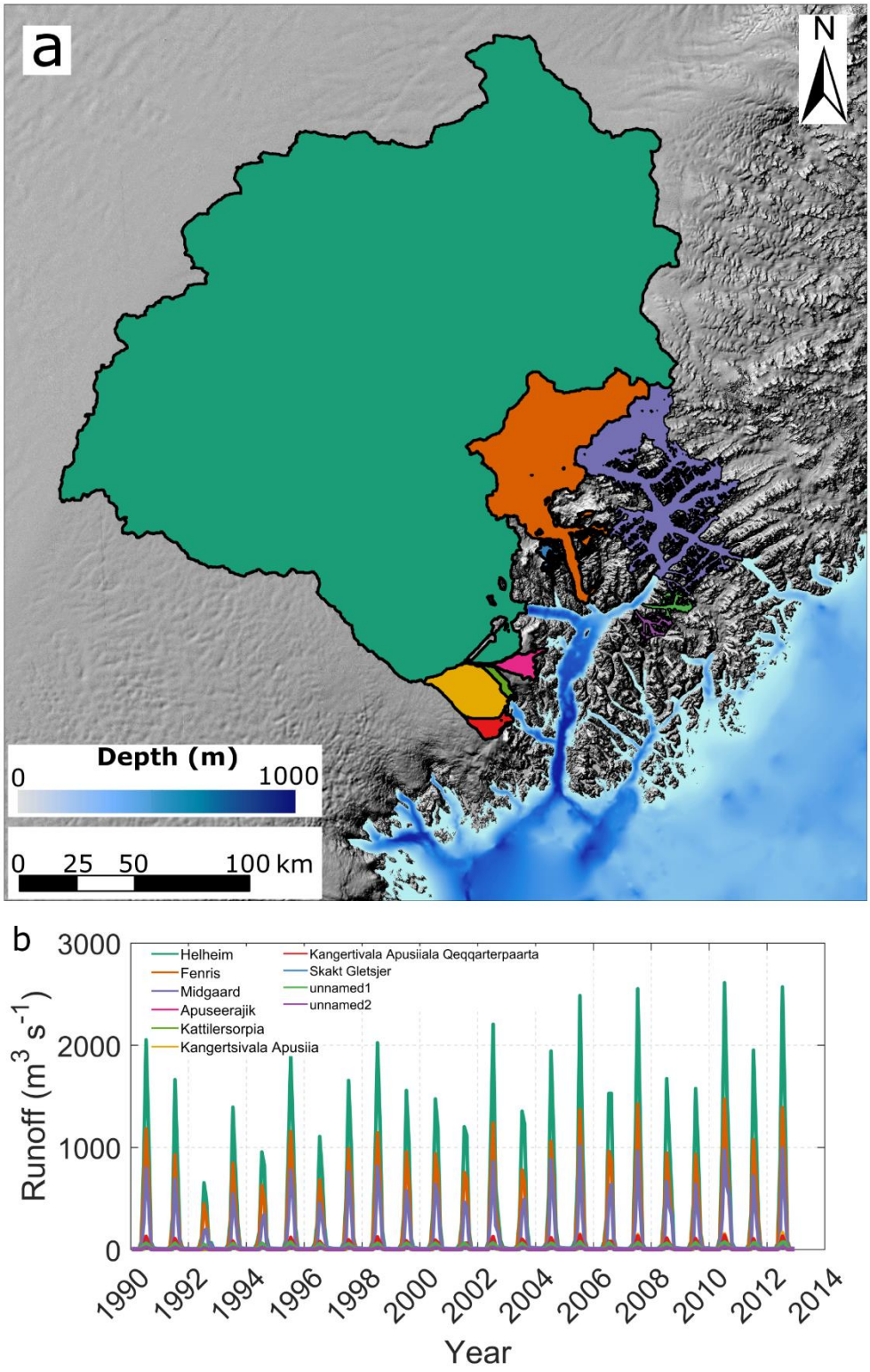

Figure S2.10. Glacier drainage basins and runoff in Sermilik Fjord. (a) Subglacial hydrological basins (coloured shapes) overlaid on the Greenland Ice Mapping Project Digital Elevation Model (Howat et al., 2014) and BedMachine v3 (Morlighem et al., 2017) bathymetry (blue shading). (b) Estimated subglacial discharge at indicated glacier termini during 1990-2012, based on RACMO2.3 runoff (Noël et al., 2018) and simple hydrological routing. Glacier names in (b) are from Bjørk et al. (2015). The colours in (b) correspond to the drainage basin colours in (a).

Table S2.1. Model parameters. Note the thermal and salt turbulent transfer coefficients and the drag coefficient have 'adjusted' values in brackets.

Symbol	Description	Value *(adjusted)*	Units
C_i	Heat capacity of ice	2000	J kg^{-1} $°C^{-1}$
C_w	Heat capacity of water	3974	J kg^{-1} $°C^{-1}$
α	Entrainment parameter	0.10	
g	Acceleration due to gravity	9.81	m s^{-2}
T_i	Ice temperature	-10	°C
L	Latent heat of melting	3.34×10^5	J kg^{-1}
Γ_T	Thermal turbulent transfer coefficient	2.20×10^{-2} *(4.40×10^{-2})*	
Γ_S	Salt turbulent transfer coefficient	6.20×10^{-4} *(1.24×10^{-3})*	
C_d	Drag coefficient	0.0025 *(0.01)*	
λ_1	Freezing point slope	-5.73×10^{-2}	°C psu^{-1}
λ_2	Freezing point offset	8.32×10^{-2}	°C
λ_3	Freezing point depth	-7.61×10^{-4}	°C m^{-1}
ρ_o	Reference density	1027	kg m^{-3}
U_{bg}	Background velocity	0.06	m s^{-1}
f	Coriolis parameter	1.37×10^{-4}	rad s^{-1}
ρ_i	Ice density	917	kg m^{-3}
$diffK_zT,S$	Vertical Laplacian diffusion coefficient for temperature and salinity	1×10^{-5}	m^2 s^{-1}
$diffK_hT,S$	Horizontal Laplacian diffusion coefficient for temperature and salinity	30	m^2 s^{-1}
$viscA_z$	Vertical eddy viscosity	1×10^{-5}	m^2 s^{-1}
viscC2Smag	Smagorinksy non-dimensional viscosity factor	2.2	

Table S2.2. Summary of key results to a depth-varying background velocity, and iceberg size-frequency distribution. Background velocities are based on line plume simulations bounded by the summer runoff forcing scenario 'initial' and 'final' conditions (Figure S2.5).

	Total freshwater flux ($m^3 s^{-1}$)	**melting below pycnocline to total freshwater flux (%)**	**Up-fjord heat flux across mélange flux gate (TW)**
Summer runoff forcing	745	37.0	0.78
Depth-varying background velocity			
Initial	399	28.4	0.72
Final	386	26.4	0.72
Size-frequency distribution			
-1.8	767	41.4	0.78
-1.9	765	39.8	0.79

Table S2.3. Summary of simulations and associated submerged iceberg surface area. SFD simulations used different exponents on the power laws used to generate iceberg size-frequency distributions. Simulations $c_{0.2\text{-}0.8}$ had approximately 20-80% of the iceberg cover as the primary simulations (Barker, 2004). Simulations with a * were only run using 1200 m^3 s^{-1} runoff and 'channelised' drainage (Chapter 5). Simulation suites with a ** were run using all runoff values and 'channelised' drainage.

Suite		Submerged iceberg area (km^2)
no-icebergs		0
full observed cover	Depth=2.91*length$^{0.71}$ (Barker 2004 - standard)	416.77
	Depth=2.91*length$^{0.71}$ (Barker 2004 - adjusted)	416.77
	Volume = 6.0*Area$^{1.30}$ (Sulak 2017)**	390.35
	Length : keel depth ratio = 2:1*	486.57
	Length : keel depth ratio = 1.8:1*	528.36
	SFD -1.8*	423.90
	SFD -1.9*	431.01
	Max draught 150 m*	412.23
	Max draught 200 m*	398.31
	Max draught 250 m*	401.65
	Max draught 350 m*	422.09
	Max draught 400 m*	413.94
	Sensitivity: background velocity*	416.77
$c_{0.2}$*		93.74
$c_{0.4}$*		174.87
$c_{0.6}$*		266.70
$c_{0.8}$*		350.89

Bibliography

Adcroft, A., Hill, C., & Marshall, J. (1997). Representation of Topography by Shaved Cells in a Height Coordinate Ocean Model. *Monthly Weather Review*, *125*(9), 2293–2315. https://doi.org/10.1175/1520-0493(1997)125<2293:ROTBSC>2.0.CO;2

Adrian, R. J., & Westerweel, J. (2011). *Particle Image Velocimetry*. Cambridge University Press.

Ahlstrøm, A. P., Andersen, S. B., Andersen, M. L., Machguth, H., Nick, F. M., Joughin, I., et al. (2013). Seasonal velocities of eight major marine-terminating outlet glaciers of the Greenland ice sheet from continuous in situ GPS instruments. *Earth System Science Data*, *5*(2), 277–287. https://doi.org/10.5194/essd-5-277-2013

Ahlstrøm, A. P., Petersen, D., Langen, P. L., Citterio, M., & Box, J. E. (2017). Abrupt shift in the observed runoff from the southwestern Greenland ice sheet. *Science Advances*, *3*(12), 1–8. https://doi.org/10.1126/sciadv.1701169

Amundson, J. M., & Burton, J. C. (2018). Quasi-Static Granular Flow of Ice Mélange. *Journal of Geophysical Research: Earth Surface*, *123*(9), 2243–2257. https://doi.org/10.1029/2018JF004685

Amundson, J. M., Kienholz, C., Hager, A. O., Jackson, R. H., Motyka, R. J., Nash, J. D., & Sutherland, D. A. (2020). Formation, flow and break-up of ephemeral ice mélange at LeConte Glacier and Bay, Alaska. *Journal of Glaciology*, *66*(258), 577–590. https://doi.org/10.1017/jog.2020.29

Andersen, M. L., Larsen, T. B., Nettles, M., Elosegui, P., Van As, D., Hamilton, G. S., et al. (2010). Spatial and temporal melt variability at Helheim Glacier, East Greenland, and its effect on ice dynamics. *Journal of Geophysical Research: Earth Surface*, *115*(4), 1–18. https://doi.org/10.1029/2010JF001760

De Andrés, E., Slater, D. A., Straneo, F., Otero, J., Das, S., & Navarro, F. (2020). Surface emergence of glacial plumes determined by fjord stratification. *The Cryosphere Discussions, in review*(January). https://doi.org/https://doi.org/10.5194/tc-2019-264

Andresen, C. S., Straneo, F., Ribergaard, M. H., Bjørk, A. A., Andersen, T. J., Kuijpers, A., et al. (2012). Rapid response of Helheim Glacier in Greenland to climate variability over the past century. *Nature Geoscience*, *5*(1), 37–41. https://doi.org/10.1038/ngeo1349

Andrews, J. T., Milliman, J. D., Jennings, A. E., Rynes, N., & Dwyer, J. (1994). Sediment thicknesses and Holocene glacial marine sedimentation rates in three East Greenland fjords (ca. 68°N). *Journal of Geology*, *102*(6), 669–683. https://doi.org/10.1086/629711

Andrews, L. C., Catania, G. A., Hoffman, M. J., Gulley, J. D., Lüthi, M. P., Ryser, C., et al. (2014). Direct observations of evolving subglacial drainage beneath the Greenland Ice Sheet. *Nature*, *514*(7520), 80–83. https://doi.org/10.1038/nature13796

van As, D., Hasholt, B., Ahlstrøm, A. P., Box, J. E., Cappelen, J., Colgan, W., et al. (2018). Reconstructing Greenland Ice Sheet meltwater discharge through the Watson River (1949–2017). *Arctic, Antarctic, and Alpine Research*, *50*(1). https://doi.org/10.1080/15230430.2018.1433799

Van As, D., Andersen, M. L., Petersen, D., Fettweis, X., Van Angelen, J. H., Lenaerts, J. T. M., et al. (2014). Increasing meltwater discharge from the Nuuk region of the Greenland ice sheet and implications for mass balance (1960-2012). *Journal of Glaciology*, *60*(220), 314–322. https://doi.org/10.3189/2014JoG13J065

Aschwanden, A., Fahnestock, M. A., Truffer, M., Brinkerhoff, D. J., Hock, R., Khroulev, C., et al. (2019). Contribution of the Greenland Ice Sheet to sea level over the next millennium. *Science Advances*, *5*(6). https://doi.org/10.1126/sciadv.aav9396

Åström, J. a., Vallot, D., Schäfer, M., Welty, E. Z., O'Neel, S., Bartholomaus, T. C., et al. (2014). Termini of calving glaciers as self-organized critical systems. *Nature Geoscience*, *7*(12), 874–878. https://doi.org/10.1038/ngeo2290

Azetsu-Scott, K., & Syvitski, J. P. M. (1999). Influence of melting icebergs on distribution, characteristics and transport of marine particles in an East Greenland fjord. *Journal of Geophysical Research: Oceans*, *104*(C3), 5321–5328. https://doi.org/10.1029/1998jc900083

Bacon, S., Reverdin, G., Rigor, I. G., & Snaith, H. M. (2002). A freshwater jet on the East Greenland shelf. *Journal of Geophysical Research C: Oceans*, *107*(7), 5–1. https://doi.org/10.1029/2001jc000935

Bacon, S., Marshall, A., Holliday, N. P., Aksenov, Y., & Dye, S. R. (2014). Seasonal variability of the East Greenland Coastal Current. *Journal of Geophysical Research: Oceans*, *119*, 3967–3987. https://doi.org/10.1002/2013JC009279.

Barker, A., Sayed, M., & Carrieres, T. (2004). Determination of iceberg draft, mass and cross-sectional areas. *Proceedings of 14th International Offshore and Polar Engineering Conference*, 899–904.

Bartholomaus, T. C., Amundson, J. M., Walter, J. I., O'Neel, S., West, M. E., & Larsen, C. F. (2015). Subglacial discharge at tidewater glaciers revealed by seismic tremor. *Geophysical Research Letters*, n/a-n/a. https://doi.org/10.1002/2015GL064590

Bartholomaus, T. C., Stearns, L. A., Sutherland, D. A., Shroyer, E. L., Nash, J. D., Walker, R. T., et al. (2016). Contrasts in the response of adjacent fjords and glaciers to ice-sheet surface melt in West Greenland. *Annals of Glaciology*. https://doi.org/10.1017/aog.2016.19

Bartholomew, I., Nienow, P., Mair, D., Hubbard, A., King, M. A., & Sole, A. (2010). Seasonal evolution of subglacial drainage and acceleration in a Greenland outlet glacier. *Nature Geoscience*, *3*(6), 408–411. https://doi.org/10.1038/ngeo863

Bartholomew, I., Nienow, P., Sole, A., Mair, D., Cowton, T., & King, M. A. (2012). Short-term variability in Greenland Ice Sheet motion forced by time-varying

meltwater drainage: Implications for the relationship between subglacial drainage system behavior and ice velocity. *Journal of Geophysical Research: Earth Surface*, *117*, 1–17. https://doi.org/10.1029/2011JF002220

Bartholomew, I. D., Nienow, P., Sole, A., Mair, D., Cowton, T., King, M. A., & Palmer, S. (2011). Seasonal variations in Greenland Ice Sheet motion: Inland extent and behaviour at higher elevations. *Earth and Planetary Science Letters*, *307*(3–4), 271–278. https://doi.org/10.1016/j.epsl.2011.04.014

Beaird, N., Straneo, F., & Jenkins, W. (2015). Spreading of Greenland meltwaters in the ocean revealed by noble gases. *Geophysical Research Letters*. https://doi.org/10.1002/2015GL065003

Beaird, N., Straneo, F., & Jenkins, W. (2017). Characteristics of meltwater export from Jakobshavn Isbræ and Ilulissat Icefjord. *Annals of Glaciology*, *58*(74), 107–117. https://doi.org/10.1017/aog.2017.19

Beaird, N. L., Straneo, F., & Jenkins, W. (2018). Export of Strongly Diluted Greenland Meltwater From a Major Glacial Fjord. *Geophysical Research Letters*, *45*(9), 4163–4170. https://doi.org/10.1029/2018GL077000

Bendtsen, J., Mortensen, J., Lennert, K., & Rysgaard, S. (2015). Heat sources for glacial ice melt in a west Greenland tidewater outlet glacier fjord : The role of subglacial freshwater discharge. *Geophysical Research Letters*, *42*. https://doi.org/10.1002/2015GL063846

Benn, D. I., Aström, J., Zwinger, T., Todd, J., Nick, F. M., Cook, S., et al. (2017). Melt-under-cutting and buoyancy-driven calving from tidewater glaciers: New insights from discrete element and continuum model simulations. *Journal of Glaciology*, *63*(240), 691–702. https://doi.org/10.1017/jog.2017.41

Bevan, S. L., Luckman, A. J., & Murray, T. (2012). Glacier dynamics over the last quarter of a century at Helheim, Kangerdlugssuaq and 14 other major Greenland outlet glaciers. *Cryosphere*, *6*, 923–937. https://doi.org/10.5194/tc-6-923-2012

Bevan, S. L., Luckman, A., Khan, S. A., & Murray, T. (2015). Seasonal dynamic thinning at Helheim Glacier. *Earth and Planetary Science Letters*, *415*, 47–53. https://doi.org/10.1016/j.epsl.2015.01.031

Bevan, S. L., Luckman, A. J., Benn, D. I., Cowton, T., & Todd, J. (2019). Impact of

warming shelf waters on ice mélange and terminus retreat at a large SE Greenland glacier. *Cryosphere*, *13*(9), 2303–2315. https://doi.org/10.5194/tc-13-2303-2019

Bigg, G. R., Wadley, M. R., Stevens, P., & Johnson, J. A. (1996). Prediction of iceberg trajectories for the North Atlantic and Arctic Oceans. *Geophysical Research Letters*, *23*(24), 3587–3590.

Bigg, G. R., Wadley, M. R., Stevens, D. P., & Johnson, J. A. (1997). Modelling the dynamics and thermodynamics of icebergs. *Cold Regions Science and Technology*, *26*(2), 113–135. https://doi.org/10.1016/S0165-232X(97)00012-8

Biskaborn, B. K., Smith, S. L., Noetzli, J., Matthes, H., Vieira, G., Streletskiy, D. A., et al. (2019). Permafrost is warming at a global scale. *Nature Communications*, *10*(1), 1–11. https://doi.org/10.1038/s41467-018-08240-4

Bjørk, A. a., Kjær, K. H., Korsgaard, N. J., Khan, S. a., Kjeldsen, K. K., Andresen, C. S., et al. (2012). An aerial view of 80 years of climate-related glacier fluctuations in southeast Greenland. *Nature Geoscience*, *5*(6), 427–432. https://doi.org/10.1038/ngeo1481

Bjørk, A. A., Kruse, L. M., & Michaelsen, P. B. (2015). Brief Communication: Getting Greenland's glaciers right – a new dataset of all official Greenlandic glacier names. *The Cryosphere Discussions*, *9*(2), 1593–1601. https://doi.org/10.5194/tcd-9-1593-2015

Bokhorst, S., Pedersen, S. H., Brucker, L., Anisimov, O., Bjerke, J. W., Brown, R. D., et al. (2016). Changing Arctic snow cover: A review of recent developments and assessment of future needs for observations, modelling, and impacts. *Ambio*, *45*(5), 516–537. https://doi.org/10.1007/s13280-016-0770-0

Boncori, J. P. ., Andersen, M. ., Dall, J., Kusk, A., Kamstra, M., Andersen, S. B., et al. (2018). Intercomparison and validation of SAR-based ice velocity measurement techniques within the Greenland Ice Sheet CCI project. *Remote Sensing*, *10*(929). https://doi.org/10.3390/rs10060929

Böning, C. W., Behrens, E., Biastoch, A., Getzlaff, K., & Bamber, J. L. (2016). Emerging impact of Greenland meltwater on deepwater formation in the North Atlantic Ocean. *Nature Geoscience*, *9*(7), 523–527. https://doi.org/10.1038/ngeo2740

Box, J. E., Yang, L., Bromwich, D. H., & Bai, L. S. (2009). Greenland ice sheet surface

air temperature variability: 1840-2007. *Journal of Climate*, *22*(14), 4029–4049. https://doi.org/10.1175/2009JCLI2816.1

Brough, S., Carr, J. R., Ross, N., & Lea, J. M. (2019). Exceptional retreat of Kangerlussuaq Glacier, east Greenland, between 2016 and 2018. *Frontiers in Earth Science*, *7*(May), 1–11. https://doi.org/10.3389/feart.2019.00123

Bunce, C., Carr, J. R., Nienow, P. W., Ross, N., & Killick, R. (2018). Ice front change of marine-terminating outlet glaciers in northwest and southeast Greenland during the 21st century. *Journal of Glaciology*, *64*(246), 523–535. https://doi.org/10.1017/jog.2018.44

Burton, J. C., Amundson, J. M., Cassotto, R., Kuo, C. C., & Dennin, M. (2018). Quantifying flow and stress in ice mélange, the world's largest granular material. *Proceedings of the National Academy of Sciences of the United States of America*, *115*(20), 5105–5110. https://doi.org/10.1073/pnas.1715136115

Carlson, D. F., Boone, W., Meire, L., Abermann, J., & Rysgaard, S. (2017). Bergy Bit and Melt Water Trajectories in Godthåbsfjord (SW Greenland) Observed by the Expendable Ice Tracker. *Frontiers in Marine Science*, *4*(August), 1–14. https://doi.org/10.3389/fmars.2017.00276

Carr, J. R., Vieli, A., & Stokes, C. (2013). Influence of sea ice decline, atmospheric warming, and glacier width on marine-terminating outlet glacier behavior in northwest Greenland at seasonal to interannual timescales. *Journal of Geophysical Research: Earth Surface*, *118*(3), 1210–1226. https://doi.org/10.1002/jgrf.20088

Carroll, D., Sutherland, D. a., Shroyer, E. L., Nash, J. D., Catania, G. a., & Stearns, L. a. (2015). Modeling Turbulent Subglacial Meltwater Plumes: Implications for Fjord-Scale Buoyancy-Driven Circulation. *Journal of Physical Oceanography*, *45*(8), 2169–2185. https://doi.org/10.1175/JPO-D-15-0033.1

Carroll, D., Sutherland, D. A., Hudson, B., Moon, T., Catania, G. A., Shroyer, E. L., et al. (2016). The impact of glacier geometry on meltwater plume structure and submarine melt in Greenland fjords. *Geophysical Research Letters*, *43*(18), 9739–9748. https://doi.org/10.1002/2016GL070170

Carroll, D., Sutherland, D. A., Shroyer, E. L., Nash, J. D., Catania, G. A., & Stearns, L. A. (2017). Subglacial discharge-driven renewal of tidewater glacier fjords. *Journal*

of Geophysical Research: Oceans, 1–19. https://doi.org/10.1002/2017JC012962

Catania, G. A., Stearns, L. A., Moon, T. A., Enderlin, E. M., & Jackson, R. H. (2020). Future Evolution of Greenland's Marine-Terminating Outlet Glaciers. *Journal of Geophysical Research: Earth Surface*, *125*(2), 1–28. https://doi.org/10.1029/2018JF004873

Cenedese, C., & Gatto, V. M. (2016a). Impact of a localized source of subglacial discharge on the heat flux and submarine melting of a tidewater glacier: A laboratory study. *Journal of Physical Oceanography*, *46*(10), 3155–3163. https://doi.org/10.1175/JPO-D-16-0123.1

Cenedese, C., & Gatto, V. M. (2016b). Impact of two plumes' interaction on submarine melting of tidewater glaciers: A laboratory study. *Journal of Physical Oceanography*, *46*(1), 361–367. https://doi.org/10.1175/JPO-D-15-0171.1

Chandler, D. M., Wadham, J. L., Lis, G. P., Cowton, T., Sole, A., Bartholomew, I., et al. (2013). Evolution of the subglacial drainage system beneath the Greenland Ice Sheet revealed by tracers. *Nature Geoscience*, *6*(3), 195–198. https://doi.org/10.1038/ngeo1737

Chauché, N., Hubbard, A., Gascard, J.-C., Box, J. E., Bates, R., Koppes, M., et al. (2014). Ice–ocean interaction and calving front morphology at two west Greenland tidewater outlet glaciers. *The Cryosphere*, *8*(4), 1457–1468. https://doi.org/10.5194/tc-8-1457-2014

Chen, X., Zhang, X., Church, J. A., Watson, C. S., King, M. A., Monselesan, D., et al. (2017). The increasing rate of global mean sea-level rise during 1993 – 2014. *Nature Climate Change*. https://doi.org/10.1038/NCLIMATE3325

Christoffersen, P., Mugford, R. I., Heywood, K. J., Joughin, I., Dowdeswell, J. a., Syvitski, J. P. M., et al. (2011). Warming of waters in an East Greenland fjord prior to glacier retreat: mechanisms and connection to large-scale atmospheric conditions. *The Cryosphere*, *5*(3), 701–714. https://doi.org/10.5194/tc-5-701-2011

Christoffersen, P., O'Leary, M., Van Angelen, J. H., & Van Den Broeke, M. (2012). Partitioning effects from ocean and atmosphere on the calving stability of kangerdlugssuaq glacier, east greenland. *Annals of Glaciology*, *53*(60), 249–256. https://doi.org/10.3189/2012AoG60A087

Chylek, P., Dubey, M. K., & Lesins, G. (2006). Greenland warming of 1920-1930 and 1995-2005. *Geophysical Research Letters*, *33*(11), 1–5. https://doi.org/10.1029/2006GL026510

Colgan, W., Mankoff, K. D., Kjeldsen, K. K., Bjørk, A. A., Box, J. E., Simonsen, S. B., et al. (2019). Greenland ice sheet mass balance assessed by PROMICE (1995-2015). *Geological Survey of Denmark and Greenland Bulletin*, *43*, 1–6. https://doi.org/10.34194/GEUSB-201943-02-01

Cook, S., Rutt, I. C., Murray, T., Luckman, a., Zwinger, T., Selmes, N., et al. (2014). Modelling environmental influences on calving at Helheim Glacier in eastern Greenland. *The Cryosphere*, *8*(3), 827–841. https://doi.org/10.5194/tc-8-827-2014

Cook, S., Christoffersen, P., Todd, J., Slater, D., & Chauché, N. (2020). Coupled modelling of subglacial hydrology and calving-front melting at Store Glacier, West Greenland. *The Cryosphere*, *14*, 905–924. https://doi.org/10.5194/tc-2019-104

Cowton, T., Nienow, P., Sole, A., Wadham, J., Lis, G., Bartholomew, I., et al. (2013). Evolution of drainage system morphology at a land-terminating Greenlandic outlet glacier. *Journal of Geophysical Research: Earth Surface*, *118*(1), 29–41. https://doi.org/10.1029/2012JF002540

Cowton, T., Slater, D., Sole, A., Goldberg, D., & Nienow, P. (2015). Modeling the impact of glacial runoff on fjord circulation and submarine melt rate using a new subgrid-scale parameterization for glacial plumes. *Journal of Geophysical Research C: Oceans*. https://doi.org/10.1002/2014JC010324

Cowton, T., Sole, A., Nienow, P., Slater, D., Wilton, D., & Hanna, E. (2016a). Controls on the transport of oceanic heat to Kangerdlugssuaq Glacier, East Greenland. *Journal of Glaciology*, 1–14. https://doi.org/10.1017/jog.2016.117

Cowton, T., Nienow, P., Sole, A., Bartholomew, I., & Mair, D. (2016b). Variability in ice motion at a land-terminating Greenlandic outlet glacier: the role of channelized and distributed drainage systems. *Journal of Glaciology*, *62*, 451–466. https://doi.org/10.1017/jog.2016.36

Cowton, T. R., Sole, A. J., Nienow, P. W., Slater, D. A., & Christoffersen, P. (2018). Linear response of east Greenland's tidewater glaciers to ocean / atmosphere warming. https://doi.org/10.1073/pnas.1801769115

Cowton, T. R., Todd, J. A., & Benn, D. I. (2019). Sensitivity of tidewater glaciers to submarine melting governed by plume locations. *Geophysical Research Letters*, 1–9. https://doi.org/10.1029/2019gl084215

Crocker, G. B. (1993). Size distributions of bergy bits and growlers calved from deteriorating icebergs. *Cold Regions Science and Technology*, *22*(1), 113–119. https://doi.org/10.1016/0165-232X(93)90050-I

Dansereau, V., Heimback, P., & Losch, M. (2013). Simulation of subice shelf melt rates in a general circulation model: velocity-dependent transfer and the role of friction. *Journal of Geophysical Research: Oce*, (119), 1–26. https://doi.org/10.1002/2013JC008846.

Davison, B. J., Sole, A. J., Livingstone, S. J., Cowton, T. R., & Nienow, P. W. (2019). The influence of hydrology on the dynamics of land-terminating sectors of the Greenland ice sheet. *Frontiers in Earth Science*, *7*(February), 1–24. https://doi.org/10.3389/feart.2019.00010

Davison, B. J., Cowton, T. R., Cottier, F. R., & Sole, A. J. (2020). Iceberg melting substantially modifies oceanic heat flux towards a major Greenlandic tidewater glacier. *Nature Communications*, *11*(1), 1–13. https://doi.org/10.1038/s41467-020-19805-7

De Zan, F., & Guarnieri, M, A. (2006). TOPSAR: Terrain observation by progressive scanes. *IEEE Transactions on Geoscience*, 44, 2352-2360. https://doi.org/10.1109/TGRS.2006.873853

Doake, C. S. M., & Vaughan, D. G. (1991). Rapid disintegration of the Wordie Ice Shelf in response to atmospheric warming. *Nature*, *350*(6316), 328–330. https://doi.org/10.1038/350328a0

Dowdeswell, J. A., Whittington, R. J., & Hodgkins, R. (1992). The sizes, frequencies, and freeboards of East Greenland icebergs observed using ship radar and sextant. *Journal of Geophysical Research*, *97*(C3), 3515. https://doi.org/10.1029/91JC02821

Doyle, S. H., Hubbard, B., Christoffersen, P., Young, T. J., Hofstede, C., Bougamont, M., et al. (2018). Physical Conditions of Fast Glacier Flow: 1. Measurements From Boreholes Drilled to the Bed of Store Glacier, West Greenland. *Journal of Geophysical Research: Earth Surface*, *123*(2), 324–348.

https://doi.org/10.1002/2017JF004529

Edwards, T. L., Nowicki, S., Marzeion, B., Hock, R., Hoelzer, H., Seroussi, H., et al. (2021). Projected land ice contributions to twenty-first-century sea level rise. *Nature*, 593, 74-82. https://doi.org/10.1038/s41586-021-03302-y

El-Tahan, M., Venkatesh, S., & El-Tahan, H. (1987). Validation and Quantitative Assessment of the Deterioration Mechanisms of Arctic Icebergs. *Journal of Offshore Mechanics and Arctic Engineering*, *109*, 102–108. https://doi.org/10.1115/1.3256983

Enderlin, E. M., & Hamilton, G. S. (2014). Estimates of iceberg submarine melting from high-resolution digital elevation models: application to Sermilik Fjord, East Greenland. *Journal of Glaciology*, *60*(224), 1084–1092. https://doi.org/10.3189/2014JoG14J085

Enderlin, E. M., Hamilton, G. S., Straneo, F., & Sutherland, D. A. (2016). Iceberg meltwater fluxes dominate the freshwater budget in Greenland's iceberg-congested glacial fjords. *Geophysical Research Letters*, *43*(21), 11,287-11,294. https://doi.org/10.1002/2016GL070718

Enderlin, E. M., Carrigan, C. J., Kochtitzky, W. H., Cuadros, A., Moon, T., & Hamilton, G. S. (2018). Greenland Iceberg Melt Variability from High-Resolution Satellite Observations. *The Cryosphere*, (September), 1–17.

Fahnestock, M., Scambos, T., Moon, T., Gardner, A., Haran, T., & Klinger, M. (2015). Rapid large-area mapping of ice flow using Landsat 8. *Remote Sensing of Environment*, *185*, 84–94. https://doi.org/10.1016/j.rse.2015.11.023

Felikson, D., Bartholomaus, T. C., Catania, G. A., Korsgaard, N. J., Kjær, K. H., Morlighem, M., et al. (2017). Inland thinning on the Greenland ice sheet controlled by outlet glacier geometry. *Nature Geoscience*, *10*(April). https://doi.org/10.1038/ngeo2934

Felikson, D., Catania, G., Bartholomaus, T. C., Morlighem, M., & Noël, B. P. Y. (2020). Steep glacier bed knickpoints mitigate inland thinning in Greenland. *Geophysical Research Letters*, 1–10. https://doi.org/10.1029/2020gl090112

Fenty, I., Willis, J., Khazendar, A., Dinardo, S., Forsberg, R., Fukumori, I., et al. (2016). Oceans Melting Greenland: Early Results from NASA's Ocean-Ice Mission in

Greenland. *Oceanography*, *29*(4), 72–83. https://doi.org/10.5670/oceanog.2016.100

Fernández, J., Escobar, D., Bock, H., & Féménias, P. (2015). Copernicus POD Operations - Orbital Accuracy of Sentinel-1A and Sentinel-2A. *25th International Symposium on Space Flight Dynamics 4.2. An Optional Note*, 201–213.

FitzMaurice, A., & Stern, A. (2018). Parameterizing the basal melt of tabular icebergs. *Ocean Modelling*, *130*(February), 66–78. https://doi.org/10.1016/j.ocemod.2018.08.005

FitzMaurice, A., Straneo, F., Cenedese, C., & Andres, M. (2016). Effect of a sheared flow on iceberg motion and melting. *Geophysical Research Letters*, *43*(24), 12,520-12,527. https://doi.org/10.1002/2016GL071602

FitzMaurice, A., Cenedese, C., & Straneo, F. (2017). Nonlinear response of iceberg side melting to ocean currents. *Geophysical Research Letters*, *44*(11), 5637–5644. https://doi.org/10.1002/2017GL073585

Fofonoff, N. P., & Millard, R. C. (1983). Algorithms for computations of fundamental properties of seawater. UNESCO Technical Papers in Marine Science 44. Paris: UNESCO Division of Marine Sciences. *WHP Operations and Methods*, (July), 53.

Fowler, A. C. (1987). Sliding with cavity formation. *Journal of Glaciology*, *33*(115), 255–267. https://doi.org/10.1002/chin.200533194

Fraser, N. J., & Inall, M. E. (2018). Influence of Barrier Wind Forcing on Heat Delivery Toward the Greenland Ice Sheet. *Journal of Geophysical Research: Oceans*, *123*(4), 2513–2538. https://doi.org/10.1002/2017JC013464

Fraser, N. J., Inall, M. E., Magaldi, M. G., Haine, T. W. N., & Jones, S. C. (2018). Wintertime Fjord-Shelf Interaction and Ice Sheet Melting in Southeast Greenland. *Journal of Geophysical Research: Oceans*, *123*(12), 9156–9177. https://doi.org/10.1029/2018JC014435

Fried, M. J., Catania, G. A., Bartholomaus, T. C., Duncan, D., Davis, M., Stearns, L. A., et al. (2015). Distributed subglacial discharge drives significant submarine melt at a Greenland tidewater glacier. *Geophysical Research Letters*, *42*(21), 9328–9336. https://doi.org/10.1002/2015GL065806

Fried, M. J., Catania, G. A., Stearns, L. A., Sutherland, D. A., Bartholomaus, T. C.,

Shroyer, E., & Nash, J. (2018). Reconciling Drivers of Seasonal Terminus Advance and Retreat at 13 Central West Greenland Tidewater Glaciers. *Journal of Geophysical Research: Earth Surface*, *123*(7), 1590–1607. https://doi.org/10.1029/2018JF004628

Gade, H. G. (1979). Melting of Ice in Sea Water: A Primitive Model with Application to the Antarctic Ice Shelf and Icebergs. *Journal of Physical Oceanography*. https://doi.org/10.1175/1520-0485(1979)009<0189:MOIISW>2.0.CO;2

Gillard, L. C., Hu, X., Myers, P. G., Hvid Ribergaard, M., & Lee, C. M. (2020). Drivers for Atlantic-origin waters abutting Greenland. *Cryosphere*, *14*(8), 2729–2753. https://doi.org/10.5194/tc-14-2729-2020

Gillibrand, P. A., Inall, M. E., Portilla, E., & Tett, P. (2013). A box model of the seasonal exchange and mixing in Regions of Restricted Exchange: Application to two contrasting Scottish inlets. *Environmental Modelling and Software*, *43*, 144–159. https://doi.org/10.1016/j.envsoft.2013.02.008

Gladish, C. V., Holland, D. M., Rosing-Asvid, A., Behrens, J. W., & Boje, J. (2015). Oceanic Boundary Conditions for Jakobshavn Glacier: Part I. Variability and Renewal of Ilulissat Icefjord Waters, 2001-2014. *Journal of Physical Oceanography*, *45*. https://doi.org/10.1175/JPO-D-14-0044.1

Goelzer, H., Nowicki, S., Payne, A., Larour, E., Seroussi, H., Lipscomb, W. H., et al. (2020). The future sea-level contribution of the Greenland ice sheet: A multi-model ensemble study of ISMIP6. *Cryosphere*, *14*(9), 3071–3096. https://doi.org/10.5194/tc-14-3071-2020

Goldberg, D. N., Gourmelen, N., Kimura, S., Millan, R., & Snow, K. (2019). How Accurately Should We Model Ice Shelf Melt Rates? *Geophysical Research Letters*, *46*(1), 189–199. https://doi.org/10.1029/2018GL080383

Gray, A. L., Mattar, K. E., & Sofko, G. (2000). Influence of ionospheric electron density fluctuations on satellite radar interferometry. *Geophysical Research Letters*, 27, 1451-1454. https://doi.org/10.1029/2000GL000016

Gregory, J., George, S., & Smith, R. (2020). Large and irreversible future decline of the Greenland ice-sheet. *The Cryosphere Discussions*, 1–28. https://doi.org/10.5194/tc-2020-89

Guizar-Sicairos, M., Thurman, S. T., & Fienup, J. R. (2008). Efficient subpixel image registration algorithms. *Optics Letters*, *33*(2), 156. https://doi.org/10.1364/OL.33.000156

Hanna, E., Huybrechts, P., Steffen, K., Cappelen, J., Huff, R., Shuman, C., et al. (2008). Increased runoff from melt from the Greenland Ice Sheet: A response to global warming. *Journal of Climate*, *21*, 331–341. https://doi.org/10.1175/2007JCLI1964.1

Hanna, E., Fettweis, X., Mernild, S. H., Cappelen, J., Ribergaard, M. H., Shuman, C. a., et al. (2014). Atmospheric and oceanic climate forcing of the exceptional Greenland ice sheet surface melt in summer 2012. *International Journal of Climatology*, *34*(4), 1022–1037. https://doi.org/10.1002/joc.3743

Harper, J. T., Humphrey, N. F., Pfeffer, W. T., & Lazar, B. (2007). Two modes of accelerated glacier sliding related to water. *Geophysical Research Letters*, *34*(12), 1–5. https://doi.org/10.1029/2007GL030233

Harper, J. T., Humphrey, N. F., Meierbachtol, T. W., Graly, J. A., & Fischer, U. H. (2017). Borehole measurements indicate hard bed conditions, Kangerlussuaq sector, western Greenland Ice Sheet. *Journal of Geophysical Research: Earth Surface*, *122*(9), 1605–1618. https://doi.org/10.1002/2017JF004201

Harper, J. T., Humphrey, N. F., Pfeffer, T. W., Fudge, T., & O'Neel, S. (2005). Evolution of subglacial water pressure along a glacier's length. *Annals of Glaciology*, 40, 31-36. https://doi.org/10.3189/?172756405781813573

Heimbach, P., & Losch, M. (2012). Adjoint sensitivities of sub-ice-shelf melt rates to ocean circulation under the pine island ice shelf, west antarctica. *Annals of Glaciology*, *53*(60), 59–69. https://doi.org/10.3189/2012/AoG60A025

Helly, J. J., Kaufmann, R. S., Stephenson, G. R., & Vernet, M. (2011). Cooling, dilution and mixing of ocean water by free-drifting icebergs in the Weddell Sea. *Deep-Sea Research Part II: Topical Studies in Oceanography*, *58*(11–12), 1346–1363. https://doi.org/10.1016/j.dsr2.2010.11.010

Hill, E. A., Carr, J. R., & Stokes, C. R. (2017). A Review of Recent Changes in Major Marine-Terminating Outlet Glaciers in Northern Greenland. *Frontiers in Earth Science*, *4*(February), 0–23. https://doi.org/10.3389/feart.2016.00111

Hoffman, M. J., Andrews, L. C., Price, S. A., Catania, G. A., Neumann, T. A., Luethi, M.

P., et al. (2016). Greenland subglacial drainage evolution regulated by weakly-connected regions of the bed. *Nature Communications*, *7*. https://doi.org/10.1038/ncomms13903

Holland, D. M., & Jenkins, A. (1999). Modeling Thermodynamic Ice–Ocean Interactions at the Base of an Ice Shelf. *Journal of Physical Oceanography*, *29*(8), 1787–1800. https://doi.org/10.1175/1520-0485(1999)029<1787:MTIOIA>2.0.CO;2

Holland, D. M., Thomas, R. H., de Young, B., Ribergaard, M. H., & Lyberth, B. (2008). Acceleration of Jakobshavn Isbræ triggered by warm subsurface ocean waters. *Nature Geoscience*, *1*(10), 659–664. https://doi.org/10.1038/ngeo316

Hopwood, M. J., Carroll, D., Höfer, J., Achterberg, E. P., Meire, L., Le Moigne, F. A. C., et al. (2019). Highly variable iron content modulates iceberg-ocean fertilisation and potential carbon export. *Nature Communications*, *10*(1). https://doi.org/10.1038/s41467-019-13231-0

Hotzel, I. S., & Miller, J. D. (1983). Icebergs: their physical dimensions and the presentation and application of measured data. *Annals of Glaciology*, *4*, 116–123.

Howat, I. M., Smith, B. E., Joughin, I., & Scambos, T. a. (2008). Rates of southeast Greenland ice volume loss from combined ICESat and ASTER observations. *Geophysical Research Letters*, *35*(April), 1–5. https://doi.org/10.1029/2008GL034496

Howat, I. M., Box, J. E., Ahn, Y., Herrington, A., & McFadden, E. M. (2010). Seasonal variability in the dynamics of marine-terminating outlet glaciers in Greenland. *Journal of Glaciology*, *56*(198), 601–613. https://doi.org/10.3189/002214310793146232

Howat, I. M., Negrete, A., & Smith, B. E. (2014). The Greenland Ice Mapping Project (GIMP) land classification and surface elevation data sets. *The Cryosphere*, *8*(4), 1509–1518. https://doi.org/10.5194/tc-8-1509-2014

Hubbard, B., & Nienow, P. W. (1997). Alpine subglacial hydrology. *Quaternary Science Reviews*, *16*(9), 939–955. https://doi.org/10.1016/S0277-3791(97)00031-0

Hubbard, B. P., Sharp, M. J., Willis, I. C., Nielsen, M. K., & Smart, C. C. (1995). Borehole water-level variation and the structure of the subglacial hydrological system of Haut Glacier d'Arolla, Valais, Switzerland. *Journal of Glaciology*,

41(139), 572–583. https://doi.org/10.3189/s0022143000034894

Huppert, H. E., & Josberger, E. G. (1980). The Melting of Ice in Cold Stratified Water. *Journal of Physical Oceanography*. https://doi.org/10.1175/1520-0485(1980)010<0953:TMOIIC>2.0.CO;2

Hurrell, J. W. (1995). Decadal Trends in the North Atlantic Oscillation: Regional Temperatures and Precipitation. *Science*, *269*(5224), 676–679. https://doi.org/10.1126/science.269.5224.676

Iken, A. (1981). The effect of the subglacial water pressure on the sliding velocity of a glacier in an idealized numerical model. *Journal of Glaciology*.

Inall, M. E., Murray, T., Cottier, F. R., Scharrer, K., & Boyd, T. J. (2014). Oceanic heat delivery via Kangerdlugssuaq Fjord to the south-east Greenland ice sheet. *Journal of Geophysical Research: Oceans*, 631–645. https://doi.org/10.1002/2013JC009295.Received

Irvine-Fynn, T. D. L., Hodson, A. J., Moorman, B. J., Vatne, G., & Hubbard, A. L. (2011). Polythermal glacier hydrology: A review. *Reviews of Geophysics*, *49*(4), 1–37. https://doi.org/10.1029/2010RG000350

Iverson, N. ., Hanson, B., Hooke, R. L. B., & Jansson, P. (1995). Flow mechanism of glaciers on soft beds. *Science*, *267*, 80–81.

Jackson, R. H., & Straneo, F. (2016). Heat, salt, and freshwater budgets for a glacial fjord in Greenland. *Journal of Physical Oceanography*, *0*(0), 2735–2768. https://doi.org/10.1175/JPO-D-15-0134.1

Jackson, R. H., Straneo, F., & Sutherland, D. a. (2014). Externally forced fluctuations in ocean temperature at Greenland glaciers in non-summer months. *Nature Geoscience*, *7*(June), 1–6. https://doi.org/10.1038/ngeo2186

Jackson, R. H., Shroyer, E. L., Nash, J. D., Sutherland, D. A., Carroll, D., Fried, M. J., et al. (2017). Near-glacier surveying of a subglacial discharge plume: Implications for plume parameterizations. *Geophysical Research Letters*, *44*(13), 6886–6894. https://doi.org/10.1002/2017GL073602

Jackson, R. H., Lentz, S. J., & Straneo, F. (2018). The dynamics of shelf forcing in Greenlandic fjords. *Journal of Physical Oceanography*, *48*(11), 2799–2827.

https://doi.org/10.1175/JPO-D-18-0057.1

Jackson, R. H., Nash, J. D., Kienholz, C., Sutherland, D. A., Amundson, J. M., Motyka, R. J., et al. (2020). Meltwater Intrusions Reveal Mechanisms for Rapid Submarine Melt at a Tidewater Glacier. *Geophysical Research Letters*, *47*(2). https://doi.org/10.1029/2019GL085335

Jakobsson, M., Mayer, L. A., Nilsson, J., Stranne, C., Calder, B., O'Regan, M., et al. (2020). Ryder Glacier in northwest Greenland is shielded from warm Atlantic water by a bathymetric sill. *Communications Earth & Environment*, *1*(1), 1–10. https://doi.org/10.1038/s43247-020-00043-0

James, T. D., Murray, T., Selmes, N., Scharrer, K., & O'Leary, M. (2014). Buoyant flexure and basal crevassing in dynamic mass loss at Helheim Glacier. *Nature Geoscience*, *7*(8), 593–596. https://doi.org/10.1038/ngeo2204

Jenkins, A. (1991). A one-dimensional model of ice shelf-ocean interaction. *Journal of Geophysical Research*, *96*, 671–677.

Jenkins, A. (1999). The Impact of Melting Ice on Ocean Waters. *Journal of Physical Oceanography*, *29*(9), 2370–2381. https://doi.org/10.1175/1520-0485(1999)029<2370:TIOMIO>2.0.CO;2

Jenkins, A. (2011). Convection-Driven Melting near the Grounding Lines of Ice Shelves and Tidewater Glaciers. *Journal of Physical Oceanography*, *41*(12), 2279–2294. https://doi.org/10.1175/JPO-D-11-03.1

Jenkins, A., Nicholls, K. W., & Corr, H. F. J. (2010). Observation and parameterization of ablation at the base of Ronne Ice Shelf, Antarctica. *Journal of Ph*, *40*, 2298–2312. https://doi.org/10.1175/2010JPO4317.1

Jiskoot, H., Juhlin, D., Pierre, H. S. T., & Citterio, M. (2012). Tidewater glacier fluctuations in central east greenland coastal and fjord regions (1980s-2005). *Annals of Glaciology*, *53*(60), 35–44. https://doi.org/10.3189/2012AoG60A030

Jongma, J. I., Driesschaert, E., Fichefet, T., Goosse, H., & Renssen, H. (2009). The effect of dynamic-thermodynamic icebergs on the Southern Ocean climate in a three-dimensional model. *Ocean Modelling*, *26*(1–2), 104–113. https://doi.org/10.1016/j.ocemod.2008.09.007

Josberger, E. G., & Neshyba, S. (1980). Iceberg melt-driven convection inferred from field measurements of temperature. *Annals of Glaciology*, 113–117.

Joughin, I. (2002). Ice-sheet velocity mapping: A combined interferometric and speckle-tracking approach. *Annals of Glaciology*. https://doi.org/10.3189/172756402781817978

Joughin, I., Das, S. B., King, M. A., Smith, B. E., Howat, I. M., & Moon, T. (2008). Seasonal speedup along the western flank of the Greenland Ice Sheet. *Science*, *320*, 781–783. https://doi.org/10.1126/science.1153288

Joughin, I., Smith, B. E., Howat, I. M., Scambos, T., & Moon, T. (2010). Greenland flow variability from ice-sheet-wide velocity mapping. *Journal of Glaciology*, *56*(197), 415–430. https://doi.org/10.3189/002214310792447734

Joughin, I. R., Winebrenner, D. P., & Fahnestock, M. A. (1995). Observations of ice-sheet motion in Greenland using satellite radar interferometry. *Geophysical Research Letters*, *22*(5), 571–574. https://doi.org/10.1029/95GL00264

Kader, B. ., & Yaglom, a. . (1972). Heat and mass transfer laws for fully turbulent wall flows. *International Journal of Heat and Mass Transfer*, *15*(12), 2329–2351. https://doi.org/10.1016/0017-9310(72)90131-7

Kamb, B. (1987). Glacier surge mechanism based on linked cavity configuration of the basal water conduit system. *Journal of Geophysical Research*, *92*(B9), 9083–9100. https://doi.org/10.1029/JB092iB09p09083

Kehrl, L. M., Joughin, I., Shean, D. E., Floricioiu, D., & Krieger, L. (2017). Seasonal and interannual variability in terminus position, glacier velocity, and surface elevation at Helheim and Kangerlussuaq Glaciers from 2008 to 2016. *Journal of Geophysical Research: Earth Surface*, 1–18. https://doi.org/10.1002/2016JF004133

Khan, S. a., Kjær, K. H., Bevis, M., Bamber, J. L., Wahr, J., Kjeldsen, K. K., et al. (2014a). Sustained mass loss of the northeast Greenland ice sheet triggered by regional warming. *Nature Climate Change*, *4*(4), 292–299. https://doi.org/10.1038/nclimate2161

Khan, S. A., Kjeldsen, K. K., Kjær, K. H., Bevan, S., Luckman, A., Bjørk, A. A., et al. (2014b). Glacier dynamics at Helheim and Kangerdlugssuaq glaciers, southeast Greenland, since the Little Ice Age. *Cryosphere*, *8*(4), 1497–1507.

https://doi.org/10.5194/tc-8-1497-2014

Khan, S. A., Bjørk, A. A., Bamber, J. L., Morlighem, M., Bevis, M., Kjær, K. H., et al. (2020). Centennial response of Greenland's three largest outlet glaciers. *Nature Communications*, *11*(1), 1–9. https://doi.org/10.1038/s41467-020-19580-5

Khvorostovsky, K., Hauglund, K., Forsberg, R., & Engdahl, M. (2018). *Algorithm Theoretical Baseline Document (ATBD) for the Greenland_Ice_Sheet cci project of ESA's Climate Change Initiative, version 3.2, 28 Jun 2018 [Available from: http://www.esa-icesheets-cci.org/] (2018).*

Kimura, S., Holland, P. R., Jenkins, A., & Piggott, M. (2014). The Effect of Meltwater Plumes on the Melting of a Vertical Glacier Face. *Journal of Physical Oceanography*, *44*(2003), 3099–3117. https://doi.org/10.1175/JPO-D-13-0219.1

King, M. D., Howat, I. M., Jeong, S., Noh, M. J., Wouters, B., Noël, B., & Van Den Broeke, M. R. (2018). Seasonal to decadal variability in ice discharge from the Greenland Ice Sheet. *Cryosphere*, *12*(12), 3813–3825. https://doi.org/10.5194/tc-12-3813-2018

King, M. D., Howat, I. M., Candela, S. G., Noh, M. J., Jeong, S., Noël, B. P. Y., et al. (2020). Dynamic ice loss from the Greenland Ice Sheet driven by sustained glacier retreat. *Communications Earth & Environment*, *1*(1), 1–7. https://doi.org/10.1038/s43247-020-0001-2

Kirkham, J. D., Rosser, N. J., Wainwright, J., Vann Jones, E. C., Dunning, S. A., Lane, V. S., et al. (2017). Drift-dependent changes in iceberg size-frequency distributions. *Scientific Reports*, *7*(1), 1–10. https://doi.org/10.1038/s41598-017-14863-2

Kjeldsen, K. K., Korsgaard, N. J., Bjørk, A. A., Khan, S. A., Box, J. E., Funder, S., et al. (2015). Spatial and temporal distribution of mass loss from the Greenland Ice Sheet since AD 1900. *Nature*, *528*(7582), 396–400. https://doi.org/10.1038/nature16183

Krabill, W., Hanna, E., Huybrechts, P., Abdalati, W., Cappelen, J., Csatho, B., et al. (2004). Greenland Ice Sheet: Increased coastal thinning. *Geophysical Research Letters*, *31*(24), 1–4. https://doi.org/10.1029/2004GL021533

Krug, J., Durand, G., Gagliardini, O., & Weiss, J. (2015). Modelling the impact of submarine frontal melting and ice mélange on glacier dynamics. *The Cryosphere*, *9*(3), 989–1003. https://doi.org/10.5194/tc-9-989-2015

Kubat, I., Sayed, M., Savage, S. B., Carrieres, T., & Crocker, G. (2007). An operational iceberg deterioration model. *Proceedings of the International Offshore and Polar Engineering Conference*, 652–657.

De Lange, R., Luckman, A., & Murray, T. (2007). Improvement of satellite radar feature tracking for ice velocity derivation by spatial frequency filtering. In *IEEE Transactions on Geoscience and Remote Sensing*. https://doi.org/10.1109/TGRS.2007.896615

Lea, J. M. (2018). The Google Earth Engine Digitisation Tool (GEEDiT) and the Margin change Quantification Tool (MaQiT) – simple tools for the rapid mapping and quantification of changing Earth surface margins. *Earth Surface Dynamics*, 551–561. https://doi.org/10.5194/esurf-6-551-2018

Lea, J. M., Mair, D. W. F., Nick, F. M., Rea, B. R., van As, D., Morlighem, M., et al. (2014). Fluctuations of a Greenlandic tidewater glacier driven by changes in atmospheric forcing: observations and modelling of Kangiata Nunaata Sermia, 1859–present. *The Cryosphere Discussions*, *8*, 2005–2041. https://doi.org/10.5194/tcd-8-2005-2014

Lemos, A., Shepherd, A., Mcmillan, M., Hogg, A. E., Hatton, E., & Joughin, I. (2018). Ice velocity of Jakobshavn Isbræ , Petermann Glacier , Nioghalvfjerdsfjo rden and Zachariæ Isstrøm , 2015-2017 , from Sentinel 1-a / b SAR imagery. *The Cryosphere Discussions*, (February). Retrieved from https://doi.org/10.5194/tc-2017-251

Lewington, E. L. M., Livingstone, S. J., Clark, C. D., Sole, A. J., & Storrar, R. D. (2020). A model for interaction between conduits and surrounding hydraulically connected distributed drainage based on geomorphological evidence from Keewatin, Canada. *Cryosphere*, *14*(9), 2949–2976. https://doi.org/10.5194/tc-14-2949-2020

Losch, M. (2008). Modeling ice shelf cavities in a z coordinate ocean general circulation model. *Journal of Geophysical Research: Oceans*, *113*(8), 1–15. https://doi.org/10.1029/2007JC004368

Lucchitta, B. K., & Ferguson, H. M. (1986). Antarctica: Measuring glacier velocity from satellite images. *Science*, *234*(4780), 1105–1108. https://doi.org/10.1126/science.234.4780.1105

Lucchitta, B. K., Mullins, K. F., Allison, A. L., & Ferrigno, J. G. (1993). Antarctic glacier-

tongue velocities from Landsat images : first results. *Annals of Glaciology*, *17*, 356–366.

Luckman, A., Benn, D. I., Cottier, F., Bevan, S., Nilsen, F., & Inall, M. (2015). Calving rates at tidewater glaciers vary strongly with ocean temperature. *Nature Communications*, *6*. https://doi.org/10.1038/ncomms9566

Lüttig, C., Neckel, N., & Humbert, A. (2017). A combined approach for filtering ice surface velocity fields derived from remote sensing methods. *Remote Sensing*, *9*(10). https://doi.org/10.3390/rs9101062

Ma, Y., & Bassis, J. N. (2019). The Effect of Submarine Melting on Calving From Marine Terminating Glaciers. *Journal of Geophysical Research: Earth Surface*, *124*(2), 334–346. https://doi.org/10.1029/2018JF004820

Machguth, H., Macferrin, M., Van As, D., Box, J. E., Charalampidis, C., Colgan, W., et al. (2016). Greenland meltwater storage in firn limited by near-surface ice formation. *Nature Climate Change*, *6*(4), 390–393. https://doi.org/10.1038/nclimate2899

Magorrian, S. J., & Wells, A. J. (2016). Turbulent plumes from a glacier terminus melting in a stratified ocean. *Journal of Geophysical Research: Oceans*, *121*, 4670–4696. https://doi.org/10.1002/2016JC012132.

Maksym, T. (2019). Arctic and antarctic sea ice change: Contrasts, commonalities, and causes. *Annual Review of Marine Science*, *11*(September 2018), 187–213. https://doi.org/10.1146/annurev-marine-010816-060610

Mankoff, K. D., Straneo, F., Cenedese, C., Das, S. B., Richards, C. G., & Singh, H. (2016). Structure and dynamics of a subglacial discharge plume in a Greenlandic Fjord. *Journal of Geophysical Research: Oceans*. https://doi.org/10.1002/2016JC011764

Mankoff, K. D., Solgaard, A., Colgan, W., Ahlstrøm, A. P., Abbas Khan, S., & Fausto, R. S. (2019). Greenland Ice Sheet solid ice discharge from 1986 through March 2020. *Earth System Science Data*, *12*(2), 1367–1383. https://doi.org/10.5194/essd-12-1367-2020

Mankoff, K. D., Noël, B., Fettweis, X., Ahlstrøm, A. P., Colgan, W., Kondo, K., et al. (2020). Greenland liquid water discharge from 1958 through 2019. *Earth System Science Data*, *12*(4), 2811–2841. https://doi.org/10.5194/essd-12-2811-2020

Marsh, R., Ivchenko, V. O., Skliris, N., Alderson, S., Bigg, G. R., Madec, G., et al. (2015). NEMO-ICB (v1.0): Interactive icebergs in the NEMO ocean model globally configured at eddy-permitting resolution. *Geoscientific Model Development*, *8*(5), 1547–1562. https://doi.org/10.5194/gmd-8-1547-2015

Marshall, J., Adcroft, A., Hill, C., Perelman, L., & Heisey, C. (1997a). A finite-volume, incompressible Navier Stokes model for studies of the ocean on parallel computers. *Journal of Geophysical Research*, *102*(C3), 5753. https://doi.org/10.1029/96JC02775

Marshall, J., Hill, C., Perelman, L., & Adcroft, A. (1997b). Hydrostatic, quasi-hydrostatic, and nonhydrostatic ocean modeling. *Journal of Geophysical Research*, *102*(C3), 5733. https://doi.org/10.1029/96JC02776

Marson, J. M., Myers, P. G., Hu, X., & Le Sommer, J. (2018). Using Vertically Integrated Ocean Fields to Characterize Greenland Icebergs' Distribution and Lifetime. *Geophysical Research Letters*, *45*(9), 4208–4217. https://doi.org/10.1029/2018GL077676

Martin, T., & Adcroft, A. (2010). Parameterizing the fresh-water flux from land ice to ocean with interactive icebergs in a coupled climate model. *Ocean Modelling*, *34*(3–4), 111–124. https://doi.org/10.1016/j.ocemod.2010.05.001

Matsumoto, K. (1996). An iceberg drift and decay model to compute the ice-rafted debris and iceberg meltwater flux: Application to the interglacial North Atlantic. *Paleoceanography*, *11*(6), 729–742. https://doi.org/10.1029/96PA02712

McKinley, G. A., Follows, M. J., Marshall, J., & Fan, S. M. (2003). Interannual variability of air-sea O2 fluxes and the determination of CO2 sinks using atmospheric O2/N2. *Geophysical Research Letters*, *30*(3), 10–13. https://doi.org/10.1029/2002GL016044

McPhee, M. G. (1992). Turbulent heat flux in the upper ocean under sea ice. *Journal of Geophysical Research*, *97*(C4), 5365. https://doi.org/10.1029/92JC00239

McPhee, M. G., Kottmeier, C., & Morison, J. H. (1999). Ocean Heat Flux in the Central Weddell Sea during Winter. *Journal of Physical Oceanography*, *29*(6), 1166–1179. https://doi.org/10.1175/1520-0485(1999)029<1166:OHFITC>2.0.CO;2

Mellor, G. L., McPhee, M. G., & Steele, M. (1986). Ice-Seawater Turbulent Boundary

Layer Interaction with Melting or Freezing. *Journal of Physical Oceanography*. https://doi.org/10.1175/1520-0485(1986)016<1829:ISTBLI>2.0.CO;2

Meredith, M., Sommerkorn, M., Cassotta, S., Derksen, C., Ekaykin, A., Hollowed, A., et al. (2020). Special Report on Ocean and Cryosphere in a Changing Climate: Polar Regions, 203–320. https://doi.org/10.1016/S1366-7017(01)00066-6

Merino, N., Le Sommer, J., Durand, G., Jourdain, N. C., Madec, G., Mathiot, P., & Tournadre, J. (2016). Antarctic icebergs melt over the Southern Ocean : Climatology and impact on sea ice. *Ocean Modelling*, *104*, 99–110. https://doi.org/10.1016/j.ocemod.2016.05.001

Miles, K. E., Hubbard, B., Irvine-Fynn, T. D. L., Miles, E. S., Quincey, D. J., & Rowan, A. V. (2020). Hydrology of debris-covered glaciers in High Mountain Asia. *Earth-Science Reviews*, *207*(April), 103212. https://doi.org/10.1016/j.earscirev.2020.103212

Moon, T., Joughin, I., Smith, B., & Howat, I. (2012). 21st-Century Evolution of Greenland Outlet Glacier Velocities. *Science*, *336*(May), 576–578. https://doi.org/10.1126/science.1219985

Moon, T., Joughin, I., Smith, B., van den Broeke, M. R., van de Berg, W. J., Noël, B., & Usher, M. (2014). Distinct patterns of seasonal Greenland glacier velocity. *Geophysical Research Letters*, *41*(20), 7209–7216. https://doi.org/10.1002/2014GL061836

Moon, T., Joughin, I., & Smith, B. (2015). Seasonal to multiyear variability of glacier surface velocity, terminus position, and sea ice/ice mélange in northwest Greenland. *Journal of Geophysical Research: Earth Surface*, *120*, 818–833. https://doi.org/10.1002/2015JF003494

Moon, T., Sutherland, D. A., Carroll, D., Felikson, D., Kehrl, L., & Straneo, F. (2017). Subsurface iceberg melt key to Greenland fjord freshwater budget. *Nature Geoscience*. https://doi.org/10.1038/s41561-017-0018-z

Moon, T., Ahlstrøm, A., Goelzer, H., Lipscomb, W., & Nowicki, S. (2018). Rising Oceans Guaranteed: Arctic Land Ice Loss and Sea Level Rise. *Current Climate Change Reports*, *4*(3), 211–222. https://doi.org/10.1007/s40641-018-0107-0

Moon, T. A., Gardner, A. S., Csatho, B., Parmuzin, I., & Fahnestock, M. A. (2020). Rapid

Reconfiguration of the Greenland Ice Sheet Coastal Margin. *Journal of Geophysical Research: Earth Surface*, *125*(11), 1–16. https://doi.org/10.1029/2020JF005585

Moore, G. W. K., & Renfrew, I. A. (2005). Tip jets and barrier winds: A QuikSCAT climatology of high wind speed events around Greenland. *Journal of Climate*, *18*(18), 3713–3725. https://doi.org/10.1175/JCLI3455.1

Morlighem, M., Williams, C. N., Rignot, E., An, L., Arndt, J. E., Bamber, J. L., et al. (2017). BedMachine v3: Complete Bed Topography and Ocean Bathymetry Mapping of Greenland From Multibeam Echo Sounding Combined With Mass Conservation. *Geophysical Research Letters*, *44*(21), 11,051-11,061. https://doi.org/10.1002/2017GL074954

Mortensen, J., Lennert, K., Bendtsen, J., & Rysgaard, S. (2011). Heat sources for glacial melt in a sub-Arctic fjord (Godthåbsfjord) in contact with the Greenland Ice Sheet. *Journal of Geophysical Research: Oceans*, *116*(January), 1–13. https://doi.org/10.1029/2010JC006528

Mortensen, J., Bendtsen, J., Motyka, R. J., Lennert, K., Truffer, M., Fahnestock, M., & Rysgaard, S. (2013). On the seasonal freshwater stratification in the proximity of fast-flowing tidewater outlet glaciers in a sub-Arctic sill fjord. *Journal of Geophysical Research: Oceans*, *118*(3), 1382–1395. https://doi.org/10.1002/jgrc.20134

Mortensen, J., Bendtsen, J., Lennert, K., & Rysgaard, S. (2014). Seasonal variability of the circulation system in a west Greenland tidewater outlet glacier fjord, Godthåbsfjord (64°N). *Journal of Geophysical Research: Earth Surface*, 2591–2603. https://doi.org/10.1002/2014JF003267.

Mortensen, J., Rysgaard, S., Arendt, K. E., Juul-Pedersen, T., Søgaard, D. H., Bendtsen, J., & Meire, L. (2018). Local Coastal Water Masses Control Heat Levels in a West Greenland Tidewater Outlet Glacier Fjord. *Journal of Geophysical Research: Oceans*, *123*, 1–16. https://doi.org/10.1029/2018JC014549

Morton, B. R., Taylor, G., & Turner, J. S. (1956). Turbulent gravitational convection from maintained and instantaneous sources. *Proceedings of the Royal Society of London, Series A*, *234*, 1–23. https://doi.org/doi:10.1098/rspa.1956.0011

Motyka, R. J., Dryer, W. P., Amundson, J., Truffer, M., & Fahnestock, M. (2013). Rapid

submarine melting driven by subglacial discharge, LeConte Glacier, Alaska. *Geophysical Research Letters*, *40*, 5153–5158. https://doi.org/10.1002/grl.51011

Motyka, R. J., Cassotto, R., Truffer, M., Kjeldsen, K. K., Van As, D., Korsgaard, N. J., et al. (2017). Asynchronous behavior of outlet glaciers feeding Godthabsfjord (Nuup Kangerlua) and the triggering of Narsap Sermia's retreat in SW Greenland. *Journal of Glaciology*, *63*(238), 288–308. https://doi.org/10.1017/jog.2016.138

Mouginot, J., Rignot, E., Bjørk, A. A., van den Broeke, M., Millan, R., Morlighem, M., et al. (2019). Forty-six years of Greenland Ice Sheet mass balance from 1972 to 2018. *Proceedings of the National Academy of Sciences of the United States of America*, *116*(19), 9239–9244. https://doi.org/10.1073/pnas.1904242116

Moyer, A. N., Nienow, P. W., Gourmelen, N., Sole, A. J., & Slater, D. A. (2017). Estimating Spring Terminus Submarine Melt Rates at a Greenlandic Tidewater Glacier Using Satellite Imagery. *Frontiers in Earth Science*, *5*(December), 1–13. https://doi.org/10.3389/feart.2017.00107

Moyer, A. N., Sutherland, D. A., Nienow, P. W., & Sole, A. J. (2019). Seasonal Variations in Iceberg Freshwater Flux in Sermilik Fjord, Southeast Greenland From Sentinel-2 Imagery. *Geophysical Research Letters*, *46*(15), 8903–8912. https://doi.org/10.1029/2019GL082309

Murray, T., Scharrer, K., James, T. D., Dye, S. R., Hanna, E., Booth, A. D., et al. (2010). Ocean regulation hypothesis for glacier dynamics in southeast Greenland and implications for ice sheet mass changes. *Journal of Geophysical Research*, *115*(F3), F03026. https://doi.org/10.1029/2009JF001522

Myers, P. G., Kulan, N., & Ribergaard, M. H. (2007). Irminger water variability in the West Greenland Current. *Geophysical Research Letters*, *34*(17), 2–7. https://doi.org/10.1029/2007GL030419

Nagler, T., Rott, H., Hetzenecker, M., Wuite, J., & Potin, P. (2015). The Sentinel-1 Mission: New Opportunities for Ice Sheet Observations. *Remote Sensing*, *7*(7), 9371–9389. https://doi.org/10.3390/rs70709371

Nanni, U., Gimbert, F., Vincent, C., Gräff, D., Walter, F., Piard, L., & Moreau, L. (2020). Quantification of seasonal and diurnal dynamics of subglacial channels using seismic observations on an Alpine glacier. *Cryosphere*, *14*(5), 1475–1496.

https://doi.org/10.5194/tc-14-1475-2020

Neshyba, S. (1980). On the size distribution of Antarctic icebergs. *Cold Regions Science and Technology*, *1*, 241–248.

Nick, F. M., Vieli, A., Howat, I. M., & Joughin, I. (2009). Large-scale changes in Greenland outlet glacier dynamics triggered at the terminus. *Nature Geoscience*, *2*(2), 110–114. https://doi.org/10.1038/ngeo394

Nick, F. M., Vieli, A., Andersen, M. L., Joughin, I., Payne, A., Edwards, T. L., et al. (2013). Future sea-level rise from Greenland's main outlet glaciers in a warming climate. *Nature*, *497*(7448), 235–8. https://doi.org/10.1038/nature12068

Nienow, P., Sharp, M., & Willis, I. (1998). Seasonal changes in the morphology of the subglacial drainage system, Haut Glacier d'Arolla, Switzerland. *Earth Surface Processes and Landforms*, *23*(9), 825–843. https://doi.org/10.1002/(SICI)1096-9837(199809)23:9<825::AID-ESP893>3.0.CO;2-2

Nienow, P. W., Sole, A. J., Slater, D. A., & Cowton, T. R. (2017). Recent Advances in Our Understanding of the Role of Meltwater in the Greenland Ice Sheet System. *Current Climate Change Reports*. https://doi.org/10.1007/s40641-017-0083-9

Noël, B., Berg, W. J. Van De, Machguth, H., Lhermitte, S., Howat, I., & Fettweis, X. (2016). A daily , 1 km resolution dataset of downscaled Greenland ice sheet surface mass balance (1958-2015). *The Cryosphere Discussions*, (May), 1–29. https://doi.org/10.5194/tc-2016-145

Noël, B., Van De Berg, W. J., Van Wessem, J. M., Van Meijgaard, E., Van As, Di., Lenaerts, J. T. M., et al. (2018). Modelling the climate and surface mass balance of polar ice sheets using RACMO2 - Part 1: Greenland (1958-2016). *Cryosphere*, *12*(3), 811–831. https://doi.org/10.5194/tc-12-811-2018

Noël, B., van de Berg, W. J., Lhermitte, S., & van den Broeke, M. R. (2019). Rapid ablation zone expansion amplifies north Greenland mass loss. *Science Advances*, *5*(9), 2–11. https://doi.org/10.1126/sciadv.aaw0123

O'Leary, M., & Christoffersen, P. (2013). Calving on tidewater glaciers amplified by submarine frontal melting. *Cryosphere*, *7*, 119–128. https://doi.org/10.5194/tc-7-119-2013

Olver, S., & Townsend, A. (2013). Fast inverse transform sampling in one and two dimensions. *ArXiv*, 24–29. Retrieved from http://arxiv.org/abs/1307.1223

Orheim, O. (1987). Icebergs in the Southern Ocean. *Annals of Glaciology*, *9*, 241–242. https://doi.org/10.1017/s0260305500000793

Peters, I. R., Amundson, J. M., Cassotto, R., Fahnestock, M., Darnell, K. N., Truffer, M., & Zhang, W. W. (2015). Dynamic jamming of iceberg-choked fjords. *Geophysical Research Letters*, *42*(4), 1122–1129. https://doi.org/10.1002/2014GL062715

Pfeffer, W. T. (2007). A simple mechanism for irreversible tidewater glacier retreat. *Journal of Geophysical Research: Earth Surface*, *112*(August), 1–12. https://doi.org/10.1029/2006JF000590

Polyakov, I. V., Beszczynska, A., Carmack, E. C., Dmitrenko, I. A., Fahrbach, E., Frolov, I. E., et al. (2005). One more step toward a warmer Arctic. *Geophysical Research Letters*, *32*(17), 1–4. https://doi.org/10.1029/2005GL023740

Porter, C., Morin, P., Howat, I., Noh, M-J., Bates, B., Peterman, K. et al. (2018). "ArcticDEM", https://doi.org/10.7910/DVN/OHHUKH, Harvard Dataverse, V1, [13 March 2020].

Porter, D. F., Tinto, K. J., Boghosian, A., Cochran, J. R., Bell, R. E., Manizade, S. S., & Sonntag, J. G. (2014). Bathymetric control of tidewater glacier mass loss in northwest Greenland. *Earth and Planetary Science Letters*, *401*, 40–46. https://doi.org/10.1016/j.epsl.2014.05.058

Pritchard, H. D., Arthern, R. J., Vaughan, D. G., & Edwards, L. A. (2009). Extensive dynamic thinning on the margins of the Greenland and Antarctic ice sheets. *Nature*, *461*(7266), 971–5. https://doi.org/10.1038/nature08471

Rackow, T., Wesche, C., Timmermann, R., Hellmer, H. H., Juricke, S., & Jung, T. (2017). A simulation of small to giant Antarctic iceberg evolution: Differential impact on climatology estimates. *Journal of Geophysical Research: Oceans*, *122*, 3170–3190. https://doi.org/10.1002/2016JC012513.

Rada, C., & Schoof, C. (2018). Channelized, distributed, and disconnected: Subglacial drainage under a valley glacier in the Yukon. *Cryosphere*, *12*(8), 2609–2636. https://doi.org/10.5194/tc-12-2609-2018

Rezvanbehbahani, S., Stearns, L. A., Keramati, R., Shankar, S., & van der Veen, C. J. (2020). Significant contribution of small icebergs to the freshwater budget in Greenland fjords. *Communications Earth & Environment*, *1*(1), 1–7. https://doi.org/10.1038/s43247-020-00032-3

Rignot, E., & Kanagaratnam, P. (2006). Changes in the velocity structure of the Greenland ice sheet. *Nature*, 1–43.

Rignot, E., Koppes, M., & Velicogna, I. (2010). Rapid submarine melting of the calving faces of West Greenland glaciers. *Nature Geoscience*, *3*(3), 187–191. https://doi.org/10.1038/ngeo765

Rignot, E., Fenty, I., Menemenlis, D., & Xu, Y. (2012). Spreading of warm ocean waters around Greenland as a possible cause for glacier acceleration. *Annals of Glaciology*, *53*(60), 257–266. https://doi.org/10.3189/2012AoG60A136

Rignot, E., Fenty, I., Xu, Y., Cai, C., & Kemp, C. (2015). Undercutting of marine-terminating glaciers in West Greenland. *Geophysical Research Letters*, *42*, 5909–5917. https://doi.org/10.1002/2015GL064236

Rignot, E., Xu, Y., Menemenlis, D., Mouginot, J., Scheuchl, B., Li, X., et al. (2016). Modeling of ocean-induced ice melt rates of five west Greenland glaciers over the past two decades. *Geophysical Research Letters*. https://doi.org/10.1002/2016GL068784

Robel, A. A. (2017). Thinning sea ice weakens buttressing force of iceberg mélange and promotes calving. *Nature Communications*, *8*. https://doi.org/10.1038/ncomms14596

Romanov, Y. A., Romanova, N. A., & Romanov, P. (2017). Geographical distribution and volume of Antarctic icebergs derived from ship observation data. *Annals of Glaciology*, *58*(74), 28–40. https://doi.org/10.1017/aog.2017.2

Rosenau, R., Scheinert, M., & Dietrich, R. (2015). A processing system to monitor Greenland outlet glacier velocity variations at decadal and seasonal time scales utilizing the Landsat imagery. *Remote Sensing of Environment*. https://doi.org/10.1016/j.rse.2015.07.012

Röthlisberger, H. (1972). Water pressure in intra- and subglacial channels. *Journal of Glaciology*, *11*(62), 177–203.

Ryan, J. C., Hubbard, A. L., Box, J. E., Todd, J., Christoffersen, P., Carr, J. R., et al. (2015). UAV photogrammetry and structure from motion to assess calving dynamics at Store Glacier, a large outlet draining the Greenland ice sheet. *The Cryosphere*, *9*, 1–11. https://doi.org/10.5194/tc-9-1-2015

Salcedo-Castro, J., Bourgault, D., & deYoung, B. (2011). Circulation induced by subglacial discharge in glacial fjords: Results from idealized numerical simulations. *Continental Shelf Research*, *31*(13), 1396–1406. https://doi.org/10.1016/j.csr.2011.06.002

Salcedo-Castro, J., Bourgault, D., Bentley, S. J., & deYoung, B. (2013). Non-hydrostatic modeling of cohesive sediment transport associated with a subglacial buoyant jet in glacial fjords: A process-oriented approach. *Ocean Modelling*, *63*, 30–39. https://doi.org/10.1016/j.ocemod.2012.12.005

Sandwell, D., Mellors, R., Tong, X., Wei, M., & Wessel, P. (2011). An InSAR Processing System Based on Generic Mapping Tools. *Scripps Institution of Oceanography Technical Report*.

Scambos, T. A., Dutkiewicz, M. J., Wilson, J. C., & Bindschadler, R. A. (1992). Application of image cross-correlation to the measurement of glacier velocity using satellite image data. *Remote Sensing of Environment*, *42*(3), 177–186. https://doi.org/10.1016/0034-4257(92)90101-O

Schild, K. M., Hawley, R. L., & Morriss, B. F. (2016). Subglacial hydrology at Rink Isbræ, West Greenland inferred from sediment plume appearance. *Annals of Glaciology*, (April), 1–10. https://doi.org/10.1017/aog.2016.1

Schild, K. M., Sutherland, D. A., Elosegui, P., & Duncan, D. (2021). Measurements of iceberg melt rates using high-resolution GPS and iceberg surface scans. *Geophysical Research Letters*. doi: 10.1029/2020GL089765.

Schloesser, F., Friedrich, T., Timmermann, A., DeConto, R. M., & Pollard, D. (2019). Antarctic iceberg impacts on future Southern Hemisphere climate. *Nature Climate Change*, *9*(9), 672–677. https://doi.org/10.1038/s41558-019-0546-1

Schoof, C. (2007). Ice sheet grounding line dynamics: Steady states, stability, and hysteresis. *Journal of Geophysical Research*, *112*(F3), F03S28. https://doi.org/10.1029/2006JF000664

Schoof, C. (2010). Ice-sheet acceleration driven by melt supply variability. *Nature*, *468*(7325), 803–6. https://doi.org/10.1038/nature09618

Schuur, E. A. G., McGuire, A. D., Schädel, C., Grosse, G., Harden, J. W., Hayes, D. J., et al. (2015). Climate change and the permafrost carbon feedback. *Nature*, *520*(7546), 171–179. https://doi.org/10.1038/nature14338

Sciascia, R., Straneo, F., Cenedese, C., & Heimbach, P. (2013). Seasonal variability of submarine melt rate and circulation in an East Greenland fjord. *Journal of Geophysical Research: Oceans*, *118*(5), 2492–2506. https://doi.org/10.1002/jgrc.20142

Sciascia, R., Cenedese, C., Nicoli, D., Heimbach, P., & Straneo, F. (2014). Impact of periodic intermediary flows on submarine melting of a Greenland glacier. *Journal of Geophysical Research: Oceans*, 2121–2128. https://doi.org/10.1002/jgrc.20224

Shapero, D. R., Joughin, I. R., Poinar, K., Morlighem, M., & Gillet-Chaulet, F. (2016). Basal resistance for three of the largest Greenland outlet glaciers. *Journal of Geophysical Research F: Earth Surface*, *121*(1), 168–180. https://doi.org/10.1002/2015JF003643

Shepherd, A., & Nowicki, S. (2017). Improvements in ice-sheet sea-level projections. *Nature Climate Change*, *7*(10), 672–674. https://doi.org/10.1038/nclimate3400

Shepherd, A., Ivins, E., Rignot, E., Smith, B., van den Broeke, M., Velicogna, I., et al. (2020). Mass balance of the Greenland Ice Sheet from 1992 to 2018. *Nature*, *579*(7798), 233–239. https://doi.org/10.1038/s41586-019-1855-2

Shreve, R. L. (1972). Movement of water in glaicers. *J. Glaciol.*, *11*(62), 205–214.

Silva, T. A. M., Bigg, G. R., & Nicholls, K. W. (2006). Contribution of giant icebergs to the Southern Ocean freshwater flux. *Journal of Geophysical Research: Oceans*, *111*(3), 1–8. https://doi.org/10.1029/2004JC002843

Slater, D. A. (2017). Modelling submarine melting at tidewater glaciers in Greenland. *Thesis submitted to the University of Edinburgh*.

Slater, D. A., Nienow, P., Sole, A., Cowton, T., Mottram, R., Langen, P., & Mair, D. (2017). Spatially distributed runoff at the grounding line of a large Greenlandic tidewater glacier inferred from plume modelling. *Journal of Glaciology*, *63*(238),

309–323. https://doi.org/10.1017/jog.2016.139

Slater, D. A., Nienow, P. W., Cowton, T. R., Goldberg, D. N., & Sole, a. J. (2015). Effect of near-terminus subglacial hydrology on tidewater glacier submarine melt rates. *Geophysical Research Letters*, n/a-n/a. https://doi.org/10.1002/2014GL062494

Slater, D. A., Goldberg, D. N., Nienow, P. W., & Cowton, T. R. (2016). Scalings for Submarine Melting at Tidewater Glaciers from Buoyant Plume Theory. *Journal of Physical Oceanography*.

Slater, D. A., Straneo, F., Das, S. B., Richards, C. G., Wagner, T. J. W., & Nienow, P. W. (2018). Localized Plumes Drive Front-Wide Ocean Melting of A Greenlandic Tidewater Glacier. *Geophysical Research Letters*, *45*(22), 12,350-12,358. https://doi.org/10.1029/2018GL080763

Slater, D. A., Straneo, F., Felikson, D., Little, C. M., Goelzer, H., Fettweis, X., & Holte, J. (2019). Estimating Greenland tidewater glacier retreat driven by submarine melting. *Cryosphere*, *13*(9), 2489–2509. https://doi.org/10.5194/tc-13-2489-2019

Slater, D. A., Felikson, D., Straneo, F., Goelzer, H., Little, C. M., Morlighem, M., et al. (2020). Twenty-first century ocean forcing of the Greenland ice sheet for modelling of sea level contribution. *Cryosphere*, *14*(3), 985–1008. https://doi.org/10.5194/tc-14-985-2020

Sole, A., Nienow, P., Bartholomew, I., Mair, D., Cowton, T., Tedstone, A., & King, M. A. (2013). Winter motion mediates dynamic response of the Greenland Ice Sheet to warmer summers. *Geophysical Research Letters*, *40*(15), 3940–3944. https://doi.org/10.1002/grl.50764

Sole, A. J., Mair, D. W. F., Nienow, P. W., Bartholomew, I. D., King, M. A., Burke, M. J., & Joughin, I. (2011). Seasonal speedup of a Greenland marine-terminating outlet glacier forced by surface melt-induced changes in subglacial hydrology. *Journal of Geophysical Research: Earth Surface*, *116*(3), 1–11. https://doi.org/10.1029/2010JF001948

Solgaard, A., & Kusk, A. (2019). Programme for Monitoring of the Greenland Ice Sheet (PROMICE): Greenland ice velocity. Geological Survey of Denmark and Greenland (GEUS). https://doi.org/10.22008/PROMICE/DATA/SENTINEL1ICEVELOCITY/GREEN

LANDICESHEET/V1.0.0

Stammer, D., Wunsch, C., Giering, R., Eckert, C., Heimbach, P., Marotzke, J., et al. (2003). Volume, heat, and freshwater transports of the global ocean circulation 1993-2000, estimated from a general circulation model constrained by World Ocean Circulation Experiment (WOCE) data. *Journal of Geophysical Research: Oceans*, *108*(1), 1–23. https://doi.org/10.1029/2001jc001115

Starr, A., Hall, I., Barker, S., Rackow, T., Zhang, X., Hemming, S., et al. (2020). Antarctic icebergs reorganise ocean circulation during pleistocene glacials. *Nature*, *589*(January). https://doi.org/10.1038/s41586-020-03094-7

Stephenson, G. R., Sprintall, J., Gille, S. T., Vernet, M., Helly, J. J., & Kaufmann, R. S. (2011). Subsurface melting of a free-floating Antarctic iceberg. *Deep-Sea Research Part II: Topical Studies in Oceanography*, *58*(11–12), 1336–1345. https://doi.org/10.1016/j.dsr2.2010.11.009

Stern, A. A., Adcroft, A., & Sergienko, O. (2016). The effects of Antarctic iceberg calving-size distribution in a global climate model. *Journal of Geophysical Research: Oceans*, *121*(9), 5773–5788. https://doi.org/10.1002/2016JC012132.

Stevens, L. A., Behn, M. D., Das, S. B., Joughin, I., Noel, B. P. Y., van den Broeke, M. R., & Herring, T. (2016). Greenland Ice Sheet flow response to runoff variability, 1–9. https://doi.org/10.1002/2016GL070414.

Stipa, T. (2002). The dynamics of the N/P ratio and stratification in a large nitrogen-limited estuary as a result of upwelling: A tendency for offshore Nodularia blooms. *Hydrobiologia*, *487*, 219–227. https://doi.org/10.1023/A:1022990116669

Straneo, F., & Cenedese, C. (2015). The Dynamics of Greenland's Glacial Fjords and Their Role in Climate. *Annual Review of Marine Science*, *7*, 89–112. https://doi.org/10.1146/annurev-marine-010213-135133

Straneo, F., & Heimbach, P. (2013). North Atlantic warming and the retreat of Greenland's outlet glaciers. *Nature*, *504*, 36–43. https://doi.org/10.1038/nature12854

Straneo, F., Hamilton, G. S., Sutherland, D. A., Stearns, L. A., Davidson, F., Hammill, M. O., et al. (2010). Rapid circulation of warm subtropical waters in a major glacial fjord in East Greenland. *Nature Geoscience*, *3*(3), 182–186.

https://doi.org/10.1038/ngeo764

Straneo, F., Curry, R. G., Sutherland, D. a., Hamilton, G. S., Cenedese, C., Våge, K., & Stearns, L. a. (2011). Impact of fjord dynamics and glacial runoff on the circulation near Helheim Glacier. *Nature Geoscience*, *4*(5), 322–327. https://doi.org/10.1038/ngeo1109

Straneo, F., Sutherland, D. a., Holland, D., Gladish, C., Hamilton, G. S., Johnson, H. L., et al. (2012). Characteristics of ocean waters reaching Greenland's glaciers. *Annals of Glaciology*, *53*(60), 202–210. https://doi.org/10.3189/2012AoG60A059

Straneo, F., Hamilkton, G. S., Stearns, L. A., & Sutherland, D. A. (2016). Connecting the Greenland Ice Sheet and the Ocean. *Oceanography*, *29*(4).

Strozzi, T., Luckman, A., Murray, T., Wegmuler, U., & Werner, C. L. (2002). Glacier motion estimation using SAR offset-tracking procedures. *IEEE Transactions on Geoscience and Remote Sensing*, *40*, 2384–2391. https://doi.org/10.1109/TGRS.2002.805079

Sugiyama, S., Sakakibara, D., Tsutaki, S., Maruyama, M., & Sawagaki, T. (2015). Glacier dynamics near the calving front of Bowdoin Glacier, northwestern Greenland. *Journal of Glaciology*, *61*(226), 223–232. https://doi.org/10.3189/2015JoG14J127

Sulak, D. J., Sutherland, D. A., Enderlin, E. M., Stearns, L. A., & Hamilton, G. S. (2017). Iceberg properties and distributions in three Greenlandic fjords using satellite imagery. *Annals of Glaciology*, (May), 1–15. https://doi.org/10.1017/aog.2017.5

Sundal, A. V., Shepherd, A., Nienow, P., Hanna, E., Palmer, S., & Huybrechts, P. (2011). Melt-induced speed-up of Greenland ice sheet offset by efficient subglacial drainage. *Nature*, *469*(7331), 521–524. https://doi.org/10.1038/nature09740

Sutherland, D. A, Straneo, F., & Pickart, R. S. (2014a). Characteristics and dynamics of two major greenland glacial fjords. *Journal of Geophysical Research: Earth Surface*, 2121–2128. https://doi.org/10.1002/jgrc.20224

Sutherland, D. A., & Pickart, R. S. (2008). The East Greenland Coastal Current: Structure, variability, and forcing. *Progress in Oceanography*, *78*(1), 58–77. https://doi.org/10.1016/j.pocean.2007.09.006

Sutherland, D. A., & Straneo, F. (2012). Estimating ocean heat transports and submarine

melt rates in sermilik fjord, greenland, using lowered acoustic doppler current profiler (LADCP) velocity profiles. *Annals of Glaciology*, *53*(60), 50–58. https://doi.org/10.3189/2012AoG60A050

Sutherland, D. A., Straneo, F., Stenson, G. B., Davidson, F. J. M., Hammill, M. O., & Rosing-Asvid, A. (2013). Atlantic water variability on the SE Greenland continental shelf and its relationship to SST and bathymetry. *Journal of Geophysical Research: Oceans*, *118*(2), 847–855. https://doi.org/10.1029/2012JC008354

Sutherland, D. A., Roth, G. E., Hamilton, G. S., Mernild, S. H., Stearns, L. A., & Straneo, F. (2014b). Quantifying flow regimes in a Greenland glacial fjord using iceberg drifters. *Geophysical Research Letters*, *41*, 8411–8420. https://doi.org/10.1002/2014GL062256.Received

Sutherland, D. A., Jackson, R. H., Kienholz, C., Amundson, J. M., Dryer, W. P., Duncan, D., et al. (2019). Direct observations of submarine melt and subsurface geometry at a tidewater glacier. *Science*, *365*(6451), 369–374. https://doi.org/10.1126/science.aax3528

Tedesco, M., Fettweis, X., Mote, T., Wahr, J., Alexander, P., Box, J. E., & Wouters, B. (2013). Evidence and analysis of 2012 Greenland records from spaceborne observations, a regional climate model and reanalysis data. *The Cryosphere*, *7*(2), 615–630. https://doi.org/10.5194/tc-7-615-2013

Tedstone, A. J., Nienow, P. W., Gourmelen, N., & Sole, A. J. (2014). Greenland ice sheet annual motion insensitive to spatial variations in subglacial hydraulic structure. *Geophysical Research Letters*, *41*, 1–8. https://doi.org/10.1002/2014GL062386

Thielicke, W. (2014). *The flapping flight of birds: Analysis and application*. *Analysis and application*. https://doi.org/http://irs.ub.rug.nl/ppn/382783069

Thielicke, W., & Stamhuis, E. J. (2014). PIVlab – Towards User-friendly, Affordable and Accurate Digital Particle Image Velocimetry in MATLAB. *Journal of Open Research Software*, *2*(1), e30. https://doi.org/10.5334/jors.bl

Todd, J., & Christoffersen, P. (2014). Are seasonal calving dynamics forced by buttressing from ice mélange or undercutting by melting? Outcomes from full-Stokes simulations of Store Glacier, West Greenland. *The Cryosphere*, *8*(6), 2353–2365. https://doi.org/10.5194/tc-8-2353-2014

Todd, J., Christoffersen, P., Zwinger, T., Räback, P., & Benn, D. I. (2019). Sensitivity of a calving glacier to ice-ocean interactions under climate change: New insights from a 3-d full-stokes model. *Cryosphere*, *13*(6), 1681–1694. https://doi.org/10.5194/tc-13-1681-2019

Torres, R., Snoeii, P., Geudtner, D., Bibby, D., Davidson, M., Atterna, E., et al. (2012). GMES Sentinel-1 mission. *Remote Sensing of Environment*, 120, 9-24. https://doi.org/10.1016/j.rse.2011.05.028

Tournadre, J., Girard-Ardhuin, F., & Legrésy, B. (2012). Antarctic icebergs distributions, 2002-2010. *Journal of Geophysical Research: Oceans*, *117*(5), 2002–2010. https://doi.org/10.1029/2011JC007441

Tournadre, J., Bouhier, N., Girard-Ardhuin, F., & Remy, F. (2016). Antarctic icebergs distributions 1992–2014. *Journal of Geophysical Research: Oceans*, *121*, 327–349. https://doi.org/10.1002/2015JC011178.

Truffer, M., & Motyka, R. J. (2016). Where glaciers meet water: Subaqueous melt and its relevance to glaciers in various settings. *Reviews of Geophysics*. https://doi.org/10.1002/2015RG000494

Tuckett, P. A., Ely, J. C., Sole, A. J., Livingstone, S. J., Davison, B. J., van Wessem, M. J., & Howard, J. (2019). Rapid accelerations of Antarctic Peninsula outlet glaciers driven by surface melt. *Nature Communications*, *10*. https://doi.org/10.1038/s41467-019-12039-2

Vermassen, F., Bjørk, A. A., Sicre, M. A., Jaeger, J. M., Wangner, D. J., Kjeldsen, K. K., et al. (2020). A Major Collapse of Kangerlussuaq Glacier's Ice Tongue Between 1932 and 1933 in East Greenland. *Geophysical Research Letters*, *47*(4), 1–9. https://doi.org/10.1029/2019GL085954

Vijay, S., Khan, S. A., Kusk, A., Solgaard, A. M., Moon, T., & Bjørk, A. A. (2019). Resolving Seasonal Ice Velocity of 45 Greenlandic Glaciers With Very High Temporal Details. *Geophysical Research Letters*, *46*(3), 1485–1495. https://doi.org/10.1029/2018GL081503

Vore, M. E., Bartholomaus, T. C., Winberry, J. P., Walter, J. I., & Amundson, J. M. (2019). Seismic Tremor Reveals Spatial Organization and Temporal Changes of Subglacial Water System. *Journal of Geophysical Research: Earth Surface*, *124*(2),

427–446. https://doi.org/10.1029/2018JF004819

Wadhams, P. (1988). Winter observations of iceberg frequencies and sizes in the south Atlantic Ocean. *Journal of Geophysical Research*, *93*(C4), 3583. https://doi.org/10.1029/jc093ic04p03583

Wager, L. R., Deer, W. A., Wager, H. G., & Manley, G. (1937). The Kangerdlugssuak Region of East Greenland. *The Geographical Journal*, *90*(5), 393–421. https://doi.org/10.1007/978-1-349-95810-8_1024

Wagner, T. J. W., Dell, R. W., & Eisenman, I. (2017). An analytical model of iceberg drift. *Journal of Physical Oceanography*, *47*(7), 1605–1616. https://doi.org/10.1175/JPO-D-16-0262.1

van de Wal, R. S. W., Boot, W., van den Broeke, M. R., Smeets, C. J. P. P., Reijmer, C. H., Donker, J. J. A., & Oerlemans, J. (2008). Large and rapid melt-induced velocity changes in the ablation zone of the Greenland Ice Sheet. *Science*, *321*(5885), 111–3. https://doi.org/10.1126/science.1158540

Van De Wal, R. S. W., Boot, W., Smeets, C. J. P. P., Snellen, H., Van Den Broeke, M. R., & Oerlemans, J. (2012). Twenty-one years of mass balance observations along the K-transect, West Greenland. *Earth System Science Data*, *4*(1), 31–35. https://doi.org/10.5194/essd-4-31-2012

Wal, R. S. W. Van De, Smeets, C. J. P. P., Boot, W., Stoffelen, M., Kampen, R. Van, Doyle, S. H., & Wilhelms, F. (2015). Self-regulation of ice flow varies across the ablation area in south-west Greenland. *The Cryosphere*, *9*, 603–611. https://doi.org/10.5194/tc-9-603-2015

Weeks, W. F., & Campbell, W. J. (1973). Icebergs as a fresh-water source: appraisal*. *Journal of Glaciology*, *12*(65), 207–233.

Weidick, A., & Bennike, O. (2007). *Quaternary glaciation history and glaciology of Jakobshavn Isbræ and the Disko Bugt region, West Greenland: A review*. *Geological Survey of Denmark and Greenland Bulletin*. https://doi.org/10.34194/geusb.v14.4985

Wettlaufer, J. S. (1991). Heat flux at the ice-ocean interface. *Journal of Geophysical Research*, *96*, 7215–7236.

Wood, M., Rignot, E., Fenty, I., An, L., Bjørk, A., van den Broeke, M., et al. (2021). Ocean forcing drives glacier retreat in Greenland. *Science Advances*, *7*(1), eaba7282. https://doi.org/10.1126/sciadv.aba7282

Xie, S., Dixon, T. H., Holland, D. M., Voytenko, D., & Vaňková, I. (2019). Rapid iceberg calving following removal of tightly packed pro-glacial mélange. *Nature Communications*, *10*(1). https://doi.org/10.1038/s41467-019-10908-4

Xu, X., Sandwell, D. T., Tymofyeyeva, E., Gonzalez-Ortega, A., & Tong, X. (2017). Tectonic and anthropogenic deformation at the cerro prieto geothermal step-over revealed by sentinel-1A insar. *IEEE Transactions on Geoscience and Remote Sensing*, *55*(9), 5284–5292. https://doi.org/10.1109/TGRS.2017.2704593

Xu, Y., Rignot, E., Menemenlis, D., & Koppes, M. (2012). Numerical experiments on subaqueous melting of Greenland tidewater glaciers in response to ocean warming and enhanced subglacial discharge. *Annals of Glaciology*, *53*(60), 229–234. https://doi.org/10.3189/2012AoG60A139

Xu, Y., Rignot, E., Fenty, I., Menemenlis, D., & Flexas, M. M. (2013). Subaqueous melting of Store Glacier, west Greenland from three-dimensional, high-resolution numerical modeling and ocean observations. *Geophysical Research Letters*, *40*, 4648–4653. https://doi.org/10.1002/grl.50825

Zhang, T., Barry, R. G., Knowles, K., Heginbottom, J. A., & Brown, J. (2008). Statistics and characteristics of permafrost and ground-ice distribution in the Northern Hemisphere. *Polar Geography*, *31*(1–2), 47–68. https://doi.org/10.1080/10889370802175895